Development of Heat-treatable Wrought Magnesium Alloys with Excellent Formability

Zehao Li

February 2021

Development of Heat-treatable Wrought Magnesium Alloys with Excellent Formability

Zehao Li
Doctoral Program in Materials Science and Engineering

Submitted to the graduate School of
Pure and Applied Sciences
in Partial Fulfillment of the Requirements
for the Degree of Doctor of Philosophy in
Engineering

at the
University of Tsukuba

Table of Contents

Chapter 1 Literature review

1.1 General introduction

As the lightest structural metal with abundant reserves, magnesium (Mg) and its alloys are of great concern since it was first discovered in by British chemist Sir Humphry Davy [1,2]. Due to the prominent weight savings, Mg alloys have been employed for a wide range of applications including transportation industries, consumer electronics, and sporting goods [3]. However, a large portion of Mg products are concentrated in automobiles.

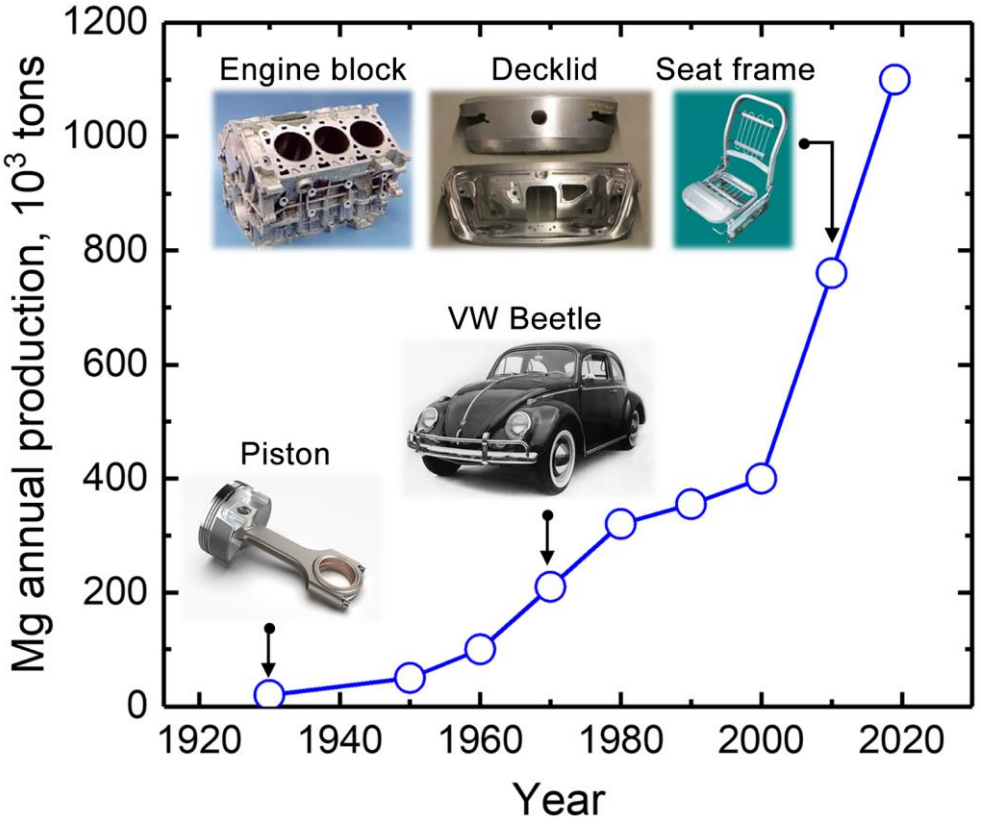

Fig. 1.1. Magnesium annual production in the period 1920−2019, and primary applications in automobiles [4,5].

Figure 1.1 shows the annual production of Mg in the past hundred years with primary applications in automotive industries [4,5]. The first utilization of Mg alloys; Mg-Al-Zn, AZ in automobile is die-cast engine pistons for racing cars in 1924. Mg productions gradually increase throughout the following 30 years with applications expanded to other casting components such as wheels, crankcases and transmission housings. With the introduction of the famous Volkswagen Beetle, the Mg consumption start to accelerate and reach a peak in 1980. The prime use of Mg in Beetles is featured by air-cooled engines and gearboxes, which save over 50 kg than those iron components. From the 1980's to 90's, Mg suffers from into a dormant period due

to the greater requirements for creep and corrosion resistance in powertrain components. The use of "high-purity" Mg-9Al-1Zn (wt.%, AZ91) and Mg-6Al-0.1Mn (wt.%, AM60) alloys lead to a higher cost compared to those of irons and steels, thus slowing down the applications of Mg products. Since 2000, a renewed attention in Mg alloys has been paid for weight-saving applications. The increasing demands for higher fuel economy and reduction of CO_2 emission stimulate the wide-range developments of Mg products in automobiles, which are not limited to casting alloys but various wrought alloys such as extrusions and sheets used for larger-scale body components. However, these wrought Mg alloys have yet to find widespread applications due to their poor formability at room temperature (RT). In addition to automotive industries, Mg alloys also show increasing applications in consumer electronics for the advantages of low density, high heat dissipation, and excellent electronic shielding capability. Fig. 1.2 shows various electronic devices fabricated by die casting, injection molding and extrusion Mg alloys [6].

Fig. 1.2. Various consumer electronics fabricated by Mg alloys [6].

1.2 Magnesium and its alloys

1.2.1 Crystal structure, deformation modes, and properties

Figure 1.3a shows a hexagonal closed packed (HCP) structure of Mg crystal; $P6_3/mmc$ space group with a staking sequence of ···ABAB··· along the [0001] direction. The lattice parameters of a = 0.321nm and c = 0.521 nm gives a c/a ratio of ~1.624, which is quite near the ideal value of 1.633 for the HCP structure. The (0001) close-packed planes and $\langle 11\bar{2}0 \rangle$ close-packed directions are indicated in Fig. 1.3b.

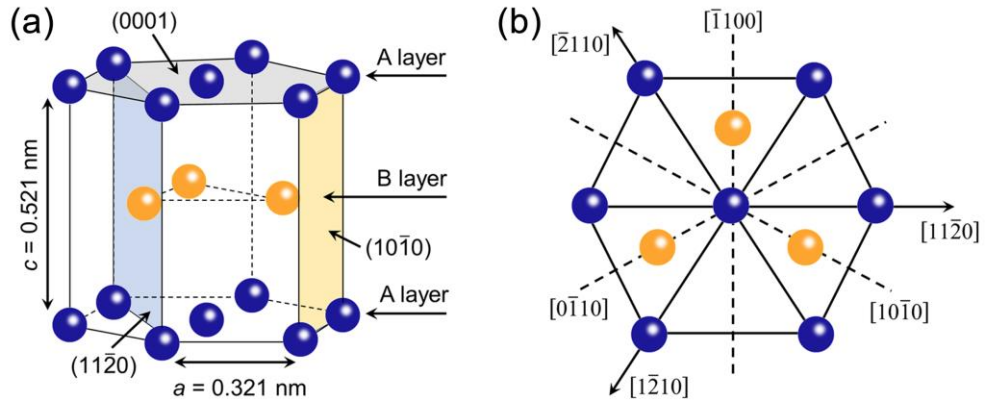

Fig. 1.3. Schematic diagrams of (a) a hexagonal unit cell of magnesium, and (b) the (0001) plane projection.

Table 1.1 summarizes the main physical and mechanical properties of Mg in comparison with other structural metals [7]. The pure Mg has the lowest density of 1.74 g/cm^3, which is 36% lighter than that of Al; 2.7 g/cm^3 and less than one quarter that of iron; 7.87 g/cm^3. The thermal conductivity of pure Mg is 156 W/(m·K), which is second to that of Al among the light metals. However, the low yield strength and poor elongation fall far behind practical applications.

Table 1.1 Physical and mechanical properties of pure Mg in comparison with other structural metals [7].

Property	Mg	Al	Fe	Ti	Cu
Density, g/cm^3	1.74	2.7	7.87	4.51	8.96
Melting point, ºC	650	660	1535	1678	1083
Thermal conductivity at 20 ~100 ºC, W/(m·K)	156	238	78	26	397
Elastic modulus, GPa	45	70	211	116	130
Yield strength, MPa	21	15-20	80-100	100-225	33
Ultimate strength, MPa	90	40-50	350	240-370	210
Specific strength, MPa·cm^3/g	51.7	18.5	44.5	82	23.4
Elongation, %	2-6	50-70	45	20	60

Figure 1.4 shows the main slip and twinning systems in Mg [8]. The characteristics of these deformation modes are summarized in Table 1.2. The $\{0001\}\langle 11\bar{2}0\rangle$ basal $\langle a\rangle$ slip is the easiest slip mode at room temperature due to the lowest critical resolved shear stress (CRSS); ~1 MPa than that of prismatic $\langle a\rangle$; 40 MPa or pyramidal $\langle c+a\rangle$ slip; 57 MPa. However, only two independent slip systems along the $\langle a\rangle$ directions by basal slip cannot satisfying arbitrary shape changes during deformation based on Von Mises criterion; at least five independent systems are required for homogenous strain. Non-basal slip on prismatic or pyramidal plane may offer additional slip systems, while the high CRSS at RT impedes their operation. Therefore, the strong anisotropy of slip modes results in the intrinsically low ductility, and thus poor formability of Mg.

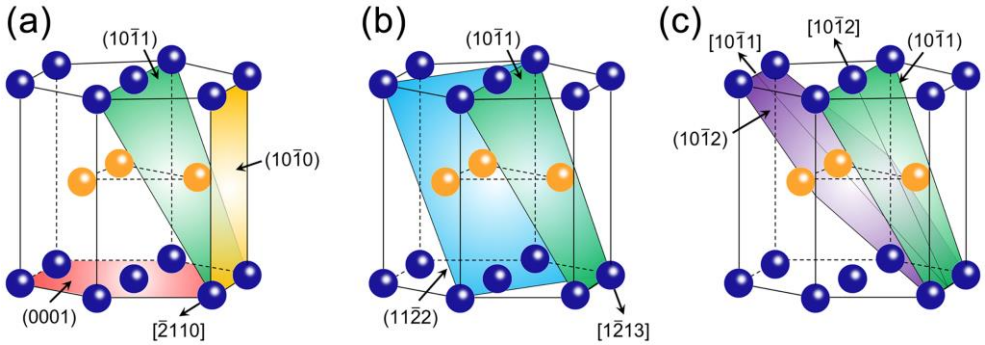

Fig. 1.4. Schematic diagrams of (a) basal, prismatic and pyramidal-I ⟨*a*⟩ slip systems, (b) pyramidal-I and II ⟨*c*+*a*⟩ slip systems, and (c) tensile and compression twin systems.

In addition to the slip deformation, twinning also plays an important role in accommodating deformation of Mg. The {10$\bar{1}$2} tensile twin with a shear strain of ~0.129 along the *c* axis is the most easily activated among various twinning modes because of a slightly higher CRSS; ~2-4 MPa than that of basal slip. Due to the high mobility of tensile twin boundaries, tensile twins can grow quickly to overtake the parent grain, resulting in high work hardening, and thus improved ductility. However, the twinning polarity, i.e. tension parallel or compression normal to the c-axis is required for operation and a relatively small shear strain; ~ 6.7% in maximum, constrain the contribution of tensile twins to deformation. In contrast, the {10$\bar{1}$1} compression twin and various double twins such as {10$\bar{1}$1}-{10$\bar{1}$2}; a secondary {10$\bar{1}$2} twin nucleates within the primary {10$\bar{1}$1} twin, Fig. 1.5 [9,10], are difficult to operate at RT due to their much higher CRSS; ~76-153 MPa than that of tensile twin. Given that favorable reorientation for basal slip; 56º and 37.5º inclined to the basal planes, the activation of compression and double twins may lead to significant strain softening and flow localization that damage the ductility.

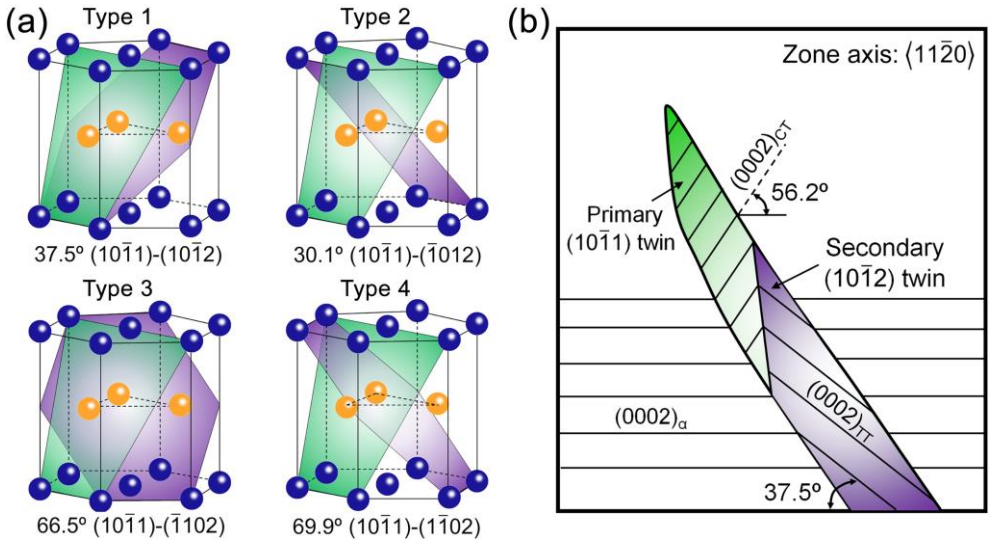

Fig. 1.5. (a) Geometrical relationships between primary {10$\bar{1}$1} compression twin (green color) and four types of secondary {10$\bar{1}$2} twin planes (purple color). (b) Schematic of a 37.5º {10$\bar{1}$1}-{10$\bar{1}$2} double twin taken from ⟨11$\bar{2}$0⟩ zone axis [9,10].

Table 1.2 The characteristics of main deformation modes in Mg [8].

Deformation mode		Burgers vector	Number of independent systems	CRSS at RT, MPa	Misorientation Axis
Basal ⟨*a*⟩ slip	{0001}⟨11$\bar{2}$0⟩		2	1	⟨1$\bar{1}$00⟩
Prismatic⟨*a*⟩ slip	{10$\bar{1}$0}⟨11$\bar{2}$0⟩	1/3⟨11$\bar{2}$0⟩	2	40	⟨0001⟩
Pyramidal-I ⟨*a*⟩ slip	{10$\bar{1}$1}⟨11$\bar{2}$0⟩		4	–	⟨10$\bar{1}$2⟩
pyramidal-II ⟨*c*+*a*⟩ slip	{11$\bar{2}$2}⟨1$\bar{2}$13⟩	1/3⟨1$\bar{2}$13⟩	5	57	⟨1$\bar{1}$00⟩
Tensile twin	{10$\bar{1}$2}⟨10$\bar{1}$1⟩			2-4	86.3º ⟨1$\bar{2}$10⟩
Compression twin	{10$\bar{1}$1}⟨10$\bar{1}$2⟩				56.2º ⟨1$\bar{2}$10⟩
Double twin	{10$\bar{1}$1}-{10$\bar{1}$2}	–	0-5	76-153	37.5º ⟨1$\bar{2}$10⟩
	{10$\bar{1}$1}-{$\bar{1}$012}				30.1º ⟨1$\bar{2}$10⟩
	{10$\bar{1}$1}-{$\bar{1}$102}				66.5º ⟨5$\bar{9}$43⟩
	{10$\bar{1}$1}-{1$\bar{1}$02}				69.9º ⟨2$\bar{4}$21⟩

1.2.2 Alloying addition

Considering the poor ductility and low strength, pure Mg is rare used for structural applications. Instead, alloying additions is an efficient approach to improve the mechanical properties of Mg alloys. Depending on the abundance and utilization cost of alloying elements, Mg alloys can be classified into Rare-Earth (RE) free alloys with common elements such as Al, Zn, Mn, Ca, and Sn etc., and RE-containing alloys which includes Ce, Gd, Y, Nd and so on. Table 1.3 summarizes the main alloying elements and their effects in Mg alloys [1]. For the non-RE elements, Al, Zn, and Sn have relatively high solubility at the eutectic temperature; 11.8, 2.4 and 3.4 at.%, which leads to considerable solid solution strengthening in the solution-treated condition. By artificial aging at low temperature e.g. 170 ºC, the solubility of these solutes substantially decreases to 6.8, 0.8, and 0.01 at.%, respectively, thus generating a large volume fraction of precipitates which provide barriers to dislocation gliding, i.e. precipitation hardening. Al, Zn, and Sn alloying also improve the ductility due to the reduced CRSS anisotropy between basal and prismatic slip. In contrast, Mn and Zr have much lower solubility in the Mg matrix, which make little effect in solid solution strengthening or precipitation hardening. However, the addition of Mn or Zr can significantly refine the grain size, thus leading to simultaneous increase of strength and ductility.

Ag and most RE elements, e.g. Y, Gd, and Nd, show similar functions as those of Al, Zn and Sn, and even higher efficiency in enhancing age-hardening response and ductility due to large atomic size and activation of non-basal slip. However, the high cost and resource scarcity limit their high-volume addition for practical use.

Instead, Ca, as a cheaper alternative to RE, has attracted considerable attention for achieving excellent formability and high strength in Mg-Zn based alloy sheets [11].

Table 1.3 Alloying elements and their effects in Mg alloys [1].

Element	Code letter	Atomic radius, Å	Solubility		Mechanical properties			
			at.%	wt.%	Solid solution strengthening	Precipitation hardening	ductility	Grain refinement
Al	A	1.43	11.8	12.7	√	√	√	–
Zn	Z	1.34	2.4	6.2	√	√	√	–
Mn	M	1.24	1.0	2.2	–	–	–	√
Ca	X	1.97	0.8	1.4	–	–	√	√
Sn	T	1.41	3.4	14.5	√	√	√	–
Zr	K	1.60	1.0	3.8	–	–	–	√
Ag	Q	1.44	3.8	15.0	√	√	√	–
Ce	E	1.82	0.1	0.5	–	–	√	–
Y	W	1.81	3.8	12.5	√	√	√	–
Gd	V	1.80	4.5	23.5	√	√	√	–
Nd	E	1.82	0.4	2.3	√	√	√	–

1.2.3 Processing of Mg alloys

According to the processing method, Mg alloys are mainly categorized into casting and wrought alloys. Figure 1.6 shows the common possessing for Mg alloy productions [4]. Casting is conventional process where the alloys are basically made by pouring the molten liquid metal into a mold, and then solidifying into the required shape, Fig. 1.6a. Among the various casting process, high pressure die casting is most commonly used for casting Mg alloys. In contrast, wrought Mg alloys are produced by subjecting casting billets or slabs to mechanical working such as extrusion and rolling operations, Fig. 1.6b and c.

Figure 1.7a shows the yield strength and elongation of commercially casting and wrought Mg alloys in comparison with 5xxx and 6xxx Al alloys [7,12]. Wrought Mg alloys have superior tensile properties to casting alloys; higher strength for extrusions, and larger elongation for sheet alloys due to the refined microstructure and reduced porosity, Fig. 1.6b and c. However, a vast majority of Mg alloy consumptions are centered on casting products, which is about ten times higher than of wrought Mg alloys, Fig. 1.7b. Considering a high proportion of wrought components, especially rolled sheets; over 60% applied for automobile bodies, Fig. 1.7c, the limited applications of wrought Mg alloys are mainly due to interior mechanical properties to their Al alloy counterparts. In order to increase the large-scale use of wrought Mg alloys in automobiles, it is essential to improve the mechanical properties of Mg sheet alloys to a level which is comparable to those of Al alloys.

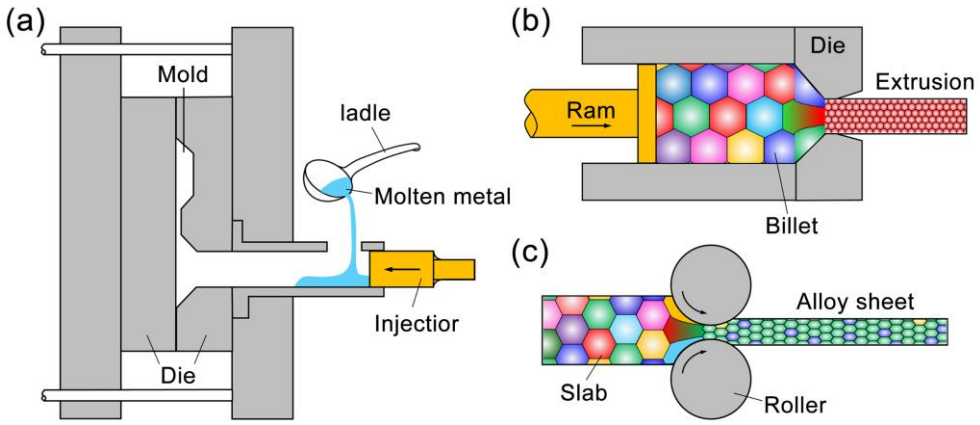

Fig. 1.6. Common processing for Mg alloy productions. (a) High pressure die-casting, (b) Extrusion, and (c) Sheet rolling.

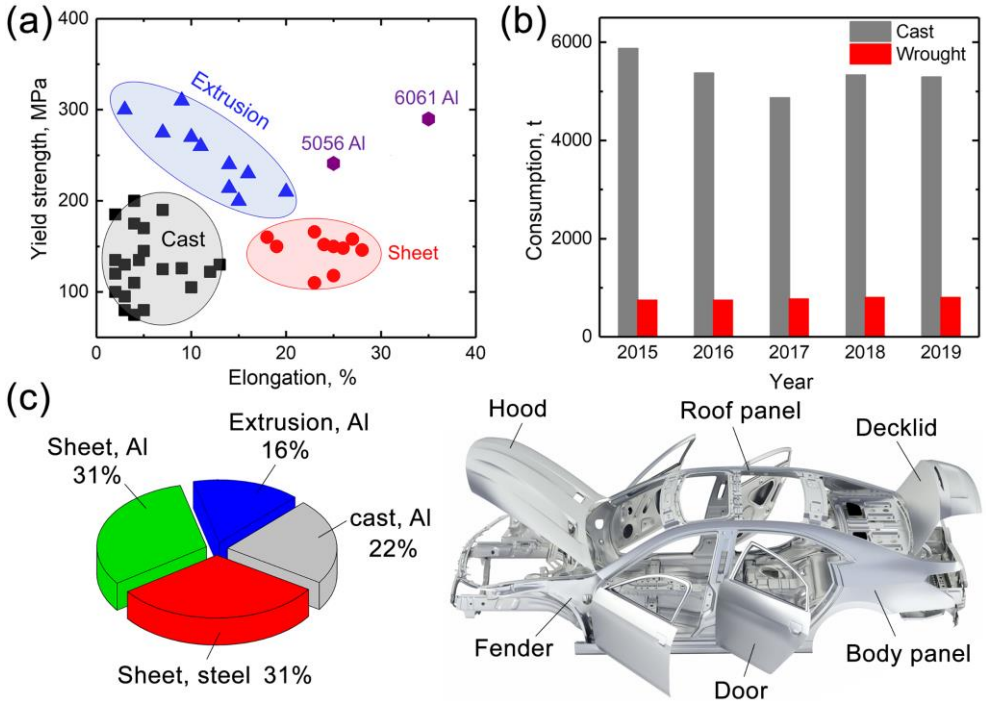

Fig. 1.7. (a) Yield strength and elongation of commercial Mg and Al alloys. (b) Consumption of Mg structural components in Japan for last five years. (c) Utilization ratio of cast and wrought metals in automobile body, and applications of sheet components.

1.3 Stretch formability and strength of Mg sheet alloys

To produce sheet components such as hood, roof panel and decklid in automobiles, the alloy sheets after the rolling process need to be further press formed to required shapes. Thus, the formability of sheet alloys, i.e. the ability to undergo plastic deformation without cracking, is critical for fulfilling the stamping process.

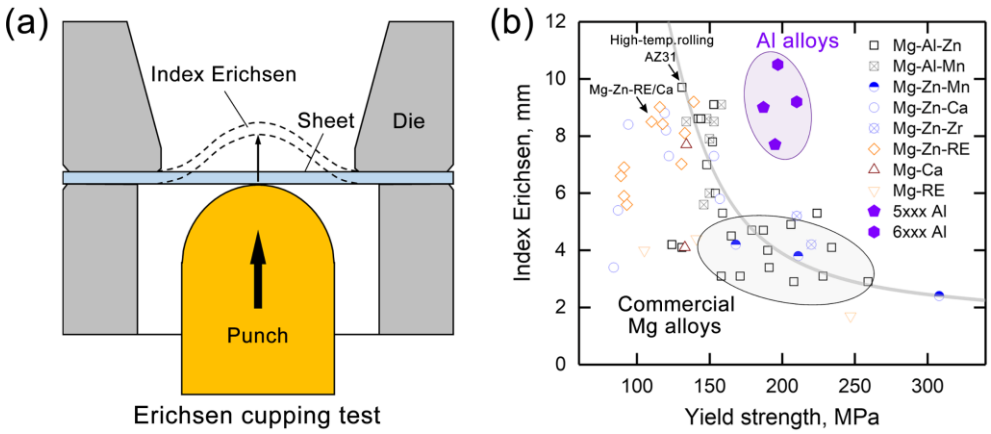

Fig. 1.8. (a) Schematic diagram of Erichsen cupping test. (b) I.E. values and yield strength of various Mg and Al alloys [5,14].

Figure 1.8a shows the schematic of Erichsen cupping test, which is commonly used to evaluate the formability of sheet metals [13]. A hemispherical punch is forced into a clamped sheet specimen until a crack appears. The final punch depth is a measure of the stretch formability of sheet alloys, so called Index Erichsen (I.E.) value. Fig. 1.8b shows I.E. values and yield strength of various Mg and Al sheet alloys [5,14]. Commercially available Mg sheet alloys such as Mg-3Al-1Zn (wt.%, AZ31) and Mg-2Zn-1Mn (wt.%, ZM21) have yield strength of ~ 200 MPa, which is sufficient for automotive body parts. However, the poor stretch formability at room temperature (RT) with I.E. values of 3 ~ 5 mm falls far behind the requirement for stamping process. In contrast, some RE and Ca-containing Mg alloy sheets, as well as AZ31 alloys by high-temperature rolling, show much higher I.E. values of 8 ~ 9 mm, which is even comparable to those of Al alloy sheets in use. However, these high formable Mg alloy sheets normally show low yield strength due to a negative correlation between the strength and formability, i.e. formability-strength trade off dilemma. Moreover, the high cost and resource scarcity also make the RE addition or high temperature rolling undesirable for industrial productions. To broaden the applications of Mg alloy sheets, it is essential to develop high-strength and RT formable Mg alloys using ubiquitous elements.

1.3.1 Formation of strong basal texture

The poor room-temperature formability of AZ31 alloy sheet is mainly due to the strong basal texture; (0002) planes of most grains aligned parallel to the sheet plane, developed during the hot rolling, and subsequent annealing process.

Figure 1.9a show the schematic of basal texture formed during rolling process. Generally, grains in the casting slab have randomized orientations, which, however, rotate to the same orientation with the c-axis parallel to the normal direction (ND) of the rolling plane. Based on the Taylor theory, the lattice rotation by dislocation slip tend to align the slip plane normal parallel to the loading axis [13]. As illustrated above, basal $\langle a \rangle$ slip and $\{10\bar{1}2\}$ tensile twinning are the major deformation modes in Mg. The grains with high Schmid

factor (SF) for basal slip tend to align the [0001] direction parallel to the ND, while those low SF grains; the initial c-axis perpendicular to the ND are favorably reoriented ~ 86° by the tension twinning, producing nearly the same orientation as led by the basal slip. Thus, the strong basal texture developed during rolling is attributed to the predominant activation of basal slip and tensile twinning, which leads to the basal planes of grains mostly parallel to the rolling plane. To concisely reveal the texture which is defined as the collection of grain orientations, the pole figure is used to show stereographic projections of a particular lattice plane on the given specimen plane. Fig. 1.9b shows the stereographic projection of (0002) planes of grains in the rolling plane, and corresponding (0002) pole figure of basal texture with a single pole strongly aligned to the ND of the rolling plane in a high pole density. For a Mg alloy sheet with such strong basal texture, the basal slip or tensile twinning is hardly activated to accommodate the strain along the ND during the Erichsen cupping test due to low SFs under the biaxial tensile stress condition; $\varepsilon_1 > 0$, $\varepsilon_2 > 0$, and $\varepsilon_3 < 0$ [15], resulting in cracking after a small strain, and thus the poor formability.

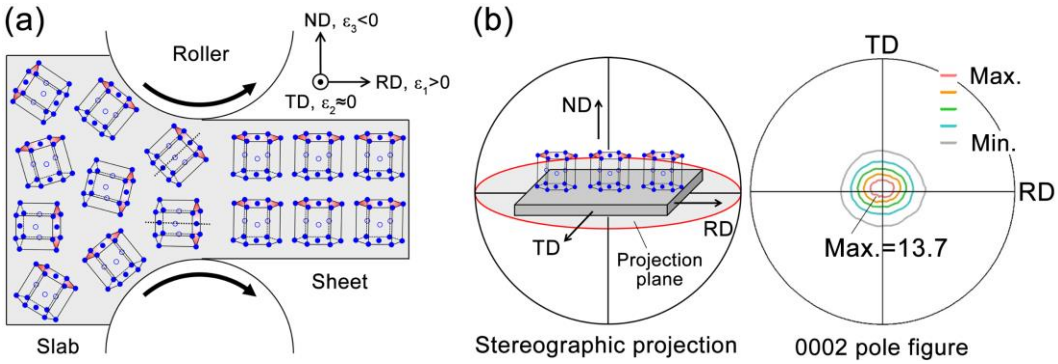

Fig. 1.9. (a) Schematic diagram of rolling process in commercial Mg alloys. (b) Stereographic projection of (0002) planes of grains in the rolling plane, and corresponding (0002) pole figure. Note that RD, TD and ND stand for rolling, transverse and normal directions, respectively.

Upon subsequent annealing, i.e. solution treatment, the basal texture in the AZ31 alloy is mostly preserved, and even becomes stronger with increased annealing temperature or time. Fig. 1.10a shows variations in basal texture intensity of AZ31 alloy sheets as a function of annealing temperature with constant soaking time of 30 min [16]. The as-rolled sample shows a strong basal texture; 12.1 m.r.d with basal poles slightly tilted towards the rolling direction (RD). This typical RD-split texture is associated with the activation of pyramidal $\langle c+a \rangle$ slip and the formation of shear bands during rolling process. The intensity of basal texture initially decreases with increasing the annealing temperature, and reach to the lowest value of 9.0 m.r.d. at 250 °C for 30 min. However, further rising temperature leads to the strengthening of basal texture; an intensity value of 12.9 m.r.d. at 500 °C for 30 min is even higher than that of as-rolled sample. Fig. 1.10b and c shows electron backscatter diffraction (EBSD) inverse pole figure (IPF) maps and corresponding (0002) pole figure of recrystallized grains in AZ31 alloys after annealed at 250 °C for 30 min and 1 h, respectively [17]. The slight texture weakening at low temperature is due to the nucleation of recrystallized grains with non-basal orientations at

grain boundaries, Fig. 1.10b, while the high temperature annealing is dominant by the overall growth of basal-oriented grains, thus resulting in the strong basal texture in the well-annealed sample, Fig. 1.10c. Therefore, the formation of strong basal texture in the commercial AZ31 alloy sheets is ascribed to the easy activation of basal slip and tension twinning upon rolling, and essentially retained deformation texture during subsequent annealing.

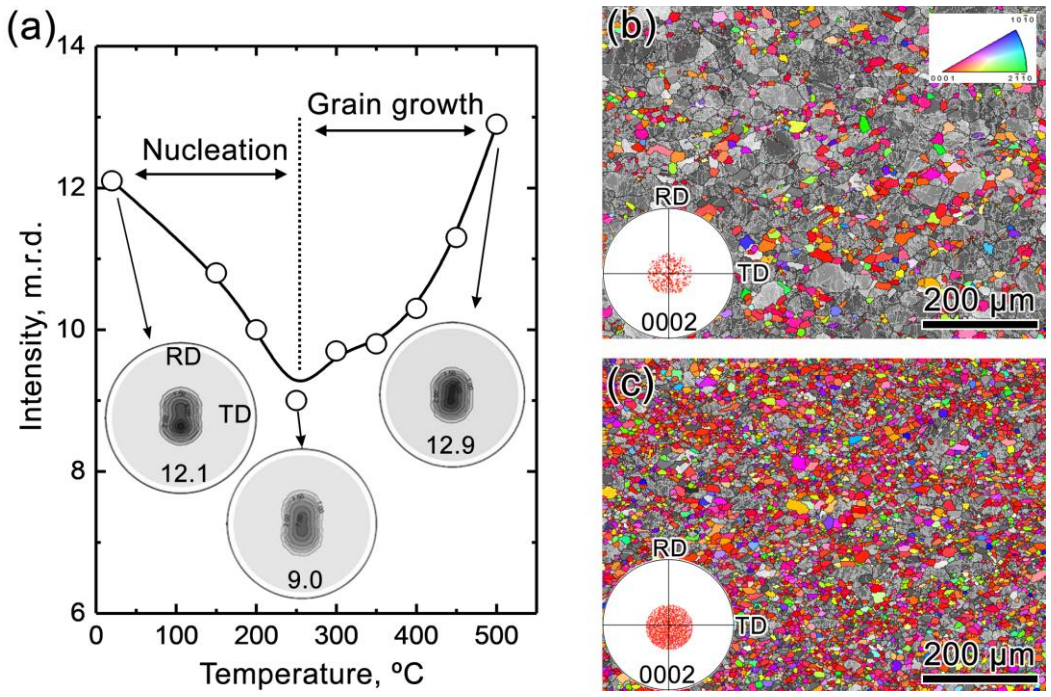

Fig. 1.10. (a) Variations in basal texture intensity as a function of annealing temperature in commercial AZ31 alloy sheets. (b) and (c) EBSD IPF maps and corresponding (0002) pole figure of recrystallized grains after annealed at 250 ºC for 30 min and 1 h, respectively [16,17].

1.3.2 Approaches to improving the stretch formability

As the strong basal texture is a key factor for the poor room temperature formability in commercial Mg alloys, the weakening of basal texture including lower texture density and modification of texture distribution is critical to improve the RT formability, thus promoting the widespread use of Mg alloy sheets.

One approach is the optimization of thermomechanical processing parameters. Figure 1.11a and c shows the nominal stress-strain curves and snapshots of Erichsen cupping tests for solution-treated AZ31 alloy sheets by different rolling process [18,19]. The sample rolled at 225 ºC shows poor RT formability; an I.E. value of 3.7 mm, and an average tensile yield strength; $\sigma_{TYS} = (\sigma_{RD} + 2\sigma_{45^o} + \sigma_{TD})/4$ of ~ 175 MPa, Fig. 1.11a. The high temperature rolling significantly improve the formability. The sample rolled at 550 ºC shows an extremely large I.E. value of 9.5 mm which is even comparable to that of 6xxx series Al alloys, while a degraded σ_{TYS} of ~ 133 MPa is much lower those of commercial sheets, Fig. 1.11b. The optical micrographs of both solution-treated samples show well-recrystallized grain structures with similar grain size; ~ 9 and 12 μm, Fig. 1.11b

and d. However, the high temperature rolling at 550 ºC substantially weaken the basal texture to a wider circular distribution with the pole intensity decreasing from 7.0 to 3.1 m.r.d.. Since a large spread of grain orientations from ND increase the number of soft grains for basal ⟨*a*⟩ slip during stretch forming, the improved RT formability is mainly attributed to the weak basal texture. Considering the high processing cost and technical issues such as oxidation and sticking of sheets, the high temperature rolling is still not commonly used for industrial productions.

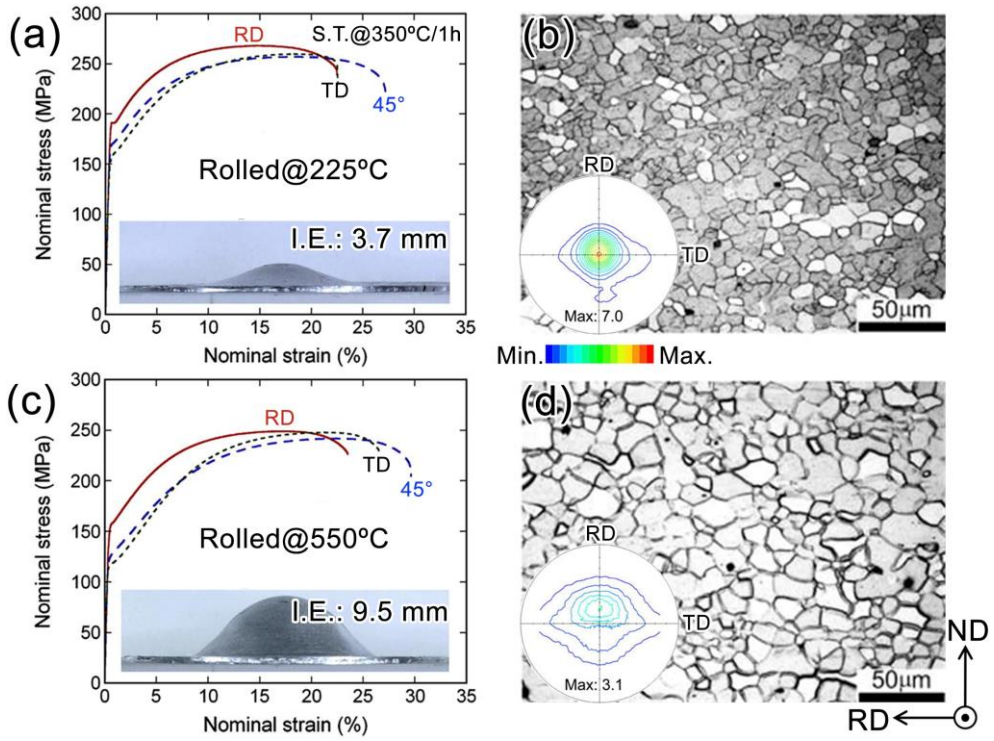

Fig. 1.11. (a,c) Nominal stress-strain curves inset with snapshots after Erichsen cupping tests at RT, and (b,d) optical micrographs and corresponding (0002) pole figures taken from the RD-ND planes of solution-treated AZ31 alloy sheets after rolled at 250 and 500 ºC, respectively. Note that the solution treatment was conducted at 350 ºC for 1 h [18,19].

Compared to the manipulation of processing conditions, optimizing the alloy composition demonstrates to be a more effective approach. The trace addition of rare earth (RE) elements into Mg-Zn based alloys can significantly improve the formability due to the weakened basal texture. Some of these alloy sheets such as Mg-1.5Zn-0.2Ce (wt.%, ZE10) and Mg-1.5Zn-0.2Y (wt.%, ZW10) exhibit large I.E. values over 9 mm at RT, which is comparable to those of 6xxx series Al alloy sheets [20,21]. However, the high cost and resource scarcity also make RE-containing alloys commercially undesirable. In contrast, the Ca addition has recently received considerable attention due to the similar role as RE elements in achieving the excellent RT formability while at much lower cost. Figure 1.12a shows snapshots of solution-treated Mg-1.5Zn and Mg-1.5Zn-0.1Ca (wt.%) alloy sheets after Erichsen cupping tests at RT [11]. The I.E value is substantially increased from 3.4 to 8.2 mm by the trace addition of 0.1 wt.% Ca. The Ca-free alloy show a typical strong basal texture with an

intensive pole density of 12.5 m.r.d.. In contrast, the Ca addition significantly broadens the texture distribution; 4.3 m.r.d. with (0002) poles inclined ~ 30º towards the transverse direction (TD), termed as 'TD-split texture'. Thus, the improved stretch formability is mainly attributed to the formation of the TD-split texture. Besides, the Ca-containing alloy shows a relatively finer grain size of ~ 32 μm than that of the Ca-free alloy; 84 μm. Since compression twinning is more active for coarser grain size, the reduced grain size by the Ca addition may inhabits the operation of compression twins, thus retarding the localized necking by twinning induced void nucleation, and premature cracking. Fig. 1.12b shows the effect of Zn contents on the stretch formability of Mg-*x*Zn-0.1Ca alloys [22]. The Zn-free alloy, i.e. Mg-0.1Ca, shows a low I.E. value of 3.6 mm which is slightly higher than that of Mg-1.5Zn alloy; 3.4 mm. The I.E. value prominently increases from 3.6 to 7.2 mm by trace addition of 0.5 wt.% Zn, indicating that co-additions of both Ca and Zn are essential for the texture weakening, and thus excellent formability in Mg-Zn-Ca alloy sheets. Excessive Zn addition over 1.5 wt.% degrades the I.E. value while the texture density is even lower than that of 0.5 wt.% Zn. Therefore, the optimization of Zn contents in Ca-containing Mg sheets alloys based on a thorough understanding of the role of Zn is quite critical.

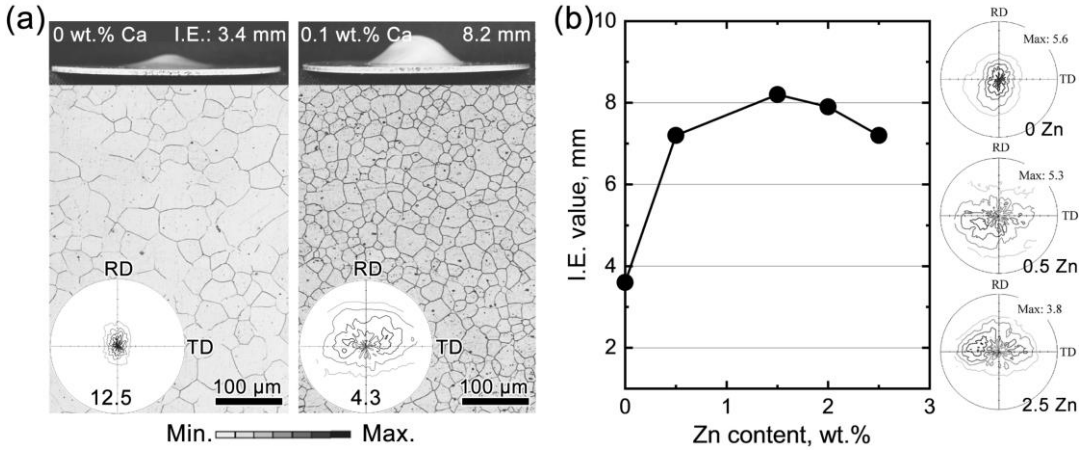

Fig. 1.12. (a) Snapshots after Erichsen cupping tests at RT, optical micrographs, and corresponding (0002) pole figures taken from the RD-ND planes of solution-treated Mg-1.5Zn and Mg-1.5Zn-0.1Ca alloy sheets. (b) Variations in I.E. values as a function of Zn contents in Mg-0.1Ca-*x*Zn alloy sheets, and (0002) pole figures by 0, 0.5, and 2.5 Zn additions. Note that the solution treatment was conducted at 350 ºC for 1.5 h [11,22].

Figure 1.13 shows the (0002) pole figures of as-rolled Mg-0.1Ca and Mg-1.5Zn-0.1Ca (wt.%) alloy sheets [11]. Both Zn-free and Zn-containing alloys show the RD-split texture with (0002) poles tilted by ~ 15º towards the RD, while the addition of Zn leads to a broader texture distribution with the density; 4.8 m.r.d. slightly lower than that of the Zn-free alloy; 6.0 m.r.d.. The Zn-free alloy remain the strong basal texture compared to that of the solution-treated sample, Fig. 1.13b. In contrast, the Zn-containing alloy shows distinct texture modification from the RD-split to the TD-split, Fig. 1.13a. Therefore, the weak TD-split texture developed by the co-addition of Zn and Ca is associated with the static recrystallization during solution treatment, however, the origin of texture weakening is still controversial.

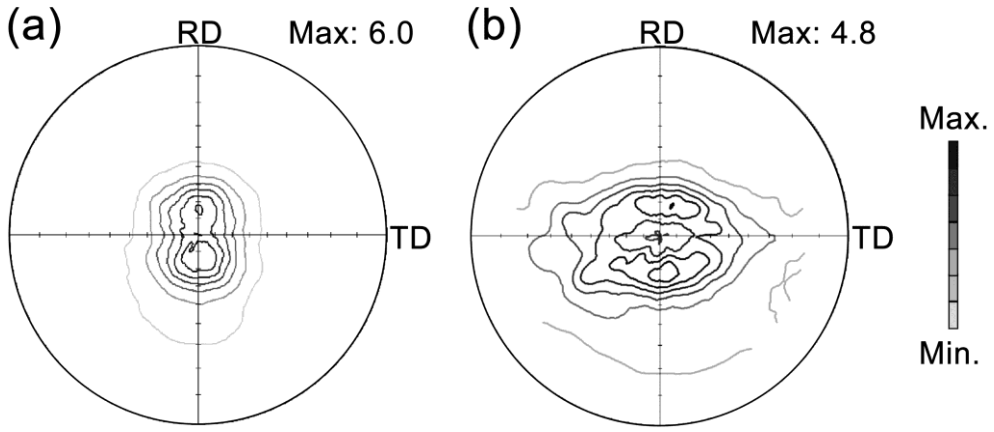

Fig. 1.13. (0002) pole figures of as-rolled (a) Mg-0.1Ca, and (b) Mg-1.5Zn-0.1Ca (wt.%) alloys [11].

1.3.3 Texture weakening mechanism during static recrystallization

Several disputed mechanisms have been proposed to explain the formation of the distinct TD-split texture in Mg-Zn-Ca/RE alloy sheets, including oriented nucleation at various sites such as grain boundaries, deformation twins, and shear bands, or preferential grain growth induced by solute segregation along specific types of boundaries [23-25].

Figure 1.14a and d shows the microstructure and texture of Mg-0.2Ca and Mg-0.8Zn-0.2Ca (wt.%) alloy sheets in the early stage of recrystallization [23]. The recrystallized grains in both Zn-free and Zn-addition alloys mainly nucleated at grain boundaries after annealed at 350 ºC for 20 s, Fig. 1.14b and e. The Zn-free alloy shows rapid recrystallization kinetics with c-axes of most recrystallized grains nearly parallel to the ND i.e. strong basal texture, Fig. 1.14b. In contrast, the recrystallized grains in the Zn-containing alloy has much lower area fraction; ~ 8% and average grain size; ~ 5 μm that those of the Zn-free alloy; ~ 31% and 13 μm, and exhibit randomized orientations with their c-axes tilted towards RD or TD, Fig. 1.14d. The STEM-EDS analysis shows the solute segregation of Ca or Ca/Zn atoms to grain boundaries in the well-recrystallized Zn-free and Zn-containing samples, respectively, Fig. 1.14c and f. Since the co-segregation of Ca and Zn to grain boundaries may have stronger solute dragging effect in reducing the boundary mobility than that of single solute, the preferential growth of basal-oriented recrystallized grains is suppressed in the Zn-containing alloy. Therefore, the texture weakening is attributed to the formation and uniform growth of recrystallized grains with randomized orientations at grain boundaries. However, these results cannot explain the formation of characteristic TD-split texture. Besides, the TD-split texture is also formed in Mg-4Y-3Nd (wt.%, WE43) and Mg-6.6Zn-0.2Ca (wt.%, ZX70) alloys where grain boundary recrystallization is heavily restricted due to a large number of pre-existing second phase particles distributed along grain boundaries [24,26].

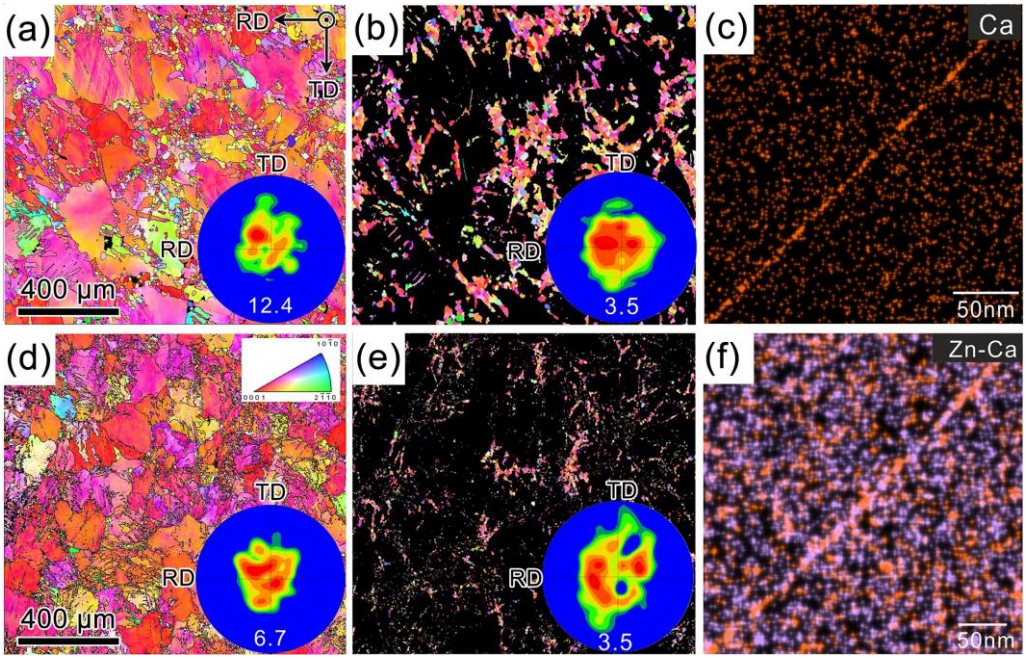

Fig. 1.14. EBSD IPF maps and corresponding (0002) pole figures of (a,d) Mg-0.2Ca and Mg-0.8Zn-0.2Ca (wt.%) alloy sheets annealed at 350 ºC for 20 s, respectively, and (b,e) corresponding recrystallized grains. (c,f) STEM-EDS mapping in grain boundaries of the samples annealed at 350 ºC for 900 s [23].

Comparatively, the recrystallization at deformation twin boundaries seems to be more plausible. Figure 1.15 shows the microstructure and texture evolution of the Mg-0.8Zn-0.2Ca alloy sheet during annealing at 350 ºC using a quasi-in-situ EBSD method, i.e. monitor the alternation of the same area after external processing such as annealing or stretching [27]. The as-rolled sample exhibit no obvious recrystallization, but a large number of dark ribbon-like region within deformed grains, Fig. 1.15a. Three distinct peaks at ~ 86°, 56° and 38° in the misorientation angle histogram indicates that these low indexed region are deformation twins i.e. $\{10\bar{1}2\}$ tensile twins, $\{10\bar{1}1\}$ compression twins, and $\{10\bar{1}1\}$-$\{10\bar{1}2\}$ double twins, Fig. 1.5. The corresponding (0002) pole figure shows an annular texture distribution with a strong basal pole; ~19.8 m.r.d. tilted ~ 30° towards the RD. After 520 s annealing, a number of fine recrystallized grains nucleate at deformation twin boundaries with randomized orientations as indicated in the pole figure, Fig. 1.15b. A pole intensity of 3.7 m.r.d is much lower than that of the deformed texture. During subsequent annealing for 880 s and 2110 s, recrystallized grains tend to grow out of twin boundaries, and consume adjacent deformed parent grains. The basal and RD-tilted components in the pole figure are also gradually replaced by the two TD-split components with a tilt angle of ~ 30°, Fig. 1.15c and d. With further annealing to 3310 s and 6910 s, the recrystallisation process is dominated by uniform grain growth with the intensity of TD-split components further increased to 4.4 m.r.d, Fig. 1.15e and f. Thus, the origin of the TD-split texture is mainly associated with the deformation twin recrystallization. However, due to limited resolution of conventional EBSD methods, the definite twin boundary type for nucleation of TD-oriented grains is still unclear.

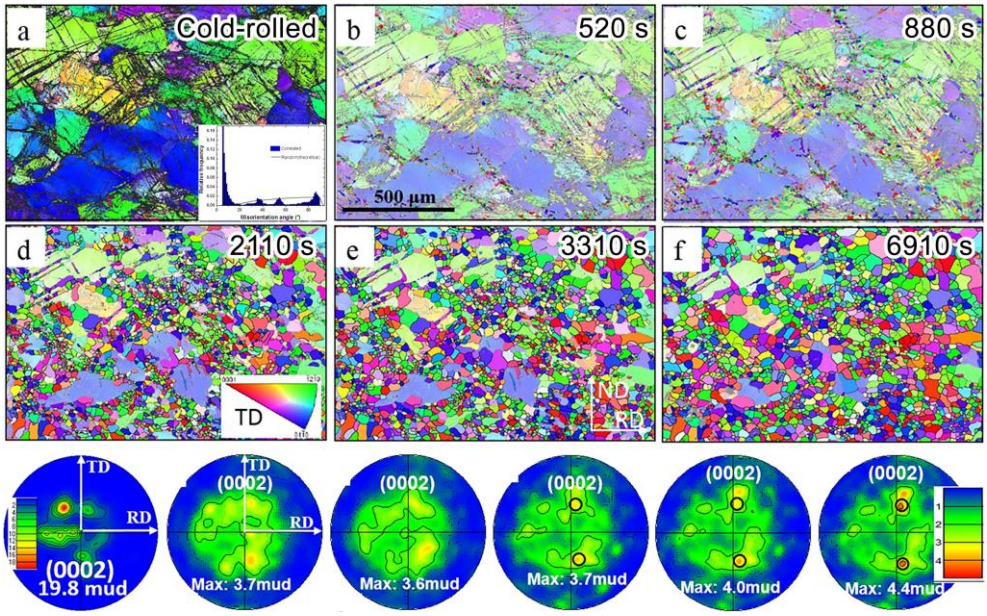

Fig. 1.15. Quasi-in-situ EBSD IPF maps and corresponding (0002) pole figures of recrystallized grains in the Mg-0.8Zn-0.2Ca (wt.%) alloy sheets annealed at 350 ºC for (a) 0 s; as-rolled, (b)520 s, (c) 880 s, (d) 2110 s, (e) 3310 s, and (f) 6910 s [27].

Shear bands; the narrow band-like regions with heavy deformation, are considered as potential nucleation sites for inducing the TD-split texture in some RE-containing alloys [25]. These low indexed areas with dark band contrast in EBSD maps actually consist of alternatively arranged compression and double twins as identified from TEM observations [28]. Therefore, the recrystallization at compression and double twin boundaries is speculated to be responsible for the final TD-split texture. Considering restricted scope and operation by TEM analysis, more fast and convenient methods are required for the large-scale characterization of heavily deformed regions. Transmission Kikuchi diffraction (TKD) technique is a powerful tool to get the high resolution and indexing orientation maps in an electron transparent sample, however, which are seldomly used for characterizing the microstructure evolution during the early stages of recrystallization. Besides, the activation of non-basal slip, especially prismatic ⟨*a*⟩ slip, is also thought to play an important role in assisting the lattice rotation of recrystallized grains to the specific TD orientation; the c-axis tilted ~ 30° away from the ND to the TD [29]. The 30° reorientation of recrystallized grains has been observed in some Mg-RE binary alloys during rolling or extrusion process, which is considered to arise from the enhanced prismatic slip activity by the RE addition. However, TD-split texture is rarely found in these Mg-RE alloys other than the Mg-Zn-RE/Ca ternary system. Therefore, the alloying effects on the texture weakening is indispensable, and further solute distribution in the deformed regions is critically required.

In summary, the applications of commercial Mg alloy sheets are severely impeded by their poor formability at RT, which arises from the strong basal texture developed during rolling process. Considerable efforts have been made to develop the RT formable Mg sheet alloys by weakening the basal texture. The trace addition of Ca into Mg-Zn based alloy proves to be a practical approach for achieving excellent RT formability due to a weak TD-split texture developed during solution treatment. Various mechanisms have been proposed

to explain the formation of TD-split texture, wherein the orientated nucleation in the deformation twin boundaries, and subsequently uniform grain growth controlled by solute drag have attracted much attention. However, the definite nucleation-related twinning types and role of solutes in twin boundary recrystallization need to be further determined. Although the Mg-Zn-Ca alloy sheets show large stretch formability, the low yield strength still limits their widespread use. Therefore, it is essential to develop the Mg sheet alloys with a good combination of high formability and strength.

1.4 Heat-treatable Mg sheet alloys

The development of heat-treatable Mg sheet alloys with excellent RT formability is an industrially feasible approach to overcome the strength-formability trade-off, Fig. 1.8b. Fig. 1.16 illustrates the thermomechanical processing of heat-treatable Mg alloy sheets. In general, the as-rolled Mg alloy sheet shows poor formability at room temperature (RT) due to the strong basal texture developed during hot rolling. However, the alloy sheet may exhibit excellent formability if texture can be weakened by solution treatment. Since such alloy sheet also shows a low strength given the inverse correlation between formability and strength, the subsequent artificial aging is conducted for improving final strength, which is associated with the precipitation of second phase particles within grains. This press-forming and subsequent paint-baking; at 150–180 °C for 15–30 min manufacturing processing has been applied in producing steels and Al automotive body panels. In order to fully implement this design strategy in Mg alloy sheets, a rapid age-hardening response during artificial aging is critical for practical applications other than above mentioned texture weakening.

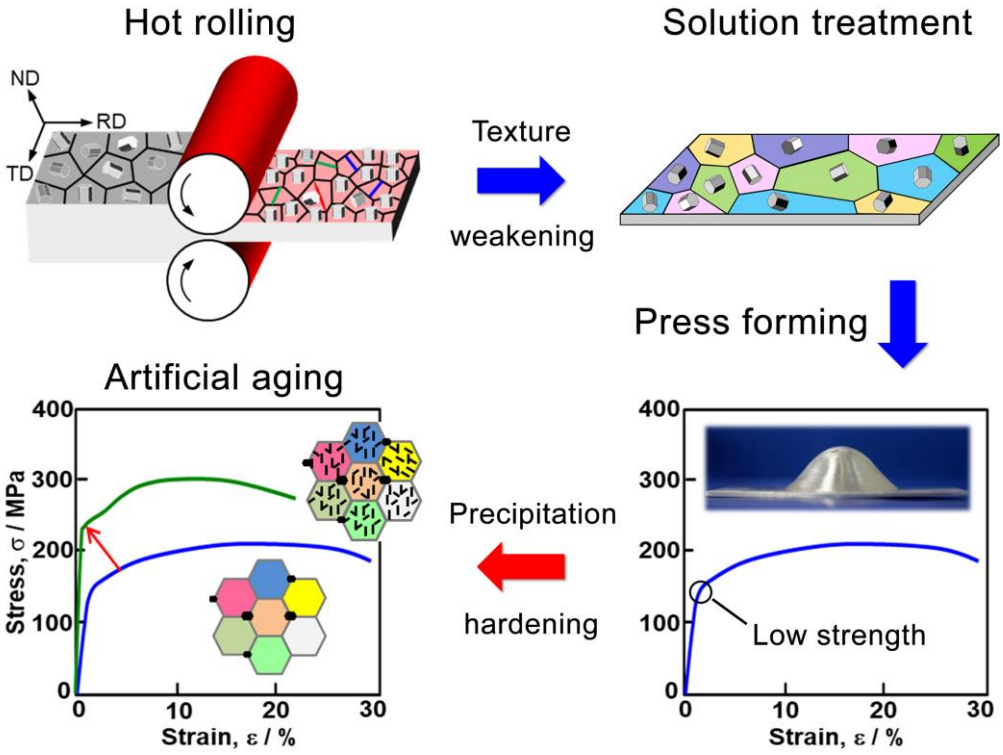

Fig. 1.16. Schematic diagram of thermomechanical processing for heat-treatable Mg alloy sheets

1.4.1 Age-hardening response in wrought Mg alloys

Figure 1.17a shows age-hardening curves of various commercial Mg and Al alloys at 200 ºC [30-37]. The Al-1.2Si-0.6Mg (wt.%, 6016Al) alloy; commonly used for automotive panels, exhibit rapid age-hardening response with the hardness rising rapidly from ~ 47 HV; solution-treated (S.T.) condition to a peak of ~ 95 HV after only 0.5 h. A large hardness increment of ~ 48 HV is attributed to a dense dispersion of rod-like Mg_9Si_5 precipitates; ~ 50 nm in length on the $(001)_\alpha$ planes of the Al matrix, Fig. 1.17b. In contrast, commercial wrought Mg alloy systems such as Mg-Al-Zn (AZ) and Mg-Zn-Zr (ZK) shows much poorer or sluggish age-hardening response. The Mg-3Al-1Zn (wt.%, AZ31) and Mg-2Zn-0.1Ce (wt.%, ZE20) alloys has negligible hardness increments; ~ 5 and 2 HV during isothermal aging. The hardness of Mg-8Al-0.5Zn (wt.%, AZ80) and Mg-6Zn-0.6Zr (wt.%, ZK60) alloys increases slowly during aging, and reaches maximum values of ~ 82 and 67 HV after 96 and 24 h. The small hardness increments of ~ 24 and 14 HV are less than half that of the 6016Al alloy, which is associated with much coarser size of $Mg_{17}Al_{12}$ basal laths and $MgZn_2$ $[0001]_\alpha$ rods; ~ 0.5–1 μm, Fig. 1.17c and d, and thus lower number density based on the Orowan strengthening mechanism. The Mg-5Y-4RE (wt.%, WE54) alloy exhibits a large age-hardening increment of ~ 41 HV comparable to that of the 6016Al alloy, which is due to the precipitation of $Mg_{12}NdY$ plates on the prismatic planes of the Mg matrix, Fig. 1.17e. However, the lengthy peak-aging time; over 200 h and a high quantity of RE additions are undesirable for practical use.

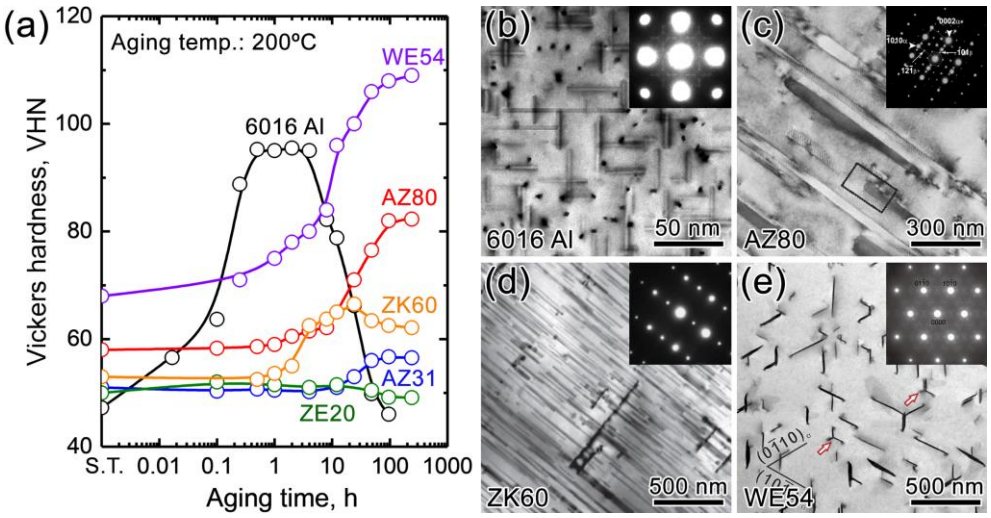

Fig. 1.17. (a) Variations in Vickers hardness as functions of aging time for commercial Mg and Al alloys at 200 ºC. (b-e) Bright-field TEM images and corresponding SAED patterns obtained from peak-aged (b) 6016 Al, (c) AZ80, (d) ZK60, and (d) WE54 alloys. Note that S.T. stands for solution treatment [30-37].

Microalloying has demonstrated to be an effective approach to enhancing the age-hardening response in various Mg alloy systems. Figure 1.18a shows the age-hardening curves of microalloyed Mg-Ca based alloys at 200 ºC [38,39]. The Mg-0.5Ca (wt.%) binary alloy exhibits a moderate age-hardening response with the hardness slowly increased from 43 HV; S.T to a peak of 52 HV after 24 h. A small hardness increment of ~ 9

HV is mainly due to a sparse distribution of cuboidal Mg_2Ca precipitates on the basal planes of the Mg matrix. However, the trace addition of Al or Zn to the binary alloy significantly enhance the age-hardening response. The hardness in Mg-0.8Ca-0.3Al and Mg-0.5Ca-1.6Zn (wt.%) alloys rises rapidly from ~ 42 and 48 HV to maximum values of ~ 72 and 69 HV after only 2 h, respectively. Relatively large hardness increments; 30 and 21 HV given the short peak-aging time in these two alloys are attributed to the dense dispersion of Guinier Preston (G.P.) zones on the basal planes as indicated by the continuous streaks along the $[0001]_\alpha$ and at the $1/3\{11\bar{2}0\}_\alpha$ and $2/3\{11\bar{2}0\}_\alpha$ in the selected area electron diffraction (SAED) patterns. The similar structures are also reported in some Mg-RE-Zn alloys. Considering the common features in these alloy systems, the formation of the G.P. zones empirically depends on combined additions of oversized and undersized alloying elements along with much larger negative enthalpy of mixing relative to Mg. As illustrated in Fig. 1.18e, the atomic radius of Ca; ~ 1.97 Å is larger than that of Mg; ~ 1.6 Å, while the Al and Zn have smaller atomic radii of ~ 1.43 and 1.33 Å, respectively. Considering much higher mixing enthalpy values of Ca-Al and Ca-Zn; ~ -20 and -22 kJ/mol than those of Mg-Ca, Mg-Al and Mg-Zn; -6, -2 and -4 kJ/mol [40], Ca and Al or Zn tend to segregate to each other in order to reduce the misfit strain led by individual Ca; 0.23 and Al/Zn atoms; -0.11 and -0.17, respectively. However, the origin of the G.P. zones along with the accelerated aging kinetics in above alloy systems remains still unclear.

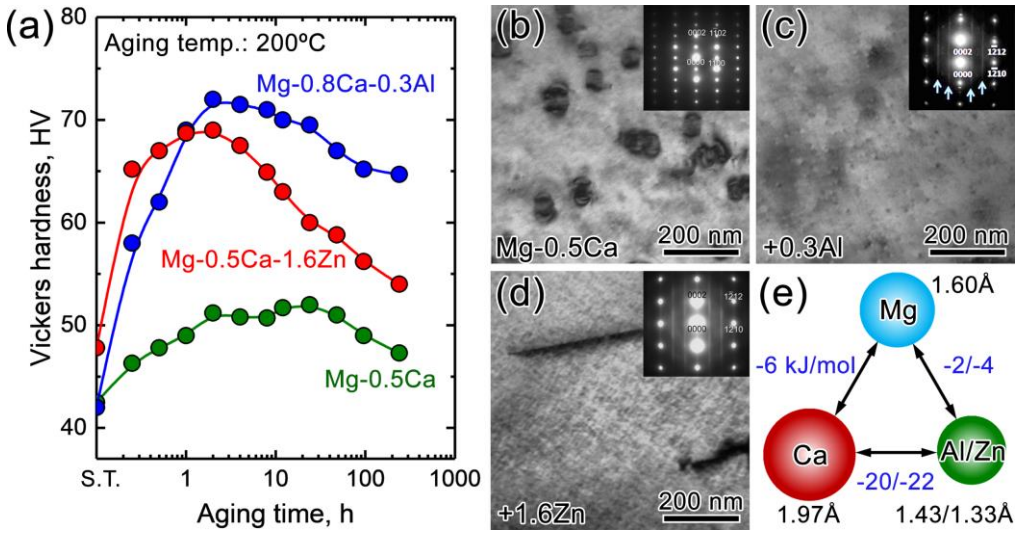

Fig. 1.18. (a) Variations in Vickers hardness as functions of aging time for microalloyed Mg-Ca based alloys at 200 °C. (b-d) Bright-field TEM images and corresponding SAED patterns obtained from peak-aged (b) Mg-0.5Ca, (c) Mg-0.8Ca-0.3Al, and (d) Mg-0.5Ca-1.6Zn (wt.%) alloys. (d) The calculated enthalpy of mixing and atomic radii in Mg-Ca-Al and Mg-Ca-Zn systems [38,39].

1.4.2 Heat-treatable Mg-Al-Ca based alloy sheets

Considering the rapid age-hardening response along with potential texture weakening, the Mg-Al-Ca-(Zn) and Mg-Ca-Zn systems are quite promising for developing heat-treatable Mg sheet alloys with excellent formability as demonstrated in recently developed Mg-Al-Ca-Mn-Zn (AXMZ) sheet alloys.

Figure 1.19a shows nominal stress-strain curves of solution-treated and peak-aged Mg-1.2Al-0.5Ca-0.4Mn (wt.%, AXM100) and Mg-1.2Al-0.5Ca-0.4Mn-0.8Zn (wt.%, AXMZ1000) alloy sheets [41]. Insets are snapshots taken from solution-treated samples after the Erichsen cupping test. The AXM100 sample exhibits moderate I.E. value of 5.9 mm and yield strength of 145 MPa in the solution-treated condition. A trace addition of 0.8 wt.% Zn produces little change to the yield strength; 144 MPa, but a considerable increase in the I.E. value; 7.7 mm. The subsequent peak-aging (T6) treatment at 200 C for only 1 h substantially improves the yield strength of AXM100 and AXMZ1000 alloys to 196 and 204 MPa, which is associated with a dense dispersion of G.P. zones enriched with Al and Ca on the basal planes of the Mg matrix. As illustrated in the benchmark, such AXMZ1000 alloy sheet has a well-balanced good stretch formability and high strength, which is comparable to those of 5xxx or 6xxx series Al alloys. The larger I.E. value for the Zn-containing alloy sheet is mainly attributed to a weaker basal texture than that of the Zn-free alloy sheet, however, the texture weakening mechanism is remain controversial. Besides, the Zn concentration may also influence the formability and strength in AXMZ dilute alloys as indicated from the Mg-Zn-Ca ternary alloy sheets, Fig. 1.11b. Therefore, it is essential to optimizing the Zn content in this new class of Mg sheet alloys with a thorough understanding of the role of Zn.

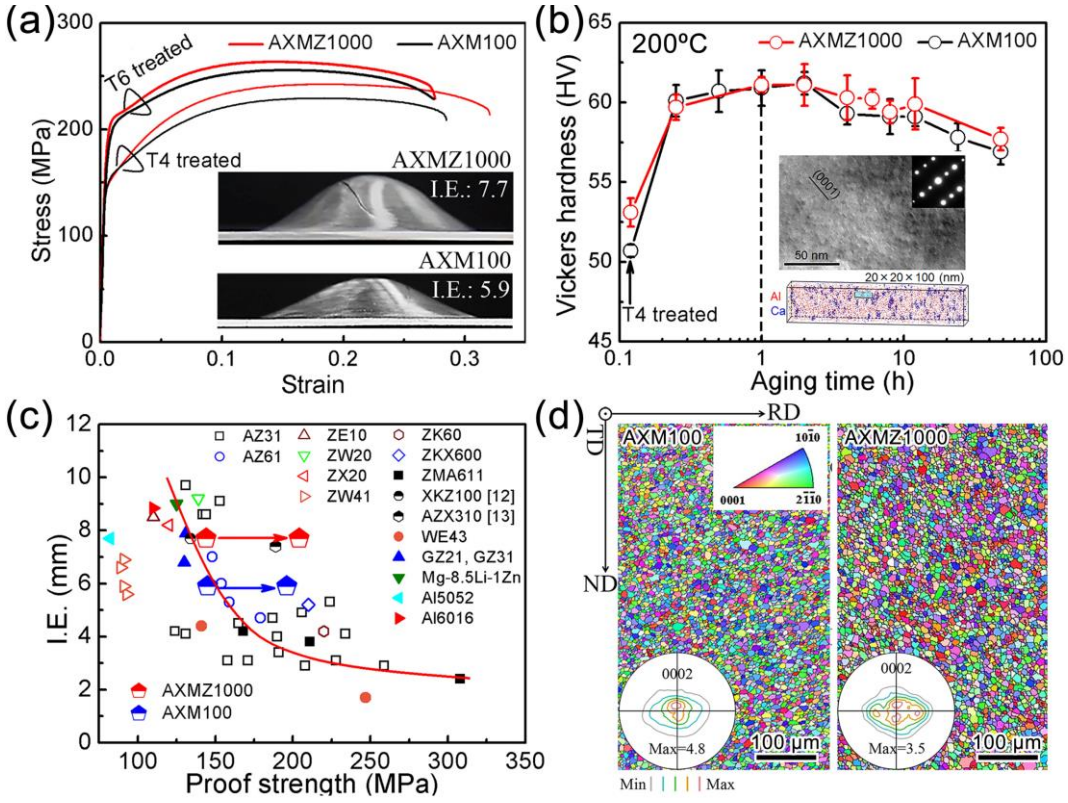

Fig. 1.19. (a) Nominal stress-strain curves of solution-treated and peak-aged AXM100 and AXMZ1000 alloy sheets. Insets are snapshots taken from solution-treated samples after the Erichsen cupping test. (b) Age-hardening curves for AXM100 and AXMZ1000 alloys at 200 ºC. Insets are TEM and 3DAP analysis for the peak-aged AXMZ1000 alloy. (c) I.E. values and yield strength for various Mg and Al sheet alloys. (d) EBSD IPF maps and (0002) pole figures of solution-treated AXM100 and AXMZ1000 alloy sheets [41].

1.4.3 Precipitation behavior in Mg-Zn-Ca system

In addition to the Mg-Al-Ca based dilute alloys, the Mg-Zn-Ca system also has a great potential for developing the heat-treatable Mg alloy sheets in view of its excellent formability and rapid age-hardening features as mentioned above, Fig. 1.12a and 1.18a. However, little attention has been paid to this alloy system probably due to its low yield strength; less than 150 MPa [11,22]. Thus, the utilization of age-hardening in the Mg-Zn-Ca alloy sheets based on a full knowledge on the precipitation behavior may guide it out of trouble.

Previous work has suggested a simple precipitation sequence for the Mg-Zn-Ca system; S.S.S.S. (supersaturated solid solution) → ordered G.P. zones → η' → η [30]. Figure 1.20a-c shows conventional TEM bright-field images and SAED patterns of metastable and equilibrium phases involved during isothermal aging process. The microstructure of peak-aged Mg-Zn-Ca dilute alloys contains a dense distribution of G.P. zones; ~ 5 nm in length surrounded with coherent strain contrast on the basal planes of the Mg matrix, Fig. 1.20a [42]. In the $[0001]_\alpha$ zone axis pattern, extra diffraction spots are visible at the $1/3\{11\bar{2}0\}_\alpha$ and $2/3\{11\bar{2}0\}_\alpha$ positions other than typical streaking feature from the $[1\bar{1}00]_\alpha$ as mentioned above, Fig. 1.18d [38]. The structure and composition of the G.P. zone is further analyzed by HAADF-STEM and 3DAP analysis. The atomic resolution image from the $[11\bar{2}0]_\alpha$ shows a bright monolayer on the basal plane, while a periodic arrangement of the brightest atomic columns with an interval of ~ 0.45 nm is clearly revealed in the $[1\bar{1}00]_\alpha$ projection, Fig. 1.20d. Considering the brightness of individual atomic columns in HAADF-STEM images approximates the square of the atomic number, the brightest columns are enriched with either Zn or Ca atoms; 30 for Zn, 20 for Ca and 12 for Mg. Along with the compositional analysis by 3DAP, the Zn/Ca ratio within G.P zones is determined to be ~ 1:1 [43]. On the basis of these results, the G.P. zone is proposed to an ordered hexagonal structure; a = 0.556 nm. However, the precise atomic coordinates and composition have not been determined.

With subsequent over-aging for a relatively short time, the fine G.P. zones are gradually replaced by larger plate-like precipitates; ~ 100 nm in the form of single or pairs on the basal planes, Fig. 1.20b [44]. These large single plates or pairs exhibit much weaker strain contrast than that of G.P. zones, indicating the loss of coherency in the precipitate/matrix interface. The $[1\bar{1}00]_\alpha$ SAED pattern shows similar continuous streaks along the $[0001]_\alpha$ as that of G.P. zones, while no additional reflection is detected in the $[0001]_\alpha$ pattern. Given the streaks may also result from the shape effect of plate-like precipitates. Thus, these large plates are lack of the ordered structure, and are designated η' phase. Combined with the 3DAP analysis that the Zn/Ca ratio in the η' phase is ~ 1:2, the η' phase is proposed to have an ordered hexagonal structure; $P6_3/mmc$, a = 0.580 nm, c =0.941 nm with a composition of Mg–18Ca–8Zn (at.%). However, A similar atomic structure as the G.P. zone from the $[11\bar{2}0]_\alpha$ direction is reported for these large plates, which are thereby still thought as G.P. zones even after long-time over-aging, Fig. 1.20e. To resolve the conflict, observations of atomic structures from other lattice directions is needed. After extended time of over-aging, larger-sized plate-like and rectangular-shaped precipitates are observed on the basal planes, Fig. 1.20c [44]. The number density of plates is decreased while the coarse rectangular-shaped precipitates are dominant within the matrix which are designated η phase. From the SAED patterns taken form $[1\bar{1}00]_\alpha$ and $[11\bar{2}0]_\alpha$ directions, the η phase is supposed to have a

hexagonal structure isomorphous to that of the Mg_2Ca phase; $P6_3/mmc$, a =0.623 nm, c =1.012 nm with a composition of $Mg_2(Ca,Zn)$ based on the energy dispersive spectroscopy (EDS) analysis. However, a high-resolution transmission electron microscopy (HRTEM) image from the $[1\bar{1}00]_\alpha$ combined with the micro-beam diffraction and EDS analysis suggest that the η phase has a trigonal structure; $P\bar{3}1c$, a = 0.97 nm, c =1.01 nm with a composition of $Mg_6Ca_2Zn_3$, Fig. 1.20f [45].

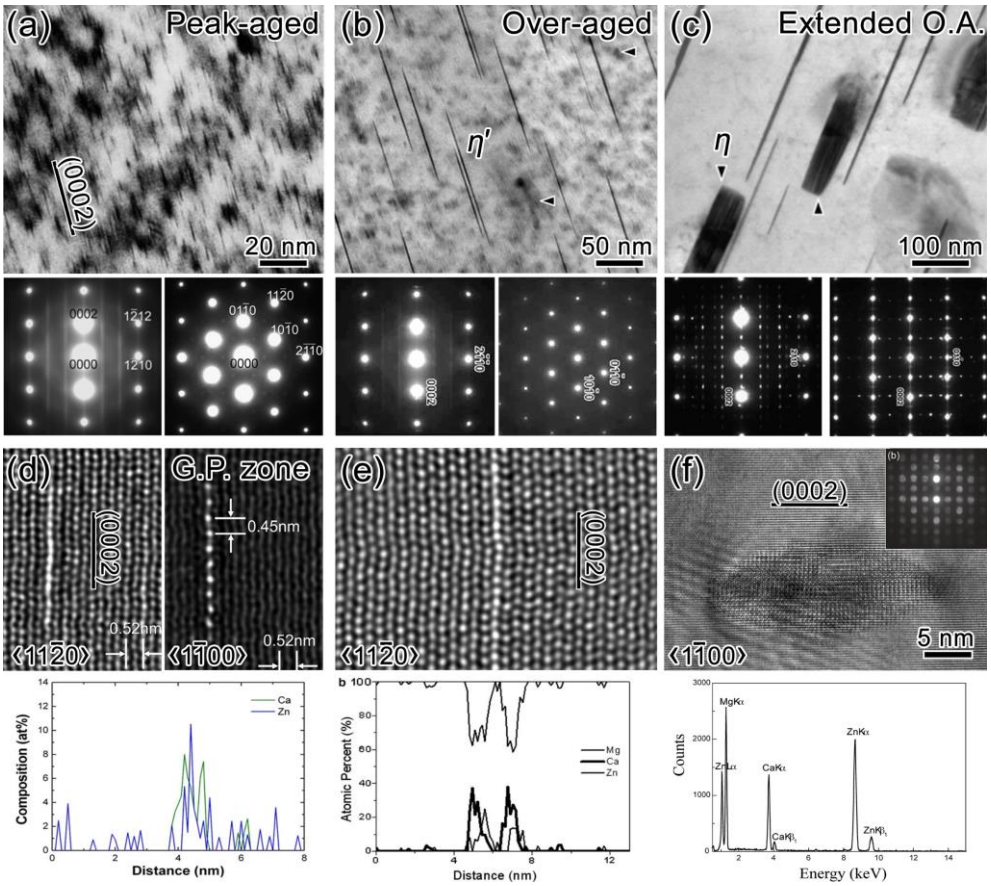

Fig. 1.20. (a-c) Bright-field TEM images and SAED patterns from $[1\bar{1}00]_\alpha$ and $[0001]_\alpha/[11\bar{2}0]_\alpha$ (d-e) High resolution HAADF-STEM or TEM (HRTEM) images of of the G.P. zone, η' and η phases [38,42-45].

In summary, the current results about structures and compositions of precipitate phases formed in the Mg-Zn-Ca dilute alloys are still controversial. It is critical to unambiguously establish the precipitation sequence using state-of-the-art characterization techniques such as aberration-corrected STEM and 3DAP analysis in this important alloy system, which is thus expected to give deeper insights into the advance in the alloy design and age-hardening response.

1.4.4. Heat-treatable Mg sheet alloys with high thermal conductivity

With the ever-growing integration and power density of modern electronic devices like camaras, laptops and mobile phones, the efficient thermal conduction along with excellent mechanical properties is essential for

structural components in electronics [46]. Lightweight Mg alloys are attractive candidates due to the good thermal conductivity and adequate strength. However, these two properties are contradictory in commercially available wrought Mg alloys, Fig. 1.21a [47]. Since the strength of most commercial Mg alloys, e.g. Mg-3Al-1Zn (wt.%, AZ31) and Mg-6Al-1Zn (wt.%, AZ61) mainly relies on dissolved solutes in the matrix, i.e. solid-solution strengthening, the lattice distortion induced by solute atoms increases the electron and phonon scattering which results in low thermal conductivity. In contrast, some Mg-Zn based alloys such as Mg-2Zn-0.6Zr (wt.%, ZK20) and Mg-3Zn-1Mn (ZM31) have relatively high thermal conductivity due to the lean alloying additions, while insufficient mechanical properties; formability and yield strength limited their widespread use.

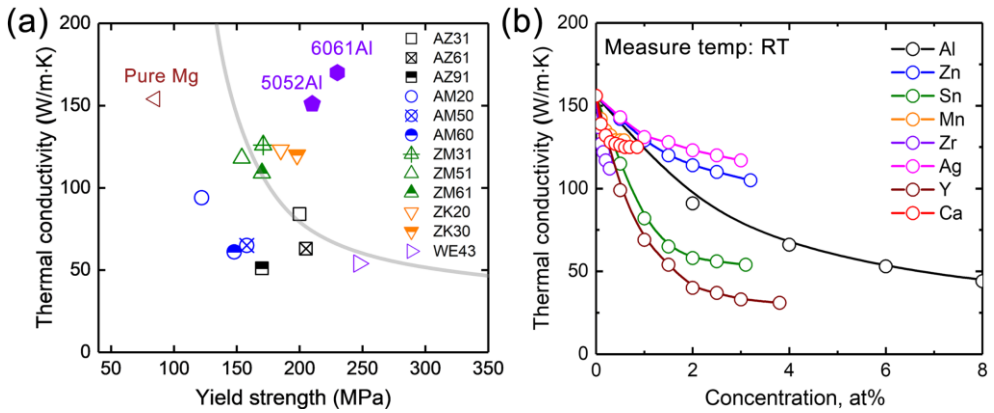

Fig. 1.21. (a) Thermal conductivity and yield strength for various commercial wrought Mg and Al alloys. (b) Variations in thermal conductivity as functions of solute concentration in various Mg binary alloys at RT [46,48].

The influence of alloying elements on thermal conductivity of Mg alloys is controlled by various factors, including atomic volume difference, chemical valency and configuration of extra-nuclear electrons [48]. Figure 1.21b shows variations in thermal conductivity as functions of solute concentration in various Mg binary alloys at RT. The addition of Y or Sn to Mg intrinsically has severe impacts on the decline of thermal conductivity due to the larger difference of atomic radii; 1.81 Å for Y and 1.6 Å for Mg, or higher solute valence; +4 for Sn and +2 for Mg based on Linde-Mott's rule. In contrast, Ag and Zn lead to a slow reduction of thermal conductivity with increased solute contents, which is associated with the close atomic size and valence. Besides, Ca, Mn, and Zr also degrade the thermal conductivity given the large size discrepancy or extra vacant sites in nucleus subshell; $4d^2$ for Zr is much lower than full $4d^{10}$ state, however, the low solubilities of these alloying elements in Mg matrix; only ~ 1 at.% diminish the negative effects. Therefore, Zn is considered as the best choice for the main alloying addition in high thermally conductive Mg alloys considering the lower cost than that of Ag.

Artificial aging is an effective approach to achieving both high strength and high thermal conductivity as demonstrated in various heat-treatable Al alloys. The commercial solution-treated Al-1.2Mg-0.6Si (wt.%, 6061Al) alloy sheet has moderate yield strength; 145 MPa and thermal conductivity; 154 W/(m·K) in the

condition. Subsequent artificial aging at 180 for 8 h significantly increases the yield strength and thermal conductivity to 276 MPa and 167 W/(m·K) due to the dense distribution of Mg_2Si precipitates along with reduced solute contents in the Al matrix. The Mg-Zn-Ca dilute alloy system is quite promising for developing heat-treatable Mg alloy sheets with high thermal conductivity due to the excellent formability and rapid age-hardening response. Besides, a trace addition of Zr into Mg-Zn based alloys can remarkably refine the grain size, which may further improve the mechanical properties.

1.5 Summary and outlook

As the lightest metallic structural material, Mg alloys have attracted considerable attention for lightweight applications in automotive, high speed trains and consumer electronics. Currently, a vast majority of Mg alloy products are fabricated by conventional casting methods. However, wrought Mg alloys, especially rolled sheets, have yet to find wide usage due to the poor formability at room temperature (RT). For example, the commercially available AZ31 alloy sheet shows a sufficient yield strength of ~ 200 MPa, while a low Index Erichsen (I.E.) value, an indicator of stretch formability, of less than 4 mm at RT falls far behind the requirement for stamping process. Such poor RT formability is mainly caused by the strong basal texture with (0002) planes of most grains parallel to the sheet plane developed during rolling process. The addition of RE and Ca may improve stretch formability of Mg alloy sheets due to the weakened basal texture. Some alloy sheets such as Mg-1.5Zn-0.2Ce (wt.%, ZE10) and Mg-1.5Zn-0.1Ca (wt.%, ZX10) exhibit high I.E. values over 9 mm at RT, which is comparable to those of 5xxx, 6xxx series Al alloy sheets. However, the improvement of formability in these RE/Ca-containing alloys is normally achieved at the expense of strength due to a negative correlation between the strength and formability; i.e. strength-formability trade-off dilemma. To broaden the applications of Mg products, it is essential to develop high-strength and RT formable Mg sheet alloys.

The development of heat-treatable Mg alloy sheets with excellent RT formability is an effective approach to overcome the strength-formability trade-off dilemma. For example, the Mg-Al-Ca dilute alloys exhibits strong age-hardening response due to the precipitation of Guinier Preston (G.P.) zones, thus are promising candidates. As demonstrated in a Mg-1.2Al-0.5Ca-0.4Mn-0.8Zn (wt.%, AXMZ1000) sheet alloy, a I.E. value of 7.7 mm and moderate yield strength of 147 MPa are obtained in the solution-treated condition. Subsequent artificial aging at 200 ºC for 1 h substantially increases the yield strength over 200 MPa, enabling this alloy sheet to overcome the dilemma. The improved formability in this alloy sheet is due to a weak basal texture developed by the trace addition of Zn, however, the texture weakening mechanism is still controversial. In order to further improve the formability and strength, it is essential to optimize the Zn content based on a thorough understanding of the role of Zn in this new class of Mg sheet alloys.

Besides the excellent formability, another notable feature for heat-treatable Mg sheet alloys is the rapid age-hardening response; the peak hardness obtained within only few hours during artificial aging, which is critical for countering the formability-strength trade off, and even realizing the bake-hardenability which has been used in steels and Al alloys. Compared to commercial Mg alloy systems such as Mg-Al-Zn (AZ) and

Mg-Zn-Zr (ZK) with very poor or sluggish age-hardening response, the trace addition of Zn into the Mg-Ca based dilute alloys can significantly enhance the age-hardening response by a dense dispersion of G.P. zones. However, the origin of accelerated age-hardening kinetics along with formation of the G.P. zones remains unclear. Thus, it is rather intriguing to study the origin of rapid age-hardening in the Mg-Ca-Zn system. In addition, previous studies suggest a simple precipitation sequence; S.S.S.S. (supersaturated solid solution) $\rightarrow$ ordered G.P. zones $\rightarrow \eta' \rightarrow \eta$ for the Mg-Ca-Zn system, while accurate structures and compositions of involved precipitate phases are still controversial. A full knowledge of the precipitation behavior is expected to give deeper insights on the alloy design and precipitation strengthening in Mg-Ca-Zn system.

In addition to extraordinary mechanical properties, additional functions such as high thermal conductivity may simultaneously be realized in heat-treatable Mg alloys. Since the strength of commercially available wrought Mg alloys, e.g. Mg-3Al-1Zn (wt.%, AZ31) and Mg-6Al-1Zn (wt.%, AZ61) mainly relies on solid-solution strengthening, the lattice distortion induced by solute atoms significantly increases electron and phonon scattering which results in low thermal conductivity. Heat-treatable Mg alloys are promising to achieve both high strength and high thermal conductivity due to the precipitation strengthening accompanied with reduced solute contents in the Mg matrix. Mg-Zn based alloys shows a minimal effect on the loss of thermal conductivity among the various binary alloys. The trace addition of Ca into dilute Mg-Zn based alloys can significantly enhance the age-hardening response and weaken basal texture in alloy sheets. Besides, Zr addition, as a powerful grain refiner for Mg-Zn based alloys, may lead to further improved mechanical properties. Thus, the heat-treatable Mg-Zn-Ca-Zr dilute alloy system is a potential candidate for simultaneously achieving high thermal conductivity, high strength and excellent RT formability in Mg sheet alloys.

Therefore, the motivations of this thesis are summarized as follows:

(1) To clarify the role of Zn on the texture weakening and mechanical properties in Mg-1.2Al-0.5Ca-0.4Mn-*x*Zn sheet alloys;

(2) To reveal the addition of Zn on the accelerated age-hardening kinetics in the Mg-Ca-Zn alloy system;

(3) To unambiguously establish the precipitation sequence in the Mg-Ca-Zn alloy system;

(4) To develop a Mg-Zn-Ca-Zr sheet alloy with an outstanding combination of excellent RT formability, high strength and high thermal conductivity.

The thesis comprises of seven chapters. Chapter 1 introduces the research background and issues in Mg sheet alloys. Chapter 2 gives the experimental procedure for sample fabrications and subsequent characterization methods. Chapter 3 describes the effects of Zn additions on the mechanical properties and texture weakening in Mg-1.2Al-0.5Ca-0.4Mn-*x*Zn sheet alloys. Chapter 4 studies the role of Zn on the accelerated age-hardening kinetics in a ternary Mg-0.5Ca-1.6Zn (wt.%) alloy. Chapter 5 investigates the precipitation sequence of the Mg-0.5Ca-1.6Zn (wt.%) alloy during isothermal aging at 200 °C. Chapter 6 reports a new Mg-1.6Zn-0.5Ca-0.4Zr (wt.%, ZXK210) sheet alloy with a combination of excellent RT formability, high strength and high thermal conductivity. Chapter 7 summarizes the above works, and put forward future prospects.

Reference

[1] M.M. Avedesian, H. Baker, ASM specialty handbook, magnesium and magnesium alloys, ASM International, Materials Park, OH, 1999.

[2] L.A. Dobrzanski, G.E. Totten, M. Bamberger, Magnesium and Its Alloys: Technology and Applications CRC Press, Taylor & Francis Group, Florida, 2020.

[3] M.K. Kulekci, Magnesium and its alloys applications in automotive industry. Int. J. Adv. Manuf. Technol. 39 (2008) 851–865.

[4] P.K. Mallick, Materials, Design and Manufacturing for Lightweight Vehicles, CRC Press, Woodhead, Oxford, 2010.

[5] J.F. Nie, K.S. Shin, Z.R. Zeng, Microstructure, Deformation, and Property of Wrought Magnesium Alloys, Metall. Mater. Trans. A, 51 (2020) 6045–6109.

[6] Http://www.lgnewsroom.com/2010/12/lg-to-utilize-only-cleaner-eco-magnesium-in-all-mobile-devices-by-2012/; https://www.dpreview.com/reviews/canoneos5dmarkii/5

[7] I. Polmear, D. StJohn, J.F. Nie, M. Qian, Light Alloys: Metallurgy of the Light Metals, Elsevier, Oxford, 2017.

[8] M.H. Yoo, Slip, twinning, and fracture in hexagonal close-packed metals, Metall. Trans. A, 12 (1981) 409-418.

[9] I.J. Beyerlein, J. Wang, M.R. Barnett, C.N. Tomé, Double twinning mechanisms in magnesium alloys via dissociation of lattice dislocations. Proc. R. Soc. a-Math. Phys. Eng. Sci. 468 (2012) 1496–1520.

[10] M.R. Barnett, Z. Keshavarz, A.G. Beer, X. Ma Non-Schmid behaviour during secondary twinning in a polycrystalline magnesium alloy, Acta Mater. 56 (2008) 5–15.

[11] Y. Chino, X. Huang, K. Suzuki, M. Mabuchi, Enhancement of stretch formability at room temperature by addition of Ca in Mg-Zn alloy, Mater. Trans., 51 (2010), pp. 818-821

[12] Http://magnesium.or.jp/topics/demand_2019-2020/

[13] M.A. Meyers, K.K. Chawla, Mechanical behavior of materials, Cambridge University Press, Cambridge 2009.

[14] J.R. Davis, H. Baker, Aluminum and Aluminum Alloys, ASM specialty Handbook, Materials Park, OH, 1993.

[15] B.C. Suh, M.S. Shim, K.S. Shin, N.J. Kim, Current issues in magnesium sheet alloys: where do we go from here? Scr. Mater. 84 (2014) 1–6.

[16] F. Kaiser, J. Bohlen, D. Letzig, K.U. Kainer, Anisotropic properties of magnesium sheet AZ31, Mat Sci Forum, 419 (2003) 315–320.

[17] S. Liang, Deformation and its Effect on Recrystallization in Mg Alloy AZ31, Master thesis, McMaster University, 2012.

[18] X.S. Huang, K. Suzuki, N. Saito, Enhancement of stretch formability of Mg–3Al–1Zn alloy sheet using hot rolling at high temperatures up to 823 K and subsequent warm rolling, Scr. Mater. 61 (2009) 445–448.

[19] X.S. Huang, K. Suzuki, Y. Chino, Influences of initial texture on microstructure and stretch formability of Mg–3Al–1Zn alloy sheet obtained by a combination of high temperature and subsequent warm rolling, Scr. Mater. 63 (2010) 395–398.

[20] Y. Chino, X. Huang, K. Suzuki, K. Sassa, M. Mabuchi, Influence of Zn concentration on stretch formability at room temperature of Mg–Zn–Ce alloy, Mater. Sci. Eng. A 528 (2010) 566-572.

[21] Y. Chino, K. Sassa, M. Mabuchi, Texture and stretch formability of a rolled Mg–Zn alloy containing dilute content of Y, Mater. Sci. Eng. A, 513 (2009) 394-400.

[22] Y. Chino, K. Sassa, X. Huang, K. Suzuki, M. Mabuchi, Effects of zinc concentration on the stretch formability at room temperature of the rolled Mg-Zn-Ca alloys, J. Jpn. Inst. Met. Mater. 75 (2011) 35-41.

[23] Z.R. Zeng, Y.M. Zhu, S.W. Xu, M.Z. Bian, C.H.J. Davies, N. Birbilis, J.F. Nie, Texture evolution during static recrystallization of cold-rolled magnesium alloys, Acta Mater. 105 (2016) 479-494.

[24] D. Guan, W.M. Rainforth, L. Ma, B. Wynne, J. Gao, Twin recrystallization mechanisms and exceptional contribution to texture evolution during annealing in a magnesium alloy, Acta Mater. 126 (2017) 132-144.

[25] D. Guan, W.M. Rainforth, J. Gao, L. Ma, B. Wynne, Individual effect of recrystallisation nucleation sites on texture weakening in a magnesium alloy: Part 2- shear bands, Acta Mater. 145 (2018) 399-412.

[26] D. Guan, X. Liu, J. Gao, L. Ma, B. Wynne, W.M. Rainforth, Effect of deformation twinning on crystallographic texture evolution in a Mg–6.6Zn–0.2Ca (ZX70) alloy during recrystallisation, J. Alloy. Compd., 774 (2019) 556–564.

[27] D. Guan, X. Liu, J. Gao, L. Ma, B. Wynne, W.M. Rainforth, Exploring the mechanism of “rare earth” texture evolution in a lean Mg-Zn-Ca alloy, Sci. Rep. 9 (2019) 7152.

[28] K.H. Kim, B.C. Suh, J.H. Bae, M.-S. Shim, S. Kim, N.J. Kim, Microstructure and texture evolution of Mg alloys during twin-roll casting and subsequent hot rolling, Scr. Mater. 63 (2010) 716-720.

[29] X. Zeng, P. Minarik, P. Dobron, D. Letzig, K.U. Kainer, S. Yi, Role of deformation mechanisms and grain growth in microstructure evolution during recrystallization of Mg-Nd based alloys, Scr. Mater. 166 (2019) 53-57.

[30] J.F. Nie, Precipitation and hardening in magnesium alloys, Metall. Mater. Trans. A 43A (2012) 3891-3939.

[31] D. Xu, K. Zhao, C. Yang, H. Li, J. Zhang, Effect of heat treatment on microstructure and mechanical properties of the AZ31/WE43 bimetal composites, Metals 8 (2018) 971-986.

[32] B. Langelier, P. Donnadieu, S. Esmaeili, Characterization of precipitation in Mg-Zn-Ce-(Ca) alloys, Mg 2012, 2012, 485–491.

[33] J.D. Robson, C. Paa-Rai, The interaction of grain refinement and ageing in magnesium–zinc–zirconium (ZK) alloys, Acta Mater. 95 (2015) 10-19.

[34] W. Lai, Y. Li, Y. Hsu, S. Trong, W. Wang, Aging behaviour and precipitate morphologies in Mg–7.7 Al–0.5 Zn–0.3 Mn (wt.%) alloy, J. Alloys Compd. 476 (2009) 118-124.

[35] C.R. Hutchinson, J.F. Nie, S. Gorsse, Modeling the Precipitation Processes and Strengthening Mechanisms in a Mg-Al-(Zn) AZ91 Alloy, Metall. Mater. Trans. A 34A (2005) 2093–2105.

[36] C.L. Mendis, K. Oh-ishi, K. Hono, Effect of Al additions on the age hardening response of the Mg–2.4Zn–0.1Ag–0.1Ca (at.%) alloy—TEM and 3DAP study, Mater. Sci. Eng. A 527 (2010) 973-980.

[37] Z. Xu, M. Weyland, J. Nie, On the strain accommodation of precipitates in magnesium alloy WE54, Acta Mater. 75 (2014) 122-133.

[38] K. Oh-ishi, R. Watanabe, C.L. Mendis, K. Hono, Age-hardening response of Mg–0.3 at.% Ca alloys with different Zn contents, Mater. Sci. Eng. A 526 (2009) 177–184.

[39] J. Jayaraj, C.L. Mendis, T. Ohkubo, K. Oh-ishi, K. Hono, Enhanced precipitation hardening of Mg–Ca alloy by Al addition, Scr. Mater. 63 (2010) 831–834.

[40] A. Takeuchi, A. Inoue, Classification of bulk metallic glasses by atomic size difference, heat of mixing and period of constituent elements and its Application to characterization of the main alloying element, Mater. Trans. 46 (2005) 2817–2829.

[41] M.Z. Bian, T.T. Sasaki, B.C. Suh, T. Nakata, S. Kamado, K. Hono, A heat-treatable Mg-Al-Ca-Mn-Zn sheet alloy with good room temperature formability, Scr. Mater. 138 (2017) 151-155.

[42] X. Gao, S.M. Zhu, B.C. Muddle, J.F. Nie, Precipitation-hardened Mg–Ca–Zn alloys with superior creep resistance, Scr. Mater. 53 (2005) 1321–1326.

[43] K. Oh-ishi, C.L. Mendis, T. Ohkubo, K. Hono, Effect of laser power and specimen temperature on atom probe analyses of magnesium alloys, Ultramicroscopy, 111 (2011) 715-718.

[44] J.C. Oh, T. Ohkubo, T. Mukai, K. Hono, TEM and 3DAP characterization of an age-hardened Mg–Ca–Zn alloy, Scr. Mater. 53 (2005) 675–679.

[45] P.M. Jardim, G. Solorzano, J.B. Vander Sande, Precipitate crystal structure determination in melt spun Mg-1.5wt%Ca-6wt%Zn alloy, Microsc. Microanal. 8 (2002) 487–496.

[46] H. Tang, Y. Tang, Z. Wan, J. Li, W. Yuan, L. Lu, Y. Li, K. Tang. Review of applications and developments of ultra-thin micro heat pipes for electronic cooling, Appl Energy, 223 (2018) 383-400.

[47] S. Li, X. Yang, J. Hou, W. Du, A review on thermal conductivity of magnesium and its alloys, J. Magnes. Alloy. 8 (2020) 78-90.

[48] H. Pan, F. Pan, R. Yang, J. Peng, C. Zhao, J. She, Z. Gao, A. Tang, Thermal and electrical conductivity of binary magnesium alloys, J. Mater. Sci. 49 (2014) 3107-3124.

Chapter 2 Experimental procedure

2.1 Alloy sheets preparation

2.1.1 Chemical composition and casting processing

Table 2.1 summaries the nomenclatures and compositions of alloy samples used in the present work. The Mg-Ca, Mg-Zn-Ca, Mg-Zn-Zr and Mg-Zn-Ca-Zr alloy ingots were prepared from high-purity Mg, ZK60 (Mg-5.5Zn-0.5Zr, wt.%), Mg–30 wt% Ca and Mg–34 wt% Zr master alloys by induction melting in a steel crucible under an Ar atmosphere at nearly 750 °C for ~ 1 h. Before casting, the surface oxidation of alloying ingredients or was removed by sandpapers. Liquid metal was stirred by an installed steel bar for three times to ensure the composition homogeneity during casing process, and then poured into a steel mold until naturally cooled to room temperature, Fig. 2.1a. The actual compositions of as-cast ingots were measured using an inductively coupled plasma (ICP) mass spectrometry, which is performed by dissolving trace amounts of sample pieces from the top, middle and bottom parts, respectively in the mixture of hydrochloric acid and nitric acid. The as-cast Mg-Ca and Mg-Zn-Ca ingots are ~ 50 g in cylinder shapes, while the Mg-Zn-Zr and Mg-Zn-Ca-Zr ingots for rolling process were ~ 5 kg with a size of ~ 300 × 90 × 90 mm^3. The ingots were sliced to slabs with a thickness of ~ 10 mm by band saw.

Table 2.1 Alloy nomenclatures and compositions in wt.% and at.%.

Alloy nomenclature	wt.%	at.%
AXM100	Mg-1.2Al-0.4Ca-0.5Mn	Mg-1.1Al-0.3Ca-0.2Mn
AXMZ1000	Mg-1.3Al-0.5Ca-0.7Mn-0.8Zn	Mg-1.1Al-0.3Ca-0.3Mn-0.3Zn
AXMZ1002	Mg-1.1Al-0.4Ca-0.6Mn-1.6Zn	Mg-1.0Al-0.3Ca-0.3Mn-0.5Zn
X1	Mg-0.5Ca	Mg-0.3Ca
ZX21	Mg-1.6Zn-0.5Ca	Mg-0.6Zn-0.3Ca
ZXK210	Mg-1.6Zn-0.5Ca-0.4Zr	Mg–0.6Zn–0.3Ca–0.1Zr
ZK20	Mg-1.6Zn-0.4Zr	Mg–0.6Zn–0.1Zr
ZXK510	Mg-5Zn-0.5Ca-0.4Zr	Mg–1.9Zn–0.3Ca–0.1Zr

The AXM and AXMZ alloy strips were fabricated by twin-roll casting (TRC) processing in Sumitomo Electric Industries Ltd. with a size of ~ 270 mm in width and 4 mm in thickness. Compared to the conventional ingot casting (IC), the TRC is a continuous casting process which can directly produce large-scale strip plates from molten metals [1,2]. Figure 2.1b shows the schematic of TRC followed by hot rolling process. The molten metal in a launder is fed into the tundish, and then dragged to the gap of two water-cooled rollers. The strip solidifies immediately to the fix width and thickness when the melt contacts with cooled rollers. Such rapid

solidification rate; ~ 10^2–10^3 K/s significantly reduces solidifying segregation, refines the grain size and intermetallic particles, and extends solid solubilities of alloying elements. Besides, the TRC is also a cost-efficient processing due to the reduced thermomechanical steps and time, thus leading to a high productivity but low energy consumption. Before the subsequent hot rolling, the strips were cut into ~100 mm long × ~ 85 mm wide.

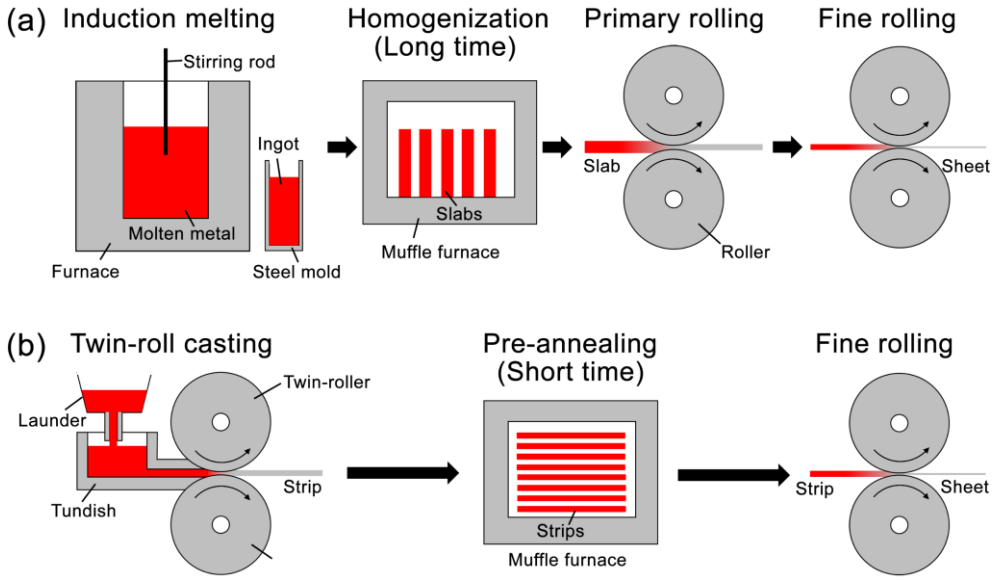

Fig. 2.1. Schematic diagram of Mg alloy sheets production procedures. (a) Conventional ingot casting followed by homogenization and hot rolling. (b) Twin-rolling casting followed by short-time pre-annealing and hot rolling.

2.1.2 Thermomechanical processing

Figure 2.2 shows detailed parameters adopted during the thermomechanical process. Before hot rolling, the TRC AXM(Z) alloy sheets were homogenized at 450 °C for 2h in a muffle furnace, followed by water quenching. The homogenized strips were subsequently rolled from ~ 4 mm to ~ 1 mm thick sheets by four passes at 100 °C with ~30% thickness reduction per pass. After each rolling pass, the sheets were reheated at 450 °C for 5 min prior to subsequent rolling. The as-rolled sheets were subjected to a solution treatment at 450 °C for 1 h and water quenched. Some samples were further artificially aged at 170 °C for 2 h (T6) in a silica oil bath.

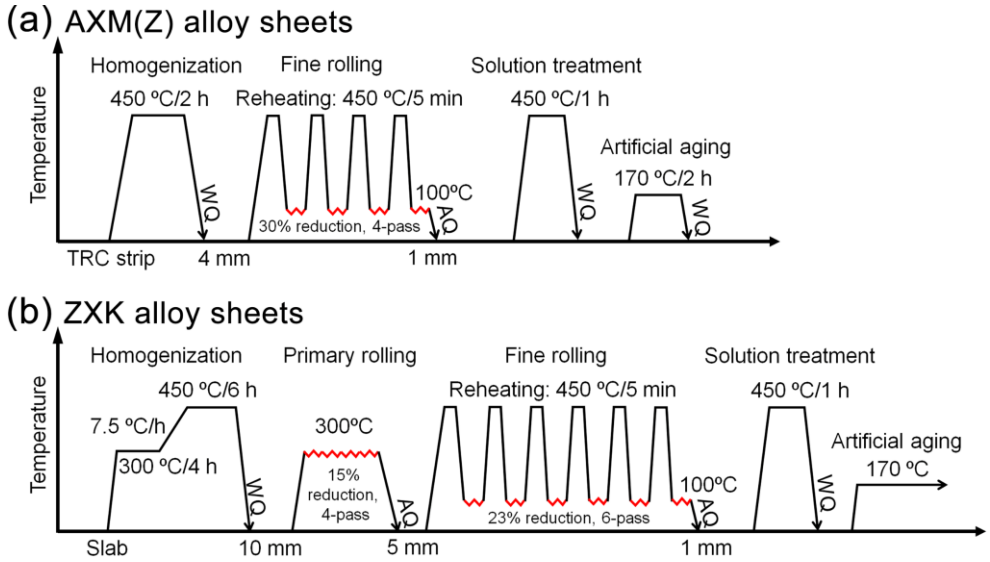

Fig. 2.2. Schematic diagram of the thermomechanical processing for (a) AXM(Z), and (b) ZXK alloy sheets.

In contrast, the as-cast ZKX slabs in 10 mm thickness were homogenized at 300 °C for 4 h and then slowly heated to 450 °C (~7.5 °C/h) maintaining for 6 h, followed by water quenching. The homogenized slabs were primarily rolled to ~5 mm thick at 300 °C by four passes with ~15% thickness reduction per pass. The 5 mm thick plates were further fine-rolled to ~1 mm at 100 °C by six passes, with in ~23% thickness reduction per pass. The sheets were reheated at 450 °C for 5 min between each pass during fine rolling. The as-rolled sheets were solution-treated at 450 °C for 1 h and water quenched. Some samples were subsequently aged at 170 °C for various time in a silicon oil bath. Besides, the Mg-Ca and Mg-Zn-Ca small ingots; ~ 50 g were homogenized at 520 °C for 2 h in a He-filled Pyrex tube, and water quenched. The homogenized samples were then cut into slices with a thickness ~ 1 mm, and aged in an oil bath at 200 °C for various time.

2.2 Mechanical properties measurements

2.2.1 Hardness testing

To study the age-hardening response of solution-treated samples, variations of hardness as a function of aging time is measured at 170 and 200 °C using a Vickers hardness tester, Mitutoyo HM-102, under a load of 0.3 kg with a dwell time of 10 s. Figure 2.3 shows the schematic of Vickers hardness testing, and the measurement of pyramidal-shape impression. The Vickers hardness is calculated as $HV = 2\sin(\gamma/2)\cdot F/(d_1 \cdot d_2)$, where γ is 136°, F is the load, d_1 and d_2 are the diagonal length of pyramidal-shape impression [3]. Before hardness testing, rectangular samples with a size of ~ 20 × 10 mm^2 are cut using a wheel saw cutting machine, Buehler IsoMet, and ground smooth using 4000-grid SiC sandpaper. After each aging treatment, the samples are slightly reground by 4000-grid sandpaper to remove minor oxidation during aging process. The average

hardness values are obtained with ten indents taken randomly on the surface of samples, and the standard deviations are calculated as error bars.

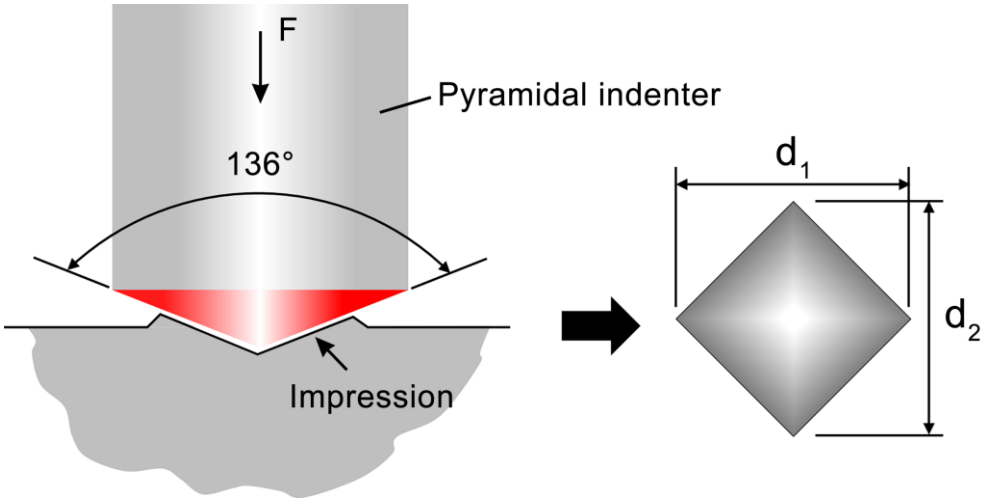

Fig. 2.3. Schematic diagram of Vickers hardness testing on the sample surface, and the measurement of pyramidal-shape impression.

2.2.2 Tensile testing

To evaluate the tensile properties of alloy sheets, tensile tests are conducted at RT using a screw-driven Instron 5567 mechanical testing machine with an extensometer. Dog-bone like tensile specimens with a gauge size of 12.5 mm in length × 5 mm in width are machined from solution-treated samples, and ground flat by 2000-grid SiC sandpaper. Some specimens are further aged at 170 °C for various time. The crosshead speed was set to 0.125 and 0.0125 mm/s, corresponding to initial strain rates of 10^{-3} s^{-1} and 10^{-4} s^{-1}, respectively. The loading directions were 0, 45 and 90° from the rolling direction (RD), which are denoted as RD, 45° and TD, respectively, Fig. 2.4a. In the nominal stress-strain curve, tensile yield strength (σ_{TYS}) and ultimate tensile strength (σ_{UTS}) are defined as the 0.2%-strain offset stress and the maximum stress, respectively, and the elongation ε_T is related to the strain at fracture, Fig. 2.4b. To evaluate the tensile anisotropy, the Lankford values, i.e. r-value, $r = \varepsilon_w/\varepsilon_t$ where ε_w is the width-direction strain and the ε_t is thickness-direction strain, are measured along the three directions; r_{RD}, $r_{45°}$, and r_{TD} with specimens stretched to a nominal strain of 9%. The average r-value, $r_{ave} = |(r_{RD} + 2r_{45°} + r_{TD})/4|$ and anisotropy of r-values, $\Delta r = |(r_{RD} - 2r_{45°} + r_{TD})/2|$ are calculated where the r_{ave} represents the variation of in-plane tensile deformation while the Δr is related to the earing tendency [4]. In general, the smaller r_{ave} and Δr values indicate lower strain anisotropy, which may lead to a higher stretch formability. To study the yielding behavior during tensile testing, the tensile tests are interrupted at ~ 2% strain. The tensile tests in each condition are repeated at least three times to ensure reproducibility of results.

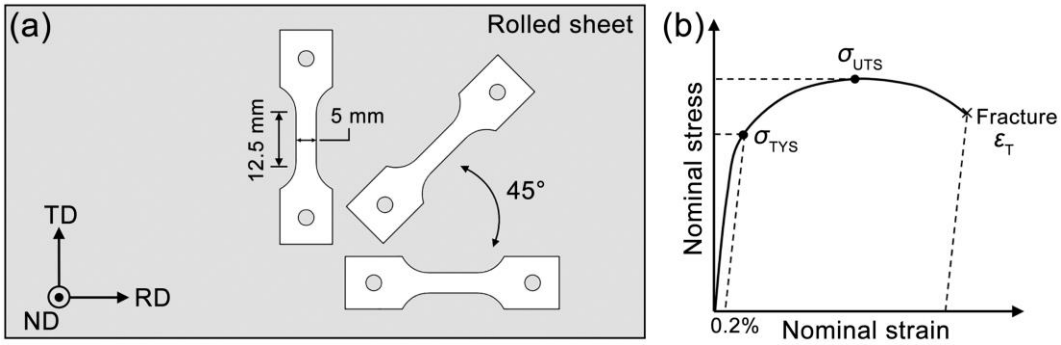

Fig. 2.4. Schematic diagram of (a) tensile specimens in various loading directions, and (b) nominal stress-strain curve.

2.2.3 Erichsen cupping testing

To evaluate the stretch formability of alloy sheets, Erichsen cupping tests were performed at RT using an Erichsen 111 sheet metal testing machine with a ϕ 20-mm hemispherical punch. The schematic diagram has been shown in Figure 1. 8a. The punch speed and blank-holder forces were ~ 6 mm/min and 10 kN, respectively. Before the testing, the as-rolled specimens are cut to 50 × 50 mm^2 using a desktop hand cutter, Sunhayato PC-310, and solution-treated at 450 °C for 1 h followed by water quenching. Then, the solution-treated samples are ground clean by 1000 grid SiC sandpaper to remove the macroscopic defects, and greased with silicon oil. At least five samples for each composition are repeated for the reproducibility of results.

2.2.4 Thermal conductivity testing

The thermal conductivity λ (W/m·K) of alloy sheets at RT was calculated based on $\lambda = \alpha \cdot C_p \cdot \rho$, where thermal diffusivity α (m^2/s) was measured using a Linseis LFA 1000 laser flash analyzer. Fig. 2.5a shows the schematic of a laser flash method [5]. The front side of a plane-parallel sample is subjected to a short laser energy pulse, and the resultant temperature rise as a function of time on the backside is recorded using an infrared detector. The thermal diffusivity is calculated from a half-time method; $\alpha = 0.1388 \cdot d^2/t_{1/2}$, where d is the thickness of the sample, and $t_{1/2}$ is the time at half of the maximum backside temperature rise, which is obtained by fitting the temperature rises versus time curve, Fig. 2.5b. The density ρ (g/cm^3) and specific heat capacity C_p (J/g·K) at RT were determined by the Archimedes method; Mettler Toledo AG285, and Neumann-Kopp rule, respectively.

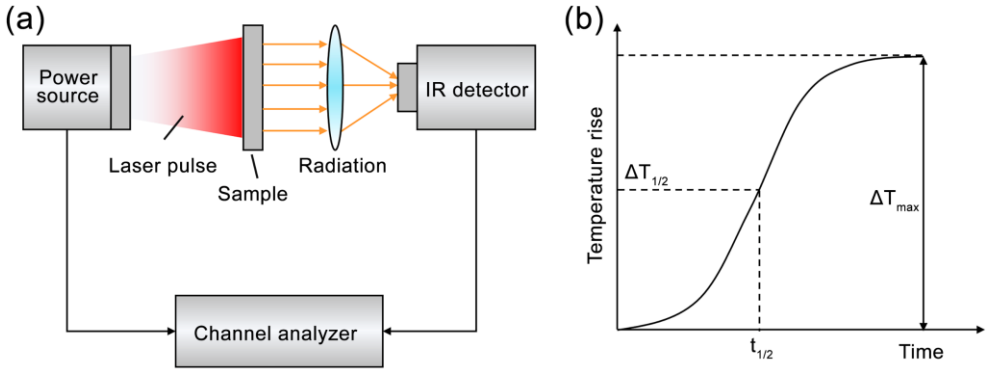

Fig. 2.5. Schematic diagram of (a) the laser flash method, and (b) variation of temperature rise as a function of time in the backside of sample.

Before the measurements, 10-mm squared specimens with a thickness of ~1 mm were prepared from the solution-treated and various aging-treated samples, and ground flat by 4000-grid SiC sandpaper. The both sides of the sample are then lightly painted with a uniform graphite-coating to improve the absorption of energy pulse on the flashed side. At least three tests are repeated for each sample to ensure the reproducibility of results. The density and specific heat capacity of the samples at RT are ~ 1.74 g/cm^3 and ~1.02 J/g·K, respectively, and the temperature rises versus time curve is fitted by a finite pulse model.

2.3 Characterization techniques

2.3.1 Digital image correlation

To quantify the yielding behavior, i.e. strain localization in AXMZ alloy sheets, digital image correlation (DIC) technique is used to characterize the distribution of local strains on the surface of specimens during tensile tests. As an optical strain-tracking method, DIC can visualize the strain distribution during deformation process in real time, and at varied length scales; from macroscale to microscale [5,6]. Figure 2.6 shows the schematic of DIC measuring system consisting of two parts; recording and measurement. The recording system captures sequential images of the stretching specimen during tensile tests. Then, the measurement system calculates the local strain distribution on the specimen surface based on the displacement of speckles in identical areas. A high-resolution CCD camera with 2456 × 2058 pixel; 3.45 × 3.45 μm^2 for each pixel is used for image recording at 10 frames/second, and the commercial software VIC-2D was employed for the strain filed calculations. Before the tensile test, the specimen surface was ground flat by 2000-grid SiC sandpaper, painted in matt white first, and then sprayed with black dots using an airbrush, which provided a black-white mixed random pattern i.e. speckled pattern in the captured images of specimens.

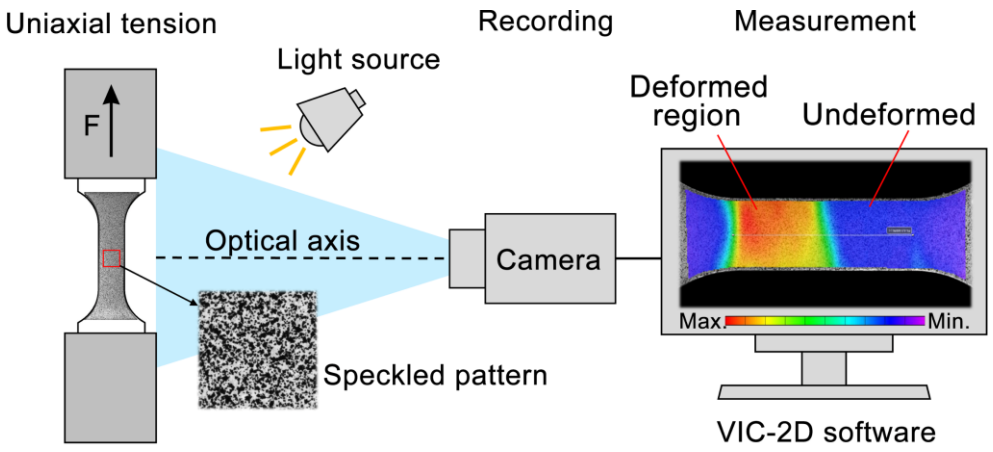

Fig. 2.6. Schematic diagram of DIC measuring system consisting of recording and measurement parts.

2.3.2 X-ray diffraction pole figure measurements

The bulk texture i.e. macrotexture of the alloy sheets is measured by X-ray diffraction (XRD) using a Rigaku Smartlab 4-axes X-ray diffractometer with a Cu $K_{\alpha 1}$ source; λ =1.54056 Å, As the most established technique for texture measurement, XRD can reveals the integral texture of a relatively large volume in a flat specimen by measuring the diffraction intensities of a chosen set of lattice planes. Fig. 2.7 show the schematic of the XRD geometries by the Schulz reflection method [7]. The pole figures are acquired by placing X-ray source and detector at various 2θ angles of a chosen set of lattice planes, which satisfy the Bragg diffraction condition to the sample. During the measurements, the sample is gradually reoriented with φ that varies between 0–360°, and χ angles; ~ 0–90° with an increment of 5° until the whole stereographic space is covered. $\{10\bar{1}0\}_\alpha$, $\{0002\}_\alpha$,$\{10\bar{1}1\}_\alpha$, $\{10\bar{1}2\}_\alpha$ and $\{10\bar{1}3\}_\alpha$ pole figures are obtained for reconstructing the texture of Mg alloy sheets with corresponding 2θ angle of ~ 32.2º, 34.4º, 36.6º, 47.8º and 63.1º, respectively.

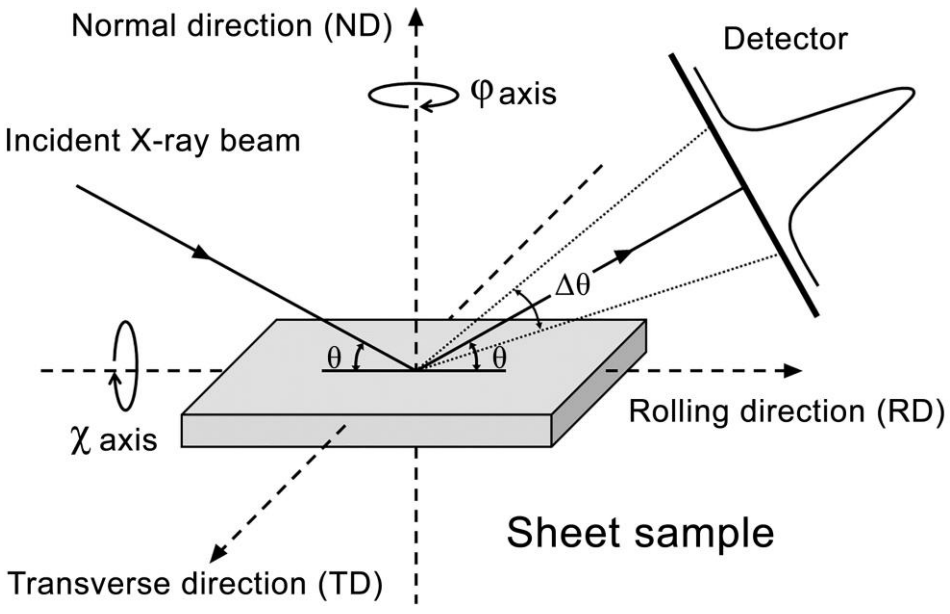

Fig. 2.7. Schematic diagram of the geometries for XRD pole figure measurements.

Before XRD analysis, rectangular samples with a size of 20 × 18 mm^2 are cut by a wheel saw cutting machine, and ground to the mid-thickness planes using 1200 and 4000-grid SiC sandpapers. Complete pole figures are determined from the orientation distribution function (ODF), which is calculated by the arbitrarily defined cells (ADC) method in a ResMat Textool 3.3 software.

2.3.3 Scanning electron microscopy

A field emission gun (FEG) scanning electron microscopy (SEM) in a secondary electron (SE) imaging mode, Carl Zeiss Cross Beam 1540EsB, is used to observe the slip traces on the top surface of 3-mm stretched formed AXMZ alloy sheets by Erichsen cupping testing machine at an accelerating voltage of 20 kV. Before SEM observations, the samples with the dimension of 50 × 50 mm^2 were mechanically ground by 2000 and 4000-grid SiC sandpaper, and subsequently polished by 250 nm colloidal silica suspension, OP-S Struers, to mirror surface. After Erichsen cupping testing to 3 mm, the dome surface of samples is observed by the SEM at an accelerating voltage of 20 kV, and a working distance of 10 mm.

2.3.4 Electron backscatter diffraction and transmission Kikuchi diffraction

Electron backscatter diffraction (EBSD) and transmission Kikuchi diffraction (TKD) are SEM based microstructural-crystallographic techniques, which can provide information about the structure, crystal orientation, phase and strain distribution in a local region of the crystalline material. Fig. 2.8a shows a schematic of experimental setup for the EBSD measurement [8,9]. In the SEM chamber, the incident electron beam is focused onto the surface of a flat crystalline sample with a tilt angle of 70°. The excited backscattered electrons at the Bragg condition will form a set of diffraction cones projected on a phosphor screen perpendicular to the objective lens, resulting in the formation of Kikuchi bands in the electron backscatter pattern (EBSP). If the sample geometry is well described, the position of indexed Kikuchi bands in the EBSP can be related to the underlying crystal phase and orientation within the electron interaction volume, thus leading to an orientation map collected by scanning the electron beam in a prescribed fashion. The orientation map may describe the crystal orientation of individual grain, integrated microtexture, boundary misorientation, and grain size etc. However, the spatial resolution of EBSD is limited to 20-50 nm because of a relatively large interaction volume between the electron beam and the sample. In contrast, the TKD is conducted on an electron transparent sample with a much smaller sample-beam interaction volume, which significantly improves the spatial resolution to 2-5 nm, Fig. 2.8b. In the current TKD setup, the phosphor screen is positioned below the sample normal to the incident beam, so called “on-axis” TKD, leading to the higher intensity and negligible gnomonic distortion of acquired Kikuchi patterns compared to the conventional “off-axis” TKD, and thus better spatial resolution.

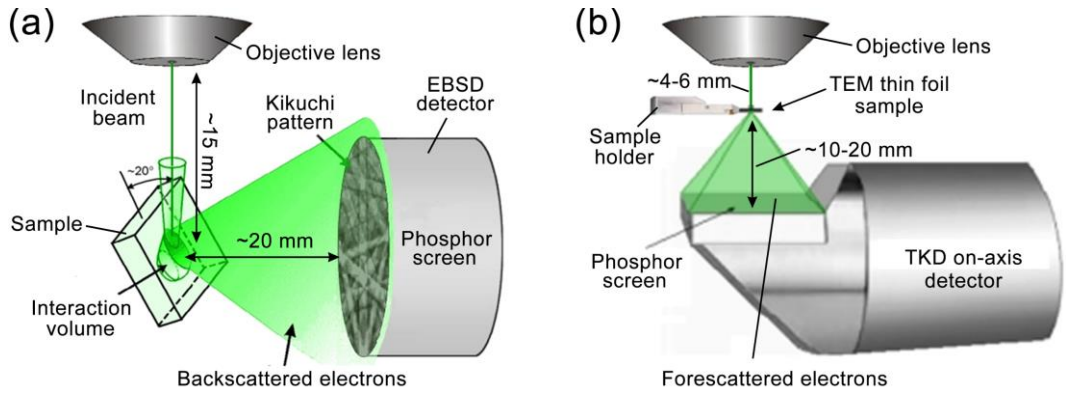

Fig. 2.8. Schematic diagram of (a) EBSD, and (b) TKD setup in the SEM.

In the present work, the EBSD was performed in the Carl Zeiss Cross Beam 1540EsB FEG SEM equipped with a Nordlys-S detector and an Oxford Instruments AZtecHKL analysis system at 20 kV and working distance of 15 mm, while the TKD is conducted using an FEI Helios NanoLab 650 dual-beam SEM installed with an on-axis OPTIMUS^{TM} TKD detector and a Bruker QUANTAX analysis system. Before the EBSD measurements, the samples were mechanically polished to mirror surface using 4000-grid SiC sandpaper followed by 250 nm diameter colloidal silica. Then the polished surface was etched by picric acid solution; 5 ml acetic acid + 6g picric acid + 10ml H_2O + 100ml Ethanol, and subsequently ion milling for 5 min using a Hitachi IM4000 machine. For the TKD analysis, the thin foil samples were prepared by punching 3 mm diameter from a 150 μm thick strip, followed by twin-jet electro polishing in a solution of 5.3 g LiCl, 11.2 g $Mg(ClO4)_2$, 500 ml methanol, and 100 ml 2-butoxy-ethanol at ~ -50° with a voltage of 90 V. Afterwards, the foils were cleaned using ion-milling (Gatan PIPS) at 2 kV, 3° for 20 min. The EBSD and TKD data are processed using a TSL OIM7.0 software, and several types of maps are attained for the data analysis as follows. Inverse pole figure (IPF) map is used to present the orientation of each grain in the described sample coordinate. Kernel average misorientation (KAM) map is are inferred to the strain distribution in the microstructure. Band contrast maps in grey scale can identify the microstructure features. Grain orientation spread (GOS) map with a threshold of 1° is used to determine the recrystallized grains. Intragranular misorientation analysis (IGMA) with disorientations of 2°-4° is used to identify the misorientation axes and corresponding geometrically necessary dislocations within deformed grains. Besides, the pole figure, average grain size, and twin boundary types can also be obtained from the EBSD and TKD data.

2.3.5 Positron annihilation spectroscopy and coincidence Doppler broadening

Positron annihilation spectroscopy (PAS) is a well-established technique for studying open-volume defects such as vacancies, dislocations, and grain boundaries etc. in materials. As a non-destructive method, the atomic-scale lattice defects are characterized by implanted positrons, the anti-particles of electrons, with high sensitivity. Based on the different data acquisition, the PAS technique is further categorized into positron lifetime annihilation spectroscopy (PALS), which determines the types and concentration of defects, and

coincidence Doppler broadening (CDB) spectroscopy that provides the local chemical information in the positron annihilation sites [10,11]. Fig. 2.9a shows the experimental setup of PALS measurements. A ^{22}Na radioisotope is commonly used to emit positrons into two bulk samples with a typical sample-source-sample sandwich geometry. The emission of γ ray with energy of 1.27 MeV from the ^{22}Na decay give a start signal to the time-to-amplitude converter (TAC) indicating the birth of positrons, while two annihilation γ rays with the end-point energy of 511 keV is released in opposite directions as the stop signal. The time intervals between the start and the end annihilation γ rays correspond to the lifetime of positrons. Considering a lower electron density of defects than that of perfect lattice, the positrons trapped in defects will leads to longer lifetime compared to that survive in the free state. Therefore, the types and concentration of defects can be obtained from the calculation of positron trapping models.

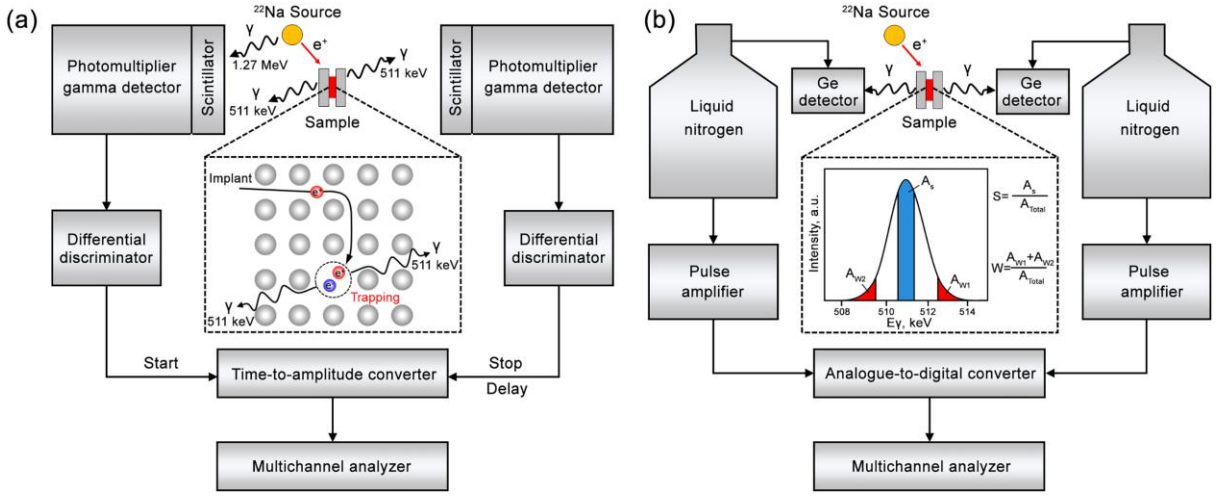

Fig. 2.9. Schematic diagram of (a) PALS, and (b) CDB measurements setup.

On the other hand, the energy shift of γ rays in the laboratory frame broadens the shape of annihilation spectrum, thus providing the momentum distribution of annihilation electrons which is unique for different elements. Fig. 2.9b exhibits a typical CDB setup. The longitudinal energy shift of annihilation rays is measured in coincidence by two high purity Ge detectors at angle of 180º, which significantly reduce the peak-to-background ratio of annihilation spectra. Due to the distinct momentum distributions for valence and core electrons annihilation, the broadening spectra is quantitatively evaluated by the S and W parameters, which corresponds to the ratio of low-momentum; central area and high-momentum; two wing areas regions to the total area, respectively. The S parameter contributed by valence electrons is highly sensitive to the presence of open volume defects, while the W parameter from the inner core electrons provides a chemically specifical signal for the annihilation sites.

In the present work, the PALS and CDB analysis was conducted at RT to investigate the vacancy-type defect evolution in the Mg-Ca-(Zn) alloys during the early stages of isothermal aging. using a conventional positron lifetime system as described elsewhere. The samples for the measurements were cut into small pieces with dimensions of 10×10×1 mm^3, and mechanically polished to mirror surface using 4000-grid SiC sandpaper

followed by 250 nm diameter colloidal silica. The S and W parameters in the CDB spectra are defined as the ratios of low momentum ($|p_L| < 4\times10^{-3}mc$) and high momentum regions ($18\times10^{-3}mc < |p_L| < 30\times10^{-3}mc$) to the total region, respectively.

2.3.6 Transmission electron microscopy

Transmission electron microscope (TEM) and allied scanning transmission electron microscopy (STEM) are powerful microscopy techniques using transmitted electrons to study the structures of materials [12,13]. Currently, (S)TEM can provide not only a high image resolution down to angstroms level, but the structural information through electron diffraction, and chemical composition through the interactions of incident electrons with core electrons of the specimen. Fig. 2.10a shows the ray diagram of a conventional TEM (CTEM) under parallel beam illumination condition. Based on the different operation modes, the CTEM techniques are mainly divided into two parts; bright-field (BF)/dark-field (DF) imaging and selected area electron diffraction (SAED). The BF image is formed by selecting the direct beam to pass through the objective aperture, while only one diffraction beam is permitted to obtain a DF image. Irrespective of mass–thickness contrast, the BF and DF images provides complementary diffraction contrast for sample observations. Specifically, a two-beam condition; only the direct beam and a diffracted beam are strong, with corresponding weak beam dark-field (WBDF) imaging are quite useful for characterizing the structures and orientations of lattice defects such as dislocations and stacking faults with a known reflection g, i.e. the operation vector. The SAED is used to record a diffraction pattern in a selected region by a given sized diffraction aperture, which may identify the phase structure or orientation relationship (OR) with other phases.

In contrast to the CTEM with limited imaging resolution; ~0.3 nm and relatively large volume for diffraction; ~100 nm in diameter, STEM imaging and convergent-beam electron diffraction (CBED) use the focused electron beam with a much finer spot size; 0.05–0.2 nm than that of CTEM; ~10 nm, leading to the higher spatial resolution; <0.1 nm and smaller diffraction volume; <10 nm. More recently, the addition of an aberration corrector to STEMs can achieve even a 0.05 nm imaging resolution and the state-of-the-art atomic-scale chemical mapping. Fig. 2.10b shows the schematic of STEM mode setup. A convergent beam is scanned over the sample in a raster illumination manner with the transmitting signals collected by different detectors; bright-field (BF), annular dark-field (ADF), and high-angle annular dark-field (HAADF). The BF detector collects signals with very small scattering angles; $\theta_{semi} < 10$ mrads, leading to a usual phase contrast analogous to that in BF-TEM images. However, a higher signal-to-noise ratio along with reduced thickness fringes and bend contours by increasing the convergence angle may facilitate the defect analysis in densely strained areas. Especially, an annular BF (ABF) detector located within the cone of the direct beam; $10 < \theta_{semi} < 25$ mrads can visualize the atomic resolution image of light elements such as oxygen or hydrogen. The ADF detector with larger semi-angles of ~ 25-50 mrads collects a dark-field image similar to that in DF-TEM due to the exclusion of the direct beam. The ADF image produced by coherent and thermal diffused, i.e. incoherent, elastic scattered electrons contains both diffraction and Z-contrasts; the column intensity is proportional to about the square of

the atomic number Z. In contrast, the HAADF-STEM with much larger collection semi-angles; ~ 50-200 mrads is more widely used for the identification of heavy atoms given only the incoherent scattered electrons contribute to the Z-contrast image.

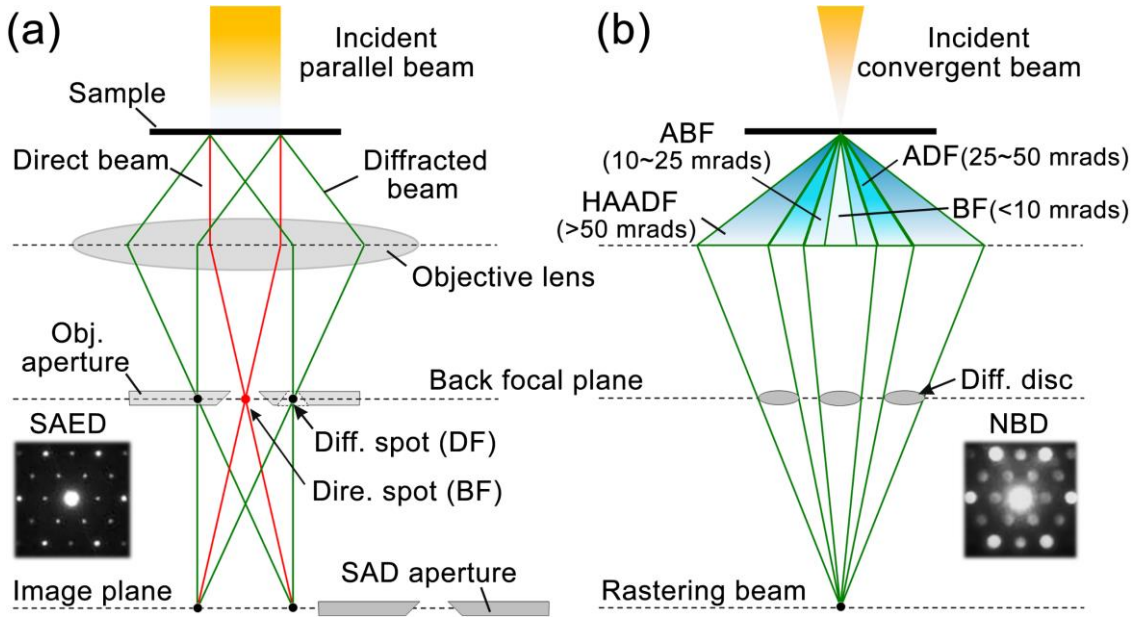

Fig. 2.10. Schematic diagram of (a) conventional TEM, and (b) STEM techniques.

CBED is a convergent beam-based diffraction technique that provides the crystallographic information from a disk diffraction pattern in a small sample area that equal to the used probe size. Since the width of diffraction disks is determined by the convergence angle of electron beam, the CBED methods are further divided into microbeam/nanobeam diffraction (NBD), which can precisely identify the crystal structure and point/space group symmetry in a nanoscale area, and large angle CBED (LACBED) with a much larger diffraction disk for the lattice defect/strain analysis. The thickness of thin-foil samples can be estimated in a two-beam CBED condition by measuring the distance of parallel Kossel-Möllenstedt (K-M) fringes in the two disks. Besides, the raster beam across the sample also enable STEM for compositional analysis using energy dispersive X-ray (EDX) spectroscopy and electron energy loss spectroscopy (EELS), where the characteristic X-rays or energy loss signals are obtained from inelastically scattered electron interactions.

In the present work, the (S)TEM analysis was carried out using the FEI Tecnai-20 TEM with a LaB_6 filament, and FEI Titan G^2 80-200 TEM equipped with a *Cs*-corrector and Super-EDX four silicon drift detectors operated at 200 kV. TEM thin foil samples were prepared by cutting slices, and then grounding to ~150 μm. The thin strip is then punched to *Φ*3 mm discs and electropolished in a twin-jet electropolishing system, Struers TenuPol-5 in a solution of 5.3 g LiCl, 11.2 g $Mg(ClO4)_2$, 500 ml methanol, and 100 ml 2-butoxy-ethanol at ~ -50° with a voltage of 90 V. Afterwards, the foils were cleaned using ion-milling (Gatan PIPS) at 2kV, 3° for 20 min. The BF imaging and SAED patterns were used for the microstructure characterization of solution-treated and isothermally aged samples. The structures and compositions of some

precipitates and interfaces were identified with a combination of HAADF-STEM (ADF) imaging, NBD patterns and EDX analysis.

2.3.7 Three-dimensional atom probe tomography

Atom probe tomography (APT) is a state-of-the-art technique for providing a three-dimensional (3D) visualization and quantitative analysis of chemical distribution within a small volume at atomic scale [14,15]. Fig. 2.11 shows the schematic of local electrode 3D atom probe (3DAP) setup with straight flight path. A needle shaped specimen with a tip radius of ~20-100 nm is attached to a local electrode applied with a direct current high voltage (HV); ~0.5-10 kV at cryogenic temperature of ~20-50 K. The resultant high electrical field; 10-50 V/nm at the apex of the tip ionizes the atoms, which are further evaporated from the surface by the repetitive voltage pulse, which is known as field evaporation process. The evaporated ions are then emitted along the almost linear trajectories, and collected by the position-sensitive detector which consists of a micro-channel plate and delay-line detector. The chemical identity of each detected ion is determined from the mass-to-charge ratio based on the time-of-flight spectrometry, while the impact positions in the detector; (x, y) coordinates, and field evaporation sequence; z-coordinates are used for the subsequent 3D reconstruction of ions in the evaporated sample volume. For the non-conducting samples or with low electrical conductivity, the field evaporation of surface atoms is assisted by thermal energy from a short laser pulse focused at the tip apex. Such laser-assisted mode is essential for broadening the application of 3DAP to a wide range of materials including semiconductors, ceramics, and even organics.

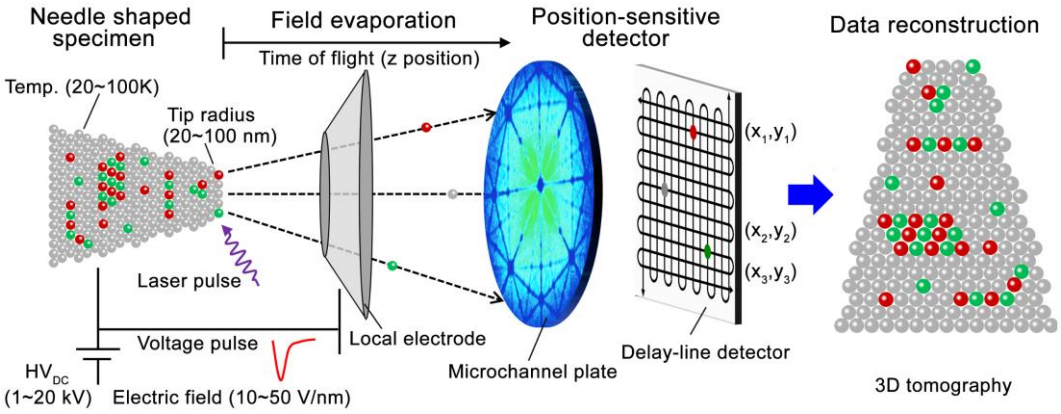

Fig. 2.11. Schematic diagram of a 3D local electrode atom probe tomography setup.

Considering the outstanding spatial resolution and detection sensitivity, 3DAP analysis is superior to investigating the atomic and nanoscale microstructural features, such as solute clustering, nano-precipitates, and chemical segregation at interfaces and defects, and light elements, i.e. Li, B, and N etc., with excellent counting statistics and compositional precision. In parallel, a variety of methods are developed for accurate data reconstruction and statistics corrections. The crystallographic structure information is used to calibrate

reconstruction parameters with the planar interspacing in a known direction. The local concentration within a region of interest can be evaluated by the ladder diagram, 1D composition profile, or proximity histogram. For the quantitative solute clustering analysis, grid-based frequency distribution methods are commonly used for different types of clusters; like-solute atom clustering is characterized from binomial frequency distribution, while contingency tables are conducted for the co-clustering between two elements. More precisely, the clustering phenomena can be unraveled by sophisticated cluster identification algorithms based on the nearest neighbor distributions.

In the present work, the 3DAP analysis was performed for studying solute clusters and precipitates in the various isothermal aged samples using a local electrode atom probe, CAMECA LEAP 5000 XS, in voltage pulse mode at a temperature of 30K with pulse fraction, pulse rate and detection rate ~ 20%, 250 kHz and 0.5-1%, respectively. The site-specific atom probe tips are prepared by the Ga source focused-ion beam (FIB) technique using FEI Helios Nanolab 650 and G4 UX dual-beam systems. Before the FIB fabrication, the target locations are determined by EBSD IPF maps where the grains with (0002) planes parallel to the sample surface are selected for analyzing precipitates on the basal planes. The wedge-shaped specimens are first cut to a size of 15 × 2 × 2 μm^3, and lift-out onto Si micro-posts. The welded samples are then sharpened to a needle-like tip with the radius less than 100 nm by annular milling methods. The accelerating voltage and diameter of the circle pattern are gradually reduced from 30 kV, 3.5/1.5 μm down to 5 kV, 3/0.2 μm. The final milling step was performed at a low voltage of 2 kV in order to reduce the extent of Ga^+ penetration in the specimen.

Reference

[1] C.J. Bettles, M. Barnett, Advances in wrought magnesium alloys: fundamentals of processing, properties and applications, Woodhead, Cambridge, 2012.

[2] S.S. Park, W.-J. Park, C.H. Kim, B.S. You, N.J. Kim, The twin-roll casting of magnesium alloys, JOM 61 (2009) 14-18.

[3] M.A. Meyers, K.K. Chawla, Mechanical behavior of materials, Cambridge University Press, Cambridge 2009.

[4] W.F. Hosford, R.M. Caddel, Metal forming: mechanics and metallurgy, second ed., Prentice Hall, Upper Saddle River, NJ, 1993

[5] B. Pan, Digital image correlation for surface deformation measurement: historical developments, recent advances and future goals, Meas. Sci. Technol., 29 (2018) 082001.

[6] N. Tsuji, M. Park, S. Gao, Y. Bai, Y. Chong, Linking local and heterogeneous deformation behavior to global deformation of materials by in-situ experimental techniques, IOP Conf. Ser.: Mater. Sci. Eng. 580 (2019) 012012.

[7] V. Randle, O. Engler, Introduction to texture analysis: macrotexture, microtexture, and orientation mapping, Gordon & Breach, Amsterdam, 2000.

[8] R. Borrajo-Pelaez, P. Hedström, recent developments of crystallographic analysis methods in the scanning electron microscope for applications in metallurgy, Crit. Rev. Solid State Mater. Sci. 43 (2018) 455-474.

[9] F. Niessen, A. Burrows, A.B.da S. Fanta, A systematic comparison of on-axis and off-axis transmission kikuchi diffraction, Ultramicroscopy 186 (2018) 158-170.

[10] A. Dupasquier, G. Kögel, A. Somoza, Acta Mater. 52 (2004) 4707–4726.

[11] J. Čížek, Characterization of lattice defects in metallic materials by positron annihilation spectroscopy: a review, J. Mater. Sci. Technol. 34 (2018) 577-598.

[12] D.B. Williams, C.B. Carter, Transmission Electron Microscopy: A Textbook for Materials Science, second ed., Springer-Verlag, New York, 2009.

[13] P.W. Hawkes, J.C.H. Spence, Springer Handbook of Microscopy, Springer, Cham, Switzerland (2019)

[14] K. Hono, Nanoscale microstructural analysis of metallic materials by atom probe field ion microscopy, Prog. Mater. Sci. 47 (2002) 621–729.

[15] B. Gault, M.P. Moody, J.M. Cairney, S.P. Ringer, Atom probe crystallography. Mater. Today 15 (2012) 378–386.

Chapter 3 Role of Zn on the room temperature formability and strength in Mg-Al-Ca-Mn sheet alloys

3.1 Introduction

Much attention has been paid to lightweight magnesium (Mg) alloys due to the increasing demand for weight reduction in automobiles [1,2]. Current applications of the Mg alloys are mostly confined to cast products, as wrought products, especially sheet products, suffer from poor formability at room temperature (RT) [3]. The poor RT formability arises from a combination of insufficient deformation modes in the hexagonal close-packed (HCP) structure at RT and the development of strong basal texture, where the c-axes of most grains are strongly aligned to the normal direction (ND) of the sheets, during the hot-rolling process [4].

Considerable efforts are being made to develop RT formable Mg sheet alloys by weakening the basal texture. One approach is the optimization of thermomechanical processing conditions [5]. The basal texture intensity can be dramatically reduced by hot rolling at high temperature over 500 °C, resulting in excellent stretch formability with the Index Erichsen (I.E.) value of 9.5 mm in commercial Mg-3Al-1Zn-0.3Mn (wt.%, AZ31) alloys [6,7]. Another promising approach is the compositional optimization. The trace addition of rare earth (RE) elements into Mg-Zn based alloys significantly lowers the basal texture intensity [8-10]. Some of these alloys such as Mg-1.5Zn-0.2Ce (wt.%) [9] and Mg-1.5Zn-0.2Y (wt.%) [10] exhibit excellent RT stretch formability over 9 mm in I.E. values, which is comparable to those of 6xxx series aluminum alloys. However, the excellent formability in these RE-containing alloys is achieved at the expense of yield strength; the yield strength of the samples with high RT formability is less than 150 MPa, which is not satisfactory for industrial applications [9,10]. Moreover, the high cost and resource scarcity also make the use of RE unacceptable in commercial structural alloys. To broaden the application of the Mg alloy sheets, it is essential to develop strong and formable Mg alloy sheets consisting of ubiquitous elements and industrially viable processing route.

Recent works report that the Mg-Al-Ca-Mn (AXM) sheet alloys is promising to conquer the strength-formability trade-off dilemma [11-13]. In a Mg-3Al-1Zn-1Mn-0.5Ca (wt.%, AZMX3110) sheet alloy, the fine-grained structure with weak basal texture is formed by twin-roll casting (TRC) and hot rolling, and have a large I.E. value of 8 mm and yield strength of 219 MPa [11]. On the other hand, the Mg-Al-Ca and Mg-Zn-Ca dilute alloys exhibit quick and notable age-hardening response due to the precipitation of Guinier Preston (G.P.) zones compared to concentrated Mg alloys such as Mg-9Al and Mg-6Zn (wt.%) [14,15]. Recent studies by Bian et al. have demonstrated that these dilute alloys are promising as heat treatable alloys. A Mg-1.2Al-0.5Ca-0.4Mn-0.8Zn (wt.%, AXMZ1000) sheet alloy shows an I.E. value of 7.7 mm and moderate yield strength of 147 MPa in the solution treated condition (T4), which can be substantially increased to 204 MP by subsequent artificial aging at 200 °C for 1 h [12]. Due to the rapid hardening kinetics, a Mg-1.3Al-0.8Zn-0.7Mn-0.5Ca

(wt.%, AZMX1110) alloy also shows bake-hardenability; the yield strength increases from 177 to 238 MPa by artificial aging at 170 ℃ only for 20 min after 2% pre-straining [13].

In the Mg-Al-Ca based dilute alloy sheets, the Zn addition is necessary to achieve the excellent RT stretch formability, suggesting that the Zn alloying strongly affects the texture evolution in the AXMZ dilute alloys [12]. The addition of Zn to the AXM sheets can also improve both strength and ductility by enhancing the age-hardening response and refining the microstructure [12,16]. Therefore, in order to open up possibilities for the development of a new class of Mg alloy sheets with high RT formability and strength, it is critical to control the Zn content in the AXMZ dilute alloys based on the full understanding of the role of Zn. Several disputed mechanisms have been proposed to explain the texture weakening by co-additions of Zn and Ca to Mg sheet alloys, including preferential nucleation at various sites or oriented grain growth by solute drag [17-19], while the effects of these alloying elements on the texture weakening is still unclear. Our study aims to clarify the role of Zn on the texture weakening and mechanical properties, such as the stretch formability and strength of Mg-1.2Al-0.5Ca-0.4Mn alloy using the state-of-the-art transmission Kikuchi diffraction (TKD) and aberration corrected scanning transmission electron microscopy (STEM).

3.2 Experimental

Alloy sheets with a dimension of 260 mm wide × 4 mm thick were produced by the TRC process. Table 1 summarizes the chemical compositions of the samples in both wt.% and at.%. The TRC sheets were homogenized at 450 °C for 2h in a muffle furnace, followed by water quenching. The homogenized samples were subsequently rolled to a thickness of around 1 mm over four passes at 100 °C, with ~30% thickness reduction per pass. After each rolling pass, the sheets were reheated at 450 °C for 5 min prior to subsequent rolling. The as-rolled samples were subjected to a solution treatment at 450 °C for 1h in a muffle furnace, water quenched, and artificially aged at 170 °C in a silica oil bath. Tensile specimens with a gauge length of 12.5 mm and a width of 5 mm were machined from the solution-treated samples. The loading directions were 0, 45 and 90° from the rolling direction, RD. Hereafter these loading directions are denoted as RD, 45° and TD, respectively.

Table 1 Alloy nomenclature and chemical compositions of samples

Alloy	wt. %	at. %
0 wt.% Zn	Mg-1.2Al-0.4Ca-0.5Mn	Mg-1.1Al-0.3Ca-0.2Mn
0.8 wt.% Zn	Mg-1.3Al-0.5Ca-0.7Mn-0.8Zn	Mg-1.1Al-0.3Ca-0.3Mn-0.3Zn
1.6 wt.% Zn	Mg-1.1Al-0.4Ca-0.6Mn-1.6Zn	Mg-1.0Al-0.3Ca-0.3Mn-0.5Zn

Erichsen cupping tests were performed on 55-mm-square samples using an Erichsen 111 sheet metal testing machine with a ϕ20-mm hemispherical punch at RT. The punch speed and blank-holder forces were around 6 mm/min and 10 kN, respectively. The age hardening responses were measured by a Vickers hardness

tester under a load of 0.3 kgf. Tensile tests were conducted at RT using a screw-driven Instron 5567 tensile test machine at an initial strain rate of 10^{-3} s^{-1}. Additional tensile tests were carried out to determine the Lankford value (r-value, r = $\varepsilon_w/\varepsilon_t$), where the width-direction strain (ε_w) and the thickness-direction strain (ε_t) were measured on specimens deformed to a nominal strain of 9%, average r-value, $r_{ave} = |(r_{RD} + 2r_{45°} + r_{TD})/4|$ and anisotropy of r-values, $\Delta r = |(r_{RD} - 2r_{45°} + r_{TD})/2|$, where r_{RD}, $r_{45°}$, and r_{TD} are the r-values obtained from the samples stretched along RD, 45°, and TD, respectively. For sheet metal forming, the r_{ave} represents the variation of in-plane tensile deformation while the Δr is related to the earing tendency, and further details can be found in [20]. To evaluate the stretch formability of the solution-treated sheets, at least five samples were tested to ensure reproducibility of the tensile and Erichsen cupping test results. Yielding behaviors during tensile tests were characterized by digital image correlation (DIC) method using a software VIC2D.

Macrotextures were measured by X-ray diffraction (XRD) in a Rigaku Smartlab 4-axis diffractometer using Cu-Ka radiation at 40 kV with 200 mA. Pole figure data were analyzed using ResMat Textool 3.3 software. Microstructure and crystallographic texture were characterized by a field emission scanning electron microscope (SEM), Carl Zeiss Cross Beam 1540EsB, equipped with an Oxford Instruments HKL Channel 5 electron backscatter diffraction (EBSD) system. The samples for the EBSD analysis were prepared by mechanical polishing and subsequent ion milling in Hitachi IM4000 system. EBSD data were analyzed using the TSL OIM 7.0 software, and a clean-up procedure was performed only once with a grain tolerance angle of 5° and a minimum grain size of 2 pixels, so as not to lose detailed orientation information. FEI Helios Nanolab 650 SEM equipped with a Bruker on-axis OPTIMUS^{TM} TKD detector was used to characterize the local microstructure of annealed samples in the early stages of recrystallization. High-angle annular dark-field STEM (HAADF-STEM) and energy dispersive X-ray (EDX) spectroscopy analysis were carried out using FEI Titan G^2 80-200 TEM operated at 200 kV. TEM investigation of peak-aged samples was carried out using FEI Tecnai 20. Thin foils for the TKD and TEM observation were prepared by punching 3 mm diameter and twin-jet electro polishing in a solution of 5.3 g LiCl, 11.2 g $Mg(ClO_4)_2$, 500 ml methanol, and 100 ml 2-butoxy-ethanol at about -50 °C with a voltage of 85 V. Afterwards, the foils were cleaned using ion-milling (Gatan PIPS) at 2 kV for 20 min. The final foil thickness is measured to be 50~100 nm using the convergent beam electron diffraction (CBED) method in a TEM. Three-dimensional atom probe (3DAP) was performed using a local electrode atom probe (CAMECA LEAP 5000 XS) in voltage pulse mode at a temperature of 30K. Sharp needle-like specimens for the 3DAP analysis were prepared by the focused ion beam (FIB) lift-out and annular milling techniques using a FEI Helios G4 UX.

3.3 Results

3.3.1 Effects of Zn additions on the mechanical properties

Figure 1 shows the snapshots of the three solution-treated Mg-1.2Al-0.5Ca-0.4Mn-*x*Zn samples with *x*=0, 0.8 and 1.6 wt.% after the Erichsen cupping tests at RT. The I.E. value is remarkably increased from 6.3 mm

to 7.3 mm by the addition of 0.8 wt.%Zn. A further increase in Zn content to 1.6 wt.% improves the I.E. value to 8.2 mm, which is much higher than that of commercial AZ31 alloy (3-5 mm), and even comparable to that reported for 6xxx series Al alloys [21].

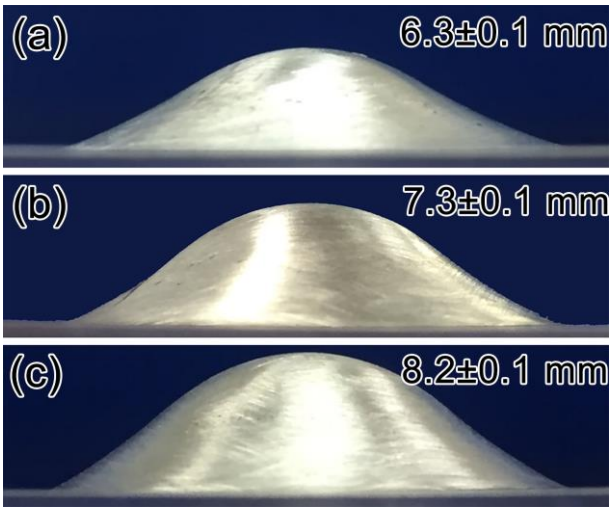

Fig. 1. Snapshots of fractured samples after the Erichsen cupping tests at room temperature for the solution-treated (a) 0 wt.% Zn, (b) 0.8 wt.% Zn and (c) 1.6 wt.% Zn alloy sheets.

Figure 2 shows variations in Vickers hardness of the 0 wt.% Zn, 0.8 wt.% Zn, and 1.6 wt.% Zn alloys as functions of aging time at 170 °C. Note that S.T. and P.A. in Fig. 2 stand for the solution-treated and peak-aged conditions, respectively. All the samples reach their peak hardness at 2 h. The 0 wt.% Zn alloy reaches its peak of 62.8 ± 0.4 HV with a hardness increment of 8.6 HV. The Zn addition of 0.8 wt.% increases the peak value to 66.2 ± 1 HV with a higher increment of 9.4 HV. Further Zn addition to 1.6 wt.% does not result in a significant increase in the peak hardness value as it shows a peak of 66.5 ± 1.1 HV with a hardness increment of 9.1 HV.

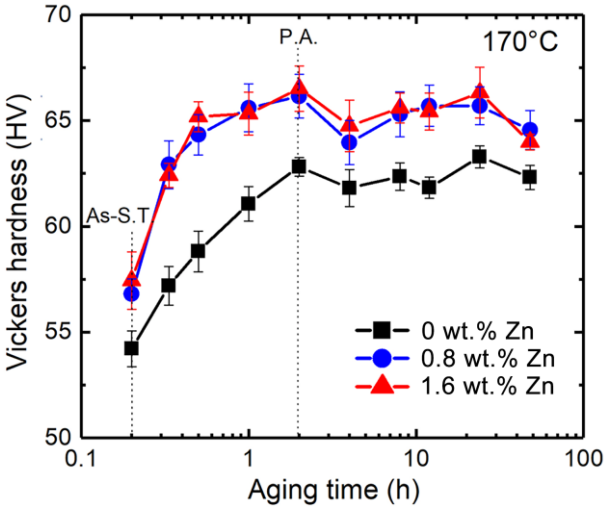

Fig. 2. Variations in Vickers hardness as functions of aging time for the 0 wt.%, 0.8 wt.% and 1.6 wt.% Zn alloys during artificial aging at 170 °C. Note that S.T. and P.A. stand for solution-treated and peak-aged condition, respectively.

Figure 3a-c show the nominal tensile stress-strain curves of the solution-treated (T4) and peak-aged (T6) 0 wt.% Zn, 0.8 wt.% Zn, and 1.6 wt.% Zn alloys stretched along the RD, 45° and TD, respectively. Table 2 summarizes the tensile yield strength, σ_{TYS}, ultimate tensile strength, σ_{UTS} and elongation to failure, ε_T. As shown in Fig. 3a, the solution-treated 0 wt.% Zn alloy shows the σ_{TYS} and σ_{UTS} of 149 and 234 MPa along the RD, which are slightly higher than those along TD and 45°; the σ_{TYS} and σ_{UTS} are 136 and 228 MPa for TD and 142 and 233 MPa for 45°. The ε_T along TD and 45° are 29.7 and 31.9%, which are larger than that along RD, 27.2%. The peak aging at 170 °C for 2 h (T6) resulted in substantial increment in the strengths for all loading directions without significant loss of the elongation. The σ_{TYS} are 183, 180 and 179 MPa and σ_{UTS} are 255, 256 and 255 MPa for RD, TD and 45°, respectively. The solution-treated 0.8 wt.% Zn alloy exhibits σ_{TYS} and σ_{UTS} of 165 MPa and 259 MPa along the RD, which are higher than those of solution-treated 0 wt.% Zn alloy, Fig. 3b.

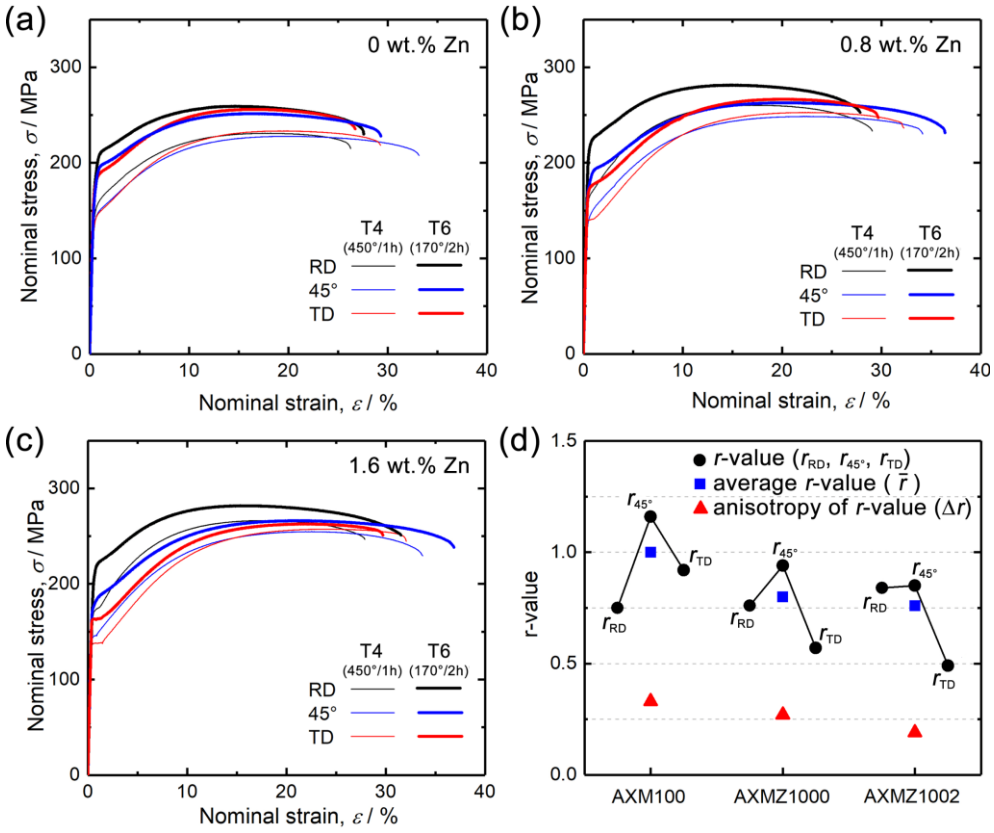

Fig. 3. Nominal stress-strain curves of solution-treated and peak-aged samples. (a) 0 wt.% Zn, (b) 0.8 wt.% Zn and (c) 1.6 wt.% Zn alloys. (d) The *r*-values, average *r*-values ($\bar{r}$) and anisotropy of r-value (Δr) of solution-treated 0 wt.%, 0.8 wt.% and1.6 wt.% Zn alloys.

However, the addition of 0.8 wt.% Zn causes a slight increase in the mechanical anisotropy; the σ_{TYS} and σ_{UTS} are 141 and 253 MPa for TD and 139 and 248 MPa for 45°. The ε_T along TD and 45° are 31.1 and 32.9%, which are larger than that along RD, 28.5%. The T6 treatment resulted in substantial increase in the strengths for all the loading directions without loss of the elongation. The strength increment along the RD is larger

compared to those along TD and 45°; the σ_{TYS} and σ_{UTS} along RD reaches 209 and 277 MPa while those along TD and 45° are 172 and 262 MPa, and 173 and 267 MPa, respectively. The solution-treated 1.6 wt.% Zn alloy exhibits σ_{TYS} and σ_{UTS} of 170 MPa and 268 MPa along the RD, which are slightly higher than those of solution-treated 0.8 wt.% Zn alloy, Fig. 3c. 1.6 wt.% Zn addition leads to a further increase in the mechanical anisotropy; the σ_{TYS} and σ_{UTS} are 138 and 257 MPa for TD and 142 and 255 MPa for 45°. The ε_T along the TD and 45° are 30.9 and 32.6%, which are larger than that along RD, 26.5% but slightly lower than those of the 0.8 wt.% Zn alloy. The T6 treatment resulted in substantial increase in the strengths for all loading directions without loss of the elongation. The strength increment along the RD is larger compared to those along TD and 45°; the σ_{TYS} and σ_{UTS} along RD reaches 210 and 282 MPa while those along TD and 45° are 175 and 265 MPa, and 164 and 263 MPa, respectively.

Table 2 RT tensile properties of solute-treated (S.T.) and peak-aged (P.A.) 0 wt.%, 0.8 wt.% and 1.6 wt.% Zn samples stretched along the RD, 45° and TD, respectively.

Alloy	Condition	RD			45°			TD		
		σ_{TYS}, MPa	σ_{UTS}, MPa	ε_T, %	σ_{TYS}, MPa	σ_{UTS}, MPa	ε_T, %	σ_{TYS}, MPa	σ_{UTS}, MPa	ε_T, %
0 wt.% Zn	S.T.	149 ± 1	234 ± 3	27.2 ± 1.9	136 ± 1	228 ± 1	31.9 ± 1.5	142 ± 1	233 ± 2	29.7 ± 2.5
	P.A.	183 ± 2	255 ± 1	26.1 ± 1.5	179 ± 2	255 ± 1	33.1 ± 1.7	180 ± 1	256 ± 1	26.1 ± 1.7
0.8 wt.% Zn	S.T.	165 ± 1	259 ± 1	28.5 ± 0.4	139 ± 1	248 ± 1	32.9 ± 0.8	141 ± 2	253 ± 1	31.1 ± 1.7
	P.A.	209 ± 1	277 ± 1	26.4 ± 0.9	172 ± 1	262 ± 1	35.1 ± 1.3	173 ± 1	267 ± 1	29.2 ± 0.1
1.6 wt.% Zn	S.T.	170 ± 1	268 ± 2	26.5 ± 1.1	142 ± 3	255 ± 1	32.6 ± 1.7	138 ± 1	257 ± 1	30.9 ± 0.8
	P.A.	210 ± 2	282 ± 2	30.1 ± 2.2	175 ± 2	265 ± 1	36.3 ± 1.2	164 ± 1	263 ± 1	28.3 ± 1.1

Figure 3d shows the r-values, r, average r-values, r_{ave}, and anisotropy of r-values, Δr obtained from the samples stretched along RD, 45°, and TD, respectively. The results are summarized in Table 3. The highest r-value is obtained along 45° in all the samples. The 0 wt.% Zn alloy shows the lowest r-value along RD, while the lowest r-value is obtained along TD in the Zn-containing alloys. The $\bar{r}$ and Δr values are decreased with the addition of Zn. The 1.6 wt.% Zn alloy shows the lowest $\bar{r}$ and Δr values of 0.76 and 0.19, respectively.

Table 3 Lankford values (r-values) of the solution-treated 0 wt.%, 0.8 wt.% and 1.6 wt.% Zn alloy sheets. r_{RD}, $r_{45°}$, and r_{TD} represent the r-values obtained from the samples stretched along RD, 45°, and TD, respectively. Calculation formula of r_{ave} and Δr that represent the average r-value and anisotropy of r-value are adapted from Ref. [20].

Alloy	r_{RD}	$r_{45°}$	r_{TD}	r_{ave}	Δr
0 wt.% Zn	0.75	1.16	0.92	1	0.33
0.8 wt.% Zn	0.76	0.94	0.57	0.8	0.27
1.6 wt.% Zn	0.84	0.85	0.49	0.76	0.19

3.3.2 Microstructure and texture of Zn-free and Zn-addition alloys

Figure 4 shows the inverse pole figure (IPF) maps and (0002) pole figures of the solution-treated 0 wt.% Zn, 0.8 wt.% Zn, and 1.6 wt.% Zn alloys. Note that the IPF maps were obtained by EBSD and taken from the planes normal to TD, and the (0002) pole figures analyzed by the XRD are measured from the sheet normal direction (ND). These samples consist of equi-axed grains with a similar average grain size of ~ 8.6 ± 2.1 μm regardless of the Zn content, Fig. 4 a-c. The (0002) poles in the 0 wt.% Zn alloy are tilted by ~ 15° towards RD, which means the development of an RD-split texture, Fig. 4a. The 0.8 wt.% Zn addition changes the textured feature partially from the RD split to the TD split since the basal poles are tilted not only by ~ 15° towards the RD, but also by about ± 40° towards the TD, Fig. 4b. Further Zn addition up to 1.6 wt.% results in the development of the TD-split texture as demonstrated in Fig. 4c. Note that the textured features observed in the solution treated samples would not be changed by the subsequent artificial aging at 170 °C because of the much lower aging temperature than that for the solution treatment.

Figure 5 shows IPF maps, corresponding image quality (IQ) maps, and (0002) pole figures obtained from the as-rolled 0 wt.% Zn and 1.6 wt.% Zn alloys. Note that the IPF maps were taken from the planes normal to TD, and the (0002) pole figures were constructed from the ND. Inclined band-like structures appear in the as-rolled 0 wt.% Zn alloy as indicated by arrows in the IQ maps, which are considered to be shear bands, Fig. 5a. The as-rolled 1.6 wt.% Zn alloy, in contrast, shows no obvious shear bands, while a larger number of deformation twins are observed in the deformed grains compared to the 0 wt.% Zn alloy as indicated by arrows in Fig. 5b. The (0002) pole figures show that the as-rolled 0 wt.% Zn alloy has an RD-split texture with a higher texture intensity compared to the solution-treated sample, Fig. 5a. As shown in Fig. 5b, the as-rolled 1.6 wt.% Zn alloy also shows a strong RD-split texture unlike the solution-treated 1.6 wt.% Zn alloy that shows the weak TD-split texture, Fig. 4c. These results suggest that the development of the TD-split texture in the Zn-containing alloy is closely associated with the static recrystallization that occurs during the solution treatment.

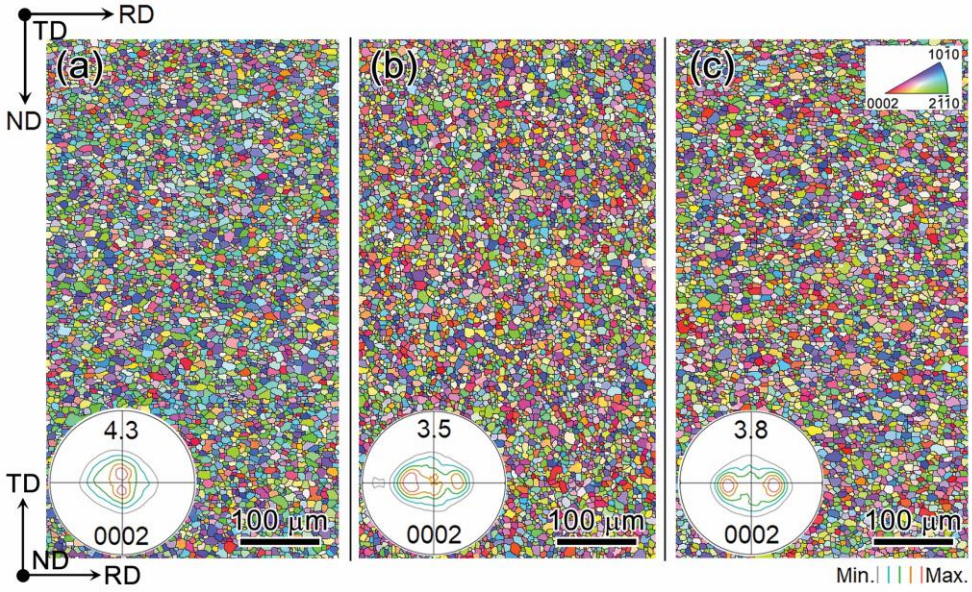

Fig. 4. EBSD IPF maps and (0002) pole figures of the solute-treated (a) 0 wt.% Zn, (b) 0.8 wt.% Zn and (c) 1.6 wt.% Zn alloys. Note that the IPF maps were taken from the planes normal to TD, and the (0002) pole figures were constructed from the ND.

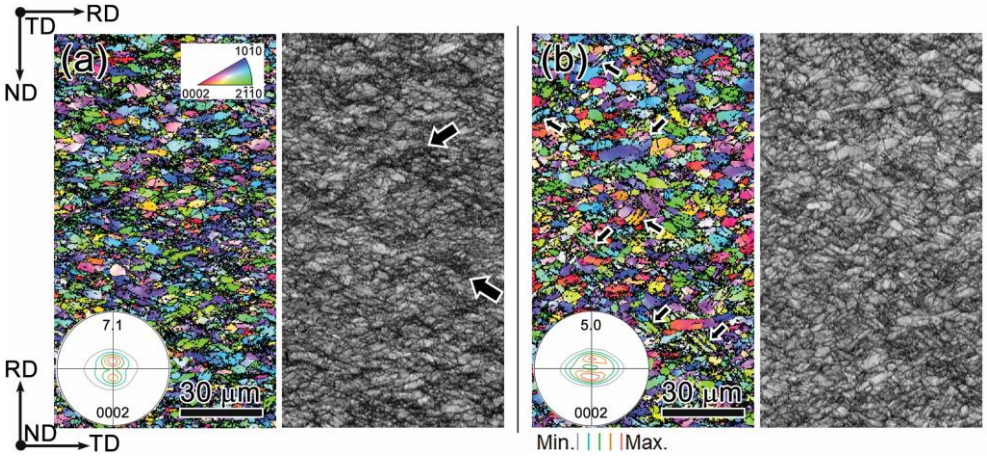

Fig. 5. EBSD IPF maps, corresponding IQ maps, and (0002) pole figures of the as-rolled (a) 0 wt.% Zn and (b) 1.6 wt.% Zn alloys. Note that the IPF maps were taken from the planes normal to TD, and the (0002) pole figures were constructed from the ND.

To identify the active slip modes during the stretch forming, an EBSD-assisted slip trace analysis was performed for the top surface after 3 mm stretch deformation. Figure 6a and b show the secondary electron SEM images of the stretch deformed 0 wt.% Zn and 1.6 wt.% Zn alloys, where the lines of red, yellow and green color represent the slip traces generated by basal ⟨a⟩, prismatic ⟨a⟩ and pyramidal ⟨c+a⟩ slips, respectively. Profuse red lines are observed in both alloys, indicating that basal ⟨a⟩ slip is the dominant deformation mode during the stretch forming regardless of the addition of Zn. The prismatic ⟨a⟩ and pyramidal II ⟨c+a⟩ slips are also activated to accommodate the plastic strain, and these deformation modes are activated more by the

addition of Zn as shown in the number fraction of three slip modes in the stretch formed samples, Figs. 6c and d. The frequency of prismatic ⟨a⟩ slip in the 1.6 wt.% Zn alloy is 25% larger than that of the 0 wt.% Zn alloy, 9%.

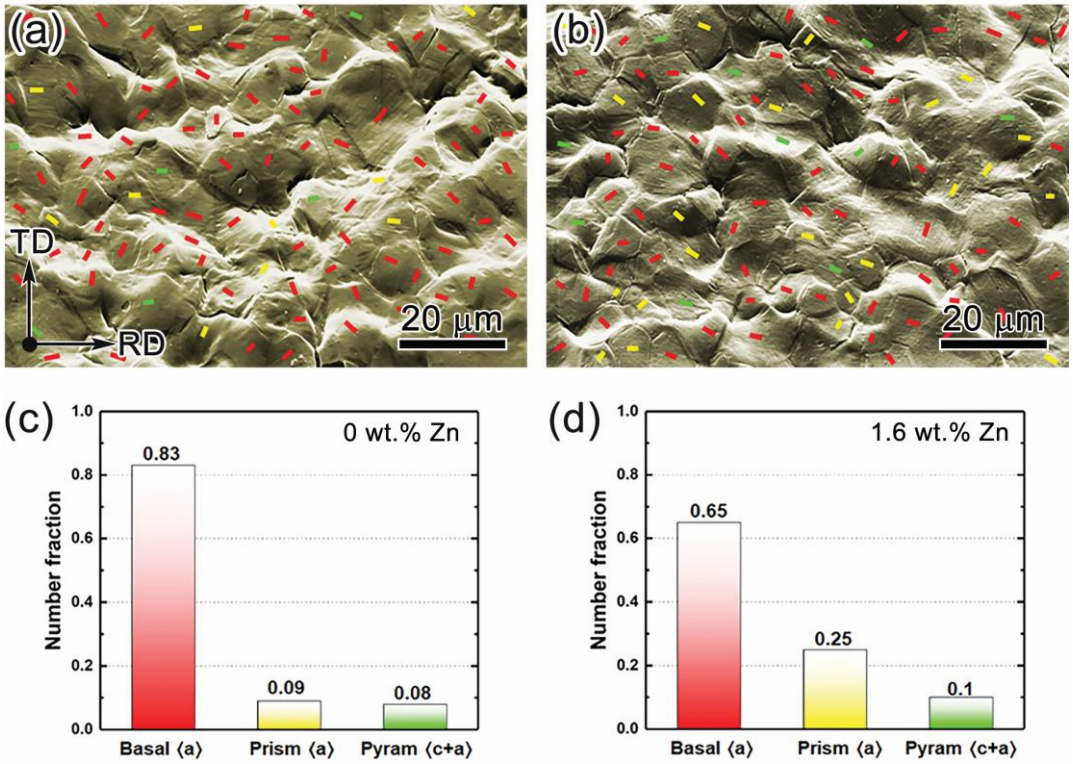

Fig. 6. SEM micrographs illustrating various slip traces on the top surface of the 3 mm stretch formed samples and corresponding frequency of slip traces. (a) and (c) 0 wt.% Zn alloy, (b) and (d) 1.6 wt.% Zn alloys. Methodology used for slip trace analysis is adapted from Refs. [23].

Figures 7a and d exhibit bright field TEM images of peak-aged 0 wt.% Zn and 1.6 wt.% Zn alloys taken from the zone axis of $[11\bar{2}0]_\alpha$. Fine plate-like G.P. zones lying on the basal planes of the Mg matrix are observed in both samples as linear strain contrasts along with the trace direction of the $(0001)_\alpha$ planes in the bright field TEM images and continuous streaking features along the $[0001]_\alpha$ direction at the $1/3(11\bar{2}0)$ and $2/3(11\bar{2}0)$ positions in the selected area diffraction (SAD) patterns [12,24]. 3D atom maps obtained with the analysis direction parallel to the $[0001]_\alpha$ confirm the plate-like feature of the G.P. zones, Figs. 7b and e. The corresponding 1D chemical profile show that the G.P. zones in the 0 wt.% Zn alloy are enriched with Al and Ca atoms while those in the 1.6 wt.% Zn alloy are enriched in Al, Ca and Zn, Figs. 7c and f. The number density of the G.P. zones is calculated to be $2.33 \pm 0.12 \times 10^{24}$ m^{-3} for the 1.6 wt.% Zn alloy, which is higher than that for the 0 wt.% Zn alloy, $1.32 \pm 0.08 \times 10^{24}$ m^{-3}.

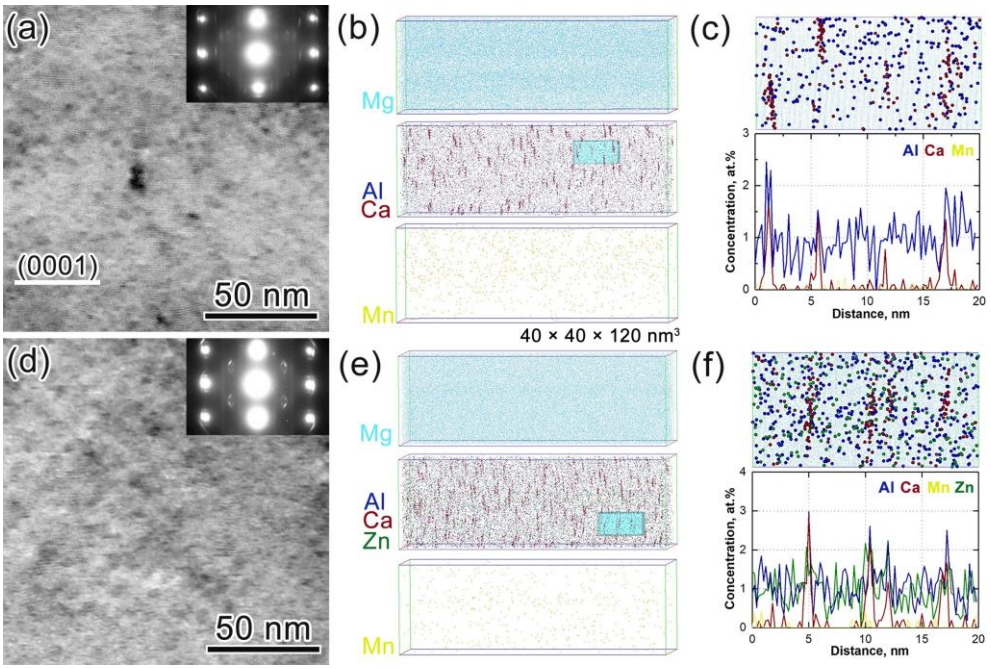

Fig. 7. Bright field TEM images and corresponding SAD patterns, 3D atom maps of Mg, Al, Ca, Mn and Zn and the selected 3DAP volumes with 1D concentration profiles obtained from of the peak-aged (a-c) 0 wt.% Zn and (d-f) 1.6 wt.% Zn alloys. Note that the TEM images were taken from the zone axis of $[11\bar{2}0]_\alpha$and the SAD patterns were recorded from the $[10\bar{1}0]_\alpha$zone axis. The 3DAP data was acquired with the analysis direction parallel to the [0001] axis of the α-Mg matrix.

3.3.3 Texture evolution of Zn-free and Zn-addition alloys

To further reveal the texture evolution during the solution treatment, and considering the limited resolution by conventional EBSD analysis, TKD analysis was conducted in as-rolled 0 wt.% Zn and 1.6 wt.% Zn alloys as well as the 2 s annealed samples. Fig. 8 shows IPF maps, corresponding boundary misorientation maps and the misorientation profiles for the as-rolled 0 wt.% Zn and 1.6 wt.% Zn alloys obtained by the TKD. Four different types of twins are identified according to the misorientation angle profiles; $\{10\bar{1}2\}$ tensile twin at misorientation angle of 86 ± 5°, $\{10\bar{1}1\}$ compression twins at 56° ± 5°, and two variants of $\{10\bar{1}1\}$-$\{10\bar{1}2\}$ double twins of DTW_a and DTW_b at 38 ± 5° and 70 ± 5°, respectively [22]. The locations of these twins are highlighted with different colors in the boundary misorientation maps, Figs. 8c and d. Since the double twin involves the $\{10\bar{1}2\}$ tensile twin propagating inside $\{10\bar{1}1\}$ compression twins, the frequency of misorientation angle at around 86° in Figs. 8e and f are categorized as double twins based on the boundary misorientation maps of both alloys. The dominant twin type is double twin in both alloys, while the frequency of misorientation angle ~70° in the 1.6 wt.% Zn alloy is much higher than that of the 0 wt.% Zn alloy, indicating that a larger number of double twins are developed by the Zn addition.

Figures 9a and c show IPF maps of 0 wt.% Zn and 1.6 wt.% Zn alloys annealed at 450 °C for 2 s obtained by TKD. The corresponding boundary misorientation and grain orientation spread (GOS) maps are present in

Figs. 9b and d. A maximum GOS of 1° was used for extracting the recrystallized grains. A number of recrystallized grains nucleate along the grain boundaries in the 0 wt.% Zn alloy, Fig. 9b, and the (0002) poles of the recrystallized grains are strongly tilted to the RD. The 1.6 wt.% Zn alloy, in contrast, the recrystallization along the grain boundaries is not as significant as that in the 0 wt.% Zn alloy. Instead, the majority of the recrystallized grains nucleate along the twin boundaries that were formed during the hot rolling process, Fig. 9d. The (0002) pole figure shows that the basal poles of the recrystallized grains are tilted towards the TD.

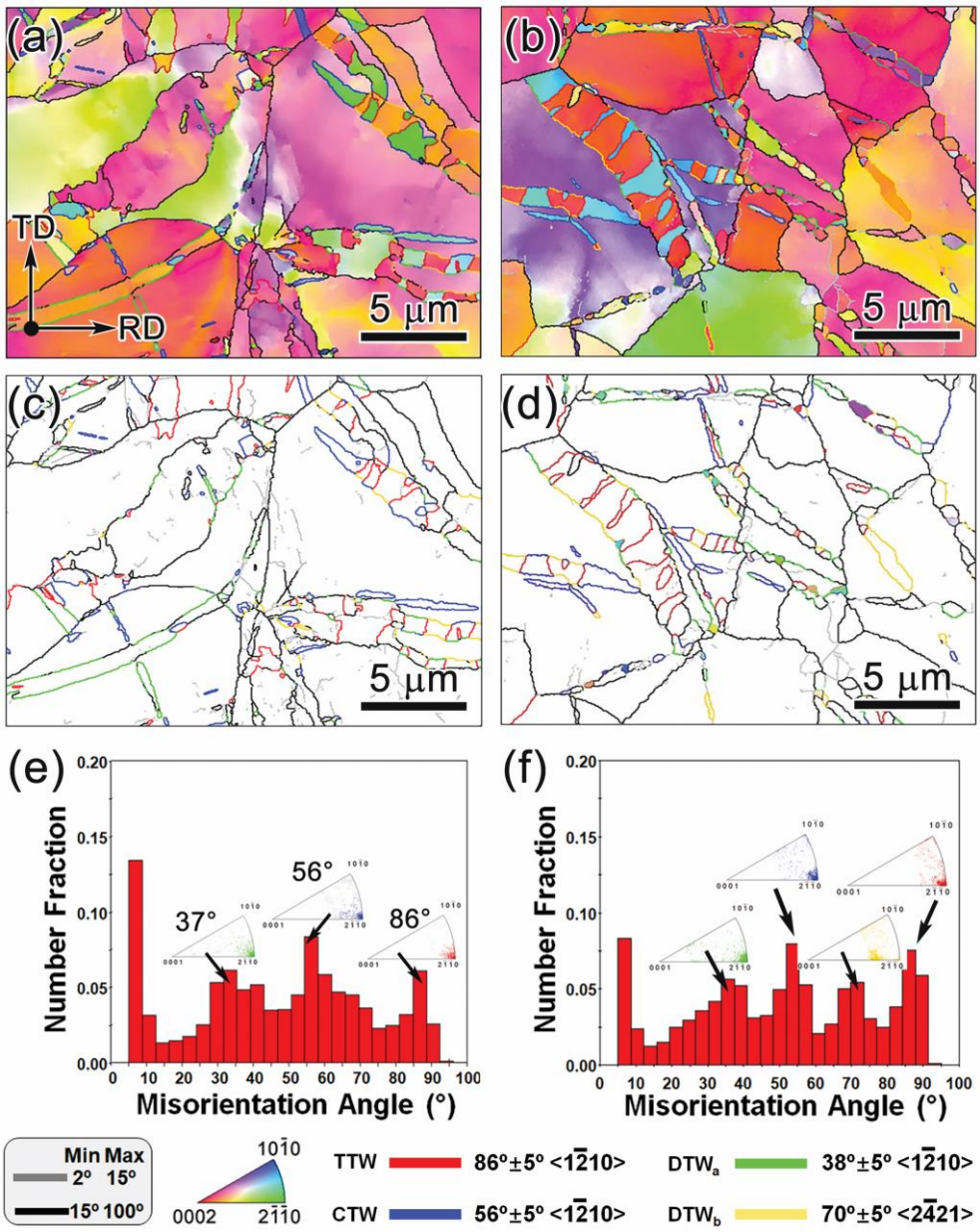

Fig. 8. TKD IPF maps, corresponding boundary misorientation maps, and misorientation angle distribution plots of the as-rolled (a-c) 0 wt.% Zn, and (d-f) 1.6 wt.% Zn alloys.

Figures 10a and b show low magnification HAADF-STEM images of the $\{10\bar{1}1\}$ compression twin and the grain boundary taken from the zone axis of $[11\bar{2}0]_\alpha$ in the as-rolled 1.6 wt.% Zn alloys. A large number of

dislocations, stacking faults and nanoscale particles, which are considered as Al_2Ca and Al_8Mn_5 phases [11], are observed within and along the twin boundaries (TBs) as well as in the vicinity of grain boundaries (GBs). The atomic resolution HAADF-STEM image of the twin boundary from the selected region in Fig. 10a exhibits stepped fully-coherent twin boundaries with ~ 62° angle between the basal plane of Mg matrix and the TB terrace plane as indicated by the dashed lines in Fig. 10c. The enlarged image in the inset reveals that the twin boundary was decorated by a periodic distribution of bright dots, which are considered to be enrichment of Zn atoms since the intensity of individual atomic columns in the HAADF image is proportional to the square of the atomic number, Z=30 for Zn, which is larger than that of Ca and Mg. The corresponding EDX elemental map and EDS line scan analyzed across the TB show that Zn and minor Al atoms co-segregate along the twin boundary, where the concentration of Zn is higher than that of Al, Fig. 10c and d. Comparatively, the atomic resolution HAADF-STEM image of the GB exhibits stronger bright-line contrast than that of the TB, Fig. 10e. Unlike the TB, the corresponding EDX elemental maps show the segregation of Ca in addition to Zn and Al atoms along the GB. The EDX line scan across the GB reveals that the concentration of Zn solutes is much higher than that of Al and Ca, Fig. 10f, and the amount of Zn segregated along the GB is also higher than that in the TB.

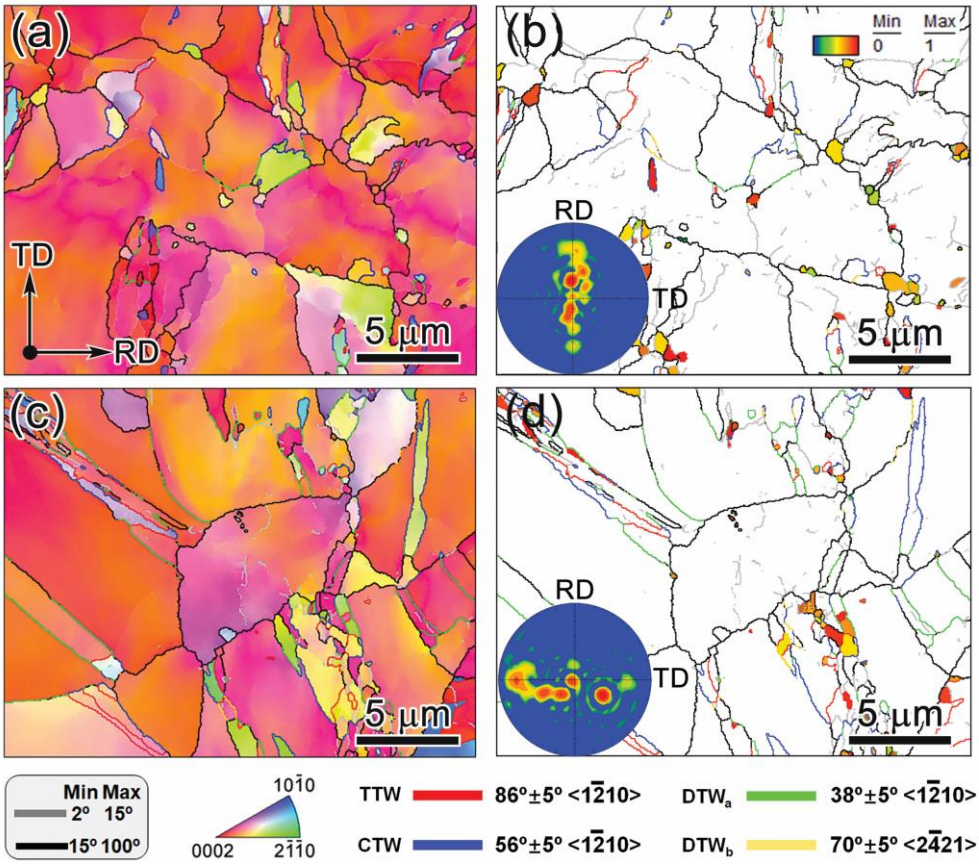

Fig. 9. TKD IPF maps, GOS maps of recrystallized grains, and corresponding (0002) pole figures of the (a,b) 0 wt.% Zn, and (c,d) 1.6 wt.% Zn alloys after 2 s annealing at 450 °C.

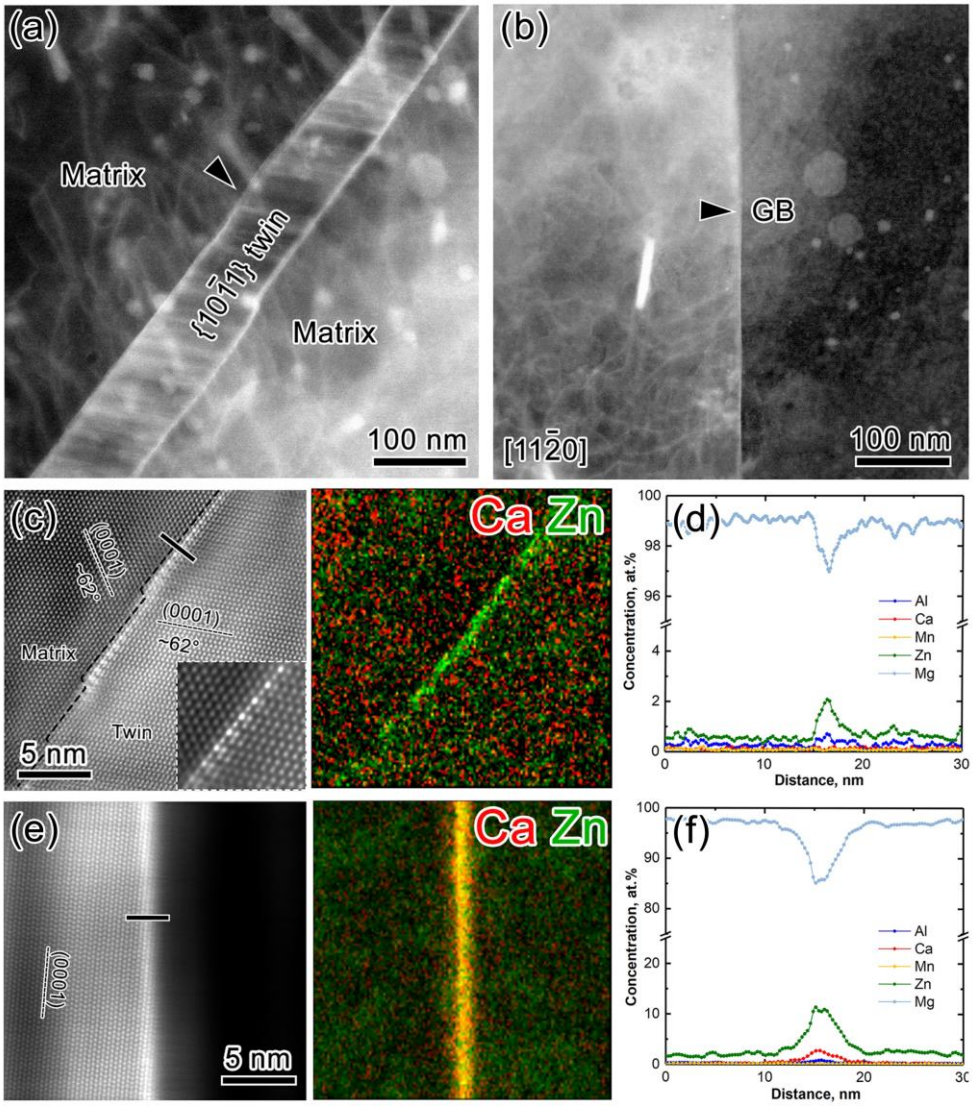

Fig. 10. Low magnification HAADF-STEM images, atomic scale HAADF-STEM images and corresponding STEM-EDX elemental maps of Al, Ca, Mn and Zn, and the compositional profiles of the (a-c) {10$\bar{1}$1} twin boundary, and (d-f) grain boundary obtained from the as-rolled 1.6 wt.% Zn alloy.

3.3.4 Role of Zn on the yielding phenomenon

Fig. 11 shows tensile stress-strain curves of the 0 wt.% Zn and 1.6 wt.% Zn specimens and local strain maps obtained from DIC analysis. The 0 wt.% Zn specimens show nearly isotropic mechanical properties along the RD and TD with the 0.2% offset yield strength; $\sigma_{0.2\%}$ of 148 and 143 MPa, ultimate tensile strength; σ_{UTS} of 234 and 233 MPa and total elongation to failure, ε_T of 30.1 and 35.2%, respectively, Fig. 11a. The enlarged curve along the TD shows a continuous flow pattern over the yielding stage with no localized deformation band occurred in the corresponding strain maps, Fig. 11b. In contrast, a prominent mechanical anisotropy is observed in the 1.6 wt.% Zn specimens with $\sigma_{0.2\%}$ of 170 and 138 MPa, σ_{UTS} of 274 and 278 MPa and ε_T of 25.4 and 37.1% along the RD and TD, respectively, Fig. 11c. Specifically, a discontinuous yielding appears in the tensile curves along both directions. The enlarged curve along the TD shows a small yield-drop

followed by a stress plateau, which corresponds to a Lüders band with an initial local strain of ~ 1% nucleating at the lower shoulder of the specimen, and then propagating towards the upper end of the gauge section, Fig. 11d.

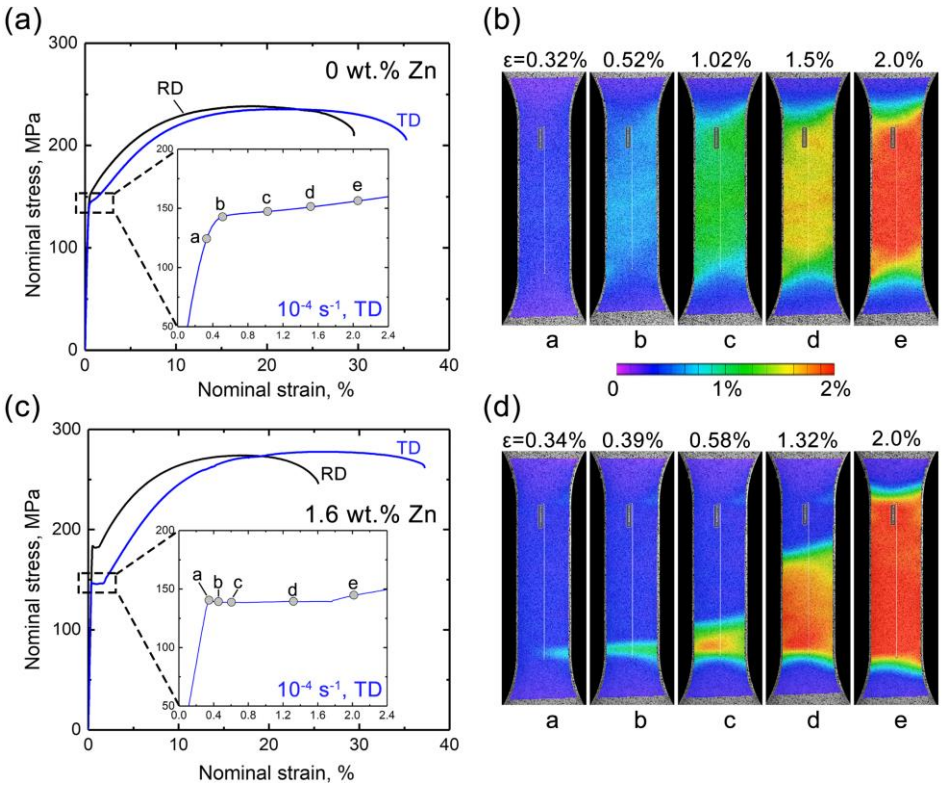

Fig. 11. (a,c) Nominal stress-strain curves along the RD and TD with enlarged curves of the yielding stages taken from rectangular frames, and (b,d) local strain maps covering the whole gauge section during the yielding stages of the 0 wt.% and 1.6 wt.% Zn specimens.

Figure 12 shows microstructure evolution of the 0 wt.% Zn and 1.6 wt.% Zn specimens before and after 2% tensile strain along the TD using a quasi-in-situ EBSD method. The vast majority of grains in the 0 wt.% Zn sample shows no significant change of crystallographic orientations after 2% strain with a few $\{10\bar{1}2\}$ tensile twins activated within the grains, Fig. 12a and b. The 1.6 wt.% Zn sample also shows similar grain orientations between undeformed and 2%-strain states, where the twin area fraction is slightly higher than that in the 0 wt.% Zn alloy, Fig. 12c and d. Therefore, dislocation slip is the dominant deformation mechanism during the yielding stages regardless of the Zn addition.

Figure 13 shows tensile stress-strain curves of the 0 wt.% Zn and 1.6 wt.% Zn specimens pre-strained to 2% along the TD and following aged at 80, 110 and 170 °C for 20 min, respectively. The 0 wt.% Zn sample retains a continuous yielding with a small yield strength increment of ~ 2 MPa by strain-aging at 80 °C. However, a yield-drop phenomenon gradually appears with increasing the aging temperature. The 170 °C-strain-aged 0 wt.% Zn sample show an obvious discontinuous yielding with a higher yield strength increment of ~ 20 MPa compared to that of the sample strain-aged at 110 °C; ~ 11 MPa. In contrast, the 1.6 wt.% Zn sample still shows a yield drop but with the decreased Lüders strain after strain-aged at 80 °C. A yield strength increment

of ~ 4 MPa is slightly higher than that of the 0 wt.% Zn sample. Further increased aging temperature results in more prominent yield-drop along with extended Lüders deformation. The strain-aged 1.6 wt.% Zn samples at 110 and 170 °C show the yield strength increment of ~ 20 and 42 MPa, respectively, which are twice larger than those of the 0 wt.% Zn samples.

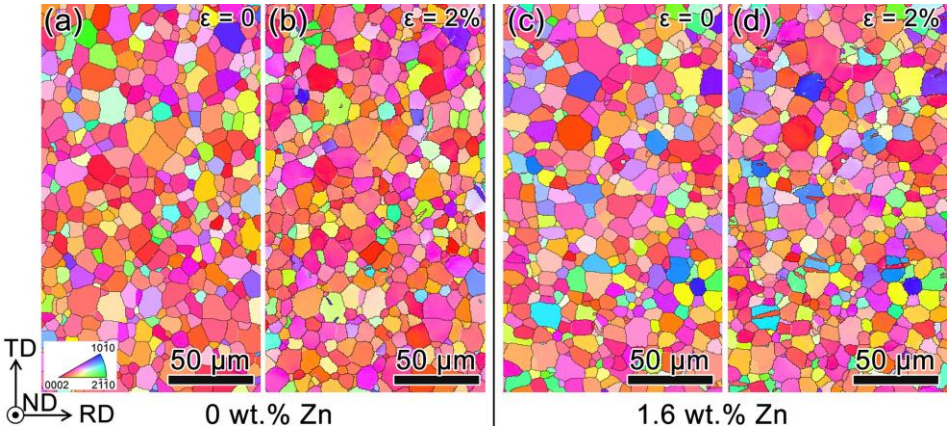

Fig. 12. Quasi-in-situ EBSD IPF maps of (a,c) undeformed; solution-treated, and (b,d) 2% tensile stretched 0 wt.% and 1.6 wt.% Zn specimens. Note that IPF maps were taken from planes normal to the ND.

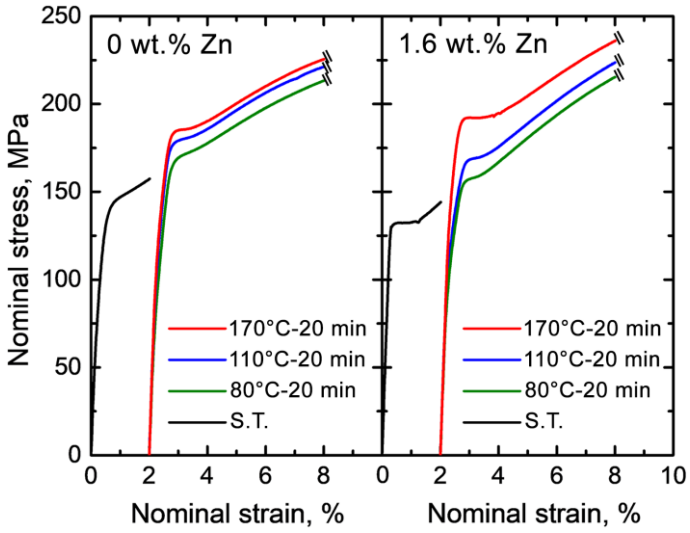

Fig. 13. Nominal stress-strain curves of solution-treated and strain-aged; 2% strain followed aging at various temperature for 20 min. (a) 0 wt.% Zn, and (b) 1.6 wt.% Zn specimens.

Figure 14a shows 3D atom maps of Mg, Al, Ca. Mn and Zn obtained from the strain-aged 1.6 wt.% Zn sample at 80 °C for 20 min. The elements are uniformly distributed in the reconstructed maps down to the nano-scale. 1D concentration profiles from a cuboid region of interest (ROI) marked in the map show small fluctuations for solute elements within the uncertainties, Fig. 14b, revealing the chemical homogeneity. Fig. 14c shows the frequency distribution of 2nd-order nearest neighbor (NN) distance between solute atoms obtained from the ROI. The experimental histograms of solute atoms are well consistent with their random curves, indicating a uniform distribution of elements within the selected volume.

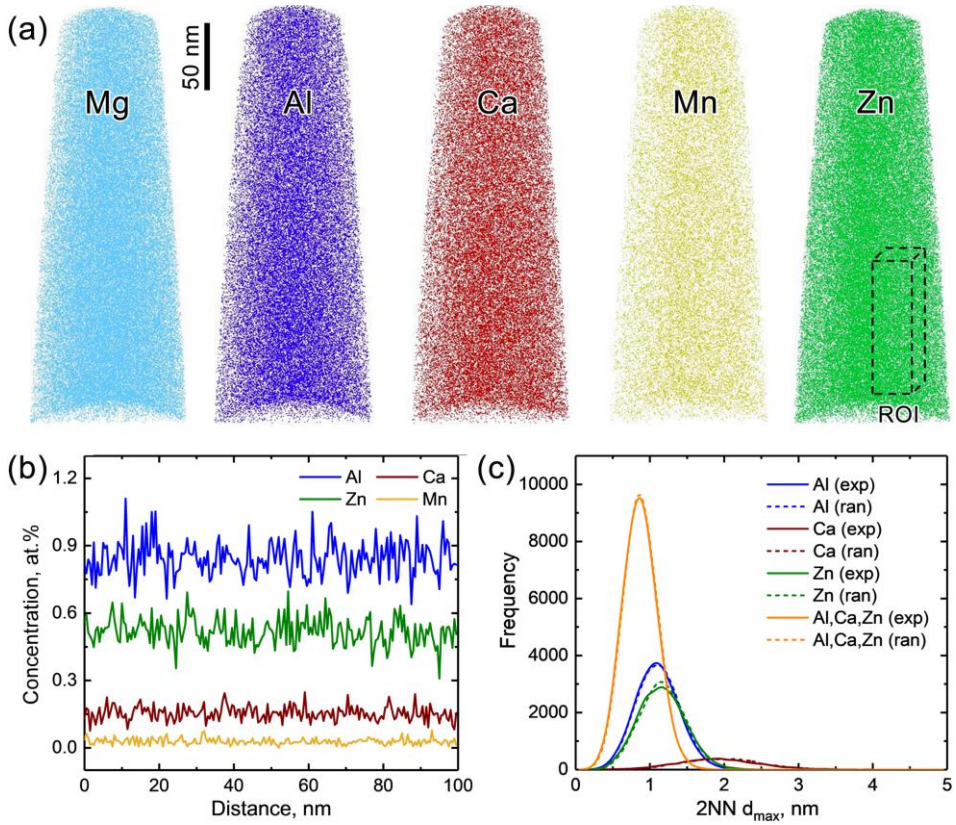

Fig. 14. (a) 3D atom maps of Mg, Al, Ca, Mn and Zn obtained from the strain-aged 1.6 wt.% Zn sample at 80 °C for 20 min. (b) 1D concentration profiles, and (c) Frequency histograms obtained from the marked cuboid region of interest with a volume of 100 × 30 × 30 nm^3.

Figure 15a and c shows the HAADF-STEM images of the solution-treated 0 wt.% Zn and 1.6 wt.% Zn samples near grain boundaries (GB) where the left sides taken from the $[11\bar{2}0]_\alpha$ zone axis. The GB of the 1.6 wt.% Zn sample exhibits a brighter imaging contrast than the grain interiors as well as that of the 0 wt.% Zn sample, implying a strong segregation of solute atoms. The corresponding EDX elemental maps and line-scan analysis across the GB of the 0 wt.% Zn sample shows the segregation of Al and Ca with a total concentration of ~ 5 at.%, Fig. 14b. In contrast, the 1.6 wt.% Zn sample shows a stronger segregation of Al, Ca and Zn to the GB with a total concentration; ~ 25 at.% five time larger than that of the 0 wt.% Zn sample, Fig. 14d.

To reveal the detailed deformation mechanism of individual grains in the 0 wt.% Zn and 1.6 wt.% Zn specimens, a correlative EBSD-TEM analysis was conducted where crystallographic orientations of grains were first identified by EBSD, and then the dislocation activities within these grains were examined by two-beam BF-TEM analysis. Figure 16a shows the EBSD IPF map of the 0 wt.% Zn TEM sample included with a perforated area. The RD- and TD-oriented grains are labeled as A and B given their c-axes tilted towards rolling and transverse directions, respectively as indicated in the inserted pole figure. Both grains show profuse ⟨a⟩ dislocations on the basal planes based on the g·b = 0 invisibility criterion, while a number of dislocation segments are detected parallel to the traces of prismatic planes in the RD-oriented grain as indicated by arrows, Fig. 16c and e. Similarly, basal ⟨a⟩ dislocations are also predominant in the 1.6 wt.% Zn sample regardless of

grain orientations, while the grain D; TD-oriented shows a denser distribution of dislocations than that of the grain C; RD-oriented, Fig. 16d and f.

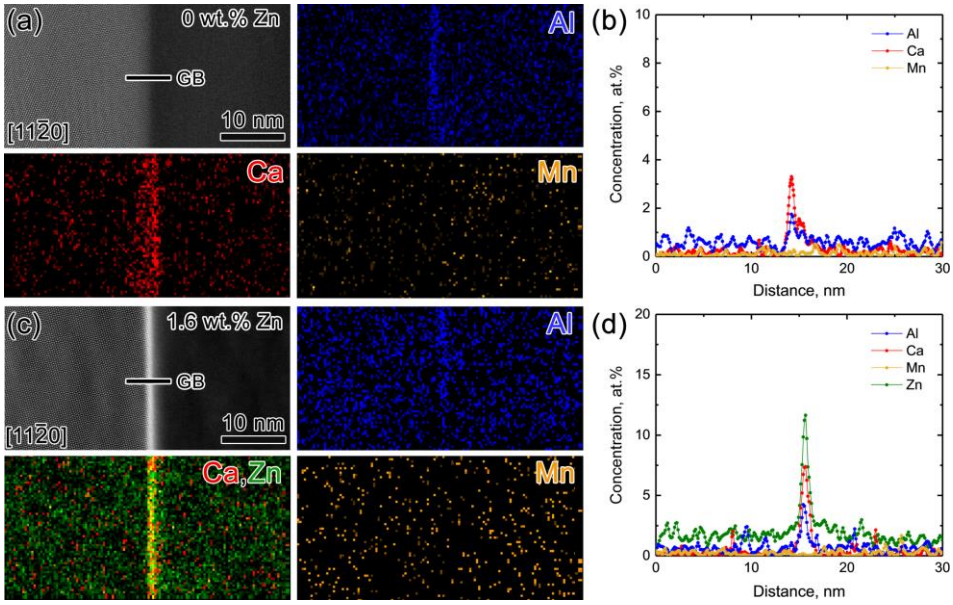

Fig. 15. (a,c) HAADF-STEM images and corresponding STEM-EDX elemental maps of Al, Ca, Mn and Zn, and (b,d) compositional profiles across grain boundaries obtained from the solution-treated 0 wt.% Zn and 1.6 wt.% Zn samples.

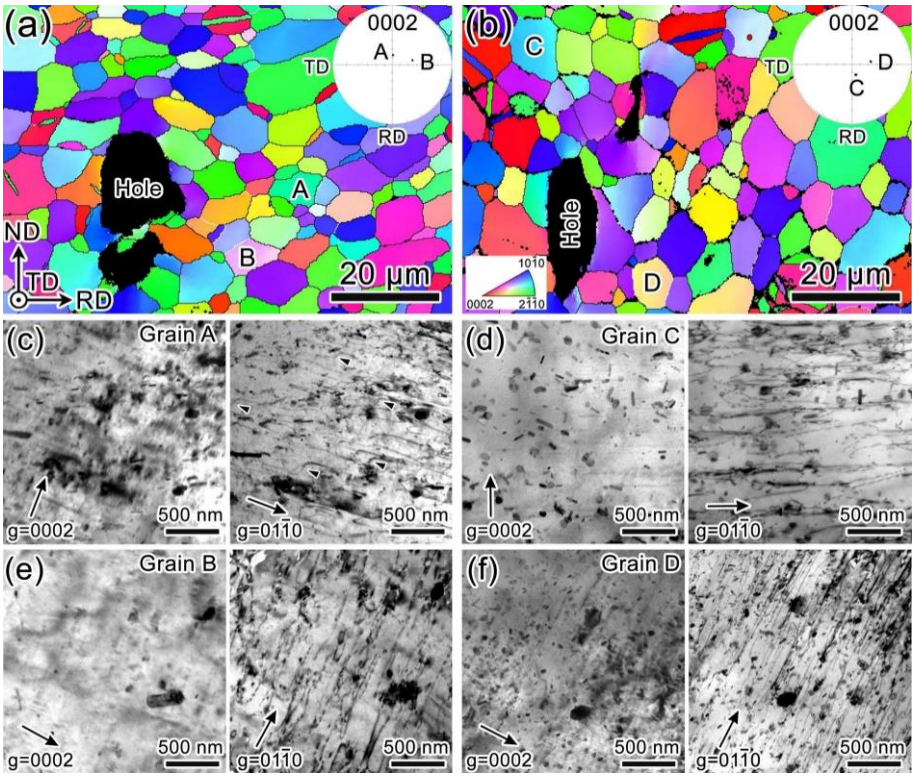

Fig. 16. EBSD IPF maps of TEM thin foils near electropolished perforation regions and corresponding two-beam BF-TEM images of the labeled grains in (a,c,e) 0 wt.% Zn and (b,d,f) 1.6 wt.% Zn samples. Note that the IPF maps were taken from thin-foil planes normal to the TD.

3.4 Discussion

In this work, we investigated the role of Zn on the mechanical properties and microstructure of the Mg-1.2Al-0.5Ca-0.4Mn-*x*Zn (wt.%, *x*=0, 0.8, and 1.6) sheet alloys fabricated by TRC and hot rolling. Figure 12 summarizes the I.E. values and yield strengths of various Mg and Al sheet alloys [4,11-13,25,26]. It clearly shows that better strength-formability relationship is achieved by the addition of Zn; the 1.6 wt.% Zn alloy exhibits excellent RT formability with a large I.E. value of 8.2 mm in the solution-treated condition and a high yield strength of 210 MPa in the peak-aged condition, which is comparable to those of 6xxx series Al alloys. Therefore, Zn is a critical alloying element to achieve ultimate property in Mg-Ca(-Al) based dilute alloy sheets.

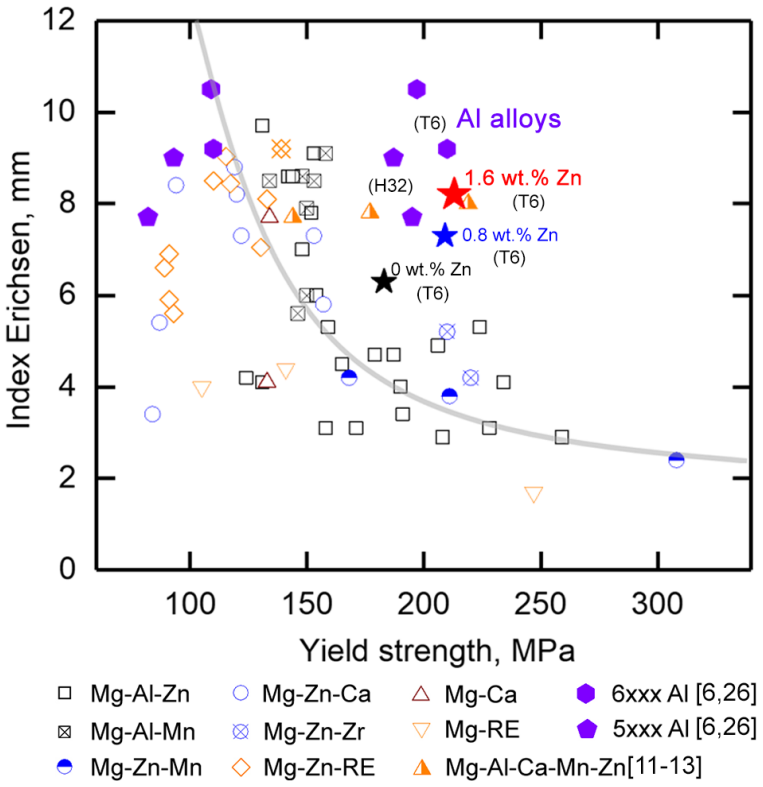

Fig. 16. I.E. values and yield strength of various Mg and Al sheet alloys. Data for other sheet alloys for comparison are from [4], unless otherwise stated.

The 0 wt.% Zn alloy shows a moderate stretch formability with the I.E. value of ~6.3 mm, which is slightly higher than that of commercial AZ31 alloy, 3–5 mm. Such relatively good stretch formability is due to the RD-split texture, in which the (0002) poles are slightly tilted by ~ 15° towards the RD. The RD-split texture allows a larger number of grains favorably oriented for the operation of basal ⟨a⟩ slip during the stretch forming compared to the strong basal texture developed in the AZ31 alloy where the c-axes of grains are predominantly parallel to the ND [27]. The addition of Zn further improves the RT stretch formability from 6.3 to 8.2 mm with increasing the Zn content from 0 to 1.6 wt.%, Fig. 1. The large stretch formability is mainly attributed to the formation of weak TD-split texture in which the (0002) poles are largely tilted by ~ 45° towards the TD,

Fig. 4. In addition to the TD-split texture, ease operation of prismatic ⟨a⟩ slip also contribute to the excellent RT formability in the Zn-addition alloys as indicated by the detailed EBSD analysis, Fig. 6. Yuasa *et al*. suggested that the ratio of unstable stacking fault energy (SFE) for basal and prismatic ⟨a⟩ slips in the Mg-Zn-Ca alloy is larger than that in the Mg-Ca alloy, indicating that the prismatic ⟨a⟩ slip could occur more easily by the addition of Zn [28]. Therefore, we can conclude that the improved stretch formability by the Zn addition is attributed to the development of the weak TD-split texture as well as the activation of the non-basal slip.

The development of the TD-split texture in the 1.6 wt.% Zn alloy is closely associated with the recrystallization during the solution treatment since both as-rolled 0 wt.% Zn and 1.6 wt.% Zn alloys show the RD-split texture, Figs. 4 and 5. TKD analysis shows that the Zn addition promote the formation of double twins during hot rolling, Fig. 8. The majority of the recrystallized grains in the 1.6 wt.% Zn alloy nucleated along the double twin boundaries while the nucleation of the recrystallized grain occurs along the grain boundaries during the solution treatment in the 0 wt.% Zn alloy, Fig. 9. Therefore, the formation of TD-split texture is strongly associated with a higher frequency of twin recrystallization. The 1.6 wt.% Zn alloy shows the different types of solute segregation in the TB and GB; a low segregation of Zn with minor Al to the TB while a higher amount of Al, Ca and Zn co-segregate to the GB, Fig. 10. This may cause a significant difference in the boundary energy [15,29]. The strong co-segregation of Al, Ca and Zn along the GB is expected to result in a large reduction in boundary energy due to the atomic size effect of segregated solutes as demonstrated in Mg-Gd(-Zn) alloy [30]. On the other hand, the moderate solute segregation in TBs would have a lower dragging effect on the boundary mobility than that in GBs, and thus energetically favors the twin recrystallization. Among various nucleation sites for recrystallization, e.g. GBs, shear bands, TBs, and secondary phase particles [19-21,31,32], double twin boundary recrystallization is demonstrated to be the main mechanism for the nucleation of majority of the TD-tilted recrystallized grains in the AZXM1100 alloy by a series of microstructure analyses as well as in other Mg-Zn-RE(Ca) alloys [18,19,33-35]. This double twin recrystallization behavior can be explained in terms of the difference in the amount and species of solute elements segregated along the GBs and TBs. In addition, orientations of recrystallized grains are also affected by the subgrain rotation via the activation of prismatic ⟨a⟩ slip in Mg alloys [36,37]. However, a clear correlation between the formation of the specific TD-split orientation, i.e., c-axis tilted 30°-45° away from the ND to the TD, and double twin recrystallization or prismatic ⟨a⟩ slip induced recrystallized grain rotation still remains unclear. Further work will shed light on the interactions of dislocation and twin boundary in the orientation of static recrystallized nuclei by in-situ TEM heating experiments.

The addition of Zn increases the age hardening response; the hardness increments by peak aging, ΔHv, were 9.4 and 8.6 HV for the 1.6 wt.% Zn and 0 wt.% Zn alloys, respectively, Fig. 2. This is because of the slight increase in the number density of the G.P. zones from $1.32 \pm 0.08 \times 10^{24}$ to $2.33 \pm 0.12 \times 10^{24}$ m^{-3} by the addition of Zn, Fig. 10. The increment of the σ_{TYS}, along RD by peak aging is consistent with that of the hardness, Fig. 3 and Table 2. However, it is not the case for the increments of σ_{TYS} along 45° and TD; while ΔHv of the 1.6 wt.% Zn alloy is larger than that of the 0 wt.% Zn alloy, the increment in σ_{TYS} is smaller. The 0 wt.% Zn alloy exhibits the RD-split texture, but the TD-split texture is observed in the 1.6 wt.% Zn alloy.

Considering such different textured feature, we can conclude that the flow behavior in tension along TD is controlled by prismatic ⟨a⟩ slip in the 0 wt.% Zn alloy, while basal ⟨a⟩ slip is dominant in the 1.6 wt.% Zn alloy due to its high Schmid factor along the TD. Since the G.P. zones contribute less resistance to basal ⟨a⟩ slip as compared to prismatic ⟨a⟩ slip as reported by Bhattacharyya *et al.* [38], the strengthening anisotropy depending on loading directions may result from the intrinsic effect of the G.P. zones interactions with various dislocations.

One drawback led by the addition of Zn is large mechanical anisotropy. The large yield anisotropy can be explained by the different distribution of the (0002) poles in the texture. The 0 wt.% Zn sample shows a slightly lower σ_{TYS} along the RD compared to that along the TD since the RD-split texture allows the operation of the basal ⟨a⟩ slip at slightly lower stress along the RD than the TD. In contrast, the tilt angle of the (0002) poles in the 1.6 wt.% Zn sample are larger than those of the 0 wt.% Zn sample, Fig. 4 (a) and (c), thus leading to a bigger difference in the σ_{TYS} along RD and TD. Besides, a discontinuous yielding along with the typical Lüders band deformation is induced by the Zn addition regardless of tensile directions, Fig. 11. The 0 wt.% Zn sample shows a continuous yielding after strain-aged at 80 °C for 20 min, while a yield-drop still occurs in the 1.6 wt.% Zn sample, Fig. 13. Since no solute cluster is detected by 3DAP in such low temperature, Fig. 14, the yield-drop in the Zn-containing alloy is mainly attributed to the dislocation locking by solute atoms. Moreover, the 1.6 wt.% Zn sample shows a stronger solute segregation at GBs than that of the 0 wt.% Zn sample in the solution-treated condition, Fig. 14. Based on the GB pile-up theory, the solute segregation in the Zn-containing alloy may increase the energy barrier for dislocation emission from GBs [39,40], and thus the stress required to initiate plastic deformation. From the EBSD-TEM correlative analysis, the 2% strained 1.6 wt.% Zn sample shows a higher dislocation density; ~ 3.8×10^{14} /m^3 and twinning fraction; ~ 10.6% than those in the 0 wt.% Zn sample; ~ 7.3×10^{13} /m^3 and ~ 5.3%, Fig. 15 due to higher Schmid factors of basal ⟨a⟩ slip and $\{10\bar{1}2\}$ tensile twinning along the TD. Thus, the followed yield point elongation is associated with the rapid multiplication of basal $\langle a \rangle$ dislocations as well as activation of tensile twinning.

3.5 Conclusion

This work clarified the critical role of Zn in achieving excellent RT formability and high strength simultaneously in the heat-treatable Mg-1.2Al-0.5Ca-0.4Mn-*x*Zn (wt.%, *x*=0, 0.8 and 1.6) sheet alloys through detailed microstructure characterizations using EBSD, TEM and 3DAP. A large I.E. value of 8.2 mm with a tensile yield strength of 210 MPa was obtained in the developed Mg-1.2Al-0.5Ca-0.4Mn-1.6Zn alloy, exhibiting a better formability-strength balance comparable with the 6xxx series Al alloys.

(1) The addition of 1.6 wt.% Zn to the Mg-1.2Al-0.5Ca-0.4Mn alloy results in a significant improvement in the I.E. value from 6.3 to 8.2 mm in the solution-treated samples due to the texture weakening and enhanced activity of prismatic ⟨a⟩ slip during the stretch forming process.

(2) The development of TD-split texture by the Zn addition is strongly associated with the nucleation of the TD-oriented recrystallized grains at double twin boundaries, which are induced during the hot rolling. The

segregation of Zn to the TBs and GBs is responsible for the enhanced twin recrystallization and suppression of grain boundary recrystallization.

(3) The Zn addition causes a larger number density of G.P. zones formed by the peak-aging treatment, which leads to the improvement of yield strength from 170 to 210 MPa along the RD. However, the smaller strength increments along 45° and TD are due to the increased anisotropy of TD-split texture.

Reference

[1] W.J. Joost, P.E. Krajewski, Towards magnesium alloys for high-volume automotive applications, Scr. Mater. 128 (2017) 107-112.

[2] A.A. Luo, Materials comparison and potential applications of magnesium in automobiles. Essential Readings in Magnesium Technology, Springer, Cham, 2016.

[3] N.J. Kim, Critical Assessment 6: magnesium sheet alloys: viable alternatives to steels? Mater. Sci. Technol. 30 (2014) 1925-1928.

[4] B.C. Suh, M.S. Shim, K.S. Shin, N.J. Kim, Current issues in magnesium sheet alloys: where do we go from here? Scr. Mater. 84 (2014) 1-6.

[5] J. Hirsch, T. Al-Samman, Superior light metals by texture engineering: optimized aluminum and magnesium alloys for automotive applications, Acta Mater. 61 (2013) 818-843.

[6] X. Huang, K. Suzuki, N. Saito, Enhancement of stretch formability of Mg–3Al–1Zn alloy sheet using hot rolling at high temperatures up to 823 K and subsequent warm rolling, Scr. Mater. 61 (2009) 445-448.

[7] X. Huang, K. Suzuki, Y. Chino, Influences of initial texture on microstructure and stretch formability of Mg–3Al–1Zn alloy sheet obtained by a combination of high temperature and subsequent warm rolling, Scr. Mater. 63 (2010) 395-398.

[8] T. Al-Samman, X. Li, Sheet texture modification in magnesium-based alloys by selective rare earth alloying, Mater. Sci. Eng. A 528 (2011) 3809-3822.

[9] Y. Chino, X. S. Huang, K. Suzuki, K. Sassa, M. Mabuchi, Influence of Zn concentration on stretch formability at room temperature of Mg-Zn-Ce alloy. Mater. Sci. Eng. A 528 (2010) 566-572.

[10] Y. Chino, K. Sassa, M. Mabuchi, Texture and stretch formability of a rolled Mg-Zn alloy containing dilute content of Y. Mater. Sci. Eng. A 513 (2009) 394-400.

[11] T.T.T. Trang, J.H. Zhang, J.H. Kim, A. Zargaran, J.H. Hwang, B.-C. Suh, N.J. Kim, Designing a magnesium alloy with high strength and high formability, Nat. Commun. 9 (2018) 2522.

[12] M.Z. Bian, T.T. Sasaki, B.C. Suh, T. Nakata, S. Kamado, K. Hono, A heat-treatable Mg-Al-Ca-Mn-Zn sheet alloy with good room temperature formability, Scr. Mater. 138 (2017) 151-155.

[13] M.Z. Bian, T.T. Sasaki, T. Nakata, Y. Yoshida, N. Kawabe, S. Kamado, K. Hono, Bake-hardenable Mg-Al-Zn-Mn-Ca sheet alloy processed by twin-roll casting, Acta Mater. 158 (2018) 278-288.

[14] J. Jayaraj, C.L. Mendis, T. Ohkubo, K. Oh-ishi, K. Hono, Enhanced precipitation hardening of Mg–Ca alloy by Al addition, Scr. Mater. 63 (2010) 831–834.

[15] K. Oh-ishi, R. Watanabe, C.L. Mendis, K. Hono, Age-hardening response of Mg–0.3 at.%Ca alloys with different Zn contents, Mater. Sci. Eng. A 526 (2009) 177–184.

[16] T. Nakata, C. Xu, K. Suzawa, K. Yoshida, N. Kawabe, S. Kamado, Enhancing mechanical properties of rolled Mg-Al-Ca-Mn alloy sheet by Zn addition, Mater. Sci. Eng. A 737 (2018) 223-229.

[17] Z.R. Zeng, Y.M. Zhu, S.W. Xu, M.Z. Bian, C.H.J. Davies, N. Birbilis, J.F. Nie, Texture evolution during static recrystallization of cold-rolled magnesium alloys, Acta Mater. 105 (2016) 479-494.

[18] D. Guan, W.M. Rainforth, L. Ma, B. Wynne, J. Gao, Twin recrystallization mechanisms and exceptional contribution to texture evolution during annealing in a magnesium alloy, Acta Mater. 126 (2017) 132-144.

[19] D. Guan, X. Liu, J. Gao, L. Ma, B. Wynne, W.M. Rainforth, Exploring the mechanism of "rare earth" texture evolution in a lean Mg-Zn-Ca alloy, Sci. Rep. 9 (2019) 7152.

[20] W.F. Hosford, R.M. Caddell, Metal Forming: Mechanics and Metallurgy, fourth ed. Cambridge University Press, New York, 2011.

[21] J. Hirsch, Aluminium alloys for automotive application, Mater. Sci. Forum 242 (1997) 33-50.

[22] M.R. Barnett, Z. Keshavarz, A.G. Beer, X. Ma, Non-Schmid behaviour during secondary twinning in a polycrystalline magnesium alloy, Acta Mater. 56 (2008) 5-15.

[23] Y.B. Chun, C.H.J. Davies, Investigation of prism ⟨a⟩ slip in warm-rolled AZ31 alloy, Metall. Mater. Trans. A 42 (2011) 4113–4125.

[24] D.H. Ping, K. Hono, J.F. Nie, Atom probe characterization of plate-like precipitates in a Mg-RE-Zn-Zr casting alloy, Scr. Mater. 48 (2003) 1017–1022.

[25] J.R. Davis, H. Baker, Aluminum and Aluminum Alloys, ASM specialty Handbook, Materials Park, OH, 1993.

[26] T. Nakata, C. Xu, Y. Uehara, T.T. Sasaki, S. Kamado, Origin of texture weakening in a rolled ZEX4101 alloy sheet and its effect on room temperature formability and tensile property, J. Alloys Compd. 782 (2019) 304-314.

[27] B.C. Suh, J.H. Kim, J.H. Bae, J.H. Hwang, M.S. Shim, N.J. Kim, Effect of Sn addition on the microstructure and deformation behavior of Mg-3Al alloy, Acta Mater. 124 (2017) 268-279.

[28] M. Yuasa, N, Miyazawa, M. Hayashi, M. Mabuchi, Y. Chino, Effects of group II elements on the cold stretch formability of Mg-Zn alloys, Acta Mater. 83 (2015) 294-303.

[29] J.D. Robson, Effect of rare-earth additions on the texture of wrought magnesium alloys: the role of grain boundary segregation, Metall. Mater Trans. A 45 (2014) 3205-3212.

[30] J.F. Nie, Y.M. Zhu, J.Z. Liu, X.Y. Fang, Periodic segregation of solute atoms in fully coherent twin boundaries, Science 340 (2013) 957-960.

[31] L.W.F. Mackenzie, B. Davis, F.J. Humphreys, G. W. Lorimer, The deformation, recrystallisation and texture of three magnesium alloy extrusions, Mater. Sci. Technol. 23 (2007) 1173-1180.

[32] D. Guan, W.M. Rainforth, J. Gao, B. Wynne, Individual effect of recrystallisation nucleation sites on texture weakening in a magnesium alloy: Part 2- shear bands, Acta Mater. 145 (2018) 399-412.

[33] Q. Wang, B. Jiang, A. Tang, C. He, D. Zhang, J. Song, T. Yang, G. Huang, F. Pan, Formation of the elliptical texture and its effect on the mechanical properties and stretch formability of dilute Mg-Sn-Y sheet by Zn addition, Mater. Sci. Eng. A 746 (2019) 259-275.

[34] J. Victoria-Hernández, S. Yi, D. Klaumünzer, D. Letzig, Recrystallization behavior and its relationship with deformation mechanisms of a hot rolled Mg-Zn-Ca-Zr alloy, Mater. Sci. Eng. A 716 (2019) 138054.

[35] J.H. Kim, B.C. Suh, T.T.T. Trang, J.H. Hwang, N.J. Kim, Orientations of dynamically recrystallized grains nucleated at double twins in Mg-4Zn-1Sn alloy, Scr. Mater. 170 (2019) 11-15.

[36] C. Ha, J. Bohlen, S. Yi, X. Zhou, H.G. Brokmeier, N. Schell, D. Letzig, K.U. Kainer, Influence of Nd or Ca addition on the dislocation activity and texture changes of Mg-Zn alloy sheets under uniaxial tensile loading, Mater. Sci. Eng. A 761 (2019) 138053.

[37] X. Zeng, P. Minarik, P. Dobron, D. Letzig, K.U. Kainer, S. Yi, Role of deformation mechanisms and grain growth in microstructure evolution during recrystallization of Mg-Nd based alloys, Scr. Mater. 166 (2019) 53-57.

[38] J.J. Bhattacharyya, T.T. Sasaki, T. Nakata, K. Hono, S. Kamado, S.R. Agnew, Determining the strength of GP zones in Mg alloy AXM10304, both parallel and perpendicular to the zone, Acta Mater. 171 (2019) 231-239.

[39] D. Akama, N. Nakada, T. Tsuchiyama, S. Takakia, A. Hironaka, Discontinuous yielding induced by the addition of nickel to interstitial-free steel, Scr. Mater. 82 (2014) 13-1.

[40] S. Takaki, D. Akama, N. Nakada, T. Tsuchiyama, Effect of grain boundary segregation of interstitial elements on Hall-Petch coefficient in steels, Mater. Trans. 55 (2014) 28-34

Chapter 4 Role of Zn on the rapid age hardening and formation of the G.P. zone in Mg-Ca-Zn alloys

4.1 Introduction

Heat treatable Mg-Ca-Zn based wrought alloys have received considerable attention due to the good combination of strength and formability, as such being promising candidates for lightweight applications [1,2]. In comparison with commercial wrought Mg alloys such as Mg-3Al-1Zn (wt.%, AZ31) and Mg-6.2Zn-0.6Zr (wt.%, ZK60), which usually show low or sluggish age-hardening response, one notable feature in Mg-Ca-Zn alloys is the rapid age-hardening with the peak hardness obtained within only few hours, which may therefore open up possibilities for developing bake-hardenable Mg alloys; press-forming at RT and then paint baking at 150-180 °C for 15-30 min [3]. Unlike in various heat-treatable Al alloys, e.g. Al-Cu-Mg and Al-Mg-Si alloys, where the rapid age hardening phenomenon has been extensively studied [4,5], the origin of this characteristic behavior in the Mg-Ca-Zn system is seldomly visited since it was firstly reported in twenty years ago; the trace addition of Zn in a Mg-1Ca (wt.%) binary alloy can lead to a substantial increase in peak hardness [6]. Subsequently, Oh-ishi et al. found that the improved age-hardening response was attributed to the dense dispersion of fine Guinier Preston (G.P.) zones in a peak-aged Mg-0.5Ca-1.6Zn (wt.%) alloy [7]. However, the origin of the G.P. zones along with the accelerated aging kinetics was not elucidated.

Quenched-in vacancies are recognized to play a key role in enhancing the diffusion rate of solute atoms, and thus the aging kinetics in Al alloys [4,5]. With a combination of positron annihilation lifetime spectroscopy (PALS), coincidence Doppler broadening (CDB) of positron annihilation radiation and 3D atom probe (3DAP) analysis, the information of vacancies and solute clusters within the matrix; which act as heterogenous sites for nucleation of the G.P. zones can be obtained as well as the solutes bound to vacancies, i.e. the vacancy-solute complexes [8]. However, such studies are quite limited in Mg alloys, especially for clarifying vacancy-solute interactions on the aging kinetics. The aim of this work is to investigate solute clustering and precipitation during the early stages of aging using a combination of PALS, (S)TEM, and 3DAP analysis, so as to achieve a deep understanding into the role of Zn on the rapid age-hardening response in the Mg-Ca-Zn system.

4.2 Experimental

Alloy ingots with nominal compositions of Mg-0.3Ca and Mg-0.3Ca-0.6Zn in at.% or Mg-0.5Ca and Mg-0.5Ca-1.6Zn in wt.% were prepared by induction melting high-purity pure Mg, Zn and Mg-30 wt.% Ca master alloys in a steel crucible under Ar atmosphere. Hereafter, all alloy compositions are described in at.%. The ingots were then homogenized at 520 °C for 2 h in a He-filled Pyrex tube, and water quenched. The sliced samples were aged in an oil bath of 200 °C for various time. Vickers hardness was measured from ten

individual indentations with a 0.3 kg load. PALS analysis was carried out using a conventional positron lifetime system as described elsewhere [9]. The ^{22}Na positron source was sandwiched between two identical specimens with dimensions of 10 × 10 × 1 mm^3. Doppler broadening spectra were measured with two Ge detectors in coincidence. The spectra were characterized by the S and W parameters. The S and W parameters are defined as the ratios of low momentum ($|p_L| < 4\times10^{-3}mc$) and high momentum regions ($18\times10^{-3}mc < |p_L| < 30\times10^{-3}mc$) to the total region in CDB spectra. The S parameter increases when positrons are trapped at vacancy-type defects along with the decreased W parameter. Besides, the W parameter strongly depends on chemical environment of trapping sites [10]. Microstructure characterization was carried out using FEI Tecnai 20 and Titan G^2 80-200 transmission electron microscopes (TEM) operating at 200 kV. Thin foil specimens for the (S)TEM observations were prepared by punching 3 mm diameter discs and twin-jet electro-polishing at about -50 °C with a voltage of 90 V. A Digital Micrograph plug-in; FRWR tools was used for geometric phase analysis (GPA) of atomic ADF-STEM images [11]. 3DAP were performed on needle-shaped tips using a local electrode atom probe (CAMECA LEAP 5000 XS) in high-voltage pulsing mode with a pulse fraction of 20% and a pulse rate of 250 kHz at a temperature of 30 K. Binomial and contingency table analysis are used to evaluate statistically both the possibility and relative degree of like-solute atom clustering (Ca-Ca and Zn-Zn) and Ca-Zn co-clustering, respectively, and the method is described elsewhere [12]. Cluster identification was carried out using the core-linkage algorithm in which the d_{max} is determined by the 2nd-order nearest neighbor (2NN) solute atom (Ca and Zn) distance histograms.

4.3 Results

4.3.1 Positron annihilation lifetime analysis

Figure 1a shows the evolution of Vickers hardness and average positron lifetime in the Mg-0.3Ca and Mg-0.3Ca-0.6Zn alloys during isothermal aging at 200 ºC until 10 h. The Mg-0.3Ca alloy has a hardness of 37.8 ± 1.6 HV in the as-quenched condition, and gradually increase to a maximum value of 47.6 ± 1.3 HV after 6 h. The addition of Zn substantially enhances the age-hardening response; the hardness value of the Mg-0.3Ca-0.6Zn alloy rises rapidly from 43.3 ± 1.7 to a peak of 65.8 ± 1.3 HV in only 1.6 h. For the PASL analysis, both Mg-0.3Ca and Mg-0.3Ca-0.6Zn alloys show a similar positron lifetime of ~ 223 ps in the as-quenched condition close to that of well-annealed pure Mg; ~220 ps, indicating a low concentration of free monovacancies within the matrix regardless of Zn addition. Following the aging, the Mg-0.3Ca alloy shows a monotonic increase of positron lifetime to a peak value of ~ 245 ps in 6 h, suggesting an increased concentration of vacancy-type defects with the aging time. In contrast, a slightly decrease followed by a lifetime plateau until 1.6 h; peak-aged is observed in the Mg-0.3Ca-0.6Zn alloy, which is associated with the positron annihilation at coherent aggregates such as solute clusters and the G.P. zones [4]. The subsequently increase of positron lifetime is attributed to the gradual loss of coherency within precipitates [8].

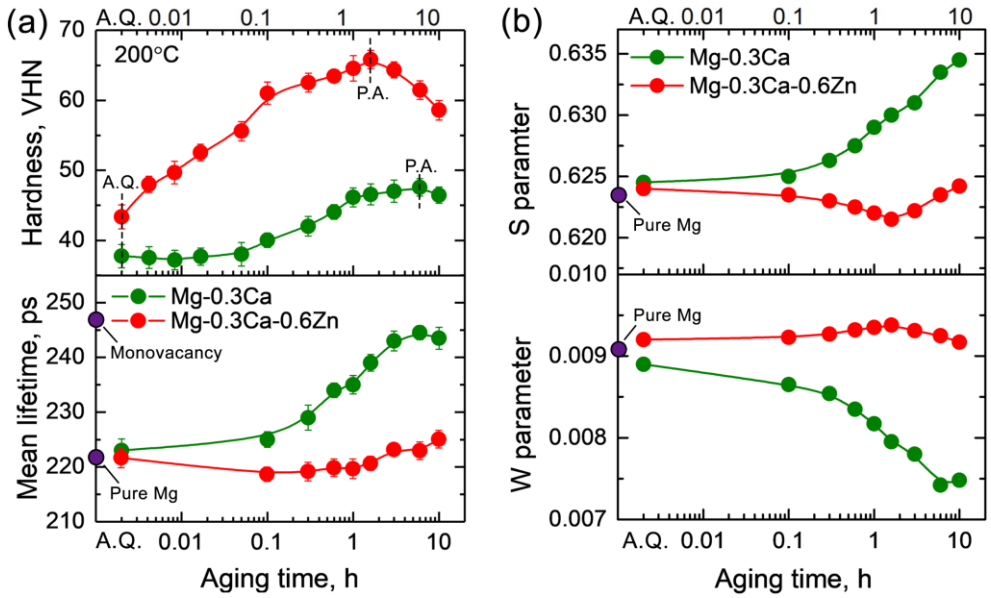

Fig. 1. (a) Variations in Vickers hardness and average positron lifetime as functions of aging time, and (b) S and W plots of the Mg-0.3Ca and Mg-0.3Ca-0.6Zn alloys during isothermal aging at 200 °C. Note that A.Q. and P.A. stand for as-quenched and peak-aged condition, respectively.

Fig. 1b shows the evolution of S and W parameters with the aging time deduced from the CDB analysis. The Mg-0.3Ca alloy show an increased S parameter along with a deceased W parameter upon aging, which is accordance with the rise of positron lifetime, i.e. the increased vacancy-type defects bound to Ca in the matrix. In contrast, the S parameter in the Mg-0.3Ca-0.6Zn alloy gradually decreases until the peak-aged condition, indicating a reduced concentration of vacancy-type defects in the matrix. Combined with the concurrently increased W parameter, the positron annihilation may be attributed to the progressive formation of coherent aggregates bound to Zn/Ca atoms given the 3d electrons of Zn may contribute to a higher W parameter compared to Ca with no 3d electron. Subsequently increased S parameter along with decreased W parameter is associate with the incorporation of Ca atoms into semi-coherent metastable precipitates.

4.3.2 TEM analysis of Zn-free and Zn-addition alloys

To verify the results from the PALS and CDB analysis, and considering the intimate interaction between quenched-in vacancies and dislocation structures such as dislocation loops and helices, the microstructural evolution of the Mg-0.3Ca and Mg-0.3Ca-0.6Zn alloys during the isothermal aging are revealed by TEM. Figure 2 shows a series of bright-field (BF) TEM images of as-quenched, 0.1 and 1.6 h aged samples observed under a two-beam condition with the diffraction vector of $g= [1\bar{1}01]_{\alpha}$ near the $\langle 11\bar{2}3\rangle_{\alpha}$ zone axis. The as-quenched Mg-0.3Ca alloy exhibits a number of dislocation segments, whereas a few ones presents in the Mg-0.3Ca-0.6Zn alloy, Fig.2a and d. Following aging for 0.1 h, the dislocations in the Mg-0.3Ca alloy tend to tangle with each other, and very fine precipitates are detected in the vicinity of dislocations, Fig. 2b. In contrast, the Mg-0.3Ca-0.6Zn alloy shows a number of dislocation loops and helical dislocations, Fig. 2e. From the

previous work, such loops lie on $\{0002\}_\alpha$ planes with an 1/6 $\langle 20\bar{2}3\rangle_\alpha$ type Burgers vector. After 1.6 h aging, Mg-0.3Ca alloy shows a dense dispersion of tangled dislocations decorated by coarse precipitates, Fig. 2c, while helical dislocations are sparsely distributed in the Mg-0.3Ca-0.6Zn alloy, Fig. 2f.

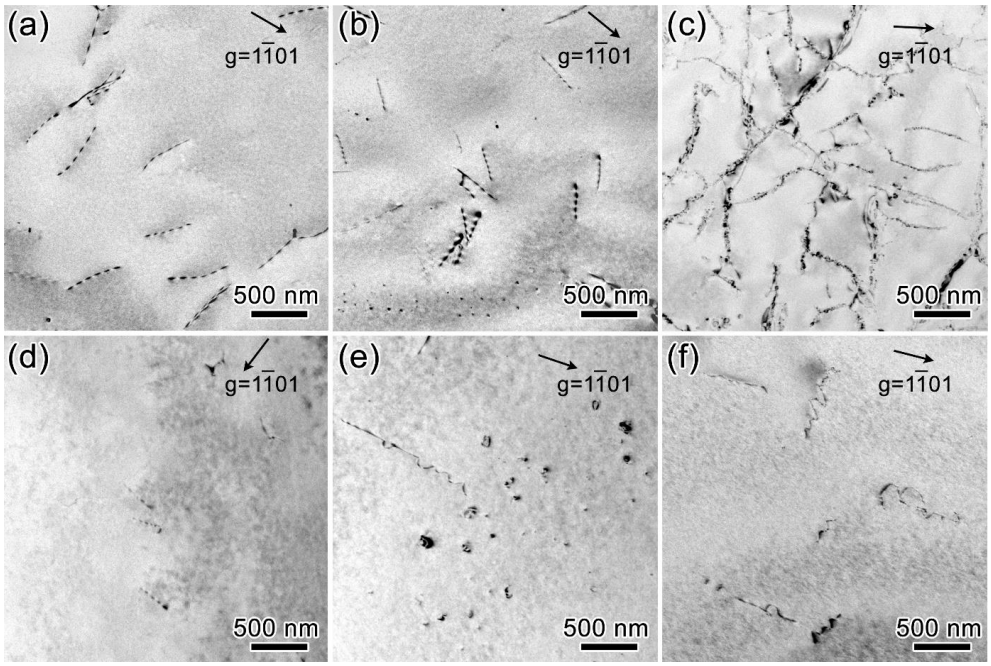

Fig. 2. Bright-field TEM images of the (a-c) Mg-0.3Ca and (d-f) Mg-0.3Ca-0.6Zn alloys aged at 200 ºC for 0 h; as-quenched, 0.1 h and 1.6 h, respectively. Note that TEM images were taken in the two-beam condition with the diffraction vector g = $[1\bar{1}01]_\alpha$ near the $\langle 11\bar{2}3\rangle_\alpha$ zone axis.

To further identify the precipitates formed in the Mg-0.3Ca and Mg-0.3Ca-0.6Zn alloys, TEM observations were conducted under g= $[0001]_\alpha$ with corresponding selected area electron diffraction (SAED) patterns recorded from $\langle 10\bar{1}0\rangle_\alpha$ zone axis, Figure 3. Both as-quenched alloys show no obvious precipitation contrast in the BF images or extra reflections from the SAED patterns, Fig. 3a and d. The dislocation density observed under g= $[0001]_\alpha$ is much less than those under g = $[1\bar{1}01]_\alpha$, Fig. 2a and d, indicating that most of as-quenched dislocations have a Burgers vector b= 1/3 $\langle 11\bar{2}0\rangle_\alpha$, while the visible dislocations must contain a ⟨c⟩ component based on the g·b = 0 invisibility criterion [14]. Following aging for 0.1 h, very fine precipitates are found to nucleate on the dislocations parallel to the trace of basal planes in the Mg-0.3Ca alloys, Fig. 3b. The SAED pattern from the precipitates is indexed as the Mg_2Ca phase with a hexagonal structure; $P6_3/mmc$, a = 0.627 nm, c = 1.017 nm, and the orientation relationship (OR) between Mg_2Ca and α-Mg phases is such that $(0001)_{Mg2Ca}$ // $(0001)_\alpha$, $[11\bar{2}0]_{Mg2Ca}$ // $[1\bar{1}00]_\alpha$. In contrast, the Mg-0.3Ca-0.6Zn alloy shows no significant precipitation on the dislocations, but a 'tweed contrast' in the matrix, Fig. 3e. The extra diffraction spots are clearly detected in the SAED pattern, indicating the presence of extremely fine precipitates. After 1.6 h aging, coarse Mg_2Ca precipitates in cuboidal shape are sparsely distributed along the dislocations and surrounding matrix of the Mg-0.3Ca alloy, Fig. 3c. The typical "coffee-bean" contrast is visible on both upper and lower sides of precipitates, indicating a coherent strain within the (0001) habit planes. However, the Zn addition

leads to a dense dispersion of fine plate-like precipitates on the basal planes of the α-Mg matrix, Fig. 3f. Considering the continuous streaks along the $[0001]_\alpha$ and at the $1/3\{11\bar{2}0\}_\alpha$ and $2/3\{11\bar{2}0\}_\alpha$ positions in the SAED pattern, these fine precipitates are indexed as the ordered G.P. zones [15].

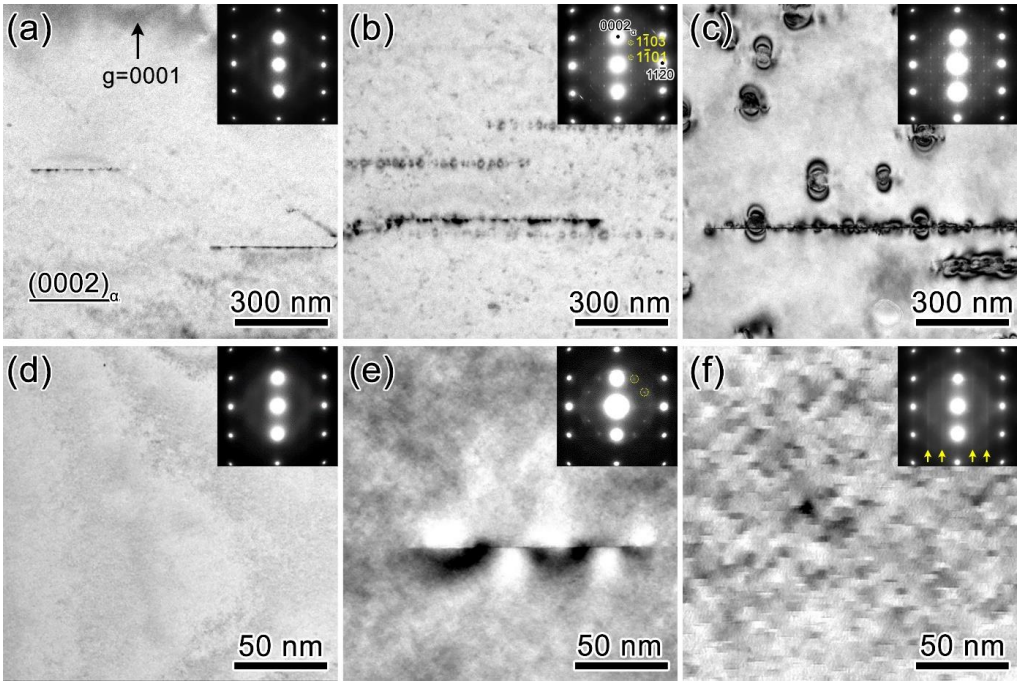

Fig. 3. Bright-field TEM images and corresponding SAED patterns of the (a-c) Mg-0.3Ca and (d-f) Mg-0.3Ca-0.6Zn alloys aged at 200 ºC for 0 h; as-quenched, 0.1 h and 1.6 h, respectively. Note that TEM images were taken in the two-beam condition with the diffraction vector g = $[0001]_\alpha$ near $\langle 10\bar{1}0\rangle_\alpha$ zone axis. Diffraction spots from the precipitates and the α-Mg matrix are indexed with yellow and black characters, respectively.

4.3.3 HAADF-STEM and 3D atom probe analysis of Zn-free and Zn-addition alloys

To investigate the distributions of solute clusters during the early stages of aging, 3DAP analysis was conducted in the as-quenched and 0.1h aged samples. Figure 4a and d shows the 3D atom maps of Ca or/and Zn and frequency histograms of 2NN distance between the solute atoms obtained from the same volume of the as-quenched Mg-0.3Ca and Mg-0.3Ca-0.6Zn alloys. Some inhomogeneity appears to be discernible within the selected volumes as indicated by arrows. The experimental histograms of solute atoms in both alloys show lower peak frequency values, and slightly shift to smaller 2NN distances compared to their random curves, implying the existence of solute clustering [16].

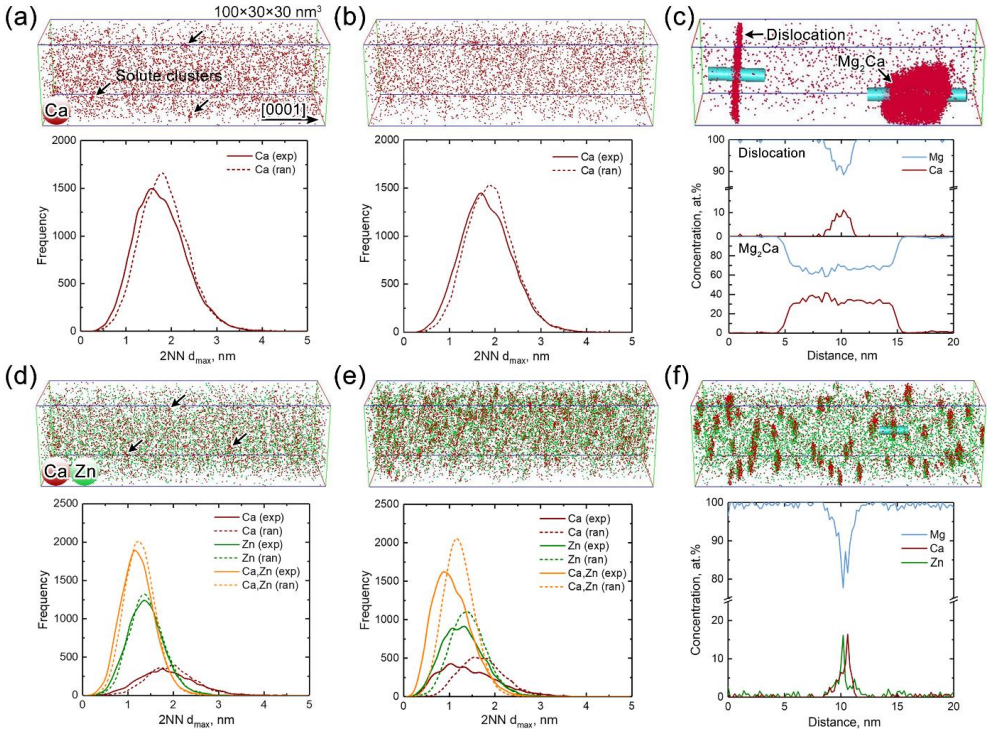

Fig. 4. 3D atom maps, frequency histograms and 1D concentration profiles of Mg (blue), Ca (red) and Zn (green) in the (a-c) Mg-0.3Ca and (d-f) Mg-0.3Ca-0.6Zn alloys aged at 200 ºC for 0 h; as-quenched, 0.1 h and 1.6 h, respectively. Note that the data was analyzed along the $[0001]_{\alpha}$.

Table 1 and 2 summarize the possibility and relative degree for Ca-Ca, Zn-Zn solute clustering and Ca-Zn co-clustering, respectively. The calculated χ^2 values of 58.53, 98.59, 43.89 and 28.09 for Ca-Ca and Ca-Ca, Zn-Zn, Ca-Zn clustering in the as-quenched Mg-0.3Ca and Mg-0.3Ca-0.6Zn alloys are significantly higher than those (11.35, 11.35, 13.28 and 16.81) corresponding to 0.01 probability of a deviation greater than χ^2, indicating that the composition fluctuations observed within the matrix are strongly associated with the formation of small clusters even in the as-quenched condition [4]. Table 3 provides the number density of various types of clusters in certain size ranges, which are defined as the number of solute atoms in a cluster. The as-quenched Mg-0.3Ca alloy contains ~ 2.2×10^{24} m^{-3} Ca-Ca clusters with the size distribution mostly confined within 10 atoms. However, the Ca-Zn co-clusters is dominant in the as-quenched Mg-0.3Ca-0.6Zn alloy compared to other single-species Ca-Ca and Zn-Zn clusters with the number density; ~ 4.5×10^{24} m^{-3} twice larger than that of Ca-Ca clusters in the Mg-0.3Ca alloy. Following 0.1 h aging, the Mg-0.3Ca alloy shows a reduced clustering with the experimental histogram close to the random one, Fig. 4b. The χ^2 values of 42.9 for the Ca-Ca clustering is lower than that in the as-quenched sample, Table 1, and the number density is decreased to ~ 1.57×10^{24} m^{-3}. However, a large number of small Ca/Zn-rich regions with significant discrepancies between the experimental and random histograms are observed in the 0.1 h-aged Mg-0.3Ca-0.6Zn alloy, indicating an enhanced clustering response by the Zn addition, Fig. 4e. The χ^2 values of 1608.35, 933.99 and 940.86 for Ca-Ca, Zn-Zn, Ca-Zn clustering are much higher than those in the as-quenched sample, Table 1 and 2, and accordingly the number density of these clusters is further increased, Table 3. After 1.6 h

aging, two Ca-rich regions in different shapes are observed in the Mg-0.3Ca alloy, Fig. 4c. The corresponding 1D composition profiles shows that the cuboidal region contains ~ 67 at.% Mg and ~33 at.% Ca; close to the Mg_2Ca, while the linear region has a lower Ca concentration of ~ 10 at.%, indicating the segregation of Ca to the dislocation. In contrast, the Mg-0.3Ca-0.6Zn alloy shows a dense distribution of plate-like Ca/Zn-rich regions with the same concentration of Ca and Zn; ~ 16 at.%, Fig. 4f, which is well consistent with the G.P. zones in previous work [2].

Table 1 Binomial analysis for Ca-Ca and Zn-Zn solute clustering in the as-quenched and 0.1 h-aged Mg-0.3Ca and Mg-0.3Ca-0.6Zn alloys.

Alloy, at.%	Cluster type	χ^2 statistic	
		As-quenched	0.1 h-aged
Mg-0.3Ca	Ca-Ca	58.53 > χ^2 (0.01) = 11.35, degree of freedom = 3	42.9 > χ^2 (0.01) = 11.345, degree of freedom = 3
Mg-0.3Ca-0.6Zn	Ca-Ca	98.59 > χ^2 (0.01) = 11.35, degree of freedom = 3	1608.35 > χ^2 (0.01) = 11.345, degree of freedom = 3
	Zn-Zn	43.89 > χ^2 (0.01) = 13.28, degree of freedom = 4	933.99 > χ^2 (0.01) = 13.277, degree of freedom = 4

Table 2 Contingency tables for co-segregation of Ca and Zn in the as-quenched and 0.1 h-aged Mg-0.3Ca-0.6Zn alloys.

Condition	Solutes	observed				Expected		
As-quenched		Zn				Zn		
			0	1	2-100	0	1	2-100
	Ca	0	14455	6249	1734	14329	6322	1787
		1	2291	1119	346	2399	1058	299
		2-100	331	166	50	349	154	44
		χ^2 = 28.09 > χ^2 (0.01) = 16.81, degree of freedom = 6						
0.1 h-aged		Zn				Zn		
			0	1	2-100	0	1	2-100
	Ca	0	17098	4936	1228	16456	5200	1606
		1	2324	1046	472	2718	859	265
		2	373	239	163	548	173	54
		3-100	109	68	80	182	57	18
		χ^2 = 940.86 > χ^2 (0.01) = 16.81, degree of freedom = 6						

Table 3 Number density of solute clusters with certain size ranges in the Mg-0.3Ca and Mg-0.3Ca-0.6Zn alloys aged at 200 ºC for 0 h; as-quenched and 0.1 h.

Alloy, at.%	Cluster type	Cluster size, atoms	Number density, $\times 10^{24}$ m^{-3}	
			As-quenched	0.1 h-aged
Mg-0.3Ca	Ca-Ca	3-10	2.05	1.08
		11-50	0.15	0.49
		50+	0	0
		Total	2.2	1.57
Mg-0.3Ca-0.6Zn	Ca-Ca	3-10	1.85	1.4
		11-50	0.2	0.88
		50+	0	0
		Total	2.05	2.28
	Zn-Zn	3-10	1.01	1.55
		11-50	0.45	1.08
		50+	0	0.08
		Total	1.46	2.71
	Ca-Zn	3-10	2.84	3.57
		11-50	1.65	2.17
		50+	0	0.09
		Total	4.49	5.83

Since positron traps are also strongly affected by the coherency of precipitates with matrix, the precipitate-matrix interface in both 1.6 h-aged alloys are further characterized by STEM imaging. Figure 5a shows an atomic ADF-STEM image of the local interfacial structure between the Mg_2Ca and α-Mg matrix viewed along the $[1\bar{1}00]_\alpha$. A regular distribution of Ca-rich columns in brighter contrast; Z = 12 for Mg and 20 for Ca is observed in the interface with a neighboring distance of 0.542 nm. Six $(3\bar{3}00)_{Mg2Ca}$ planes matches with seven $(11\bar{2}0)_\alpha$ planes, indicating a semi-coherent interface within the habit plane. By masking the $(11\bar{2}0)_\alpha$ matrix and $(3\bar{3}00)_{Mg2Ca}$ diffraction spots in the fast-Fouier transform (FFT) pattern, an array of misfit dislocations is clearly identified at the end of extra half planes with a spacing of ~ $11d_{(11\bar{2}0)\alpha}$ from the corresponding inverse FFT (IFFT) image, Fig. 5b. The measured interplanar spacing of $d_{(3\bar{3}00)Mg2Ca}$ and $d_{(11\bar{2}0)\alpha}$ are ~ 0.181 and 0.161 nm, thus leading to a large misfit of 12.4% between the Mg_2Ca and α-Mg matrix. To locate the cores of misfit dislocations, GPA is used to display the strain distribution in the IFFT image [17], Fig. 5c. The extension region in light-yellow color and compression region in dark-blue color are highlighted around each dislocation cores. Based on the corresponding atomic distribution, the extension regions are concentrated in Ca-rich columns. In contrast, the G.P. zone shows a monolayer structure with a periodic arrangement of Zn-rich columns; Z = 30 for Zn along the $[11\bar{2}0]_\alpha$ in an interval of every two columns; ~ 0.482 nm, Fig. 5d. One

$(3\bar{3}00)_{G.P.}$ plane matches well with one $(11\bar{2}0)_{\alpha}$ plane, indicating a fully-coherent interface with the α-Mg matrix. The corresponding IFFT image shows no extra half plane but small displacements of lattice fringes within the G.P. zone, Fig. 5e. Accordingly, an alternating distribution of extension region in red color and compression region in blue color are observed in the GPA map, Fig. 5f, revealing an ordered arrangement of Ca and Zn atoms in the G.P. zones.

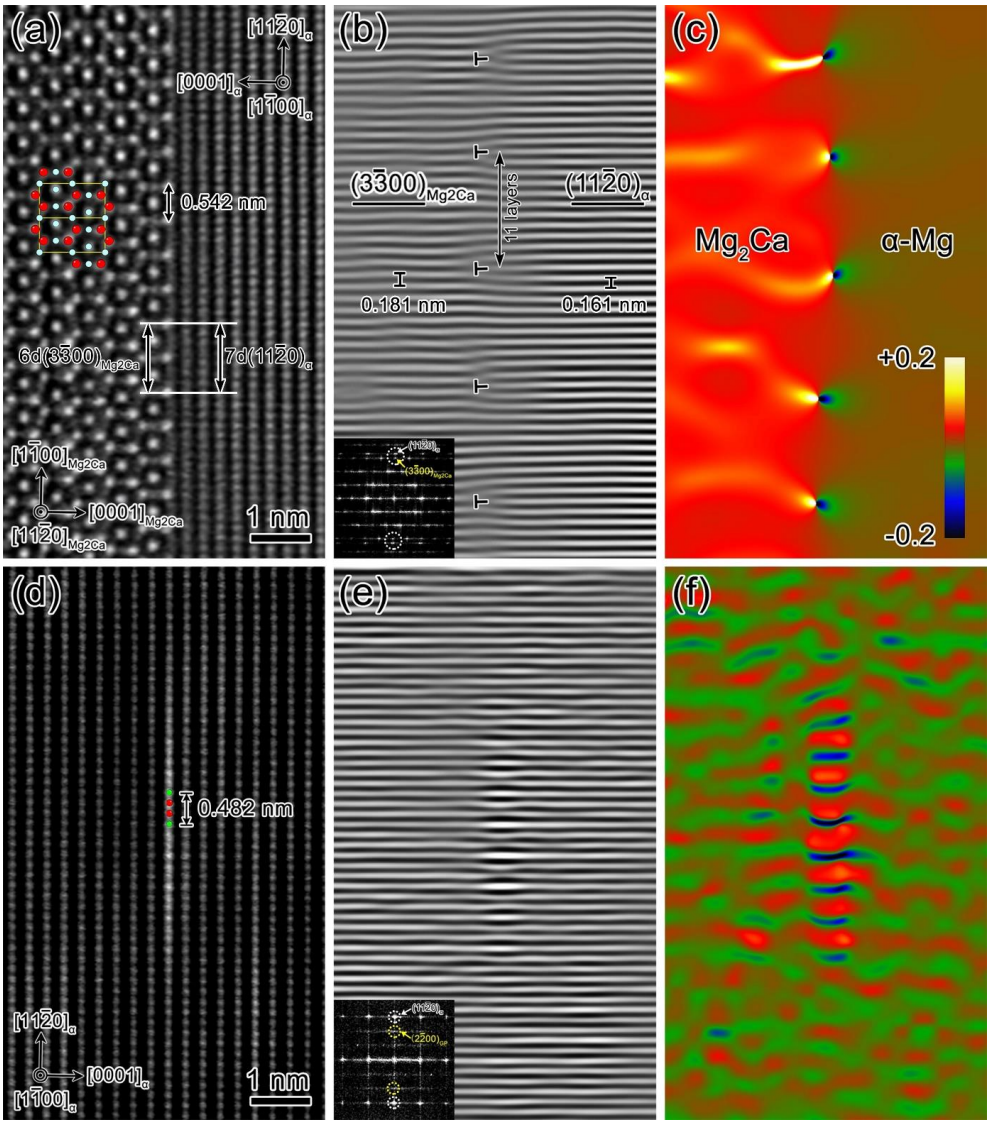

Fig. 5. Atomic resolution ADF-STEM images, corresponding IFFT images and GPA strain maps of interfacial structures between the precipitates and the α-Mg matrix in the 1.6 h-aged (a-c) Mg-0.3Ca and (d-f) Mg-0.3Ca-0.6Zn alloys. Note that electron beam in (a,d) is parallel to $[1\bar{1}00]_{\alpha}$ and symbol ⊥ represents a misfit dislocation.

4.4 Discussion

In this work, the role of Zn on the microstructural evolution of the Mg-0.3Ca-(0.6Zn) alloys during the early stages of aging at 200 °C is thoroughly investigated by a combination of PALS/CDB, (S)TEM, and 3DAP

analysis. The positron lifetime in both as-quenched Zn-free and Zn-addition alloys is almost same as that of well-annealed pure Mg, Fig. 1a, indicating that quenched-in vacancies may not directly play a role in accelerating the aging kinetics like that observed in the Al alloys [4,5]. Instead, most of vacancies are trapped by solute atoms, leading to the formation of vacancy-solute complexes. Higher W parameters for the Zn-containing alloy compared to that of pure Mg indicates that vacancies are mainly bound to the Zn atoms, i.e. vacancy-Zn-Ca complexes, while lower W parameters in the Zn-free alloy corresponds to vacancy-type defects bounded to Ca atoms, Fig. 1b. Since vacancy-solute complexes act as precursors for solute clusters, the number density of complexes can be reflected from the solute clusters. The number density of the Ca-Ca clusters; ~ 2.2 ×1024 m-3 in the as-quenched Zn-free alloy is less than half of the Ca-Zn co-clusters; ~ 4.5×1024 m-3 in the Zn-addition alloy, Table 3, thus the addition of Zn may stabilize more vacancies in the form of vacancy-Ca-Zn complexes. Considering the larger atomic radius of Ca; 0.197 nm and smaller for Zn; 0.133 nm referring to Mg; 0.160 nm, and large negative enthalpy of -22 kJ/mol between Ca and Zn [18], the co-clustering of Ca and Zn is energetic favorable for minimizing the elastic strain induced by individual Ca or Zn atoms, thus leading to a high number density of vacancy-Ca-Zn complexes in the as-quenched condition. Due to the high mobility of vacancy-solute complexes, the formed vacancy-Ca-Zn complexes are responsible for the accelerated solute transport in the following aging. Following aging for 0.1 h, the Zn-free alloy shows reduced Ca-Ca clusters in the matrix; ~ 1.6 ×1024 m-3, which is attributed to the segregation of vacancy-Ca complexes to dislocations, Fig. 3b and 4c. Considering a large compression strain induced by replacing Mg with Ca, the segregation of Ca to dislocations can relieve the strain field and assist the nucleation of Mg2Ca precipitates. A large lattice misfit of ~ 12.4% between the Mg2Ca and the matrix leads to periodical misfit dislocations arranged at Mg2Ca-matrix interfaces, which serve as efficient positron trapping sites for the increased positron lifetime, Fig. 5a-c. In contrast, the number density of Ca-Zn co-clusters and other types of like-solute clusters further increases in the Zn-containing alloy; ~ 5.8 ×1024 m-3 in total, Fig. 4e. This is due to the re-trap of most vacancies by Zn or Zn-Ca dimers after solute-vacancy complexes reach solute clusters [8], which is consistent with the slight decrease of positron lifetime, Fig. 1b. After 1.6 h aging, the Zn-free alloy shows a rapid coarsening of Mg2Ca precipitates due to the high interfacial energy of incoherent interface and pipe diffusion of solutes along dislocations, which results in further increased positron time, Fig. 1a and 5a. However, the maintained lifetime plateau in the Zn-containing alloy is attributed to a dense dispersion of the G.P. zones which originate from Ca-Zn co-clusters that provide heterogeneous sites, Fig. 3f and 4f.

The vacancy-stabilizing effect of Zn is also verified from the evolution of dislocation structures during the aging process. The as-quenched Zn-free alloy show a much higher density of dislocations compared to the Zn-containing alloy due to a larger atomic radius of Ca; 0.197 compared to Mg; 0.160 nm, Fig. 2a and d. These dislocations act as vacancy sinks, thus leading to the decreased quenched-in vacancies in the matrix of the Zn-free alloy. Following aging for 0.1 h, the vacancy-Ca complexes with large compression strains preferentially move to the pre-existing dislocations, resulting in the rapid multiplication and tangles of dislocations, Fig. 2b and c. In contrast, a number of fine dislocation loops are formed in the Zn-containing alloy, which is mainly due to collapse of vacancies slowly freed by the progressive formation of solute clusters [4], Fig. 2e. The

growth of dislocation loops further leads to the formation of helical dislocations with the absorption of more vacancies, Fig. 2f. As the G.P. zones increase coherency strains in the adjoining lattices, vacancies trapped at the G.P. zones may assist the relief of elastic stress, thus leading to a low density of helical dislocations formed in the Zn-containing alloy.

4.5 Conclusion

In summary, this work demonstrates that quenched-in vacancies in the Mg-0.3Ca-0.6Zn alloy do not play a direct role in accelerating the aging kinetics due to the low concentration. Instead, the role of Zn is as a vacancy-stabilizer that promotes the formation of vacancy-Ca-Zn complexes, and sustained growth during the early stages of aging. Considering the high mobility of vacancy-solute complexes, the rapid age-hardening response is attributed to the the formation of vacancy-Ca-Zn complexes and resultant Ca-Zn co-clusters, which further provide heterogeneous nucleation sites for a densely distributed G.P. zones. Our finding is expected to give insights for the rational design and development of rapid age-hardenable wrought Mg alloys.

Reference

[1] K. Hono, C.L. Mendis, T.T. Sasaki, K. Oh-ishi, Scr. Mater. 63 (2010) 710–715.

[2] Z.H. Li, T.T. Sasaki, T. Shiroyama, A. Miura, K. Uchida, K. Hono, Mater. Res. Lett. 8 (2020) 335–340.

[3] M.Z. Bian, T.T. Sasaki, T. Nakata, Y. Yoshida, N. Kawabe, S. Kamado, K. Hono, Acta Mater. 158 (2018) 278–288.

[4] R.K.W. Marceau, G. Sha, R. Ferragut, A. Dupasquier, S.P. Ringer, Acta Mater. 58 (2010) 4923–4939.

[5] R.K.W. Marceau, A. de Vaucorbeil, G. Sha, S.P. Ringer, W.J. Poole, Acta Mater. 61 (2013) 7285–7303.

[6] J.F. Nie, B.C. Muddle, Scr. Mater. 37 (1997) 1475–1481.

[7] K. Oh-ishi, R. Watanabe, C.L. Mendis, K. Hono, Mater. Sci. Eng. A 526 (2009) 177–184.

[8] A. Dupasquier, G. Kögel, A. Somoza, Acta Mater. 52 (2004) 4707–4726.

[9] A. Uedono, S. Takashima, M. Edo, K. Ueno, H. Matsuyama, H. Kudo, H. Naramoto, S. Ishibashi, Phys. Status Solidi B 25 (2015) 22794–2801.

[10] Y. Nagai, K. Takadate, Z. Tang, H. Ohkubo, H. Sunaga, H. Takizawa, M. Hasegawa, Phys. Rev. B 67 (2003) 224202.

[11] C.T. Koch, Ultramicroscopy, 108 (2008) 141–150

[12] M.P. Moody, L.T. Stephenson, A.V. Ceguerra, S.P. Ringer, Microsc. Res. Tech. 71 (2008) 542–550.

[13] Y. Nagai, Z. Tang, M. Hasegawa, Radiat. Phys. Chem. 58 (2000) 737–742.

[14] D.B. Williams, C.B. Carter, Transmission Electron Microscopy: A Textbook for Materials Science, second ed., Springer-Verlag, New York, 2009.

[15] D.H. Ping, K. Hono, J.F. Nie, Scr. Mater. 48 (2003) 1017–1022.

[16] B. Gault, M.P. Moody, J.M. Cairney, S.P. Ringer, Atom Probe Microscopy, first ed., Springer-Verlag, New York, (2012).

[17] M.J. Hÿtch, E. Snoeck, R. Kilaas, Ultramicroscopy 74 (1998) 131–146.

[18] A. Takeuchi, A. Inoue, Mater. Trans. 46 (2005) 2817–2829.

[19] D.A. Porter, K.E. Easterling, Phase Transformations in Metals and Alloys, third ed., Chapman & Hall, London, 2009.

Chapter 5 Precipitation evolution in a Mg-0.3Ca-0.6Zn alloy

5.1 Introduction

The development of heat-treatable high strength magnesium (Mg) alloys is anticipated to stimulate the adoption of Mg wrought products in the transportation vehicles, which may lead to prominent weight reduction [1,2]. Recently, Mg-Ca-Zn based dilute alloys have attracted considerable attention due to their potential to fulfill the good formability and high strength concurrently without the addition of rare-earth elements [3-5]. As demonstrated in a Mg–0.6Zn–0.3Ca–0.1Zr (at.%, ZXK200) sheet alloy, the excellent room temperature formability with an I.E. value of 8.0 mm is achieved in the solution treated condition [5]. Subsequent artificial aging (T6) significantly increases the yield strength from 165 to 213 MPa, enabling this alloy to have well-balanced formability and strength comparable to 6xxx series of aluminum alloys. Given that the improvement of strength by T6 treatment is attributed to the dense dispersion of Guinier Preston (G.P.) zones, the precipitation hardening is crucial for this alloy to overcome the formability-strength trade-off dilemma.

The precipitation sequence of the Mg-Ca-Zn system has been demonstrated as [6-10]:

SSSS (supersaturated solid solution) → ordered G.P. zones → η' → η.

Oh-ishi et al. reported that the G.P. zones are mono-layer plates with an internally ordered structure on the $(0002)_\alpha$ planes [7]. The ordered structure is the same as that was observed for Mg-RE-Zn alloys based on the selected area electron diffraction (SAED) patterns of the G.P. zone showing the extra diffraction spots and continuous streaks at the $1/3\{11\bar{2}0\}_\alpha$ and $2/3\{11\bar{2}0\}_\alpha$ positions along $\langle 0001\rangle_\alpha$ and $\langle 1\bar{1}00\rangle_\alpha$ zone axes, respectively [8]. However, the definite atomic coordinates and composition have not been determined until now. The η' phase remains the plate-like shape on the basal plane with a much larger size than that of the G.P zones [9]. The corresponding SAED pattern along the $[1\bar{1}00]_\alpha$ zone axis shows similar streaking feature, while no additional reflection is detected in the one obtained from the $[0001]_\alpha$ zone axis. Thus, the η' phase is reported to have a hexagonal structure; $P6_3/mmc$, a = 0.580 nm, c =0.941 nm with a composition of Mg–18Ca–8Zn (at.%) deduced from a three-dimensional atom probe (3DAP) [9]. However, an atomic resolution high-angle annular dark-field scanning transmission electron microscopy (HAADF-STEM) image taken from the zone axis of $[11\bar{2}0]_\alpha$ shows that these large plates have a similar arrangement of atomic columns on the basal planes as the G.P. zones, which are thereby not considered as a new phase [7]. For the equilibrium η phase, it is initially proposed to have a hexagonal structure; $P6_3/mmc$, a =0.623 nm, c =1.012 nm isomorphous to that of the Mg_2Ca phase; $Mg_2(Ca,Zn)$ [9]. The orientation relationships (OR) between η and α-Mg matrix are such that $(0001)_{\eta'} // (01\bar{1}0)_\alpha$, $[\bar{1}2\bar{1}0]_{\eta'} // [2\bar{1}\bar{1}0]_\alpha$, and $(0001)_{\eta'} // (0001)_\alpha$, $[\bar{1}2\bar{1}0]_{\eta'} // [01\bar{1}0]_\alpha$. However, the high-resolution transmission electron microscopy (HRTEM) observations suggested that the η phase has a trigonal structure; $P\bar{3}1c$, a = 0.97 nm, c =1.01 nm and a composition of $Mg_6Ca_2Zn_3$ [7,10], which adopts ORs of $(11\bar{2}0)_\eta // (0001)_\alpha$, $[0001]_\eta // [11\bar{2}0]_\alpha$, and $(11\bar{2}0)_\eta // (0001)_\alpha$, $[0001]_\eta // [21\bar{3}0]_\alpha$. Therefore, the crystal structures and compositions of these precipitates need for further elucidation.

The aim of this work is to unambiguously establish the precipitation sequence in the Mg-Ca-Zn system, which was recently reported to be rather promising alloy system for developing bake-hardenable sheet alloys [5,11], using aberration-corrected STEM and 3DAP analysis. A full knowledge about the precipitation sequence from the present study is expected to give deeper insights into the role of precipitate phases on the strengthening of the Mg-Ca-Zn alloy, which may guide for the rational design of new alloy compositions, and thus a development of further improved high-strength and formable wrought Mg sheet alloys.

5.2 Experimental

Alloy ingots with a nominal composition of Mg-0.3Ca-0.6Zn in at.% or Mg-0.5Ca-1.6Zn in wt.% were prepared from high purity Mg, Zn and Mg-30 wt.% Ca master alloy by induction melting in a steel crucible and casting into a steel mould in an argon (Ar) atmosphere. Hereafter, the alloy composition is described in at.% as we deal with atomic feature of metastable phases. The ingots were encapsulated in He-filled Pyrex tubes, solution-treated at 520 ºC for 2h, and then quenched in water. 2-mm-thick samples sectioned from the as-quenched ingots were subsequently aged in an oil bath at 200 ºC for various times. The age-hardening responses were determined from the average value of 10 individual indentations in each aging condition using a Vickers hardness tester under a load of 0.3 kg

HAADF-STEM observations were carried out using Titan G^2 80-200 TEMs equipped with a probe corrector and a Super-X energy-dispersive X-ray (EDX) spectrometer operating at 200 kV. Thin foil specimens for the (S)TEM observations were prepared by punching 3 mm diameter discs and twin-jet electro-polishing using a solution of 5.3 g LiCl, 11.16 g $Mg(ClO_4)_2$, 500 ml methanol, and 100 ml 2-butoxy-ethanol at about -50 °C with a voltage of 90 V. 3D atom probe (3DAP) analysis is performed using a local electrode atom probe (CAMECA LEAP 5000 XS) in voltage pulse mode at a temperature of 30 K. Sharp needle-like specimens for the 3DAP analysis were prepared by the focused ion beam (FIB) lift-out and annular milling techniques using a FEI Helios G4 UX.

5.3 Results

5.3.1 Precipitation evolution during aging at 200 ºC

Figure 1 shows the age-hardening curves of the Mg-0.3Ca, Mg-0.6Zn, and Mg-0.3Ca-0.6Zn alloys during isothermal aging at 200 °C. The binary Mg-0.3Ca and Mg-0.6Zn alloys have Vickers hardness values of 38.4 ± 1.8 and 49.3 ± 0.4 HV in the as-quenched condition, respectively, and show little or sluggish age-hardening response with a peak-hardness increment of ~ 0 and 9.1 HV upon the subsequent aging, respectively. In contrast, the as-quenched Mg-0.3Ca-0.6Zn alloy has a hardness value of 50.1 ± 1.1 HV, and exhibits a rapid age-hardening kinetics during the early stage of aging; the hardness increases to a peak value of 63.6 ± 1.3 HV

within only 0.3 h. After reaching the peak hardness, the hardness curve shows a short plateau of ~ 3 h, and then gradually decreases to 40.3 ± 1.2 HV after 1000 h.

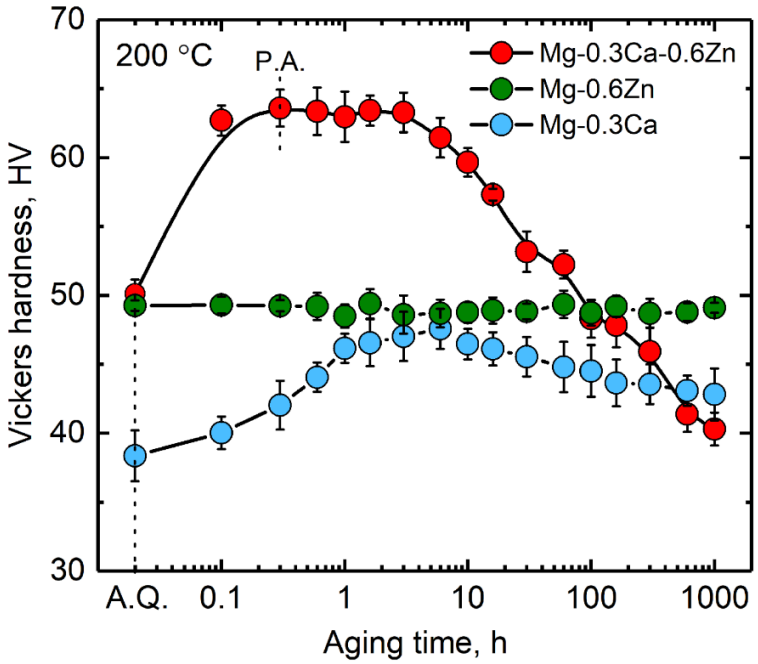

Fig. 1. Variations in Vickers hardness as functions of aging time for the Mg-0.3Ca, Mg-0.6Zn, and Mg-0.3Ca-0.6Zn alloys during artificial aging at 200 °C. Note that A.Q. and P.A. stand for as-quenched and peak-aged condition, respectively.

Figure 2 shows HAADF-STEM images and SAED patterns of the samples aged at 200 °C for various aging time. Note that HAADF-STEM images were taken from the zone axis of $[11\bar{2}0]_\alpha$, and the SAED patterns were taken from $[0001]_\alpha$ and $[1\bar{1}00]_\alpha$ zone axes, respectively. In the under-aged condition; 0.1 h, the faint diffraction spots and streaks in the $[0001]_\alpha$ and $[1\bar{1}00]_\alpha$ SAED patterns suggests the presence of $(0001)_\alpha$ plate-like stacks, although the microstructure does not show any obvious precipitate contrast, Fig. 2a. For the peak-aged sample; 0.3 h, a dense distribution of fine plate-like precipitates is seen on the basal planes of the α-Mg matrix with an average diameter of 3.6 ± 0.8 nm, Fig. 2b. These plates are brightly imaged with respect to the α-Mg matrix, indicating an enrichment of Zn (Z=30) and/or Ca (Z=20). Extra reflections and continuous streaks at the $1/3\{11\bar{2}0\}_\alpha$ and $2/3\{11\bar{2}0\}_\alpha$ positions in the $[0001]_\alpha$ and $[1\bar{1}00]_\alpha$ patterns indicates the formation of the G.P. zones [7,8]. Following over-aging; 2-10 h, the fine G.P. zones are gradually replaced by larger basal plates with the average diameter increasing from ~ 7.8 ± 1.3 nm to ~ 14.7 ± 3.2 nm, while the number density of the precipitates is decreased, Fig. 2c-d. After 100 h aging, the larger basal plates with an average diameter of 25.7 ± 5.6 nm tend to form in pairs other than single ones, Fig. 2e. In the 300 h-aged sample, only the sparsely distrusted plate pairs and stacks with a larger diameter of 45.3 ± 8.7 nm are observed in the matrix, Fig. 2f. The extra reflections and continuous streaking features are also detected in the $[0001]_\alpha$ and $[1\bar{1}00]_\alpha$ patterns of the over-aged samples, indicating that these large precipitate plates remain ordered structures.

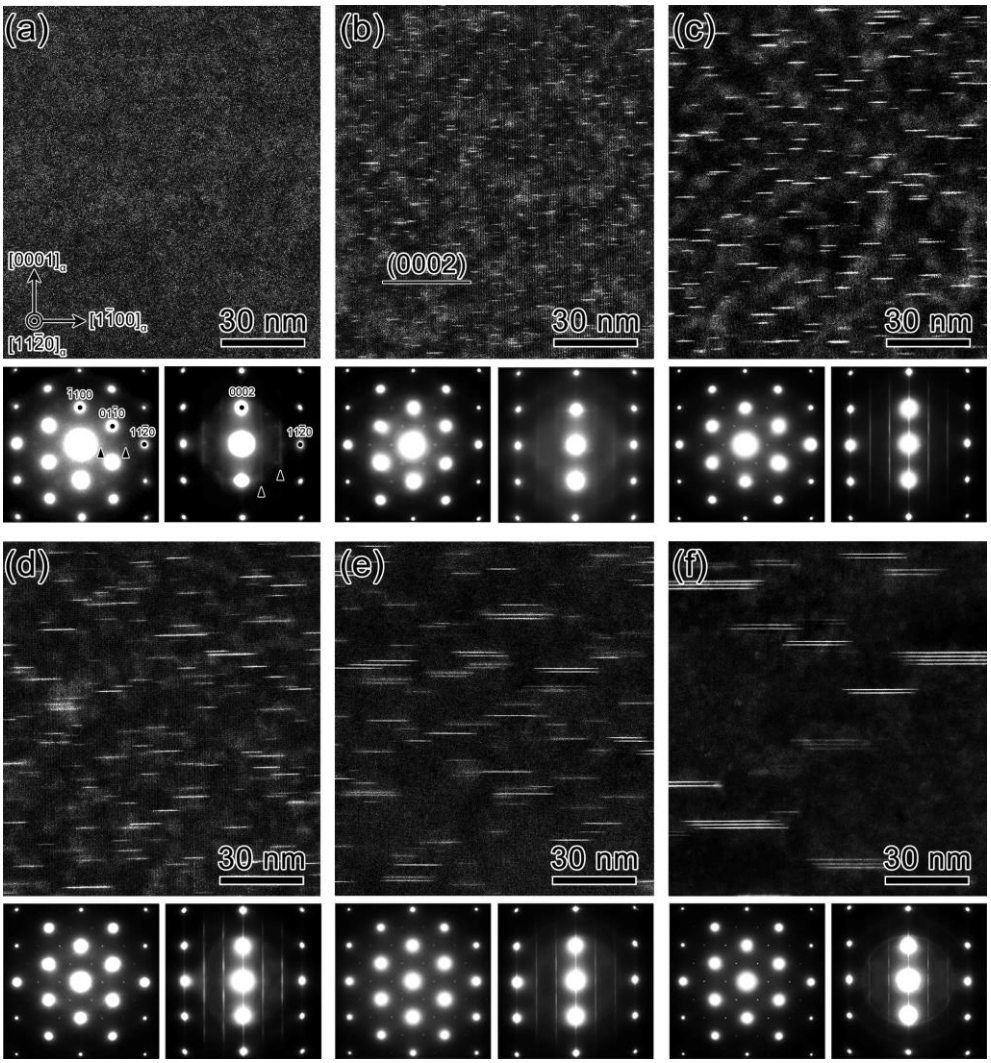

Fig. 2. HAADF-STEM images and SAED patterns of Mg-0.3Ca-0.6Zn alloy aged for (a) 0.1 h, (b) 0.3 h; peak-aged, (c) 2 h, (d) 10 h, (e) 100 h and (f) 300 h, respectively, at 200 °C. Note that the images were taken from the $[11\bar{2}0]_\alpha$ and SAED patterns were recorded from $[0001]_\alpha$ and $[10\bar{1}0]_\alpha$ directions.

To clearly reveal the precipitate shape, the HAADF-STEM images were also taken from the $[1\bar{1}00]_\alpha$ zone axis of the samples aged at 200 °C for various aging time, Figure 3. Fig. 3a shows no obvious precipitate contrast in the microstructure of the 0.1 h-aged sample; 0.1 h. In the peak-aged condition; 0.3 h, a dense distribution of fine plate-like precipitates is seen on the basal planes of the α-Mg matrix with an average diameter of 3.4 ± 0.5 nm, Fig. 3b. These plates are brightly imaged with respect to the α-Mg matrix, which are identified as the G.P. zones. Following over-aging; 2-10 h, the fine G.P. zones are gradually replaced by larger basal plates with the average diameter increasing from ~ 7.3 ± 1.6 nm to ~ 15.2 ± 2.4 nm, while the number density of the precipitates is decreased, Fig. 3c and d. After 100 h aging, the larger basal plates with an average diameter of 25.1 ± 4.8 nm tend to form in pairs other than single ones, Fig. 3e. In the 300 h-aged sample, only the sparsely distrusted plate pairs and stacks with a larger diameter of 46.8 ± 7.9 nm are observed in the matrix, Fig. 3f. Based on the combined observations from the $[11\bar{2}0]_\alpha$ and $[1\bar{1}00]_\alpha$ zone axes, the precipitates in each aging condition are determined to have a disc-like shape on the basal planes.

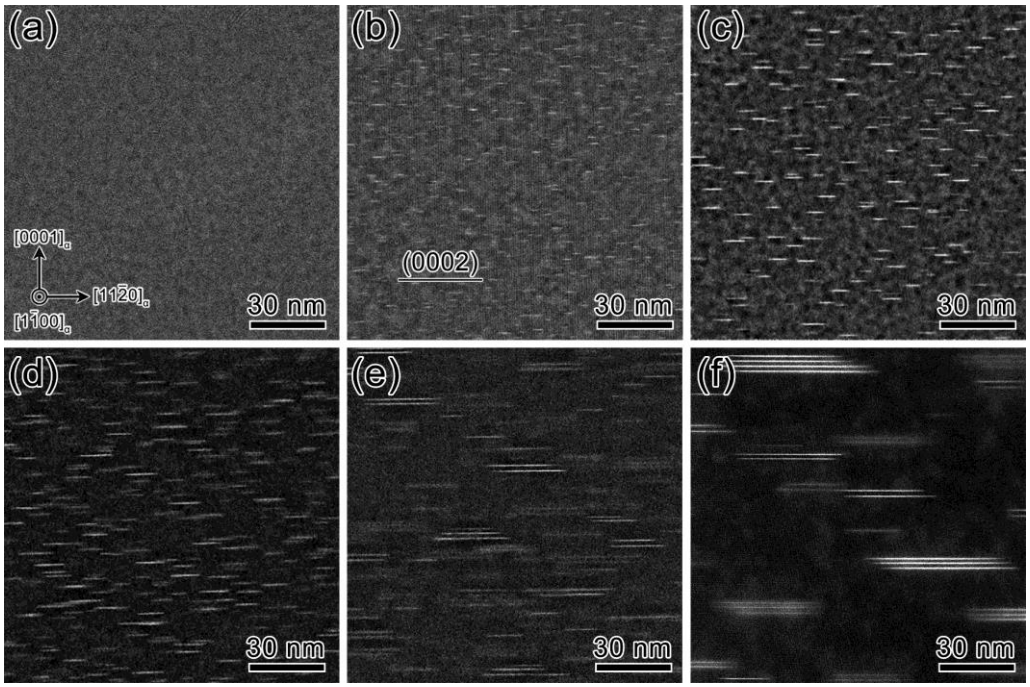

Fig. 3. HAADF-STEM images taken from the $[10\bar{1}0]_\alpha$ of Mg-0.3Ca-0.6Zn alloy aged for (a) 0.1 h, (b) 0.3 h; peak-aged, (c) 2 h, (d) 10 h, (e) 100 h and (f) 300 h, respectively, at 200 °C.

5.3.2 TEM and 3D atom probe analysis of precipitate phases

Figure 4a shows an atomic resolution HAADF-STEM image and the corresponding fast Fourier transformation (FFT) pattern of the G.P. zone in the peak-aged sample viewed along the $[11\bar{2}0]_\alpha$ zone axis. The brightly imaged atomic columns containing either Ca or Zn are closely arranged on a single $(0002)_\alpha$ plane with pronounced streaking visible along the $[0001]_\alpha$ at the $(000)_\alpha$ and $\{1\bar{1}00\}_\alpha$ positions of the FFT pattern. The HAADF-STEM image taken from the $[1\bar{1}00]_\alpha$ zone axis shows a periodic distribution of Zn/Ca-rich columns in the G.P. zones with an interval of every two columns; ~ 0.48 nm, Fig. 4b. The corresponding FFT pattern shows the same streaking feature as the above SAED pattern. Fig. 4c shows the inverse FFT processed fringe images of $(0002)_\alpha$ planes and the corresponding intensity profile taken from the regions across the G.P. zone and the Mg matrix in Fig. 4b. The interplanar spacing between the two adjacent $(0002)_\alpha$ centering the G.P. zone is measured to be ~ 0.51 nm, thus leading to a misfit of -0.032 along the normal direction of the $(0002)_\alpha$ habit plane assuming that the lattice parameters of the α-Mg matrix are a = 0.321 and c = 0.521 nm. Fig. 4d shows the 3D atom map of Mg, Ca and Zn obtained from the peak-aged sample with a volume of 120 × 25 × 25 nm^3, and a large number of small regions enriched with Ca and Zn atoms are detected. Table 1 summarizes the solute concentration, interplanar spacing, and number density of precipitates in the various aging time. The number density and planar interspace of the G.P. zones are estimated to be ~ 1.22 ×10^{24} m^{-3} and 14.5 nm based on $\lambda=\left(\frac{0.953}{\sqrt{f}}-1\right)d_t$ [12]. The 1D concentration profile obtained from a selected volume shows that these G.P. zones contain nearly same concentration of Ca an Zn; ~ 16 at.%,

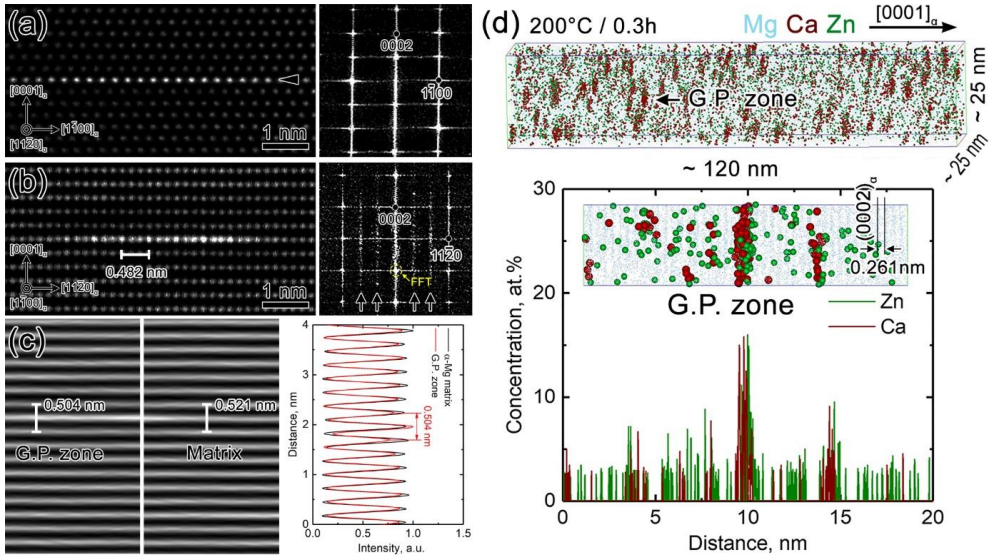

Fig. 4. (a) and (b) Atomic resolution images of the G.P. zone and corresponding FFT patterns taken from $[11\bar{2}0]_\alpha$ and $[1\bar{1}00]_\alpha$ directions of the 0.3 h-aged sample, respectively. (c) IFFT processed fringe images and the corresponding intensity profile from the regions in (b). (d) 3D atom maps of Mg, Ca and Zn obtained from the 0.3 h-aged sample and the corresponding 1D concentration profile of the G.P. zone. Note that the data was collected by locating the $(0001)_\alpha$ pole towards the detector analysis.

Table 1 Solute concentration, volume fraction, number density and planar interspace of precipitates in the various aging time.

Aging time, h	Precipitate	Solute concentration of precipitates, at.%			Volume fraction	Number density, $\times 10^{23}$ m^{-3}	Planar interspace, nm
		Mg	Ca	Zn			
0.3	G.P. zone	68.3 ± 2.3	15.7 ± 1.3	16.1 ± 1.8	0.036	12.2	14.5
2	η''	68.2 ± 2.5	13.2 ± 1.5	18.6 ± 2.2	0.051	4.47	25.1
10	η'	60.2 ± 1.6	15.6 ± 2.1	24.2 ± 1.5	0.031	1.57	64.9
100	η' *pair*	52.7 ± 1.3	26.2 ± 0.8	21.1 ± 0.7	0.018	0.36	156.9
300	η' or η'' cluster	25.1 ± 2.5	50.2 ± 2.1	24.7 ± 1.4			
	η	57.2 ± 0.4	17.6 ± 0.3	25.2 ± 0.3	—	—	—

Figure 5a and b show atomic resolution HAADF-STEM images and the corresponding FFT patterns of the precipitate plate followed 2 h aging taken from the zone axes of $[11\bar{2}0]_\alpha$ and $[1\bar{1}00]_\alpha$, respectively. In contrast to the monolayer G.P. zones, this plate consists of three atomic layers with a periodic distribution of the brightest atomic columns in the middle layer, and are designated η'' phase. The thickness of the η'' phase is measured to be ~ 0.51 nm, leading to a lattice misfit of -0.029 along the normal direction of the $(0002)_\alpha$ habit plane, which is slightly lower than that of the G.P. zone. The 3D atom map obtained from the 2 h-aged sample shows larger volume enriched with Ca and Zn in addition to the G.P. zones as indicated by arrows, Fig. 5c, while the number density of precipitates is reduced to ~ 4.47 $\times 10^{23}$ m^{-3} with the planar interspace increasing to ~ 25.1 nm. The concentrations of Ca and Zn in the η'' are evaluated to be ~ 13 and 19 at.%. The combined observations from HAADF-STEM images and 3DAP analysis suggest that the η'' remains a hexagonal structure; a = 0.56 nm and c = 0.51 nm with a composition of $Mg_{11}Ca_2Zn_3$. The OR between η'' and the α-Mg matrix is described as $(0001)_{\eta''}$// $(0001)_\alpha$, $[10\bar{1}0]_{\eta''}$// $[11\bar{2}0]_\alpha$. Following 10 h aging, another type of precipitate with a similar three-layer structure are observed in the vicinity of the η'', Fig. 5d, which are designated as η' phase. Compared to η'', the middle layer of the η' phase shows a periodical distribution of the brightest atomic columns in every two columns, Fig. 5e, thus, the η' may evolve from the η'' by the solute diffusion and the middle layer shifting a distance of $\sqrt{3}/6$ along $\langle 1\bar{1}00\rangle_\alpha$ [13]. The thickness of the η' is measured to be ~ 0.51 nm with a normal lattice misfit of -0.035, which is similar to that of the η'', Fig. 4b. The 3D atom map of the 10 h-aged sample shows a number of precipitates with a distinct plate-like morphology and lower number density of ~ 1.57 $\times 10^{23}$ m^{-3}, Fig. 5f. The concentration profile of the selected precipitate plate shows higher concentrations of Ca and Zn atoms; ~ 16 and 24 at.%, respectively than those of the η'' phase. Therefore, the η' phase is proposed to have an ordered hexagonal structure; a = 0.56 nm and c = 0.50 nm with a composition of $Mg_7Ca_2Zn_3$. The OR between η'' and the α-Mg matrix is same as that of the η'' phase, and the habit plane was parallel to $(0001)_{\eta'}$// $(0001)_\alpha$.

Figure 6a-d show atomic resolution HADDF-STEM images and corresponding FFT patterns of large single plates and pairs in the 100 h-aged samples viewed along the zone axes of $[11\bar{2}0]_\alpha$ and $[1\bar{1}00]_\alpha$, respectively. Two groups of precipitate plates with different atomic arrangements are clearly revealed from the $[1\bar{1}00]_\alpha$ projections, Fig. 5b and d. Due to the structural similarity, these two precipitates may have evolved from the η' and η'' precipitates, respectively. The FFT patterns of both plate pairs shows the similar features as the corresponding single η' and η'' phases, Fig. 5b and e, thus, the interlayers between two neighboring plates are considered to be the α-Mg matrix. Following 300 h aging, the single plates and pairs are mostly transformed to the pairs and stacks. The combined observations from the atomic resolution images and corresponding FFT patterns reveal that these stacks consist of 3-4 individual plates with the same structures as the corresponding η' and η'' phases, Fig. 6f-i. Since the single η' or η'' components in the plate pairs and stacks are irregularly separated by the α-Mg layers, these pairs and stacks cannot be defined as new phases. However, considering the interspacing between the neighboring plates are mostly concentrated in 4 or 5 layers, they may act as precursors to further transformation. The 3D atom map obtained from the 100 h-aged sample shows large single precipitate plates and pairs arranged on $(0002)_\alpha$ planes with the number density of precipitates

significantly reduced to ~ 3.6 ×10^{22} m^{-3}, Fig. 5e. The 1D concentration profile analyzed from the selected volume in the inset shows that the concentration of Ca and Zn is nearly the same; ~ 20 and 25 at.% for each columns, thus verifying that this plate pair is composed of two individual η' plates. In addition, some plate stacks with a thickness over 20 matrix layers are also detected in the 3D atom map of the 100 h-aged sample, Fig. 6j. The 1D concentration profile of the selected volume shows one plate stack with a four-columns structure. The average concentrations of Ca and Zn is measured to be ~ 50 and 20 at.% for each column, which are much higher than those of η' and/or η'' phase. Considering that the evaporation field of Ca; 18 V/nm is lower than those of Zn and Mg; 33 and 21 V/nm, the Ca content may be over-estimated in this four-layered structure [9].

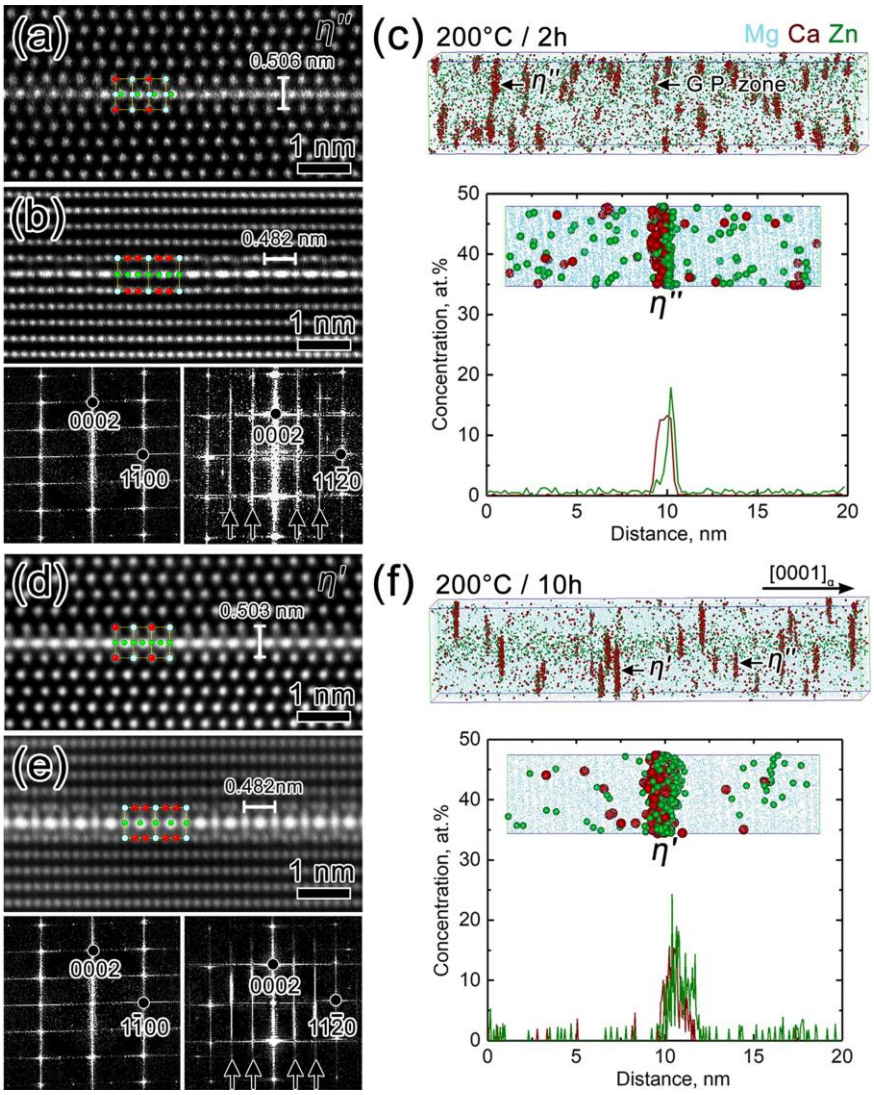

Fig. 5. (a,b) and (d,e) atomic resolution images and corresponding FFT patterns of the η'' and η' phases taken from $[11\bar{2}0]_\alpha$ and $[1\bar{1}00]_\alpha$ directions of the 2 h and 10 h-aged samples, respectively. (c) and (f) 3D atom maps of Mg, Ca and Zn obtained from 2 h and 10 h-aged samples and the corresponding 1D concentration profile of the η'' and η', respectively. Note that the same method as shown in Fig. 3(c) was conducted to measure the thickness of the η'' and η' phases.

In addition to the dense distribution of fine basal plates, some coarse precipitates also appear in the Mg matrix with the increased aging time. Figure 7a shows a low magnification HAADF-STEM image of the 100 h-aged sample taken from the zone axis of $[1\bar{1}00]_{\alpha}$. Coarse lath and rod-like precipitates are clearly visible, meanwhile a few thin but very long platelets; ~ 400 ± 100 nm lie on the (0001) planes solely or link with coarse precipitates as indicated by arrows. Enlarged image shows that these basal plates is much thicker than the aforementioned fine plates with a much larger aspect ratio; length over thickness of ~ 150: 1, Fig. 7b. These precipitates are designated as η_1 or η_2, respectively depending on the structural differences, Fig. 7c-d. Close inspections along the longitudinal direction of a η_1 plate reveal that this coarse basal plate originate from a single η' phase, which then stacks along the $[0001]_{\alpha}$ with a bright column separating from each other, Fig. 7e-g. On the other hand, the η_1 phase may evolve from an η' and/or η'' pair, where the interlayers of α-Mg are gradually replaced by the η' and two bright columns, Fig. 7h-j.

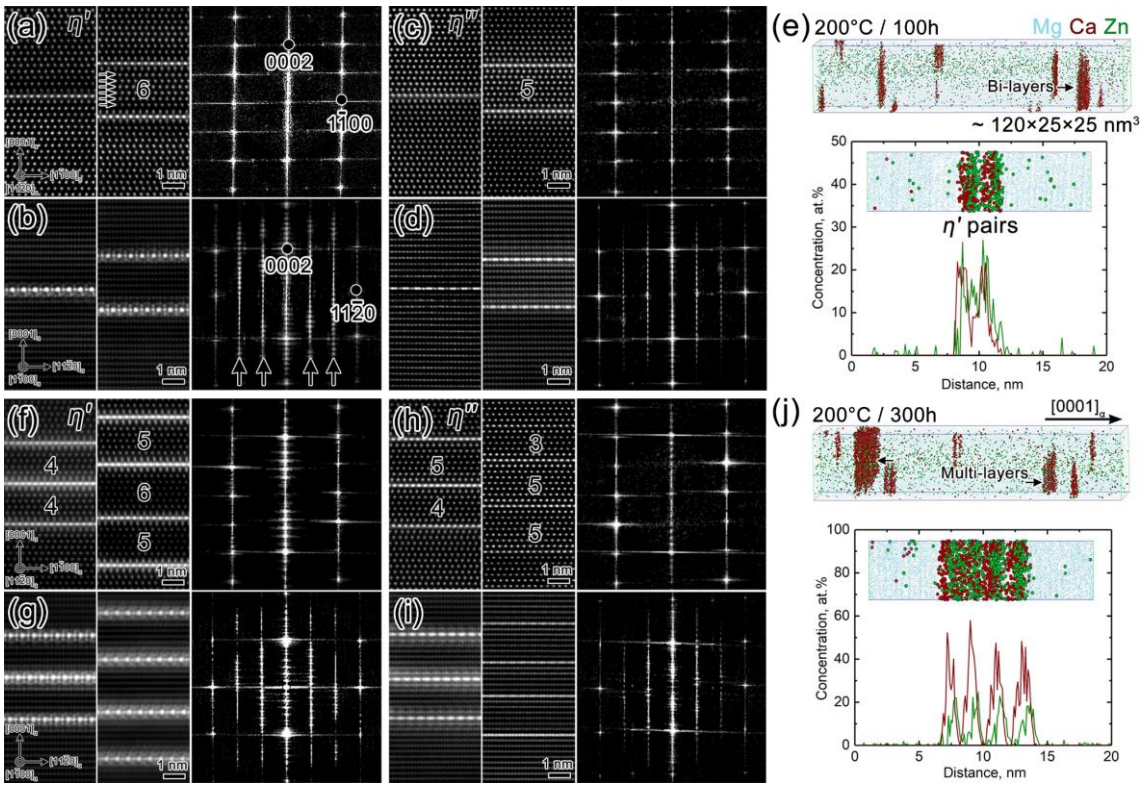

Fig. 6. (a,b) and (c,d) atomic resolution images and corresponding FFT patterns of the η' and η'' single and paired plates taken from $[11\bar{2}0]_{\alpha}$ and $[1\bar{1}00]_{\alpha}$ directions of the 100 h-aged sample, respectively. (f,g) and (h,i) atomic resolution images and corresponding FFT patterns of the η' and η'' clusters taken from $[11\bar{2}0]_{\alpha}$ and $[1\bar{1}00]_{\alpha}$ directions of the 300 h-aged sample, respectively. (e) and (j) 3D atom maps of Mg, Ca and Zn obtained from 100 h and 300 h-aged samples and corresponding 1D concentration profiles of the η'' and η' phases, respectively.

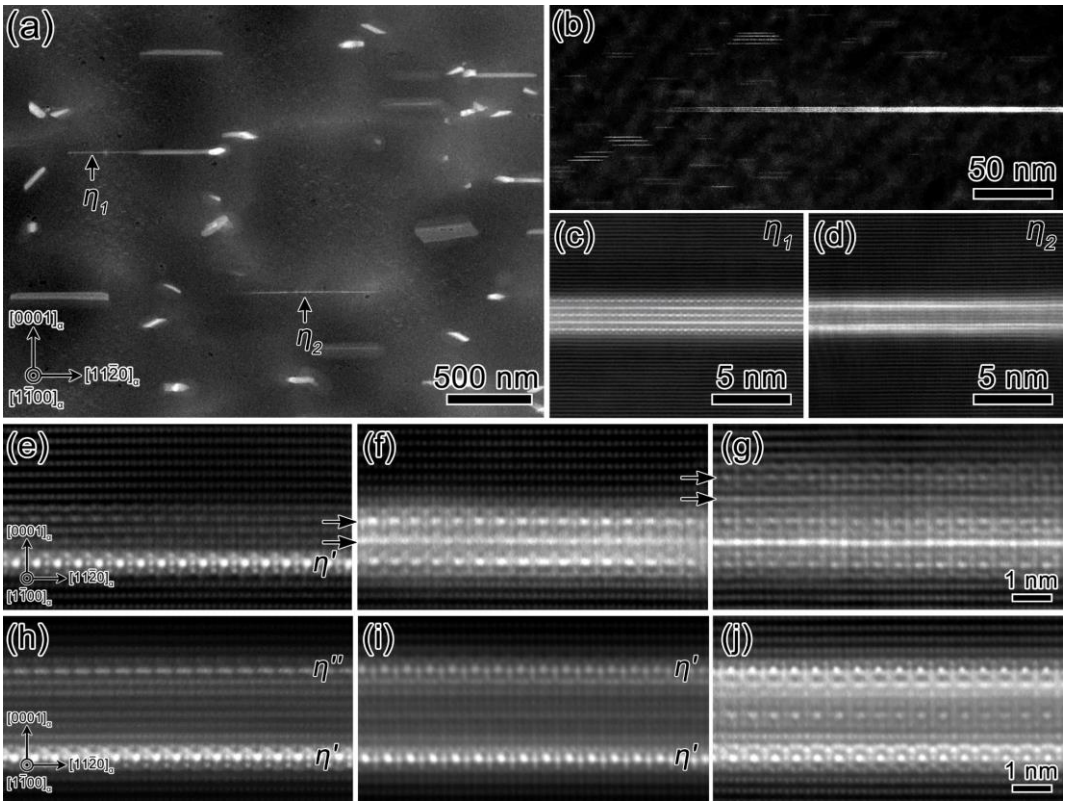

Fig. 7. HAADF-STEM images of metastable η_1 and η_2 phases in the Mg-0.3Ca-0.6Zn alloy aged at 200 °C for 100 h. (a,b) Low magnification image taken from the $[1\bar{1}00]_\alpha$. (c,d) enlarged images of the η_1 and η_2 phases in (a). (e-g) atomic resolution images of the η_1 phases stacking along the thickness direction as indicated by arrows, and (h-j) the in-situ transformation from the η' and/or η'' pairs.

Figure 8a shows atomic resolution HAADF-STEM images of the η_1 plate viewed along the $[11\bar{2}0]_\alpha$ zone axis. The layered atomic columns with brighter contrast are periodically arranged along the $[0001]_\alpha$. The $[1\bar{1}00]_\alpha$ projection clearly reveals the stacking structure with the η' plates separated by single atomic layers, Fig. 8b. The corresponding FFT pattern from the $[11\bar{2}0]_\alpha$ shows a similar streaking along the $[0001]_\alpha$ like the aforementioned precipitates, while the extra dotted-line diffraction spots are visible near the $1/3\{11\bar{2}0\}_\alpha$ and $2/3\{11\bar{2}0\}_\alpha$ positions in the $[1\bar{1}00]_\alpha$ pattern as indicated by arrows, which are different from that of the η' phase. Standardless quantitative analysis from an EDX spectrum indicates that the η_1 phase has an average composition of Mg-14.7 ± 2 Ca-19.2 ± 1 Zn (at.%), Fig. 8c. The combined HAADF-STEM observations and EDS analysis indicate that the η_1 phase has an ordered hexagonal structure; a = 0.57 nm, c = 1.04 nm and a composition of $Mg_{17}Ca_4Zn_5$. The OR between η_1 and the α-Mg matrix is such that $(0001)_{\eta_1}$ // $(0001)_\alpha$, $[0001]_{\eta_1}$ // $[11\bar{2}0]_\alpha$. Fig. 8d and e show the HAADF-STEM images of the η_2 plate with a thickness of ~25 nm viewed along the $[11\bar{2}0]_\alpha$ and $[1\bar{1}00]_\alpha$, respectively. The enlarged atomic resolution images in the insert shows the ordered arrangements of brightest columns in the two projections, indicating a long-period superlattice structure with 14 closely packed planes in the unit cell. The corresponding FFT pattern from the $[1\bar{1}00]_\alpha$ shows five sets of streaks along the $[0001]_\alpha$ and at the $1/6\{11\bar{2}0\}_\alpha$, $2/6\{11\bar{2}0\}_\alpha$, $3/6\{11\bar{2}0\}_\alpha$, $4/6\{11\bar{2}0\}_\alpha$, and

5/6$\{11\bar{2}0\}_{\alpha}$, and 11/12$\{11\bar{2}0\}_{\alpha}$positions as indicated by arrows [14]. The EDS analysis suggests that the average composition of the η_2 phase is Mg-8.0 ± 1 Ca-15.7 ± 1 Zn (at.%), Fig. 8f. Thus, the η_2 phase is proposed to have an ordered hexagonal structure; a = 0.58 nm, c = 3.49 nm with a composition of $Mg_{10}Ca_1Zn_2$. The OR between η_2 and the α-Mg matrix is such that $(0001)_{\eta_2}$// $(0001)_{\alpha}$, $[0001]_{\eta_2}$// $[11\bar{2}0]_{\alpha}$.

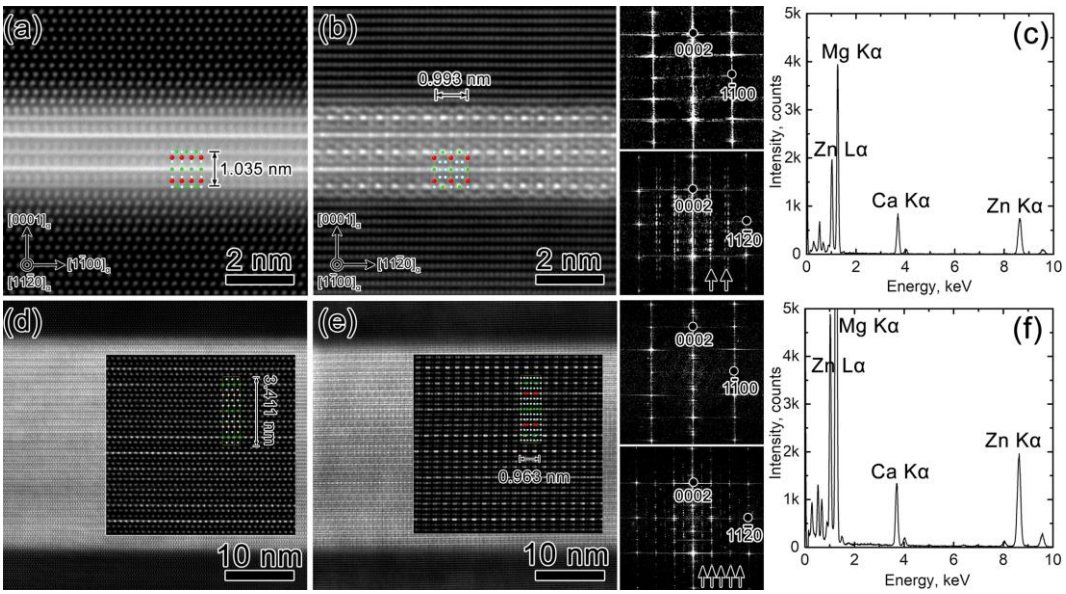

Fig. 8. Atomic resolution HAADF-STEM images, corresponding FFT patterns and EDX spectra recorded from the metastable (a-c) η_1, and (d-f) η_2 phases. Note that electron beam is parallel to the (a,d) $[11\bar{2}0]_{\alpha}$ and (b,e) $[1\bar{1}00]_{\alpha}$, respectively.

Figure 9a and b shows low-magnification HAADF-STEM images of the Mg-0.3Ca-0.6Zn alloy aged at 200 °C for 1000 h taken from the $[11\bar{2}0]_{\alpha}$ and $[0001]_{\alpha}$, respectively. Coarse precipitates are dominantly distributed in the Mg matrix, and the majority of them are lying on the basal plane, Fig. 9a. Lens and rod-like precipitates lie on the $(0001)_{\alpha}$ with growth directions parallel to the $\langle 11\bar{2}0\rangle_{\alpha}$ as indicated by arrows 1 and 2, respectively, Fig. 9b. The lenticular precipitates are ~ 250-450 nm in length, ~ 60-100 nm in width, and ~ 20-40 nm in thickness, while the $\langle 11\bar{2}0\rangle_{\alpha}$ rods have a larger aspect ratio with an average length of ~ 800 nm and the thickness of 20 nm. Another $(0001)_{\alpha}$ plate shows a hexagonal shape with an small size and thickness of ~ 70 and 20 nm as indicated by arrow 3. Polygonal-shaped precipitates are also clear with their facets parallel to $(0001)_{\alpha}$ and $(1\bar{1}00)_{\alpha}$ as indicated by arrows 4, Fig. 9a. The polygons have a rhombic shape in the $[0001]_{\alpha}$ projection with a larger length, width, and thickness of ~ 260, 130, and 100 nm, respectively, Fig. 9b. In addition, two lath-like precipitates lying on the non-basal planes are indicated by arrow 5 and 6, Fig. 9a. Careful trace analysis reveals that the laths 5 form on the $\{10\bar{1}3\}_{\alpha}$ with the projection of long axes aligned to the $\langle 1\bar{1}00\rangle_{\alpha}$, while the laths 6 are on the $\{20\bar{2}1\}_{\alpha}$ with the long axes slightly deviated from the $\langle 11\bar{2}0\rangle_{\alpha}$, Fig. 9b. The average size of these two precipitates is similar; ~ 300, 80 and 20 nm in length, width and thickness, respectively. The corresponding EDS elemental maps along the $[0001]_{\alpha}$ indicate that all the precipitates are enriched in Mg, Ca, and Zn, Fig. 8c. The standardless quantitative analysis of the EDX spectra recorded from the above precipitates

indicates that except the $\langle 11\bar{2}0\rangle_\alpha$ rods, i.e. precipitates 3, which have a low Ca/Zn concentration with an average composition of Mg-17 ± 1 Zn-7 ± 1 Ca (at.%), Fig. 9d, other five precipitates show a high concentration of Ca and Zn with a similar composition of Mg- 30 ± 1 Zn - 16 ± 1 Ca (at.%), Fig. 9e. Thus, the $\langle 11\bar{2}0\rangle_\alpha$ rod is designated as δ phase that is hitherto unreported, while the other five precipitates are designated η phase which has a similar composition as those reported previously.

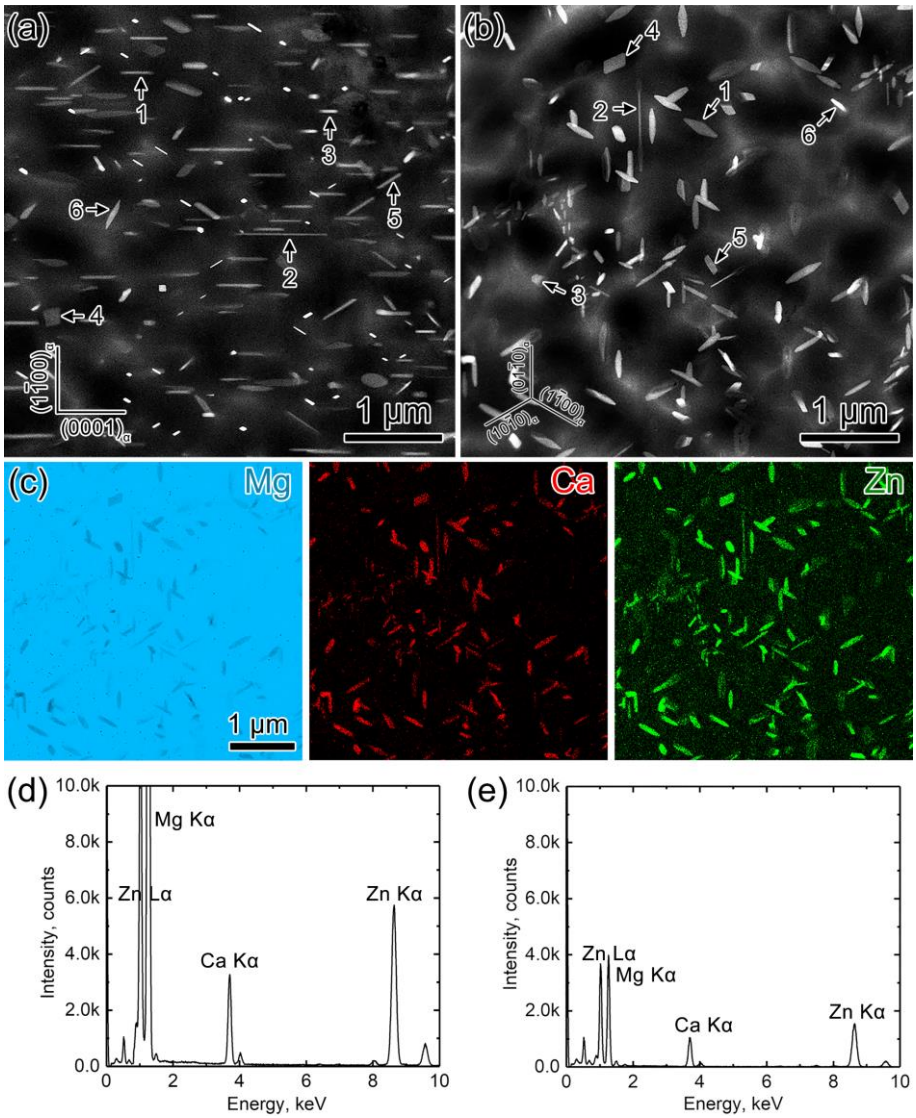

Fig. 9. (a,b) low magnification HAADF-STEM images of the Mg-0.3Ca-0.6Zn alloy aged at 200 °C for 1000 h with the electron beam parallel to the $[11\bar{2}0]_\alpha$ and $[0001]_\alpha$, respectively. (c) The corresponding STEM-EDX elemental maps of Mg, Ca, and Zn in (a). (d,e) EDX spectra recorded from the equilibrium δ and η phases.

Figure 10 a-b show the atomic resolution HAADF-STEM images of the η phase taken from the $[0001]_\eta$ and $[11\bar{2}0]_\eta$, respectively. The brightest dots in each image represent the atomic columns containing Zn, while the columns with intermediate brightness are considered as co-occupation by Zn/Mg or Zn/Ca atoms. From the corresponding nanobeam electron diffraction (NBED) patterns, the η phase has a hexagonal structure with lattice parameters of a = 1.00 nm and c = 1.01 nm, Fig. 10 c-d. The crystal point group of the η phase is

determined by noting the symmetries in the NBED patterns and assigning the corresponding diffraction groups [15-17]. Table 2 summarizes the symmetries and possible diffraction groups for the $\langle 0001 \rangle_\eta$, $\langle 11\bar{2}0 \rangle_\alpha$ and $\langle 1\bar{1}00 \rangle_\eta$ NBED patterns. Three possible point group; m3m, 6/mmm and 622 are consistent with the diffraction groups allowed for each zone axis pattern. Since the cubic Bravais lattice associated with point group m3m is incompatible with the indexed hexagonal lattice, and the observed pattern symmetries (2mm) from the $[10\bar{1}3]_\eta$ and $[10\bar{1}1]_\eta$ is not consistent with that (m) for point group 622, Figure 11, the point group of the η phase is exclusively inferred to the 6/mmm. The space group of the η phase is further identified by consideration of reflection conditions in the NBED patterns. Of the four space groups based on the point group 6/mmm, only the $P6_3/mmc$ has the same reflection conditions as the obtained NBED patterns, Table 3.

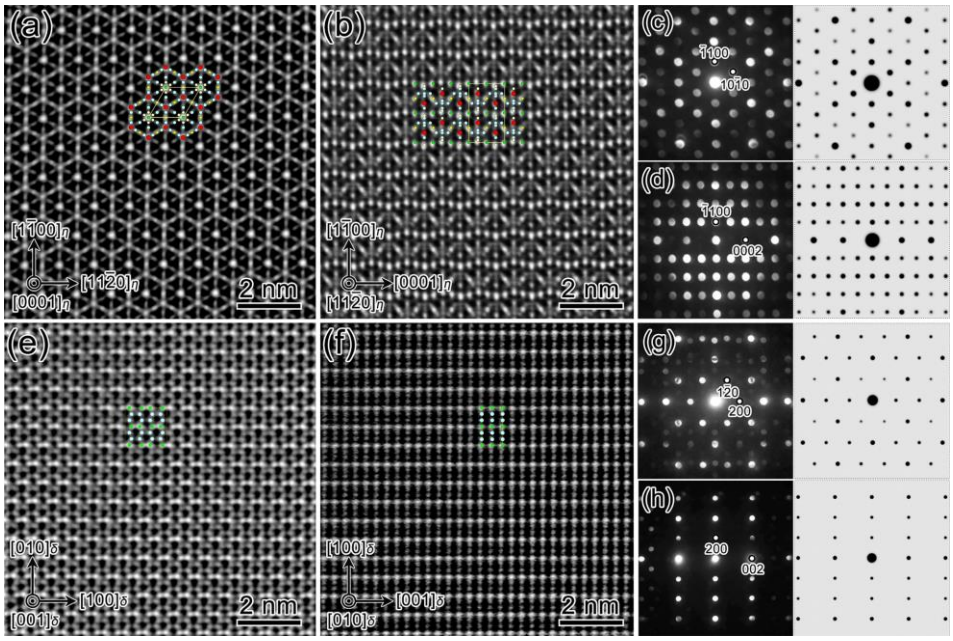

Fig. 10. (a-d) atomic resolution HAADF-STEM images, corresponding NBED patterns and simulated electron diffraction patterns of the equilibrium η phase taken from $[0001]_\eta$ and $[11\bar{2}0]_\eta$, respectively. (e-h) atomic resolution HAADF-STEM images, corresponding NBED patterns and simulated electron diffraction patterns of the δ phase taken from $[001]_\delta$ and $[010]_\delta$, respectively.

Table 2 NBED pattern symmetries, possible diffraction and point groups obtained from experimental NBED patterns of the η phase

Zone axis	Ideal ZOLZ symmetry	Possible diffraction groups	Possible point groups
$\langle 0001 \rangle_\eta$	6mm	$6m_Rm_R$, $6mm1_R$, 6mm, 6_Rmm_R	m3m, 6/mmm, 6mm, 622, $\bar{3}$m
$\langle 11\bar{2}0 \rangle_\eta$ $\langle 1\bar{1}00 \rangle_\eta$	2mm	$2m_Rm_R$, $2mm1_R$, 2mm, 2_Rmm_R	m3m, m3, 6/mmm, 622, 4/mmm, 422

Table 3 Reflection conditions obtained from experimental NBED patterns of the η phase

Space group	$hh\bar{2}hl$	$h\bar{h}0l$	$000l$	$hkil$
P6/mmm	—	—	—	—
P6/mcc	$l = 2n$	$l = 2n$	$l = 2n$	$l = 2n$
$P6_3$/mcm	—	$l = 2n$	$l = 2n$	$l = 2n$
$P6_3$/mmc	$l = 2n$	—	$l = 2n$	$l = 2n$

Figure 12 shows the 3D atom maps of Mg, Ca and Zn obtained from the 300 h-aged sample with a volume of 120 × 25 ×25 nm^3. The data was collected near the (0001) crystallographic pole of the sample, revealing the $\{0001\}_\alpha$ planes perpendicular to the $[0001]_\alpha$ analysis direction. A lath-like precipitate is observed with the long facets tilted ~ 32º away from the $(0001)_\alpha$, i.e. near the $(\bar{1}103)_\alpha$, Fig. S3a. Fig. S3b shows the enlarged image from the local region through the precipitate. The lattice planes of the precipitate parallel to $(0001)_\alpha$ planes have a planar interspacing of ~ 0.53 nm, which is well matched with the $\{11\bar{2}0\}_\eta$ planes; ~ 0.51 nm of the η phases deduced from the NBED pattern. From a proximity histogram across the precipitates/matrix interface, the chemical composition of the η phases is determined to be Mg-30.4 Zn-17.1 Ca (at.%), which is designated as $Mg_9Zn_4Ca_3$. On the basis of HAADF-STEM images and 3D atom probe analysis, the η phase is determined to have a $P6_3$/mmc space group with a composition of $Mg_9Zn_4Ca_3$. On the other hand, the δ phase shows a different distribution of Zn atoms compared to the η phase, Fig. 10e-f. The corresponding NBED patterns along the $[001]_\delta$ and $[010]_\delta$ suggest that the δ phase has an orthorhombic structure with lattice parameters of a = 1.01 nm, b = 1.11 nm and c = 0.55 nm, Fig. 10g-h. The combined analysis of HAADF-STEM images and NBED patterns suggested that the δ phase has a P/mmm space group with a composition of $Mg_9Zn_2Ca_1$. Furthermore, the simulated electron diffraction patterns are consistent with the experimental NBED patterns, indicating the validity of proposed structural models for the η and δ phase. Note that some diffraction spots in the experimental patterns exhibit weaker intensities than those in the simulated images. This difference can be attributed to a partial replacement of Zn atoms by Mg or Ca atoms.

To evaluate the orientation relationships between the equilibrium η/δ phases and Mg matrix, detailed HAADF-STEM observations are conducted in the precipitates with various orientations as indicated in Fig. 9a. Figure 13a-e shows the atomic resolution HAADF-STEM images of interfacial structures between the η phases and Mg matrix with low magnification images inserted in the top-right parts. One set of lens-like η phases (precipitate 1) exhibit an spindle-shaped cross-section when they are observed along the zone axis of $[11\bar{2}0]_\alpha$, Fig. 13a. Close inspection of the interfacial structure indicates that such "end on" η phase; the long axes parallel to the incident electron beam; has a fully coherent interface with the Mg matrix as the $(22\bar{4}0)_\eta$ plane matches well with the $(1\bar{1}01)_\alpha$ plane across the interface. The OR between the lens-like η phase and Mg matrix is such that $(11\bar{2}0)_\eta$ // $(0001)_\alpha$, $[0001]_\eta$ // $[11\bar{2}0]_\alpha$. Hexagonal-shaped $(0001)_\alpha$ η plate (precipitate 3) is enclosed by three groups of facets lying on the $\{1\bar{1}00\}_\alpha$, Fig. 13b. The atomic resolution image of these facets shows an atomically flat interface with a number of misfit dislocations arranged along the $[11\bar{2}0]_\alpha$. The

interplanar spacings of $(10\bar{1}1)_\alpha$ and $(22\bar{4}0)_\eta$ are 0.28 and 0.26 nm, respectively, leading to a misfit of 9.1%. The OR between the $(0001)_\alpha$ η plate and Mg matrix is such that $(11\bar{2}0)_\eta$ // $(1\bar{1}00)_\alpha$, $[0001]_\eta$ // $[0001]_\alpha$. The polygon-shaped η phase; precipitate 4 shows a rectangular cross-section with two groups of facets parallel to the $(0001)_\alpha$ and $(1\bar{1}00)_\alpha$, respectively, Fig. 13c. Close inspection of broad interface on the $(0001)_\alpha$ reveal an atomically flat plane with the Zn-rich columns periodically arranged along the $[1\bar{1}00]_\alpha$; the distance between two neighboring columns is measured to be ~ 0.87 nm. The $(3\bar{3}02)_\eta$ plane matches well with the $(1\bar{1}01)_\alpha$ plane, indicating a fully coherent interface in this region. The OR between the polygon-shaped η phase and Mg matrix is such that $(0001)_\eta$ // $(0001)_\alpha$, $[11\bar{2}0]_\eta$ // $[11\bar{2}0]_\alpha$. The lath-like η phase; precipitate 5 shows two group of facets with the long sides parallel to the $(\bar{1}103)_\alpha$ which tilt ~ 32° away from the $(0001)_\alpha$, Fig. 13d. The atomic resolution image of interfacial structure along the long side also shows a fully coherent interface with the Zn-riched columns periodically separated by ~ 1.02 nm. The OR between the lath-like η phase and the matrix is such that $(01\bar{1}0)_\eta$ // $(\bar{1}103)_\alpha$, $[0001]_\eta$ // $[11\bar{2}0]_\alpha$. Another lath-like η phase; precipitate 6 shows two group of facets with the long side tilted ~ 65° away from the $(0001)_\alpha$, Fig. 13e. The atomic resolution image of interfacial structure along the long side also shows a fully coherent interface with the $(\bar{4}222)_\eta$ plane matches well with the $(1\bar{1}01)_\alpha$ plane. The OR between this lath-like η phase and Mg matrix is expressed as $[10\bar{1}3]_\eta$ // $[11\bar{2}0]_\alpha$ and $(2\bar{4}20)_\eta$ slightly tilts 4.8° away from $(0001)_\alpha$. Fig. 13f shows the atomic resolution HAADF-STEM images of interfacial structures between the δ phase and Mg matrix taken from the $[0001]_\alpha$. The broad plane parallel to the $(1\bar{1}00)_\alpha$ is atomically flat and fully coherent with the Mg matrix. The OR between the δ phase and Mg matrix is such that $(100)_\delta$ // $(1\bar{1}00)_\alpha$, $[001]_\delta$ // $[0001]_\alpha$.

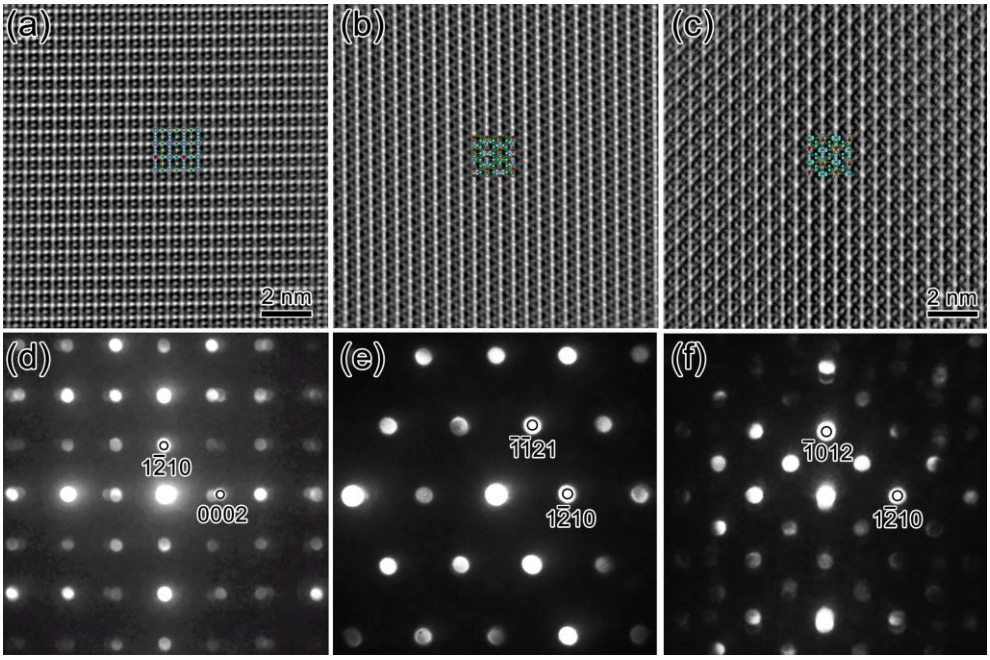

Fig. 11. (a-c) atomic resolution HAADF-STEM images and (d-f) corresponding NBED patterns of the equilibrium η phase taken from $[10\bar{1}0]_\eta$, $[10\bar{1}3]_\eta$ and $[10\bar{1}1]_\eta$ respectively.

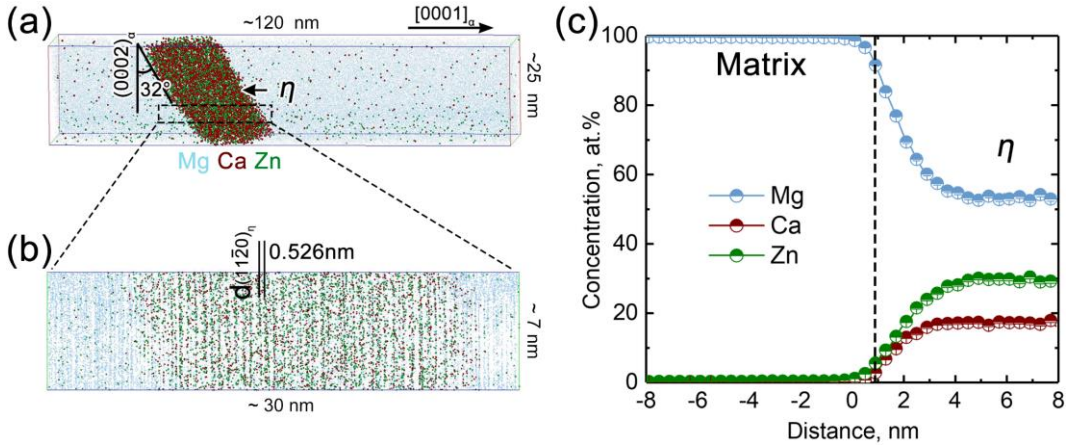

Fig. 12. (a) 3D atom maps of Mg, Ca and Zn of a η precipitate after aging at 200 °C for 300 h. (b) enlarged 2D projection of the selected region in (a). (c) proximity histogram of the η precipitate.

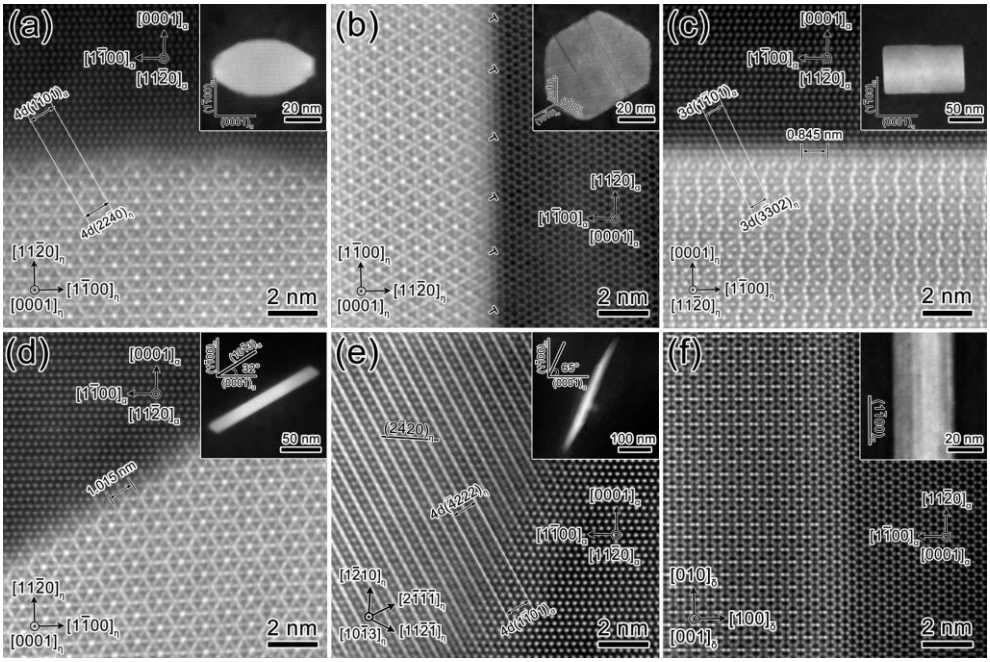

Fig. 13. Atomic resolution HAADF-STEM images of interfacial structures between the (a-e) η and (f) δ phases and Mg matrix. Low magnification HAADF images of precipitates are inserted in the upper-right parts. Note that electron beam is parallel to (a, c, d, and e) the $[11\bar{2}0]_\alpha$ and (b, f) $[0001]_\alpha$, respectively.

5.4 Discussion

In this work, in-depth characterization was performed for the precipitation process of the Mg-0.3Ca-0.6Zn alloy during isothermal aging at 200 °C, and the structures of the precipitates using STEM and 3DAP analyses. In contrast to the results of previous reports., the present work demonstrates the formation of a series of hitherto

unreported metastable phases i.e. η'', η', η_1, η_2 and equilibrium δ phase. Besides, the equilibrium η phase is determined to have a hexagonal structure with space group of $P6_3/mmc$ and lattice parameters of a = 1.00 nm, c = 1.01 nm and a composition of $Mg_9Zn_4Ca_3$, which is different from the commonly acknowledged $Mg_6Ca_2Zn_3$; space group $P\bar{3}1c$, a = 0.97 nm, c = 1.0 nm [9,10]. Based on the above observations, following precipitation sequence is proposed;

$$\text{S.S.S.S} \rightarrow \text{solute clusters} \rightarrow \text{G.P. zones} \rightarrow \eta'' \rightarrow \eta' \rightarrow \eta_1 \rightarrow \eta.$$
$$\eta'' \rightarrow \eta_2 \rightarrow \delta.$$

Figure 14 schematically illustrates the precipitation evolution in the Mg-0.3Ca-0.6Zn alloy during isothermal aging at 200 °C viewed along the zone axis of $[11\bar{2}0]_\alpha$. In the peak-aged condition; 0.3 h, a dense dispersion of monolayer G.P. zones form on the $(0002)_\alpha$ planes of the α-Mg matrix, Fig. 2b. These G.P. zones are fully coherent with the matrix, and shows a small lattice misfit of -0.032 along the $[0001]_\alpha$, thus resulting in a high nucleation rate and number density [18]. Since no precipitate is detected before the peak-aged condition, Fig. 2a, the G.P. zones are supposed to originate from the very tiny clusters which may form in the early stage of aging [19]. Following 2 h aging, the fine monolayer G.P. zones gradually evolve to the larger η'' phases with a thickness equivalent to single unit cell height of the α-Mg, Fig. 5a-c. The η'' phase has a slightly lower normal misfit of -0.029 than the G.P. zones due to the increased volumetric strain with aging time. With the continued aging to 10 h, a part of η'' plates can transform to the η' plates by further solute diffusion and lattice accommodation with the normal misfit slightly increased to -0.035, Fig. 5d-f. Considering that both η'' and η' phases have similar lattice misfits with the Mg matrix, we can understand that these two phases may co-exist in the later aging stages. Upon 100 h aging, the η' and η'' phases tend to form in pairs and stacks with irregular interspacing of 3─6 α-Mg layers, Fig. 6. The volumetric strain induced by these plate pairs or stacks is much larger than that of single plates, thus the number density of the precipitates is significantly reduced in order to moderate the total strain energy of the system. Besides, some η'/η'' single plates or pairs may transform to the larger η_1 or η_2 basal platelets with a thickness of 3 to 5-unit cell heights, Fig. 7. The thickening of these η_1 and η_2 phases can proceed by the replicated stacking of η'/η'' unit cells on the one side of single plates, or the in situ structural transformation within the interspace of plate pairs, Fig. 7e-j. The η_1 phase shows a higher normal misfit of -0.071 along the $[0001]_\alpha$ than the η' phase due to the increased plate thickness, which leads to greater strain energy, Fig. 8a and b. Considering the board coherent interface and the uneven distribution in the matrix, these large basal plates may nucleate at dislocations which might have disappeared during the prolonged aging [20]. The η_2 phase is fully coherent with the Mg matrix; not only within the $(0002)_\alpha$ plane but also along the $[0001]_\alpha$, and the shear strain associated with the formation of the η_2 plate is approximately zero, Fig. 8d and e, thus resulting in a higher thickening rate vertically to the $(0002)_\alpha$ plane [21]. After an extend aging of 1000 h, almost all the metastable precipitates have transformed into the equilibrium η in majority and minor δ phases, Fig. 9. The η phase are unevenly distributed in the matrix with five different shapes and orientation relationships, while the δ phase exclusively shows a rod shape along the $\langle 11\bar{2}0\rangle_\alpha$, Fig. 13.

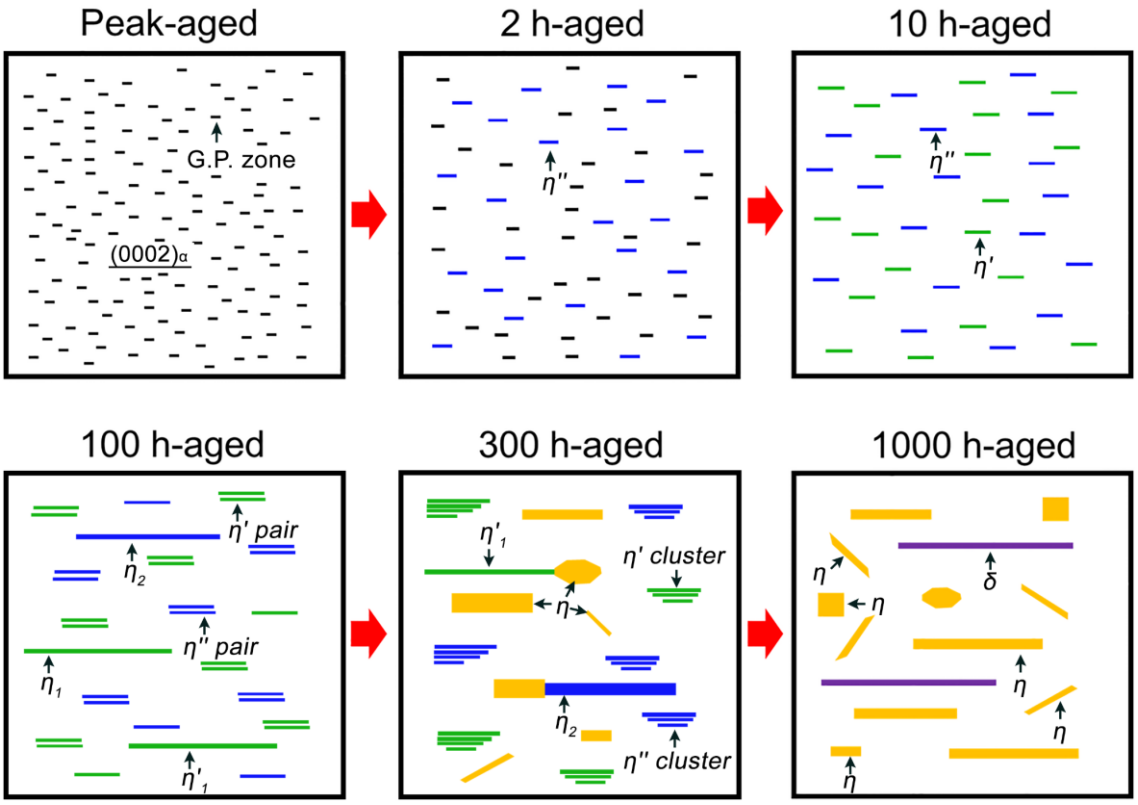

Fig. 14. Schematic illustration of the precipitate evolution in the Mg-0.3Ca-0.6Zn alloy during isothermal aging at 200 °C. Note that the perspective view of the precipitates is along the $[11\bar{2}0]_{\alpha}$ of Mg matrix.

The structures and compositions of precipitates during the 200 °C aging process are carefully characterized based on the combination of HAADF-STEM imaging and 3DAP analysis. The detailed information is summarized in Table 4. The G.P. zone is a monolayer plate with an internally ordered structure; a = 0.56 nm with a chemical composition of Mg_4CaZn, Fig. 4. However, these monolayer G.P. zones are not thermally stable at 200 °C, which quickly transform into the η'' phases with single unit cell height after the peak-aged condition. The η'' phase is proposed to have an ordered hexagonal structure; $P\bar{6}2m$, a = 0.56 nm, c = 0.51 nm with a chemical composition of $Mg_{11}Ca_2Zn$, Fig. 5a-c, which is similar to that reported γ″ phase in the Mg-1Gd-0.4Zn (at.%) alloy [19]. With the prolonged aging, a part of η'' phase evolve to the η' phase with atomic positions in the middle layer shifted a distance of $\sqrt{3}/6$ along $\langle 1\bar{1}00\rangle_{\alpha}$; $P\bar{6}2m$, a = 0.57 nm, c = 0.50 nm and a composition of $Mg_7Ca_2Zn_3$, Fig. 5d-f, which is analogous to those reported for the γ″ phase in the Mg-1.2Gd-1.8Zn or Mg-1.8Y-0.5Ag-0.4Zn-0.2Zr (at.%) alloys [13,14]. Note that the aforementioned two structures of the γ″ phase in the Mg-RE-Zn alloys are still controversial due to different HAADF-STEM observations or DFT calculations [19,22]. However, the present work clearly shows that these two structures can co-exist in the Mg matrix due to a small difference of lattice misfit. Subsequently, the η'' and η' phases individually form in pairs and stacks, Fig. 2d-e and 6. A similar paired or stacked plates structures have been observed in the Mg-RE-Zn alloys and Al-Cu alloys which refers to the G.P. II zones [14,23]. It is distinguished from the G.P. II zone which exclusively involves three Al matrix planes separated by two Cu-rich planes, the plate pairs or stacks in the Mg alloys are composed of η'' or η' phases which are irregularly spaced by the α-

Mg planes. However, an interspacing of five α-Mg layers is mostly observed within these multilayer structures, indicating a close relation to the following transformation to the η_1 or η_2 phases, Fig. 7h-j. The η_1 phase has an ordered hexagonal structure; P$\bar{6}$2m, a = 0.57 nm, c = 1.04 nm and a composition of $Mg_{17}Ca_4Zn_5$, Fig. 8a-c, which is similar to that recently reported in a high-pressure synthesized $Mg_{97}Zn_1Yb_2$ alloy [24]. The η_2 phase shows a long-period stacking structure with 14 closely packed planes in the unit cell; P$\bar{6}$2m, a = 0.58 nm, c = 3.49 nm and a composition of $Mg_{59}Ca_8Zn_{11}$, Fig. 7d-f, which is analogous to the 14H structure that has been widely observed in the Mg-RE-Zn alloys [25]. To the best knowledge of the authors, these thick plate-like η_1 and η_2 phases with high aspect ratios are firstly found in the present Mg alloys, which is quite similar to the θ' phase that has been widely studied in the Al-Cu alloys due to its great contribution to the strengthening [26]. With extended aging, the equilibrium η and δ precipitates with different orientations is predominantly contained in the α-Mg matrix, Fig. 9. The crystal structure of the η phase is characterized by combination of atomic HAADF-STEM imaging, NBED patterns and 3DAP, indicating a hexagonal structure; $P6_3/mmc$, a = 1.00 nm and c = 1.01 nm and a composition of $Mg_9Ca_3Zn_4$, Fig. 10a-c and 12. Previous studies suggested that the η phase has a trigonal structure; , a = 0.97 nm, c =1.01 nm and a composition of $Mg_6Ca_2Zn_3$ [10].

Table 4 Composition, space group and lattice parameters of strengthening precipitate phases in the Mg-0.3Ca-0.6Zn alloys.

Phase	composition	Structure	Lattice parameter, nm
G.P. zone	$Mg_2(Ca,Zn)$	_	a = 0.56 nm
η''	$Mg_{11}Ca_2Zn_3$	P$\bar{6}$2m	a = 0.56 nm, c = 0.51 nm
η'	$Mg_7Ca_2Zn_3$	P$\bar{6}$2m	a = 0.57 nm, c = 0.50 nm
η_1	$Mg_{17}Ca_4Zn_5$	P$\bar{6}$2m	a = 0.57 nm, c = 1.04 nm
η_2	$Mg_{10}Ca_1Zn_2$	P$\bar{6}$2m	a = 0.58 nm, c = 3.49 nm
η	$Mg_9Ca_3Zn_4$	$P6_3/mmc$	a = 1.0 nm, c = 1.01 nm
δ	$Mg_9Zn_2Ca_1$	P/mmm	a = 1.01 nm, b = 1.11nm, c = 0.55 nm

Since the morphology and variants number of precipitates in a defined orientation relationship are associated with the symmetry of intersection point group between the precipitate and the matrix [27], the symmetry analysis is thus employed to identify the proposed structure of the η phase, Figure 15. For the most commonly observed OR between the η phase and the matrix; $(11\bar{2}0)_\eta$ // $(0001)_\alpha$, $[0001]_\eta$ // $[11\bar{2}0]_\alpha$, a total of three crystallographically equivalent variants are observed in the matrix which refer to the lens-like precipitates (precipitate 1) with the long axis parallel to the $\langle 11\bar{2}0\rangle_\alpha$. If the point group of the η phase is $\bar{3}$1m as reported previously, the common symmetry element is a two-fold axis with a mirror plane normal to it, Figure. 15a. The intersection point group is defined as 2/m with an order of 4. Since the point group of the matrix phase is 6/mmm and of order 24, then symmetry requires 24/4 or six variants of the lens-like η phase in the matrix, which is not consistent with the experimental observations, Fig. 9b. In contrast, the intersection point group is mmm if the point group of the η phase is 6/mmm as indicated in the present work; the common symmetry

elements are three two-fold axes with three mirror planes normal to the individuals, Figure. 15b. Thus, symmetry requires 24/8 or three variants in the matrix which is clearly supported by the experimental observations. Moreover, the observed precipitate shape along the $[0001]_{\eta}$ is well matched with the symmetry required pinacoid shape, which further verifies the validity of the proposed structure [28]. The δ phase is a hitherto unreported phase with an orthorhombic structure; P/mmm, a = 1.01 nm, b = 1.11 nm and c = 0.55 nm and a composition of $Mg_9Zn_2Ca_1$. Similarly, an intersection point group of mmm is also determined from the observed OR; $(100)_{\delta}$ // $(1\bar{1}00)_{\alpha}$, $[001]_{\delta}$ // $[0001]_{\alpha}$. The number of variants is thus expected to be three, which is also consistent with the experimental observations, Figure. 15c.

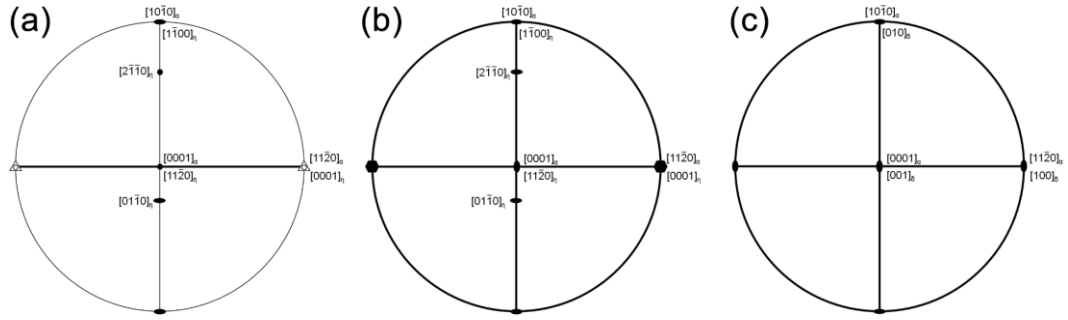

Fig. 15 Stereographic projections of the orientation relationship between the precipitate phases and the Mg matrix. (a,b) the η phase with the $\bar{3}$1m and 6/mmm point groups correspond to the OR such that $(11\bar{2}0)_{\eta}$ // $(0001)_{\alpha}$, $[0001]_{\eta}$ // $[11\bar{2}0]_{\alpha}$, respectively. (c) the δ phase with the mmm point group corresponds to the OR such that $(100)_{\delta}$ // $(1\bar{1}00)_{\alpha}$, $[001]_{\delta}$ // $[0001]_{\alpha}$.

5.5 Conclusion

The precipitation process and the structures of precipitates in the Mg-0.3Ca-0.6Zn alloy have been systematically studied with a combined use of HAADF-STEM imaging and 3DAP analysis. The main outcomes are summarized as follows;

1. Precipitation during isothermal aging at 200 °C involves the evolution from the G.P. zones to the equilibrium η and δ phases, and especially the formation of a series of hitherto unreported metastable phases; η'', η', η_1 and η_2 in the intermediate process. The precipitation sequence is proposed as:

$$\text{S.S.S.S} \rightarrow \text{solute clusters} \rightarrow \text{G.P. zones} \rightarrow \eta'' \rightarrow \eta' \rightarrow \eta_1 \rightarrow \eta.$$
$$\text{G.P. zones} \rightarrow \eta_2 \rightarrow \delta.$$

2. The η'' and η' phases form as fine $(0001)_{\alpha}$ plates with a thickness of single unit cell height. The η'' precipitate has an ordered hexagonal structure; P$\bar{6}$2m, a =0.56 nm, c =0.51 nm and a composition of $Mg_{11}Ca_2Zn_3$, while η' has a P$\bar{6}$2m structure; a = 0.57 nm, c = 0.51 nm and a composition of $Mg_7Ca_2Zn_3$. The orientation relationship between η'' and η' phases and Mg matrix is the same as that of the G.P. zone, which is such that $(0001)_{\eta'', \eta'}$ // $(0001)_{\alpha}$, $[10\bar{1}0]_{\eta'', \eta'}$ // $[11\bar{2}0]_{\alpha}$.

3. The η'' and η' precipitates tend to form in pairs and stacks on the basal planes after 100 h-aging at 200 °C. The irregular spacing between the neighboring η''/η' plates indicate that these plate pairs and stacks are not defined as new phases, while a specific five inter-layer spacing structure may play as the precursor of the η_1 or η_2 phase.

4. The η_1 and η_2 phases lying on the $(0002)_\alpha$ planes have a large aspect ratio; ~ 150 : 1 with a thickness of 3 to 5-unit cell heights. The η_1 and η_2 phases have a similar $P\bar{6}2m$ structure but different lattice parameters and compositions; a = 0.57 nm, c = 1.04 nm, $Mg_{17}Ca_4Zn_5$ and a = 0.58 nm, c = 3.49 nm, $Mg_{59}Ca_8Zn_{11}$, respectively. The orientation relationship between the η_1, η_2 phases and Mg matrix is such that $(0001)_{\eta_1/\eta_2}$ // $(0001)_\alpha$, $[0001]_{\eta_1/\eta_2}$ // $[11\bar{2}0]_\alpha$.

5. Prolonged aging up to 1000 h leads to the formation of predominant equilibrium η phase; $P6_3/mmc$, a = 1.00 nm, c = 1.01 nm with a composition of $Mg_9Ca_3Zn_4$, and sparsely distributed δ $\langle 11\bar{2}0\rangle_\alpha$ rods; P/mmm, a = 1.01 nm, b = 1.11 nm and c = 0.55 nm with a composition of $Mg_9Zn_2Ca_1$. The η phase has five different shapes and orientation relationships with the Mg matrix; the most commonly observed one is such that $(11\bar{2}0)_\eta$ // $(0001)_\alpha$, $[0001]_\eta$ // $[11\bar{2}0]_\alpha$, while the orientation relationship between the δ phase and Mg matrix is such that $(100)_\delta$ // $(1\bar{1}00)_\alpha$, $[001]_\delta$ // $[0001]_\alpha$.

Reference

[1] J. Hirsch, T. Al-Samman, Superior light metals by texture engineering: optimized aluminum and magnesium alloys for automotive applications, Acta Mater. 61 (2013) 818–843.

[2] K. Hono, C.L. Mendis, T.T. Sasaki, K. Oh-ishi, Towards the development of heat-treatable high-strength wrought Mg alloys, Scr. Mater. 63 (2010) 710–715.

[3] T. Bhattacharjee, B.-C Suh, T.T. Sasaki, T. Ohkubo, N.J. Kim, K. Hono, High strength and formable Mg–6.2Zn–0.5Zr–0.2Ca alloy sheet processed by twin roll casting, Mater. Sci. Eng. A 609 (2014) 154–160.

[4] S.J. Park, H.C. Jung, K.S. Shin, Deformation behaviors of twin roll cast Mg-Zn-X-Ca alloys for enhanced room-temperature formability, Mater. Sci. Eng. A 679 (2017) 329–339.

[5] M.Z. Bian, T.T. Sasaki, B.C. Suh, T. Nakata, S. Kamado, K. Hono, Development of heat-treatable high-strength Mg–Zn–Ca–Zr sheet alloy with excellent room temperature formability, in: D. Orlov, V. Joshi, K.N. Solanki, N.R. Neelameggham (Eds.), Magnes. Technol. 2018, Springer International Publishing, Cham, 2018, pp. 361–364.

[6] J.F. Nie, Precipitation and hardening in magnesium alloys, Metall. Mater. Trans. A 43A (2012) 3891–3939.

[7] K. Oh-ishi, R. Watanabe, C.L. Mendis, K. Hono, Age-hardening response of Mg–0.3 at.% Ca alloys with different Zn contents, Mater. Sci. Eng. A 526 (2009) 177–184.

[8] D.H. Ping, K. Hono, J.F. Nie, Atom probe characterization of plate-like precipitates in a Mg–RE–Zn–Zr casting alloy, Scr. Mater. 48 (2003) 1017–1022.

[9] J.C. Oh, T. Ohkubo, T. Mukai, K. Hono, TEM and 3DAP characterization of an age-hardened Mg–Ca–Zn alloy, Scr. Mater. 53 (2005) 675–679.

[10] P.M. Jardim, G. Solorzano, J.B. Vander Sande, Precipitate crystal structure determination in melt spun Mg-1.5wt%Ca-6wt%Zn alloy, Microsc. Microanal. 8 (2002) 487–496.

[11] M.Z. Bian, T.T. Sasaki, T. Nakata, Y. Yoshida, N. Kawabe, S. Kamado, K. Hono, Bake-hardenable Mg-Al-Zn-Mn-Ca sheet alloy processed by twin-roll casting, Acta Mater. 158 (2018) 278-288.

[12] J.F. Nie, Effects of precipitate shape and orientation on dispersion strengthening in magnesium alloys. Scr. Mater. 48 (2003) 1009–1015.

[13] X. Gu, T. Furuhara, T. Kiguchi, T.J. Konno, L. Chen, P. Yang, On the atomic structure of γ″ phase in Mg-Zn-Gd alloy, Scr. Mater. 146 (2018) 64–67.

[14] Y.M. Zhu, K. Oh-ishi, N.C. Wilson, K. Hono, A.J. Morton, J.-F. Nie, Precipitation in a Ag-containing Mg-Y-Zn Alloy, Metall. Mater. Trans. A 47 (2016) 927–940.

[15] J.P. Morniroli, J.W. Steeds, Microdiffraction as a tool for crystal structure identification and determination, Ultramicroscopy 45 (1992) 219–239.

[16] B.F. Buxton, J.A. Eades, J.W. Steeds, G.M. Rackham, The symmetry of electron diffraction zone axis patterns, Philos. Trans. Royal Soc. A 281 (1976) 171–194.

[17] T. Hahn, International Table for Crystallography, Volume A: Space-Group Symmetry, 5th ed., Springer, New York, 2005.

[18] A. Kelly, Precipitation hardening, Prog. Mater. Sci. 10 (1963) 151–391.

[19] J.F. Nie, K. Oh-ishi, X. Gao, K. Hono, Solute segregation and precipitation in a creep-resistant Mg–Gd–Zn alloy, Acta Mater. 56 (2008) 6061–6076.

[20] K. Hono, N. Sano, S.S. Babu, R. Okano, T. Sakurai, Atom probe study of the precipitation process in Al–Cu–Mg–Ag alloys, Acta Metall. Mater. 41 (1993) 829–838.

[21] H.I. Aaronson, T. Furuhara, M.G. Hall, J.P. Hirth, J.F. Nie, G.R. Purdy, W.T. Reynolds, On the mechanism of formation of diffusional plate-shaped transformation products, Acta Mater 54 (2006) 1227–1232.

[22] H. Xie, H. Pan, Y. Ren, S. Sun, L. Wang, H. Zhao, B. Liu, X. Qi, G. Qin, Magnesium alloys strengthened by nanosaucer precipitates with confined new topologically close-packed structure, Cryst. Growth Des. 18 (2018) 5866–5873.

[23] H. Fujita, C. Lu, An electron microscope study of G.P. zones and θ′-phase in Al-1.6at%Cu crystals, Mater. Trans. 33 (1992) 892–896.

[24] N. Fujita, M. Matsushita, R. Tsukamoto, M. Yamasaki, Y. Kawamura, T. Irifune, E. Abe, The structure of a novel long-period superlattice phase in $Mg_{97}Zn_1Yb_2$ alloys, Scr. Mater. 150 (2018) 78–81.

[25] Y.M. Zhu, A.J. Morton, J.F. Nie, The 18R and 14H long-period stacking ordered structures in Mg–Y–Zn alloys, Acta Mater. 58 (2010) 2936–2947.

[26] L. Bourgeois, C. Dwyer, M. Weyland, J.F. Nie, B.C. Muddle, Structure and energetics of the coherent interface between the θ′ precipitate phase and aluminium in Al–Cu, Acta Mater. 59 (2011) 7043–7050.

[27] G.R. Hugo, B.C. Muddle, The morphology of precipitates in an A1–Ge alloy ─II. Analysis using symmetry, Acta Metall. Mater. 38 (1990) 365–374.

[28] M.J. Buerger, Application of Point-Group Symmetries to Crystals, McGraw-Hill, New York, 1971.

Chapter 6 Simultaneous achievement of high thermal conductivity, high strength and formability in Mg-Zn-Ca-Zr sheet alloy

6.1 Introduction

Lightweight magnesium (Mg) alloys with good thermal conductance and high strength are attractive for structural components in portable devices [1,2]. However, these characteristics are contradictory in commercially available wrought Mg alloys, e.g. Mg-3Al-1Zn (wt.%, AZ31) and Mg-6Al-1Zn (wt.%, AZ61) [3]; the lattice distortion induced by solute atoms can degrade the thermal conductivity due to the increased electron scattering [4]. For example, the AZ31 sheet alloy shows an adequate yield strength of above 200 MPa, while the poor thermal conductivity of ~ 86 W/(m·K), which is much lower than 158 W/(m·K) in pure Mg, may not meet the growing requirements [3].

Precipitation hardening is an effective approach to achieve the high strength and thermal conductivity simultaneously as evidenced in aluminum alloys [5]. Among various Mg alloys, Mg-Zn system is age-hardenable and shows a minimal effect on the loss of thermal conductivity; the binary Mg-Zn alloy maintains above 100 W/m·K even Zn is alloyed to 8 wt.% [6]. A Mg-2Zn-Zr (wt.%) alloy exhibits a high thermal conductivity of 132.1 W/m·K and yield strength of 196 MPa [7], while the enhancement of age hardenability is expected to further improve the properties. The trace addition of Ca into dilute Mg-Zn based alloys can significantly enhance the age-hardening response by the precipitation of Guinier Preston (G.P.) zones; a maximum hardness increment is obtained by the addition of 0.5 wt.% Ca into the Mg-1.6Zn (wt.%) cast alloy [8]. The addition of Ca is also known to weaken the strong basal texture in Mg sheet alloys, which improves the poor RT formability of sheet alloys [9]. Zr addition also leads to concurrent achievement of excellent RT formability and high strength by the formation of fine dispersion of $Mg(Zn,Zr)_2$ precipitates in fine-grained structure [10].

In this study, we fabricated a Mg-1.6Zn-0.5Ca-0.4Zr (ZXK210, wt%) sheet alloy and demonstrate a novel approach to achieve high thermal conductivity, high strength and large RT formability simultaneously. The state-of-the-art aberration corrected high-angle annular dark-field scanning transmission electron microscopy (HAADF-STEM) and three-dimensional atom probe (3DAP) analysis are used to unveil the quantitative correlation between the thermal conductivity and structure of nanoscale precipitates along with solutes distribution, which has been difficult to quantify in dilute alloys. These results are expected to give critical insights into the rational design of thermally conductive magnesium alloys with excellent mechanical properties.

6.2 Experimental

The ZXK210 alloy ingot was prepared by induction melting using a high-purity pure Mg, ZK60 (Mg-5.5Zn-0.5Zr, wt.%), Mg-30 wt.% Ca and Mg-34 wt.% Zr master alloys in a steel crucible under an Ar atmosphere. 10-mm-thick plates machined from the cast ingot were first homogenized at 300 °C for 4 h and then slowly heated to 450 °C (~7.5 °C/h) maintaining for 6 h, followed by water quenching. The homogenized plates were primarily rolled to ~5 mm thick at 300 °C with ~15% thickness reduction per pass. The 5 mm thick plate were further fine-rolled to ~1 mm thick sheet at 100 °C in ~23% thickness reduction per pass along with reheating at 450 °C for 5 min between each pass. The as-rolled sheets were solution-treated at 450 °C for 1h, water quenched and subsequently aged at 170 °C in an oil bath. For reference, Mg-1.6Zn-0.4Zr (wt.%, ZK20) and Mg-5Zn-0.5Ca-0.4Zr (wt.%, ZXK510) alloys were also prepared by the similar process. The age hardening response was measured by a Vickers hardness tester (Mitsutoyo HM-100) under a load of 0.3 kgf. The thermal conductivity λ (W/m·K) was measured by a Linseis LFA 1000 laser flash analyzer at 298 K. Tensile properties were evaluated at RT using an Instron 5567 tensile testing machine with an initial strain rate of 10^{-3} s^{-1}. Specimens for thermal conductivity measurements (~ ϕ10-mm disc) and tensile tests (gauge length of 12.5 mm and 5 mm in width) was machined from the solution-treated and artificially aged samples. Texture was characterized using a field emission scanning electron microscope (SEM), Carl Zeiss Cross Beam 1540EsB, equipped with an Oxford Instruments AZtec HKL electron backscatter diffraction (EBSD) system. (S)TEM observations were carried out by FEI Tecnai 20 and Titan G^2 80-200 TEMs. Thin foil samples for TEM observations were prepared by electro-polishing using an electrolyte consisting of 5.3 g LiCl, 11.2 g $Mg(ClO_4)_2$, 500 ml methanol, and 100 ml 2-butoxy-ethanol at -50 °C and 90 V. 3DAP analyses were performed using a local electrode atom probe (CAMECA LEAP 5000 XS) in voltage pulse mode at a temperature of 30K.

6.3 Results

6.3.1 Thermal conductivity and mechanical properties

Fig. 1a shows snapshots of the solution-treated ZK20, ZXK210 and ZXK510 alloy sheets after the Erichsen cupping tests at RT. The ZK20 alloy sheet show moderate RT formability with an I.E. value of 6.5 mm. The trace addition of Ca into the ZK20 alloy sheet remarkably improves the formability; an I.E. value of 8.1 mm in the ZXK210 alloy sheet is comparable to those of 6xxx series Al alloys. Further increasing the Zn content to 5 wt.%, i.e. the ZXK510 alloy sheet deteriorates the RT formability with the I.E. value significantly reduced from 8.1 to 4.5 mm. Fig. 1b exhibit the age-hardening curve of the three alloy sheets at 170 °C. The ZK20 alloy has a hardness value of 49.3 ± 0.4 HV in the solution-treated condition, and show little age hardening response during isothermal aging. The 0.5 wt.% Ca addition to the ZK20 alloy significantly enhance the age-hardening response. The hardness value of the ZXK210 alloy rises rapidly from 52.8 ± 1.6 HV;

solution-treated to a peak of 66.1 ± 1.5 HV in 4 h; T6, and then decreases to 52.3 ± 1.3 HV after 1000 h; over-aged. A further increase in the Zn content from 1.6 to 5 wt.% produces little change to the solution-treated hardness; 52.3 ± 2.1 HV but retards the age-hardening kinetics. The ZXK510 alloy reaches to a peak hardness of 68.7 ± 1.5 HV after 45 h, which is much slower than that of the ZXK210 alloy. Fig. 1c shows the variations of thermal conductivity with the aging time in the three alloy sheets. The solution-treated ZK20 alloy has a thermal conductivity of ~ 130.2 ± 0.4 W/(m·K), and remains almost unchanged during isothermal aging. The addition of Ca to the ZK20 alloy decreases the thermal conductivity from 130.2 ± 0.4 W/(m·K) to 123.3 ± 0.8 W/(m·K) in the solution-treated condition. However, the thermal conductivity of the ZXK210 alloy increases from 123.3 ± 0.8 to 128.6 ± 0.5 W/(m·K) by peak-aging at 170 °C for 4 h, and further reaches to 135.8 ± 0.6 W/(m·K) by over-aging for 1000 h. Increasing the Zn content to 5 wt.% substantially reduces the thermal conductivity of the solution-treated ZXK210 alloy from 123.3 ± 0.8 to 113.9 ± 1.1 W/(m·K). The thermal conductivity of the ZXK510 alloy rises to 123.7 ± 1.2 and 128.3 ± 0.8 W/(m·K) by 45 and 1000 h-aging, respectively.

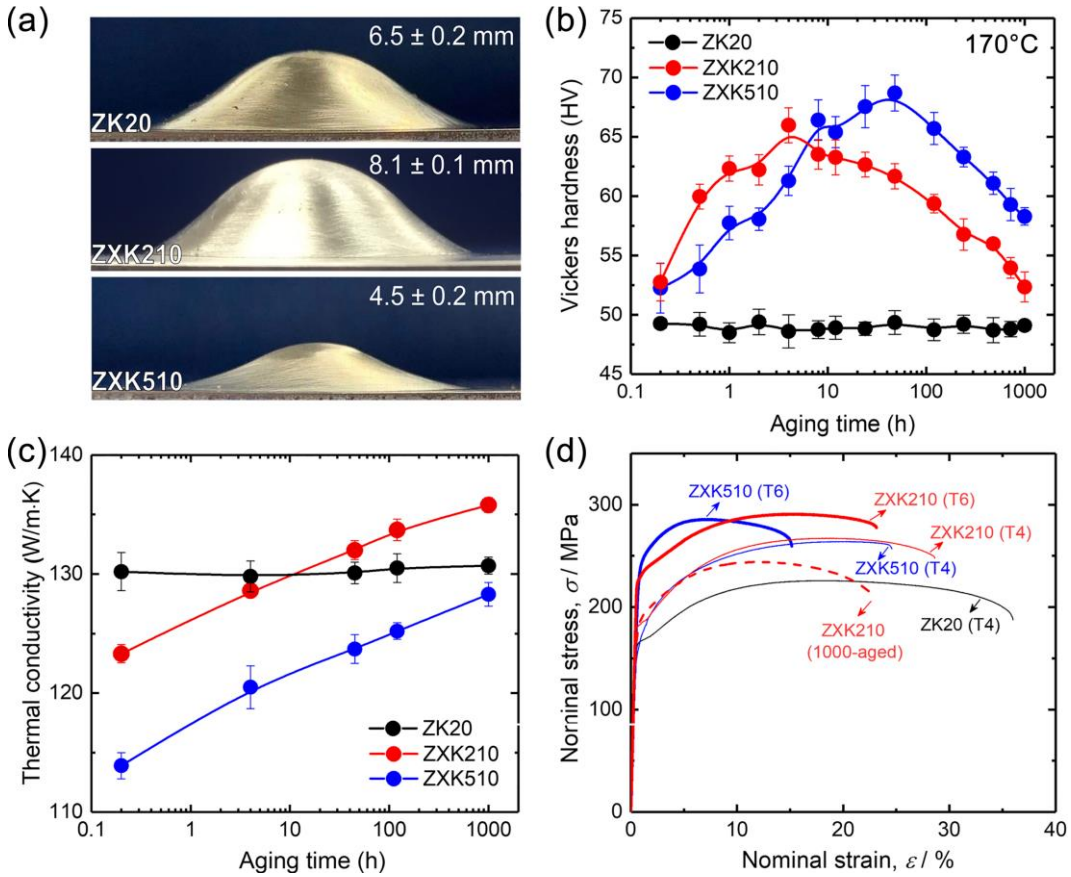

Fig. 1. (a) Snapshots of fractured solution-treated ZK20, ZXK210 and ZXK510 alloy sheets after Erichsen cupping tests at RT. (b and c) Variations in Vickers hardness and thermal conductivity as functions of aging time for the ZK20, ZXK210 and ZXK510 alloys during artificial aging at 170 °C. (d) Nominal tensile stress-strain curves for solution-treated, peak-aged and over-aged samples stretched along the RD.

Fig. 1d shows nominal tensile stress-strain curves for solution-treated, T6-treated and 1000 h-aged samples stretched along the rolling direction (RD). Table 1 summarizes the tensile yield strength, σ_{TYS}, ultimate tensile strength, σ_{UTS} and elongation to failure, ε_T of the ZXK210 alloy sheets along both RD and TD. The solution-treated ZK20 alloy sheet has the σ_{TYS} and σ_{UTS} of 159 and 225 MPa with a ε_T of 35.9% along the RD. The Ca addition to the ZK20 alloy slightly increases the yield strength with a small loss of elongation in the solution-treated condition. The solution-treated ZXK210 alloy sheet exhibits an average σ_{TYS} and σ_{UTS}; (σ_{RD} + σ_{TD}) / 2 of 160 and 255 MPa with an elongation to failure (ε_T) of 27.3%. However, the subsequent T6-treatment; 170 °C for 4 h substantially increases the average σ_{TYS} and σ_{UTS} to 202 and 278 MPa at a slight expense of ε_T to 21.9%. After extended over-aging for 1000 h, the σ_{TYS}, σ_{UTS} and ε_T are decreased to 159 MPa, 232 MPa and 22%, respectively. Further increased Zn content reduces the yield strength and elongation in the solution-treated condition but enhances the strength increment during isothermal aging. The solution-treated ZXK510 alloy sheet exhibits the σ_{TYS} and σ_{UTS} of 150 and 264 MPa with a ε_T of 24.5% along the RD, while the T6 treatment; 45 h at 170 °C remarkably increases the σ_{TYS} and σ_{UTS} to 227 and 286 MPa at an expense of ε_T to 15.1 %.

Table 1 Mechanical properties and thermal conductivity of the ZXK210 alloy sheet. S.T., T6 and O.A. stand for solution-treated, peak-aged and over-aged conditions.

Alloy sheet	Condition	RD			TD			λ, W/(m·K)
		σ_{TYS}, MPa	σ_{UTS}, MPa	ε_T, %	σ_{TYS}, MPa	σ_{UTS}, MPa	ε_T, %	
ZXK210	S.T. (450 °C/1 h)	181 ± 1	265 ± 2	28.2 ± 1.6	138 ± 2	245 ± 1	26.4± 0.8	123.3 ± 0.8
	T6 (170 °C/4 h)	227 ± 2	291 ± 1	22.6 ± 1.3	176 ± 3	264 ± 3	21.2 ± 1.2	128.6 ± 0.5
	O.A. (170 °C/1000 h)	171 ± 1	242 ± 1	23.8 ± 1.1	147 ± 1	221 ± 1	20.2 ± 2.2	135.8 ± 0.6

6.3.2 Microstructure and texture of the ZXK210 alloy sheet

Figure 2 shows EBSD inverse pole figure (IPF) maps and (0002) pole figure obtained from the solution-treated ZK20, ZXK210 and ZXK510 alloy sheets. Note that IPF maps were obtained from the middle regions of sheet plane along the transverse direction (TD), and reconstructed along the normal direction (ND). The average grain size of the ZK20 and ZXK200 alloy sheet are measured to be ~ 7.5 ± 3.5 and ~ 6.6 ± 2.8 μm, respectively, which are much smaller than that of the ZXK510 alloy sheet, ~ 13.6 ± 6.3 μm. The ZK20 alloy sheet show an RD-split texture in which the (0002) poles are mainly tilted ~ 15°–30° away from the ND toward the RD with a maximum intensity of 4.3 m.r.d. The trace addition of 0.5 wt.% Ca to the ZK20 alloy sheet

results in the development of a weaker TD-split texture; the basal poles tilt ~ 30°–45° towards the TD with the maximum intensity decreased to 3.3 mrd in the ZXK210 alloy sheets. In contrast, the ZXK510 alloy sheet shows a typical strong basal texture with the maximum intensity of basal poles; 5.3 m.r.d parallel to the ND.

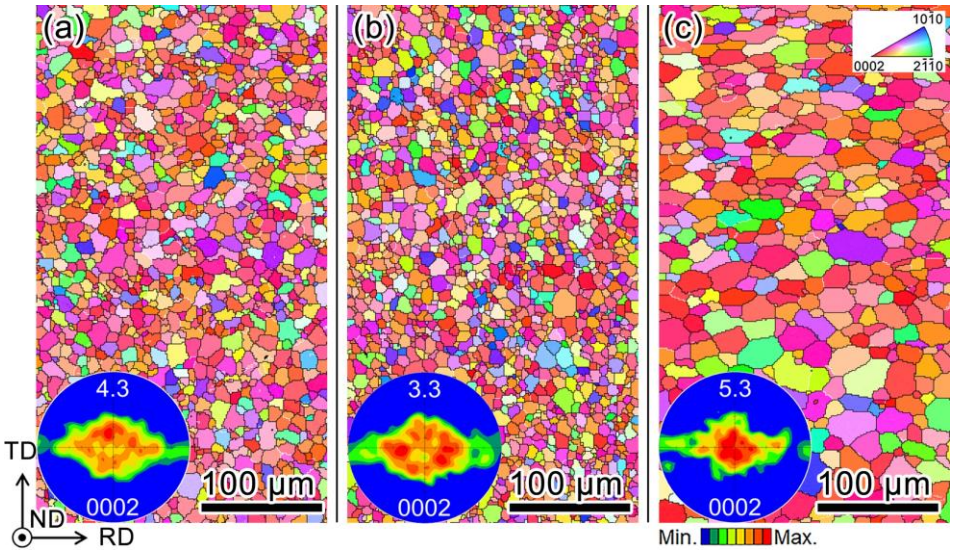

Fig. 2. EBSD IPF maps and (0002) pole figure of the solute-treated (a) ZK20 alloy, (b) ZXK210 and (c) ZXK510 alloy sheets.

Figure 3 shows bright-field TEM images of the solution-treated, T6-treated, and overaged ZXK210 alloys taken from the zone axis of $[11\bar{2}0]_\alpha$. A large number of nanoparticles are observed along grain boundaries and within grains in the solution-treated sample, Fig. 3a. The nanobeam diffraction patterns taken from the blocky and rod-shaped precipitates indicated by arrows 1 and 2 are indexed as Zn_2Zr_3 and Zn_2Zr phases, respectively [12]. For the T6-treated sample, the diffraction contrast indicates a distribution of nanoscale precipitates on the basal plane of the matrix, Fig. 3b. The diffraction patterns taken from the zone axes of $[01\bar{1}0]_\alpha$ and $[0001]_\alpha$ show continuous streaks along the $[0001]_\alpha$ direction and extra diffraction spots at the $1/3\{\bar{2}110\}_\alpha$ and $2/3\{\bar{2}110\}_\alpha$ positions, indicating the precipitation of ordered G.P. zones on the basal planes of the matrix. A number of pairs of coarse precipitates with a length of 10-50 nm are formed on the $(0001)_\alpha$ basal planes in the overaged samples, Fig. 3c. Since the diffraction patterns are similar to those observed in the T6-treated sample, the coarse precipitates are considered to be evolved from the G.P. zones.

Figure 4 shows HAADF-STEM images obtained from the T6-treated and overaged ZXK210 alloys taken from the zone axis of $[11\bar{2}0]_\alpha$. The G.P. zones are imaged with bright contrast, indicating that they are enriched with Zn and/or Ca, Fig. 4a and b. The average size of the G.P. zones in the T6-treated sample is ~ 3.2 ± 0.4 nm, which is much smaller than those in the overaged sample, ~ 35 ± 10 nm. The atomic resolution image of the T6-treated sample shows that the G.P. zones are brightly imaged as single atomic columns arranged on the $(0001)_\alpha$ planes, Fig. 4c. No misfit dislocation is observed on the surface or edge of the G.P. zone, suggesting a fully coherent interface with the Mg matrix. In contrast, a pair of basal precipitates with two brightly imaged atomic columns of ~0.2 nm distance is observed in the over-aged sample, Fig. 4d. These precipitates have an

ABCA stacking sequence along the (0001) plane, indicating the formation of metastable η' phase as reported in Mg-Gd-Zn alloys [13].

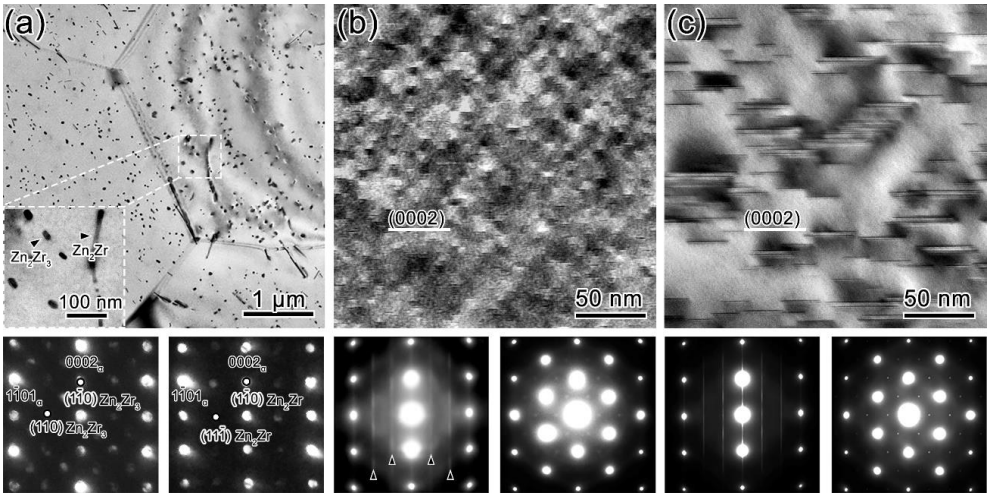

Fig. 3. Bright-field TEM images and SAED patterns obtained from the (a) solution-treated, (b) T6-treated, and (c) overaged samples. Note that the TEM images of T6-treated and 1000 h aged samples were taken from the zone axis of $[11\bar{2}0]_{\alpha}$, and the SAED patterns were recorded from the $[10\bar{1}0]_{\alpha}$, and $[0001]_{\alpha}$ directions.

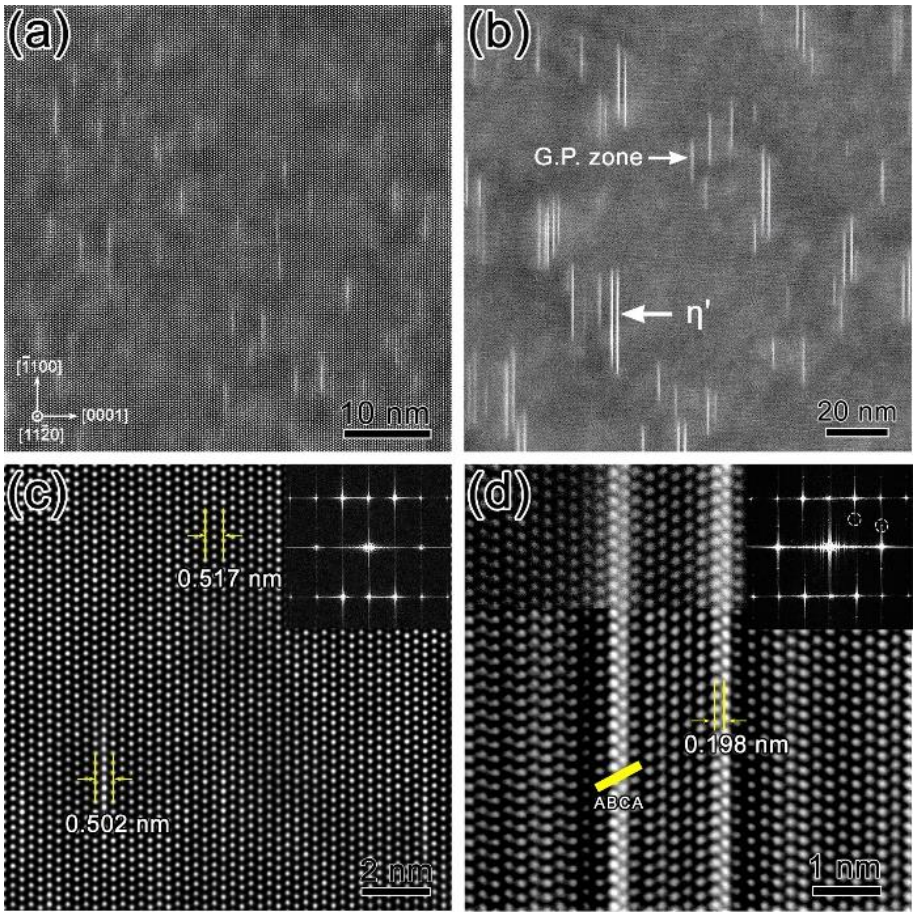

Fig. 4. HAADF-STEM images of the (a and c) T6-treated and (b and d) overaged ZXK210 alloy. Note that the images are taken from the zone axis of $[11\bar{2}0]_{\alpha}$.

Figures 5 shows the atomic resolution HAADF-STEM images of the peak-aged ZXK210 sample from the $[11\bar{2}0]_\alpha$ in which the G.P. zones appear as brightly single columns lying on the $(0001)_\alpha$ planes. Fig. S3b is the inverse fast Fourier transform (IFFT) processed fringe image corresponding to Fig. S3a showing a much clear lattice planes from $[0001]_\alpha$ direction. To measure the inter-planar distance more precisely, the intensity profiles are extracted from the selected regions across the G.P. zone and Mg matrix in Fig. S3b. The distance between the G.P. zone's two adjacent $\{0001\}_\alpha$ planes is measured to be ~ 0.502 ± 0.003 nm, while the distance between these two planes in the Mg matrix region is ~ 0.517 ± 0.015 nm which is quite near the theoretical value; 0.519 nm. Therefore, misfit strain is associated with the G.P. zone formation leading to the inter-planar distance reduction near the interface.

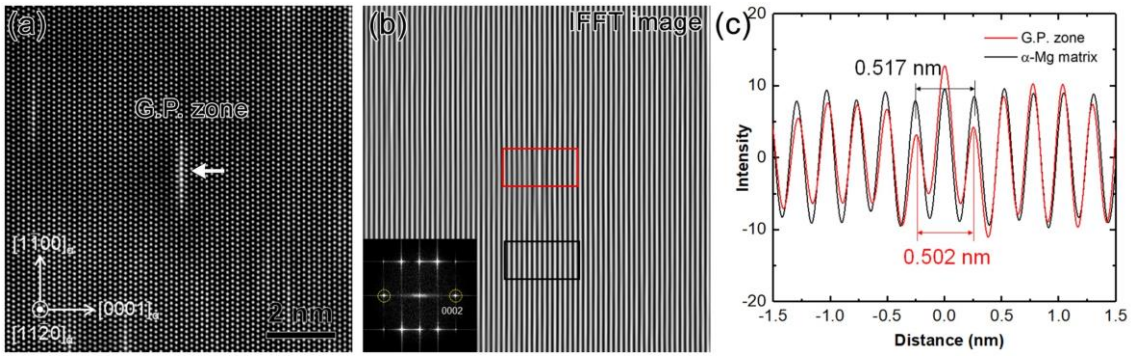

Fig. 5. (a) Atomic resolution HADDF-STEM image showing monolayer G.P. zones in the peak-aged ZXK210 sample. (b) IFFT processed fringe image corresponding to (a) and (c) the intensity profiles from selected rectangular regions shown in (b).

6.3.3 3D atom probe analysis of precipitation process

Figures 6a-c show 3D atom maps of Mg, Zn, Ca and Zr obtained from the solution-treated, T6-treated and over-aged ZXK210 alloys with volumes of 40 × 40 × 200 nm^3. Table 2 summarizes the solute content in the matrix, planar interspace and number density of precipitates in the T6-treated and over-aged samples. The concentration of Zn, Ca and Zr are 0.412, 0.241, and 0.001 at.% in the solution-treated sample. The frequency distribution of 1st-order nearest neighbor (1NN) solute atoms distance shows a consistency between experimental and random distributions, indicating that the elemental distribution in the solution treated sample is uniform, Fig. 6d. The T6-treatment resulted in the depletion of Zn and Ca in the matrix to 0.195 and 0.111 at.% due to the precipitation of fine plate-like G.P. zones with average Zn and Ca concentrations of 17.4 and 16.3 at%, Fig. 6b and e. The number density and effective planar interspace of the precipitates are calculated to be ~ 9.9 ×10^{23} m^{-3} and 8.9 nm based on $\lambda = \left(\frac{0.953}{\sqrt{f}} - 1\right) d_t$ [14]. By over-aging to 1000 h, Zn and Ca solutes are further depleted from the matrix with the contents decreased to 0.071 and 0.003 at.%, respectively. The η' phase has the average Zn and Ca concentrations of ~ 34.1 and 39.1 at.%, respectively. The number density

of the η' is ~ 1.5 ×10^{23} m^{-3}, which is much lower than that of the G.P. zones observed in the T6-treated sample, Fig. 5c and f. Such low number density leads to a larger effective planar interspace of ~ 95.1 nm.

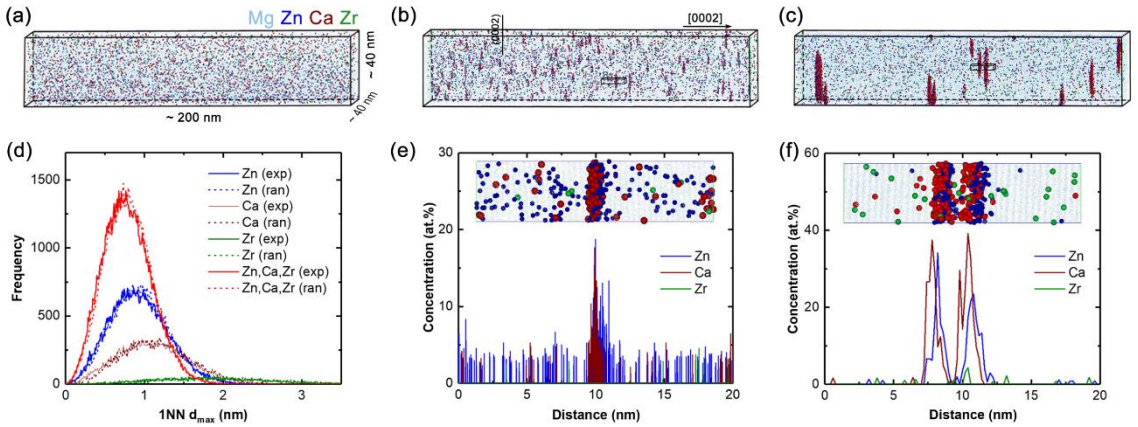

Fig. 6. (a-c) 3D atom maps of Mg, Zn, Ca and Zr obtained from the (a) solution-treated, (b) T6-treated and (c) 1000 h-aged ZXK210 samples. (d) Frequency distribution plot of 1NN distance between Zn-Zn, Ca-Ca, Zr-Zr and all the solute atoms in (a). d_{max} refers to the maximal distance separating two solutes. (e and f) The 1D concentration profiles of Zn, Ca and Zr obtained from the selected volumes in (b) and (c), respectively.

Table 2 Matrix compositions, planar interspace and number density of the precipitates in the solution-treated, T6-treated and over-aged ZXK210 alloy.

Condition	Mg (at.%)	Zn (at.%)	Ca (at.%)	Zr (at.%)	Planar interspace (nm)	Number density (× 10^{23} m^{-3})
S.T. (450 °C/1 h)	Bal.	0.412 ± 0.023	0.241 ± 0.016	0.001	_	_
T6 (170 °C/4 h)	Bal.	0.195 ± 0.012	0.111 ± 0.008	0.001	8.9	9.9
O.A. (170 °C/1000 h)	Bal.	0.071 ± 0.015	0.003 ± 0.001	0.001	95.1	1.5

6.4 Discussion

The present work reports an approach to achieve high thermal conductivity, high strength and excellent RT formability simultaneously. Figure 7 compares the thermal conductivity and yield strength for various Mg sheet alloys [2,3,7,11]. The T6-treated ZXK210 alloy sheet shows the best strength-conductivity balance among various samples; 227 MPa and 128.6 W/(m·K) in the peak-aged condition. In contrast, the ZK20 alloy sheet shows a high thermal conductivity of 130.2 W/(m·K) but a low yield strength of 159 MPa due to little age-hardening response. The ZXK510 alloy sheet exhibits a high yield strength of 227 MPa with a moderate thermal conductivity of 123.7 W/(m·K). However, considering the excellent stretch formability and the quick

age hardenability, Fig. 1a and b, the dilute ZXK210 alloy sheet would have a great potential for the development of thermally conductive Mg sheet alloys with excellent mechanical properties.

The thermal conductivity of the ZXK210 alloy increases from 123.3 to 128.6 W/(m·K) by the T6-treatment, Fig. 1b, due to the precipitation of the G.P. zones, which significantly decrease the Zn and Ca content within the matrix from 0.412 and 0.241 at.% to 0.195 and 0.111 at.%, respectively, Fig. 5 and Table 2. Since the thermal conductivity of conductive metals is mainly contributed by electrons rather than phonons [15], the depletion of solute atoms leads to the reduced electron scattering, resulting in the improvement of the thermal conductivity [4]. Besides, the effective planar interspace of precipitates increases to 95.1 nm by overaging, which is one order larger than that in the T6 treated samples, 8.7 nm, Table 2. Considering the electron mean free path in our alloy should be shorter than that in pure Mg; ~ 22 nm at RT [16], the precipitates in the over-aged sample no longer influence the thermal conductivity. Thus, the high thermal conductivity in the over-aged sample is also attributed to the increased planar interspace of precipitates.

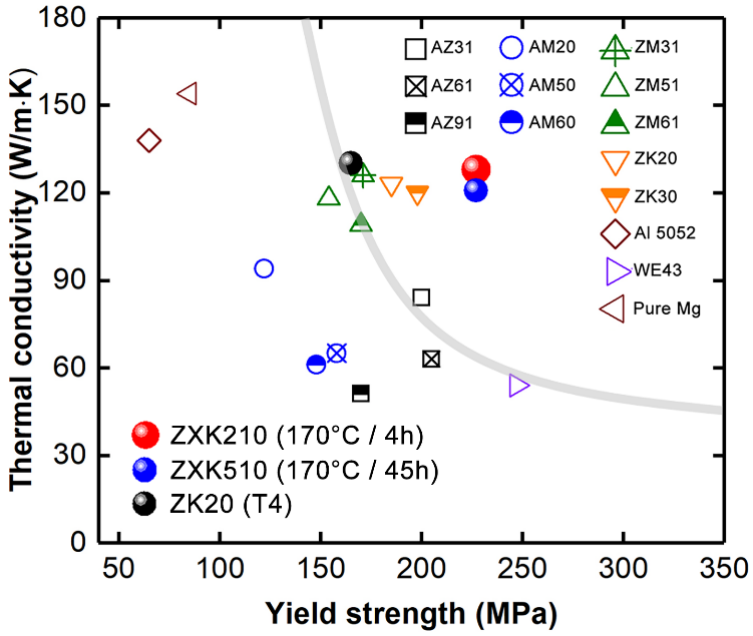

Fig. 7. Yield strength and thermal conductivity for various Mg sheet alloys. Data for other alloy sheets for comparison are from Refs. [2,3,8,12].

The precipitation of the G.P. zones also leads to the substantial improvement of the yield strength from 181 to 227 MPa at 170 °C for 4 h, Fig. 1d, leading to the excellent strength-thermal conductivity relationship ever reported in the Mg alloy sheets, Fig. 6. The solution-treated ZKX210 alloy shows excellent RT formability with an I.E. value of 8.1 mm which is much larger than those of ZK20 and ZXK510 alloys and even comparable to that of 6xxx series Al alloys [17]. The improved formability is predominantly attributed to the weak TD-split texture, Fig. 3, where a greater number of grains are favorably oriented for the operation of basal ⟨a⟩ slip and $\{10\bar{1}2\}$ tensile twinning during bi-axial loading in comparison with the RD-texture developed in the ZK20 and a strong basal texture in the ZXK510 alloy sheets [18,19]. Therefore, we conclude that the heat-treatable

dilute ZXK210 alloy is promising to develop strong and formable Mg sheet alloy with high thermal conductivity. However, the large yield asymmetry and strength degradation by over-aging are the issues to be overcome via the texture modification and improvement of age hardening behavior by microalloying.

6.5 Conclusion

This study demonstrates that the heat-treatable Mg-1.6Zn-0.5Ca-0.4Zr dilute alloy can achieve an outstanding combination of excellent RT formability, high strength of 227 MPa and high thermal conductivity of 128.6 W/(m·K), which has never been reported in other Mg sheet alloys. The simultaneous increase in the strength and thermal conductivity is associated with the precipitation of the G.P. zones enriched with Zn and Ca, resulting in the depletion of solute atoms from the matrix. Such extraordinary properties are achievable only in heat treatable dilute alloys strengthened by the precipitation of G.P. zones.

Reference

[1] Luo AA. Recent magnesium alloy development for elevated temperature applications. Int. Mater. Rev. 2004;49(1):13-30.

[2] Li S, Yang X, and Hou J et al. A review on thermal conductivity of magnesium and its alloys. J. Magnes. Alloys. 2020;8:78-90.

[3] Avedesian MM, Baker H. Magnesium and Magnesium Alloys. Ohio (OH): ASM International; 1999.

[4] Madelung O, White GK. Thermal conductivity of pure metals and alloys. Berlin: Springer; 1991.

[5] Lumley RN, Polmear IJ, Groot H, et al. Thermal characteristics of heat-treated aluminum high-pressure die-castings. Scr. Mater. 2008;58:1006-1009.

[6] Pan H, Pan F, Yang R, et al. Thermal and electrical conductivity of binary magnesium alloys. J Mater Sci. 2014;49(8):3107-3124.

[7] Li B, Hou L, Wu R, et al. Microstructure and thermal conductivity of Mg-2Zn-Zr alloy. J. Alloys Compd. 2017;722:772-777.

[8] Oh-ishi K, Watanabe R, Mendis CL, et al. Age-hardening response of Mg-0.3 at.% Ca alloys with different Zn contents. Mater. Sci. Eng. A 2009;526:177-184.

[9] Chino Y, Sassa K, Huang X, et al. Effects of Zinc Concentration on the Stretch Formability at Room Temperature of the Rolled Mg-Zn-Ca Alloys. J. Japan Inst. Metals 2011;75:35-41.

[10] Homma T, Mendis CL, Hono K, et al. Effect of Zr addition on the mechanical properties of as-extruded Mg–Zn–Ca–Zr alloys. Mater. Sci. Eng. A 2010;527:2356-2367.

[11] Shin HS, Leon MD, Parametric study in similar ultrasonic spot welding of A5052-H32 alloy sheets. J. Mater. Process. Technol. 2015;224:222-232.

[12] Gao X, Muddle BC, Nie JF. Transmission electron microscopy of Zr-Zn precipitate rods in magnesium alloys containing Zr and Zn. Philos. Mag. Lett. 2009;89(1):33-43.

[13] Nie JF, Oh-ishi L, Gao X, et al. Solute segregation and precipitation in a creep-resistant Mg–Gd–Zn alloy. Acta Mater. 2008;56:6061-6067.

[14] Nie JF, Effects of precipitate shape and orientation on dispersion strengthening in magnesium alloys. Scr. Mater. 2003;48:1009-1015.

[15] Ashcroft NW, Mermin, ND. Solid State Physics. Orlando (FL): Saunders College; 1976.

[16] Gall D. Electron mean free path in elemental metals. J. Appl. Phys. 2016;119(8):085101.

[17] Hirsch J. Aluminium alloys for automotive application. Mater. Sci. Forum 1997;242:33-50.

[18] Bian MZ, Zeng ZR, Xu SW, et al. Improving formability of Mg–Ca–Zr sheet alloy by microalloying of Zn. Adv. Eng. Mater. 2016;18:1763-1769.

[19] Suh BC, Kim JH, Hwang JH, et al. Twinning-mediated formability in Mg alloys, Sci. Rep. 2016;6:1-8.

Chapter 7 Summary and future work

7.1 Summary

Heat-treatable wrought magnesium (Mg) alloys are anticipated to stimulate the adoption of light-weight Mg products in transportation, electronics and other sectors given their potential for achieving excellent room-temperature (RT) formability and high strength simultaneously. Recently, the heat-treatable Mg-Al-Ca-Mn-Zn (AXMZ) sheet alloys have attracted considerable attention due to the superior mechanical properties comparable to those of commercial Al alloy counterparts. However, the texture weakening associated with excellent stretch formability and the short time aging for improved yield strength in this alloy system are still untraveled. This thesis firstly aims to further improve formability and strength in the AXMZ sheet alloys by the compositional optimization, and reveal the role of Zn on the texture weakening mechanism. The rapid age-hardening characteristic along with the precise precipitation sequence is then clarified in an important Mg-Ca-Zn base alloy. Subsequently, a heat-treatable Mg-Zn-Ca-Zr sheet alloy is developed to achieve not only good RT formability, but high thermal conductivity and strength simultaneously based on the thorough understanding of texture weakening and precipitation process in the Mg-Ca-Zn alloy system.

In chapter 3, the role of Zn on the mechanical properties and texture weakening of the Mg-1.2Al-0.5Ca-0.4Mn-*x*Zn (wt.%, x = 0, 0.8, and 1.6) sheet alloys are investigated. The addition of Zn substantially improves the RT stretch formability of the solution-treated samples; the index Erichsen (I.E.) value rises from 6.3 mm to 8.2 mm with increasing Zn content from 0 to 1.6 wt.%. The improved formability is mainly due to a weak basal texture with the (0002) poles split towards the transverse direction (TD), i.e. TD-split texture developed by the Zn addition. The formation of the TD-split texture is attributed to the preferential nucleation of recrystallized grains at double twin boundaries with predominantly TD-tilted orientations. Such twin boundary recrystallization is mainly associated with a much weaker solute segregation than that in the grain boundaries. The 1.6 wt.% Zn alloy shows a higher yield strength; 210 MPa in the peak-aged condition along with a larger strength increment; 40 MPa along the rolling direction (RD) than those of the Zn-free alloy; 183 and 34 MPa, which is ascribed to a higher number density of Guinier Preston (G.P.) zones within the matrix and a lower Schmid factor (SF) for basal $\langle a \rangle$ slip along the RD. The SF difference along the RD and TD induced by the TD-split texture also leads to a larger yield anisotropy in the Zn-containing alloy; the peak-aged 1.6 wt.% Zn alloy shows much higher difference of tensile yield strength; 46 MPa than that in the 0 wt.% Zn alloy; 3 MPa. Besides, a distinct yielding behavior with the typical Lüders band deformation is observed in the Zn-containing alloy. Such discontinuous yielding is mainly attributed to the impeded dislocation emission by the strong solute segregation at grain boundaries, and the followed yield point elongation is associated with a higher Schmid factor for rapid multiplication of basal $\langle a \rangle$ dislocations as well as activation of tensile twinning.

Chapter 4 studies the role of Zn on the rapid age-hardening response in the Mg-Ca-Zn base alloy. The microstructure evolution in both Mg-0.5Ca (wt.%, Zn-free) and Mg-0.5Ca-1.6Zn (wt.%, Zn-containing) alloys

during the early stages of isothermal aging at 200 °C is investigated by a combination of positron annihilation lifetime spectroscopy (PALS), coincidence Doppler broadening (CDB), and 3D atom probe (3DAP) analysis. The positron lifetime in both as-quenched Zn-free and Zn-containing alloys is almost the same as that of well-annealed pure Mg, indicating that quenched-in vacancies do not play a direct role in accelerating the aging kinetics due to the low concentration within the matrix. Instead, the Zn addition leads to the increased vacancy trapped by solute atoms, i.e. vacancy-solute complexes in the as-quenched condition, and progressive formation of solute clusters in the subsequent early aging stages as demonstrated by the increased W parameter and number density of Ca-Zn co-clusters from ~ 4.5×10^{24} to ~ 5.8×10^{24} m^{-3} after 0.1 h aging in contrast to those in the Zn-free alloy where the W parameter and number density of Ca-Ca clusters continue to reduce with the aging time; from ~ 2.2×10^{24} to ~ 1.6×10^{24} m^{-3} due to the segregation of vacancy-Ca complexes to dislocations. Considering the high mobility of vacancies-solute complex, the rapid age-hardening kinetics in the Mg-Ca-Zn system is attributed to the formation of vacancy-Ca-Zn complexes, and resultant Ca-Zn co-clusters, which further provide heterogeneous nucleation sites for a densely distributed G.P. zones.

Besides, the precipitation process of the Mg-0.5Ca-1.6Zn (wt.%) alloy during isothermal aging at 200 °C are systematically investigated in Chapter 5. The results show that the Ca and Zn enriched fully coherent monolayer G.P. zones form on the $(0001)_\alpha$ are dominant in the peak-aged condition. The fine G.P. zones then evolve to by the larger η''; a =0.556 nm, c =0.506 nm with a composition of $Mg_{11}Ca_2Zn_3$, and η' phases; a = 0.556 nm, c = 0.503 nm and a composition of $Mg_7Ca_2Zn_3$with single unit cell heights by the following over-aging. With continued aging to 100 h, single η'' and η' basal plates start to form in pairs and clusters spaced with irregular number of α-Mg layers, and some large η_1; a = 0.573 nm, c = 1.035 nm, $Mg_{17}Ca_4Zn_5$, and η_2 phases; a = 0.582 nm, c = 3.492 nm, $Mg_{59}Ca_8Zn_{11}$ also nucleate along dislocations. After 1000 h aging, only equilibrium η and δ precipitates with various orientations are unevenly distributed in the matrix. The η phase has a hexagonal structure; $P6_3/mmc$, a = 1.002 nm, c = 1.008 nm with a composition of $Mg_9Ca_3Zn_4$, while the δ phase has an orthorhombic structure; P/mmm, a = 1.002 nm, b = 1.109 nm, c = 1.008 nm and a composition of $Mg_{47}Ca_6Zn_9$. A precise precipitation sequence for the Mg-Ca-Zn system is unambiguously established as: S.S.S.S → G.P. zones → η'' → η' → η_1, η_2 → η, δ.

Based on the fundamental research carried out in the Mg-Ca-Zn base alloy, Chapter 6 reported a heat-treatable Mg-1.6Zn-0.5Ca-0.4Zr (wt.%, ZXK210) sheet alloy, which not only exhibits a large I.E. value of 8.1 mm in the solution-treated condition, but the high thermal conductivity of ~ 130 W/(m·K) and high yield strength of 227 MPa by peak-aging at 170 °C for 4h. Such an outstanding combination of superior mechanical properties and high thermal conductivity has never been achieved in other Mg sheet alloys. The excellent formability in this alloy sheet is also attributed to the TD-split texture developed by the solution-treatment, while the simultaneous increase of thermal conductivity and yield strength is associated with a dense dispersion of the G.P. zones in the peak-aged condition. As the thermal conductivity of conductive metals/alloys is strongly impaired by the electron/phonon scattering from solute-induced lattice distortion, the rapid precipitation of the G.P. zones significantly deplete the solute concentration in the matrix, thus leading to an increased thermal conductivity in the short aging time.

7.2 Future work

Based on the summary of this thesis present above, the AXMZ and ZXK dilute alloy sheets have been demonstrated to have a well-balanced good RT formability and high strength. However, the anisotropic yield strength in these alloy sheets is quite undesirable for practical use. The yield anisotropy is mainly caused by the developed TD-split texture in which basal ⟨a⟩ slip is more easily activated along the TD compared to other direction, thus leading to the anisotropic deformation behavior during tensile tests. Such anisotropic texture also greatly limits the stretch formability as well as deep drawability. Shear-band related recrystallization has been reported to induce a random texture with an isotropic pole distribution in contrast to the TD-split texture originated from double twin recrystallization. Therefore, the predominant formation of shear-bands in the as-rolled AXMZ and ZXK alloy sheets by optimizing processing parameters is expected to develop an isotropically weak basal texture, which may remove the mechanical anisotropy, and even leads to further improvement of RT formability.

In addition to the processing modification, the alloying composition should also be further optimized to improve the production efficiency and in-service performance. Currently developed AXMZ dilute alloy sheets show poor castability on the cost-efficient twin-rolling casting process due to the narrow solidification temperature windows, and poor corrosion resistance because of the co-addition of Ca and Zn. The increase of Al content is expected to solve these two issues; however, the formability and age hardenability of the alloy sheet may be impaired with the increased Al/Ca atomic ratio. Hence, future work will focus on the development of formable and age-hardenable Mg sheet alloys with high-alloying concentration towards industrial applications.

The strength improvement of the developed age-hardenable Mg alloy sheets is mainly attributed to a dense dispersion of the G.P. zones by short-time aging. However, these plate-like G.P. zones lying on the basal planes are less effective in impeding the basal ⟨a⟩ slip based on the Orowan mechanism. In contrast, the prismatic plates are intrinsically stronger obstacles for dislocation glide, and thus leading to larger strengthening as demonstrated in various Mg-RE systems, and especially some RE-free alloys such as Mg-Ca-In and Mg-Bi-Zn. The microalloying addition of In or Bi to the Mg-Al-Ca or Mg-Zn-Ca based alloy sheets may deserve for further attempts. Moreover, the factors determining the habit plane of the G.P. zones in Mg alloys are still unclear at this stage, therefore, a fundamental study on the formation mechanism of prismatic G.P. zones will shed light on the development of high-strength heat-treatable Mg alloys.

Publications

1. **Z.H. Li**, T.T. Sasaki, M.Z. Bian, T. Nakata, Y. Yoshida, N. Kawabe, S. Kamado, K. Hono, Role of Zn on the room temperature formability and strength in Mg–Al–Ca–Mn sheet alloys. J. Alloys Compd. 847 (2020) 156347.
2. **Z.H. Li**, T.T. Sasaki, T. Shiroyama, A. Miura, K. Uchida, K. Hono, Simultaneous achievement of high thermal conductivity, high strength and formability in Mg-Zn-Ca-Zr sheet alloy, Mater. Res. Lett. 8 (2020) 335-340.
3. **Z.H. Li**, T.T. Sasaki, M.Z. Bian, T. Nakata, Y. Yoshida, N. Kawabe, S. Kamado, K. Hono, Effects of Zn additions on the room temperature formability and strength in Mg-1.2Al-0.5Ca-0.4Mn Alloy Sheets, Magnesium Technology 2020, 105-111 (2020)
4. **Z.H. Li**, T.T. Sasaki, T. Ohkubo, K. Hono, On the precipitation evolution in a Mg-0.3Ca-0.6Zn alloy, J. Magnesium Alloys, Submitted.

Acknowledgements

First and foremost, I would like to express my utmost gratitude to my supervisor, Prof. Kazuhiro Hono, for giving me the opportunity to pursue my research dream in National Institute for Materials Science (NIMS), and continuous support, advice, and generous help.

I would like to give my special thanks and gratitude to Dr. Taisuke Sasaki, who has not only taught me a lot on the experiments, facility use, discussion, presentation, and paper writing, but also in the way of thinking and solving problems, and most importantly, the spirit of never compromise!

I respect and thank the committee members: Prof. Shinji Kuroda, Prof. Heeyoung Kim and Prof. Hisanori Tanimoto Takashi for their valuable time on the thesis review, defense and insightful discussions.

I would like to acknowledge Dr. Tadakatsu Ohkubo, Dr. Mingzhe Bian, Dr. Taiki Nakata, Dr. Xiandong Xu, Dr. LungJen Chiang, Dr. Devin Giddings, Dr. Yasuo Shimizu, Ms. Kyoko Suzuki, Ms. Tsuyako Hondo, Mr. Jun Uzuhashi and Mr. Yoshiya Toyooka for experiments supporting and facility training during the Ph.D. study.

I sincerely thank Dr. I-Ching Hsiao, Dr. Jheyu Lin, Mr. Yuki Iida, Mr. Xiulei Chen, Mr. Yuda Miyazaki and other members in Magnetic Materials Analysis Group and the Research Center for Magnetic and Spintronic Materials for the fruitful discussions and friendly interactions.

I also acknowledge the Junior Researcher Assistantship of National Institute for Materials Sciences for the financial supports for my Ph.D. degree attainment, and Advanced Low Carbon Technology Research and Development Program (ALCA) and Elements Strategy Initiative for Structural Materials (ESISM) for research projects in Ph.D. studies.

Last but not least, many thanks and deep gratitude to my girlfriend, Yu Wen, and my parents who accompany with me all the way from the Central South University (CSU) to the NIMS for sharing my stress and happiness in my research avenues!